

THEORETICAL MODELLING OF BORON NITRIDE COATING

N. RAKE

THE GRADUATE SCHOOL OF NATURAL AND APPLIED SCIENCES
OF
ATILIM UNIVERSITY

NAKKA LOTFY RAKE RAKE

DOCTOR OF PHILOSOPHY THESIS
IN
THE DEPARTMENT OF MECHANICAL ENGINEERING

SEPTEMBER 2022

ATILIM UNIVERSITY 2022

THEORETICAL MODELLING OF BORON NITRIDE COATING

A THESIS SUBMITTED TO
THE GRADUATE SCHOOL OF NATURAL AND APPLIED SCIENCES
OF
ATILIM UNIVERSITY

BY

NAKKA LOTFY RAKE RAKE

IN PARTIAL FULFILLMENT OF THE REQUIREMENTS
FOR
DOCTOR OF PHILOSOPHY THESIS
IN
THE DEPARTMENT OF MECHANICAL ENGINEERING

SEPTEMBER 2022

Approval of the Graduate School of Natural and Applied Sciences, Atılım University.

Prof. Dr. Ender Keskinliç
Director

I certify that this thesis satisfies all the requirements as a thesis for the degree of **Doctor of Philosophy in Mechanical Engineering, Atılım University.**

Prof. Dr. Sadık Engin Kılıç

Head of Department

This is to certify that we have read the thesis “THEORETICAL MODELLING OF BORON NITRIDE COATING” submitted by “Nakka Lotfy Rake Rake” and that in our opinion it is fully adequate, in scope and quality, as a thesis for the degree of doctor of philosophy.

Prof. Dr. Bilgin Kaftanoğlu
Supervisor

Examining Committee Members:

Prof. Dr. Hakan Argeşo
Manufacturing Eng. Department, Atılım University _____
Prof. Dr. Bilgin Kaftanoğlu
Manufacturing Eng. Department, Atılım University _____
Assoc. Prof. Dr. Özge Sürücü
Physics group, College of Engineering, Atılım University _____
Prof. Dr. Sefer Bora Lişesivdin
Gazi University, Faculty of Science Department of Physics _____
Assoc. Dr. Doç. Dr. Sezer Özerinç
Mechanical Eng. Department, METU University _____

Date: *September 8th, 2022*

I declare and guarantee that all data, knowledge and information in this document have been obtained, processed and presented in accordance with academic rules and ethical conduct. Based on these rules and conduct, I have fully cited and referenced all material and results that are not original to this work.

Name, Last name: Nakka Rake

Signature:

ABSTRACT

THEORETICAL MODELLING OF BORON NITRIDE COATING

Rake, Nakka

PhD. Mechanical Engineering Department

Supervisor: Prof. Dr. Bilgin Kaftanoğlu

2022 September, 194 Pages

In this thesis, the magnetron sputtering (MS) technique was used to deposit a thin layer of BN coating. The MS technique is one method of Physical Vapor Deposition (PVD). In the study, the sub-processes of BN coating by MS have already been thoroughly modelled. Each of these models is characterized by using very specific scales. To model rarefied gas fluxes, the Direct Simulation Monte Carlo (DSMC) numerical approach is used. At each time step, the number of molecules (number density) and their molecular velocities are summed and stored for each cell. From these summed and averaged values of number density and velocities, all the macroscopic values such as temperature, pressure and gas fluxes, are extracted. The SamadiiTM/sciv (Statistical Contact In Vacuum) program is utilized to model the BN coating in this investigation. The purpose of the modelling is an optimization of the deposition rate, coating thickness and modelling crystal structure of BN coating. The result from models is applied in experiments to approve the validation of models' results and to optimize the MS process parameters. As a result of experimental BN coatings, thickness, crystal structure, nano hardness and adhesion of the BN coating are measured. To study the structure of BN coating and understand the correlation between BN phases, low-density phase (h-BN) and high-density phase (c-BN), CASTEP (Cambridge Serial Total Energy Package) software uses to understand the background of this correlation. CASTEP software uses to calculate the elastic, electronic and phonon properties of the h-BN and c-BN phases. In the next step, the quasi-harmonic Debye model code method is used for deriving thermal behaviour from energy versus volume.

Keywords: Magnetron sputtering(MS); Physical vapour deposition (PVD); Modelling of BN coating; Direct Simulation Monte Carlo Method (DSMC); Statistical Contact in Vacuum(Sciv); Density functional theory (DFT).

ÖZ

BOR NİTRÜR KAPLAMANIN TEORİK MEDELLENMESİ

Rake, Nakka

Doktora, Makine Mühendisliği Bölümü

Tez Yöneticisi : Prof. Dr. Bilgin Kaftanoğlu

sayfa Eylül 2022, 194 sayfa

Bu tezde, Bor Nitrür ince kaplamaları için magnetron saçtırma tekniği kullanılmıştır. Magnetron saçtırma, fiziksel buhar büyütme tekniklerinden biridir. Bu araştırmada, magnetron saçtırma yöntemi teorik olarak modellenmiştir. Her model kendi ölçeklerine göre modellenmiştir. Seyreltilmiş gaz ortamlarını modellemek için doğrudan sayısal Monte Carlo yöntemi kullanılmıştır. Her zaman aralığı için, molekül sayısı (sayı yoğunluğu) ve onların hızları her hücre için toplanmıştır. Toplam ve ortalama yoğunluk ve hız değerlerinden, tüm sıcaklık, basınç, ve gaz yoğunluk makro değerleri elde edilmiştir. Bor Nitrür (BN) kaplamaların modellenmesi için bu araştırmada “Samadii™/sciv (Statistical Contact In Vacuum)” programı kullanılmıştır. Modellemenin amacı, biriktirme hızını, kaplama kalınlığını ve BN kaplamanın kristal yapısını modelleyebilmektir. Teorik modelden elde edilen sonuçlar, deneysel veriler ile karşılaştırılmış ve magnetron saçtırma yöntemi için en uygun kaplama parametrelerinin belirlenmesi için kullanılmıştır. Bu araştırmada, BN kaplama sonucu, deneylerde, kaplama kalınlığı, kristal yapı, nano sertlik ve yapışkanlık ölçülmüştür. BN kaplamanın yapısal özelliğini anlamak, düşük yoğunluklu (h-BN) ve yüksek yoğunluklu (c-BN) fazlarını modellemek için CASTEP (Cambridge Serial Total Energy Package) yazılımı kullanılmıştır. CASTEP yazılımı, h-BN ve c-BN fazlarının elastik, elektronik ve phonon özelliklerini modellemektedir. Bir sonraki adımda, harmonik benzeri Debye modeli kullanılarak termal davranış, enerji ve hacim bilgilerinden elde edilmiştir.

Anahtar Kelimeler: Magnetron Saçtırma, Fiziksel Buhar Biriktirme, Bor Nitrür Kaplamanın Modellenmesi, Monte Carlo doğrudan Benzeşim Metodu, Vakumda İstatistiksel Temas, Özgül Ağırlık fonksiyonlar teorisi

With love
To my parents: Lotfy Rake and Sanaa Najeeb

ACKNOWLEDGMENTS

I cannot express enough thanks to all of those who continually support and encourage me to complete this thesis.

I would like to thank my supervisor Professor. Dr. Bilgin Kaftanođlu with my sincere appreciation for his excellent help, guidance and support throughout my study. Thank you, for putting so much trust in me from the very beginning onwards to the end of this journey. A PhD consists of ups and downs, but you excel in offering guidance and freedom at the same time. I have learned a lot from you, on professional and personal levels. Thank you!

I would like to thank the head of the Mechanical engineering department Prof. Dr. Sadık Engin Kılıç, I admire your critical mind, positive attitude and patience to help everyone who seeks your advice. Without your assistance, I would never be a PhD.

I would like to acknowledge jury members who have substantially contributed to the progress of my work, specifically Prof. Dr. Hakan Argeőo and Assoc. Prof. Dr. Özge Sürücü, Thank you for your great help, inspiring discussions and friendship.

I would like to thank Prof. Dr. Gökhan Sürücü for guidance, support and for helping me in this research.

I would like to thank Assoc. Dr. Baybars Oral for his important support, advice and contributions to this research.

I would like to thank Assoc. Prof. Dr. Caner Őimőir for helping me in this research.

To the Metariver research team and Mr. Judith in the Samadii Company, I would like to express my sincere gratitude for their assistance, sensitivity, support, and encouragement. This encouragement motivated me to keep working through the challenging parts of this study.

I would like to thank the Metal Forming Center of Excellence and the Department of Mechanical Engineering at ATILIM University for funding and supporting this study.

I would like to thank my friends Dr. Tuđçe Hacalođlu and Asude Aydođan for providing constant support, and friendship, helping me to make the experiments and for the use of facilities in the BOREN Center of Competence for Boron Coatings.

I want to express my gratitude to my husband and my kids for their support and love. Finally, I want to express my sincere thanks to my parents, brothers, and sisters who have been there for me through the good times and bad. I appreciate their unwavering support and love, which have helped me succeed.

TABLE OF CONTENTS

ABSTRACT	iii
ÖZ	iv
ACKNOWLEDGMENTS	vi
TABLE OF CONTENTS	vii
LIST OF TABLES	xi
LIST OF FIGURES	xiii
LIST OF ABBREVIATIONS	xviii
CHAPTER 1	1
1. INTRODUCTION	1
1.1 Introduction	1
1.2 Scope of thesis	3
CHAPTER 2	4
2. BACKGROUND OF THE STUDY AND LITERATURE REVIEW	4
2.1 Introduction	4
2.2 Physical Vapour Deposition -Magnetic sputtering	5
2.2.1 Sputtering	6
2.2.2 Glow Discharge	7
2.2.3 Plasma and Secondary Electrons Emission	7
2.2.4 Deposition of Reactive Sputter	9
2.3 Boron and Boron Nitride Definitions.....	10
2.4 Literature Review.....	15
CHAPTER 3	17
3. RESEARCH METHODOLOGY	17
3.1 Modelling of Magnetron Sputtering of BN Coating	17
3.1.1 Direct Simulation Monte Carlo (DSMC) Method	19
3.1.2 The Internal Parameters of The PVD Coating Model.....	20
3.2 Modelling of BN Coating Structure and Properties.....	21
3.3 The Basic Information of Computer That Used to Submit Simulation	21
3.4 Experimental Facilities for Magnetron sputtering	22
3.4.1 PVD Magnetron Sputtering system	22
3.4.2 Substrate preparation	23
3.4.3 Experiment of Magnetron Sputtering Steps.....	24
3.4.4 Experimental Determination of Coating Thickness	25
3.4.5 Experimental Determination of Coating Characterization.....	26
3.5 Research Motivation	27
CHAPTER 4	28

4. MODELLING OF MAGNETIC AND ELECTRIC FIELDS	28
4.1 Introduction	28
4.2 Magnetic and Type of Magnetic	29
4.2.1 Modelling of the Magnetic Field in MS System	30
4.3 Modelling of the Electric Field in MS System	33
4.3.1 Modelling of Electric Field for Different Substrate Bias Voltages The result	34
4.3.2 Modelling of Electric Field for Different Applied Power Supply on the Target Plate.....	39
4.3.3 Modelling Influence of The Substrate position on the EF Profile	40
4.3.4 Modelling Influence of the Substrate Material on the EF Profile.....	47
CHAPTER 5	50
5. THEORETICAL AND EXPERIMENTAL STUDY OF BN COATING.....	50
5.1 Introduction.....	50
5.2 Theoretical Modelling of BN Coating	50
5.2.1 Geometry and Mesh	51
5.2.2 Material Define: Ar, N ₂ , BN, 2N	52
5.2.3 Assemble.....	53
5.2.4 Boundary Setup.....	58
5.2.5 Creation of Particles.....	58
5.2.6 Electric Field and Magnetic Field Import.....	60
5.2.7 Chemical Reaction	63
5.2.8 Run Information and The Launch of Model	64
5.2.9. Solver Module.....	66
5.2.10 Progress of BN Coating Model.....	67
5.2.11 The Result	68
5.2.11.1 Deposition Efficiency of Coating	68
5.2.11.2 Deposition Analysis (Deposition Rate and Thickness of coating)	69
5.2.11.3 Deposition Uniformity	74
5.2.12 Validation of Model-A1 Result Compared with The Experiment Result.....	75
5.3 Modelling Influence of The Input Parameter on The Coating Profile.....	76
5.3.1 Modelling the influence of the substrate voltage on the deposition profile....	76
5.3.1.1 The Correlation Between Different Substrate Bias Voltage and Thickness of The Coating for Experiment and Model.	83
5.3.2 Modelling the influence of the power supply on the deposition profile	84
5.3.3 Modelling Influence of The Variable Volumetric Gas Flow Rate on The Deposition Profile.....	90
5.3.4 Modelling Influence of the substrate -Position on The Deposition Profile	94
5.3.5 Modelling Influence of The Substrate Materials on The Deposition Profile...99	
5.4 2D Field Analysis of BN Coating Model	101
5.5 Optimization of BN Coating.....	108
5.5.1 Modelling Optimization of BN Coating	108
5.5.2 Magnetron Sputtering Experiments-Optimization of BN Coating	110

5.5.2.1 FTIR Measurement Results	113
5.5.2.2 Adhesion, Hardness and Friction Measurement Results for Run 209 and Run 203	115
5.6 The Results.....	119
5.6.1 The Correlation of BN Coating Models and Experiments.....	119
5.6.2 The Result of 2D Analysis of the BN Coating Model	120
5.7 The Correlation between Input Parameters and the Coating Profile	121
5.8 The Correlation between Input Parameters and the pressure, Temperature of MS System	123
CHAPTER 6	124
6. THE STRUCTURE AND PROPERTIES OF BN ALLOTROPES	124
6.1 Introduction.....	124
6.2 Literature Review.....	125
6.3 Schrödinger Equation.....	132
6.4 Hohenberg- Kohn Theorems.....	133
6.5 Kohn–Sham Method	133
6.6 Pseudopotentials	135
6.7 Crystal Structure	136
6.8 Band Theory.....	136
6.9 Mechanical Properties.....	137
6.10 Calculations of the h-BN Structure and Properties.....	140
6.10.1 Build crystals structure of h-BN	140
6.10.2 Geometry Optimization.....	141
6.10.3 Elastic Constants	141
6.10.4 Electronic Properties	144
6.10.5 Optical properties	145
6.10.6 Phonons.....	147
6.11 Calculations of the c-BN Structure and Properties	148
6.11.1 Build crystals structure of c-BN	148
6.11.2 Geometry Optimization.....	148
6.11.3 Elastic Constants	149
6.11.4 Electronic Properties	152
6.11.5 Optical properties	154
6.11.6 Phonon of (c-BN)	154
6.12 Thermodynamic properties of h-BN and c-BN Determined Using the Quasi-harmonic Debye Model.....	155
CHAPTER 7	162
7. CONCLUSION AND SUGGESTIONS FOR FUTURE WORK	162
7.1 Conclusions	162
7.2 Suggestions for future work	165
REFERENCES	167-180
APPENDIX A.....	181-188

A. THE HISTORY FILE OF MODELLING OF BN COATING (MOEL-A1)	181
APPENDIX B	189-192
B. THE RESULTS OF THE EXPERIMENTS	189
APPENDIX C	193-194
C. THE QUASI-HARMONIC DEBYE MODEL CODE FOR THE h-BN STRUCTURE	193

LIST OF TABLES

Table 2.1 Comparison of c-BN and h-BN properties	13
Table 2.2 Classified gas flow regimes depend on Kn.....	19
Table 4.1 Boundary condition of the magnetic field	31
Table 4.2 The relative permittivity and Bulk Conductivity of different materials in the MS system	33
Table 4.3 The boundary condition of the electric field.....	34
Table 4.4 The result of the electric field for different excitations of the substrate bias voltage.....	39
Table 4.5 The result of the electric field for different power supplies and with bias substrate voltage 0 and 250 V.....	39
Table 4.6 The input parameters of modelling EF for model-E and model-E1	40
Table 4.7 The result of the electric field for multi-substrates with different positions in chamber.....	40
Table 4.8 The relative permittivity and Bulk Conductivity of different substrate materials in the MS system.....	47
Table 4.9 The input parameters of modelling EF for different substrates material....	47
Table 4.10 The result of the electric field for multi-substrates with a different type of material	47
Table 5.1 Boundary condition of MS of BN coating.....	50
Table 5.2 The result of BN coating thickness for Model-A1 compared with the experiment.	75
Table 5.3 Boundary Condition of MS Modelling and experiments for different substrate bias voltages	76
Table 5.4 Boundary Condition of MS Modelling with different power supply and substrate voltage 0 and 250 V.....	85
Table 5.5 The MS Models result -Effect of power supply on the thickness of BN coating	86
Table 5.6 The Boundary condition of MS Models with variation of gas flow rate....	90
Table 5.7 The result of MS Models with variation of gas flow rate.....	94
Table 5.8 The Boundary condition of MS Models with different T-S distances.....	94
Table 5.9 The result of MS Models with different T-S distances.....	99
Table 5.10 The Boundary condition of MS Models with different T-S distances.....	99
Table 5.11 The result of the MS Model with a different type of substrate material.	101
Table 5.12 The input parameters of the BN coating optimization -(Model-G).....	108
Table 5.13 The result of the BN coating optimization (model-G).....	109
Table 5.14 The input parameters of the BN coating optimization -(Model-G1).....	109

Table 5.15 The result of the BN coating optimization model-G1	109
Table 5.16 Compares the characteristic of the BN coating experiment Run 209 with the experiment from a literature review [94]	118
Table 5.17 The boundary conditions and results of BN coating models and experiments.	119
Table 5.18 2D field analysis of BN coating model.....	120
Table 6.1 The summarized theoretical modelling studies of BN by DFT	131
Table 6.2 The crystal systems, lattice vectors and lattice angles.....	136
Table 6.3 The Born stability criteria for different crystal phases	138
Table 6.4 The elastic constant (GPa) of h-BN	142
Table 6.5 Calculation of bulk modulus (B), shear modulus (G), Young's modulus (E), and Poisson's ratio (ν) for h-BN	142
Table 6.6 The elastic constant (GPa) of c-BN	149
Table 6.7 Calculation of bulk modulus (B), shear modulus (G), Young's modulus (E), and Poisson's ratio (ν) for c-BN	149

LIST OF FIGURES

Figure 2.1 PVD - Magnetron sputtering technique	6
Figure 2.2 Boron definition.....	10
Figure 2. 3 Periodic Table.....	11
Figure 2.4 Boron Nitride Allotropies.....	11
Figure 3.1 Steps of magnetron sputtering model	18
Figure 3.2 Parts of PVD magnetron sputtering system.....	23
Figure 3.3 Ultrasonic cleaning machine	23
Figure 3.4 PVD coating system.	24
Figure 3.5 F ₂₀ thin film thickness measurement device	25
Figure 3.6 Fourier-transform infrared spectroscopy device	26
Figure 4.1 Schematic diagram of plasma confinement for balanced and unbalanced magnetrons [90]	30
Figure 4.2 Geometry of magnetron sputtering system.....	31
Figure 4.3 Mesh of magnetic field modelling.....	31
Figure 4.4 Magnetic flux density distribution :(a) Magnetic flux density distribution in the MS system and (b) Magnetic flux density distribution on the target plate.	32
Figure 4.5 The Magnitude and direction of Magnetic field strength in the MS system.	33
Figure 4.6 The variation of voltages between the target and the substrate of Model - A1.....	35
Figure 4.7 The change of energy between the target and the substrate Model -A1...35	35
Figure 4.8 The voltage distribution in the MS system. The bias voltage is 0 V	36
Figure 4.9 The magnitude and direction of the electric field strength of Model-A1..37	37
Figure 4.10 The magnitude and direction of electric flux density Model-A1..	37
Figure 4.11 The electric field result of Model-C1. (a) The electric field strength, (b) The electric flux density.....	38
Figure 4.12 The electric field result of Model-E. (a) The electric field strength, and (b) The electric energy.	41
Figure 4.13 Voltage distribution between target plate and substrate (model-E1)	42
Figure 4.14 Modelling of Magnitude and direction of Electric Field (model-E1).	43
Figure 4.15 Energy density analysis on the substrate surface. (a) T-S distance is 80 mm and (b) T-S distance is 40 mm.	44
Figure 4.16 Electric field strength analysis on the substrate surface. (a) T-S distance is 80 mm and (b) T-S distance is 40 mm.	45
Figure 4.17 Electric field strength analysis along the path between the centre of the target plate passes through the centre of the substrate. (a) T-S distance is 80 mm and (b) T-S distance is 40 mm.	46

Figure 4.18 The electric field strength of Model-F.....	48
Figure 4.19 The electric field result of Model-F,(a) The electric flux density and (b) The electric energy.	49
Figure 5.1 Geometry of magnetron sputtering system for modelling.....	51
Figure 5.2 Mesh of magnetron sputtering system for modelling.....	52
Figure 5.3 Materials definition.....	53
Figure 5.4 The boundary condition of MS system: (a) constrained wall and (b) sputtering target	55
Figure 5.5 The boundary condition of the MS system: (a) particle inlet and (b) deposition.	56
Figure 5.6 Depart the substrate on 2D surfaces	57
Figure 5.7 Boundary condition of modelling.....	58
Figure 5.8 Creation of particles.....	58
Figure 5.9 Boltzman Distribution (velocity Vs probability density) for Ar and N ₂ in (Mod-el-A1).....	59
Figure 5.10 Export of the electric and magnetic field from Ansys Maxwell	60
Figure 5.11 Import of electric and magnetic field	61
Figure 5.12 Convert maxwell magnetic field data to Samadii/sciv magnetic field	62
Figure 5.13 Convert maxwell electric field to Samadii/sciv electric field (Model-A1)	62
Figure 5.14 Arrhenius equation of the chemical reaction.....	63
Figure 5.15 Run information of MS model	64
Figure 5.16 The applied module of the MS model	66
Figure 5.17 Progress of modelling of BN coating -Model-A1	67
Figure 5.18 Deposition efficiency of Model-A1 (t=4.8e-5 s).....	68
Figure 5.19 The average deposition rate with a 2D-area plot of Model-A1 (t=4.8e-5s)	69
Figure 5.20 The deposition rate for nanofilm and microfilm of Model-A1	70
Figure 5.21 The Ar and N ₂ particles in Model-A1.....	71
Figure 5.22 The Details of BN Particles of Model-A1	72
Figure 5.23 Deposition Efficiency of Model-A1 at Time= 1.2e-4s.....	73
Figure 5.24 The average deposition rate with a 2D-area plot of Model-A (t=1.2e-4s)	74
Figure 5.25 The uniformity with the 2D-line plot of Model-A1 at time=1.2e-4s	75
Figure 5.26 Influence of the substrate voltage on the deposition efficiency (t=4.8e-5 s)	77
Figure 5.27 Influence of the substrate voltage on the deposition rate (t=4.8e-5s).....	78
Figure 5.28 The deposition efficiency of BN particles when bias voltage=100 V at time=1.2e-4	79
Figure 5.29 The deposition efficiency of BN particles when bias voltage= 250 V at time=1.2e-4	80
Figure 5.30 The deposition rate of the substrate voltage 100 V (time=1.2e-4s)	81

Figure 5.31 The deposition rate of the substrate voltage 250 V (time=1.2e-4s)	81
Figure 5.32 The deposition rate and escaped rate of BN particles with different substrate voltages.....	82
Figure 5.33 Compare the deposition rate of the different substrate bias voltage.....	83
Figure 5.34 The substrate bias voltage vs. Thickness for models and experiments ...	84
Figure 5.35 Influence of the power supply on the deposition rate when substrate voltage is (0V).....	86
Figure 5.36 The deposition efficiency and uniformity when power supply=1200 W and substrate voltage (0V).	87
Figure 5.37 The deposition efficiency and uniformity when power supply=1500 W and substrate voltage (0V).	88
Figure 5.38 Influence of the power supply on the deposition rate at substrate voltage (250 V)	89
Figure 5.39 Influence of the variable volumetric gas when Ar: N ₂ =80:16 sccm on the deposition rate at time=4.8e-5s	91
Figure 5.40 Influence of the variable volumetric gas when Ar: N ₂ =10:2 sccm on the deposition rate at time=4.8e-5s	92
Figure 5.41 BN sputtering particles on the different volumetric flow rates of Ar and N ₂	93
Figure 5.42 Deposition rate of BN particles on different volumetric flow rates of Ar and N ₂	93
Figure 5.43 Geometry of BN modelling with different T-S distances.....	95
Figure 5.44 Deposition rate of BN coating of model-E (Sub.1 and Sub.2).....	96
Figure 5.45 Deposition rate of BN coating model-E (Sub.3 and Sub.4)	97
Figure 5.46 Thickness of BN coating Vs Substrate position (the centre point of the substrate) Model-E.....	98
Figure 5.47 Deposition rate of BN particles (Model-E1), T-S distance 40 mm	98
Figure 5.48 The 2D faces of Model-F.....	100
Figure 5.49 The chemical reaction between the BN target plate and N ₂ gas caused to produce of 2N (Model-F).....	100
Figure 5.50 Density analysis of Ar in model-A1	101
Figure 5.51 Density analysis of N ₂ in model-A1	102
Figure 5.52 Flux analysis of Ar in model-A1	102
Figure 5.53 Flux analysis of N ₂ in model-A1	103
Figure 5.54 Density and flux analysis of Ar in Model-C1, (a) Ar density and (b) Ar flux	104
Figure 5.55 Density and Flux analysis of N ₂ in model-C1, (a) N ₂ density and (b) N ₂ flux	105
Figure 5.56 The pressure of model-A1	106
Figure 5.57 The pressure of model-C1	106
Figure 5.58 Influence of bias substrate voltage on temperature distribution in the chamber, (a) model-A1 and (b) model-C1	107

Figure 5.59 The result of the BN coating model (Model-G) at optimization boundary conditions.....	108
Figure 5.60 The substrate position in experiment Run 209.....	110
Figure 5.61 Distribution of the EF between the target and the substrate with different (TSD),(a) 40 mm,(b) 100 mm,(c) 200 mm,(d) 230 mm and (e) 290 mm (Theoretical analysis of BN coating Models).....	111
Figure 5.62 Electric field strength analysis on the substrate surface as a function of TSD (Theoretical analysis of BN coating Models).....	112
Figure 5.63 FTIR analysis of D2-1 in experiment Run 203 (TSD =100 mm).....	113
Figure 5.64 FTIR analysis of D2-1 in experiment Run 209 (TSD =50 mm).....	113
Figure 5.65 FTIR analysis of D2-1 in experiment Run 217 (TSD =50 mm).....	114
Figure 5.66 Image of Adhesion measurement for substrates as a function of TSD, a.50 mm,b.100 mm ,c.200 mm ,d.230 mm and e.290 mm.	115
Figure 5.67 The scratch measurement, the residual depth and penetration depth of the substrates, a. TSD is 50 mm and b. TSD is 290 mm.	116
Figure 5.68 Result of hardness measurement as a function of TSD and thickness with different applied loads,(a) The applied load is 5 mN and (b) The applied load is 250 mN.....	117
Figure 5.69 The effect of substrate voltage and power supply on the thickness of the coating. The Ar and N ₂ flowrate is 40 and 8 sccm respectively.	121
Figure 5.70 The effect of substrate voltage and gas flow rate on the thickness of the coating at the constant power supply, The power supply is 900W.....	121
Figure 5.71 The effect of power supply and gas flow rate on the thickness of the BN coating in models at constant substrate bias voltage, The substrate bias voltage is 0V.	122
Figure 5.72 The effect of power supply and distance between target and substrate (T-S) on the thickness of the coating at constant substrate bias voltage, The bias voltage is 0V and Ar, N ₂ flowrate is 40 and 8 sccm respectively.	122
Figure 5.73 The effect of substrate bias voltage and power supply on the pressure and temperature of MS system at constant gas flow rate, The gas flow rate of Ar and N ₂ are 40 and 8 sccm.....	123
Figure 6.1 The crystal structure of h-BN, The grey atoms (N) and the green atoms (B).	141
Figure 6.2 Direction-dependent of (h-BN) (a) Young modulus, (b) linear compressibility, (c) Shear modulus, and (d) Poisson's ratio	143
Figure 6.3 Calculation of band structures	144
Figure 6.4 Calculated Density of State of h-BN	145
Figure 6.5 Calculation of dielectric function of h-BN, (real and imaginary components)	146
Figure 6.6 Phonon of h-BN.....	147
Figure 6.7 Density of Phonon State of h-BN.....	147

Figure 6.8 The crystal structure of c-BN, The grey atoms (N) and the green atoms (B)	148
Figure 6.9 Direction-dependent of (c-BN) (a) Young modulus, (b) linear compressibility, (c) Shear modulus, and (d) Poisson's ratio	151
Figure 6.10 Calculation of (c-BN) band structures and density of state by GGA functional	152
Figure 6.11 Calculation of (c-BN) band structures and density of state by HSE06 functional.	153
Figure 6. 12 Calculation of dielectric function of c-BN, (real and imaginary components).....	154
Figure 6.13 Phonon of the c-BN	154
Figure 6.14 Density of Phonon State of c-BN	155
Figure 6.15 The energy versus volume for BN with two structures h-BN and c-BN	156
Figure 6.16 The bulk modulus versus pressure for h-BN and c-BN with different temperatures	157
Figure 6.17 The volume versus pressure for h-BN and c-BN with different temperatures	158
Figure 6.18 The volume versus temperature for h-BN and c-BN with different pressure	159
Figure 6.19 The thermal expansion versus temperature for h-BN and c-BN with different pressure	160
Figure 6.20 The heat capacity versus temperature for h-BN and c-BN with different pressure	161

LIST OF ABBREVIATIONS

PVD	Physical Vapour Deposition
MS	Magnetron Sputtering
c-BN	Cubic Boron Nitride
h-BN	Hexagonal Boron Nitride
w-BN	Wurtzite Boron Nitride
r-BN	Rhombohedral Boron Nitride
e-BN	Explosive Boron Nitride
a-BN	Amorphous Boron Nitride
t-BN	Turbostratic Boron Nitride
MD	Molecular Dynamics
DFT	Density Functional Theory
MC	Monte Carlo
(DMCS)	Direct Monte Carlo Simulation
CFD	Computational Fluid Dynamic
ANN	Artificial Neural Networks
RSD2013	Reactive Sputter Deposition
SiMTra	Simulation of The Metal Transport
FEM	Finite Element Models
T-S	Target -Substrate
sciv	Statistical Contact In Vacuum
AFM	Atomic Force Microscope
SEM	Scanning Electron Microscope
FTIR	Fourier Transform Infrared Spectroscopy
Rf	Radio Frequencies
MF	Magnetic Field
EF	Electric Field
CASTEP	Cambridge Serial Total Energy Package
Induction coupled plasma pulsed laser annealing	ICP PLA

CHAPTER 1

INTRODUCTION

1.1 Introduction

Thin films are employed in a variety of fields, such as semiconductors, optical, electronic, and magnetic devices, telecommunications, biological, ornamental, and energy applications, as well as in the biomedical field. These are only a handful of the numerous, already well-known applications. An effective vacuum coating method is physical vapour deposition (PVD). PVD has been utilised to increase corrosion resistance and reduce wear.

In PVD techniques, film precursors (atoms or ions) are created through ion bombardment or heating (evaporation) (sputtering).

Both the deposition process (vapour condensation) and the transit of vapour from the source material to the substrate are carried out by physiological mechanisms with little or no chemical interaction.

Mono-layered, multi-layered, and multi-graduated coating systems, as well as unique alloy compositions and structures, can all be deposited using PVD methods.

One PVD technology is magnetron sputtering. Because phase formation is primarily driven by kinetics rather than thermodynamics in this method, low-defect-density films of high-melting-point materials can be formed on unheated substrates.

Given that it has some of the most peculiar physical and chemical characteristics of any element, boron (B) is an intriguing substance. The fundamentals of the well-known thin-film deposition technology reactive magnetron sputtering (MS) are theoretically straightforward and may be condensed into a few lines. But this seemingly straightforward event is the result of an intricate interplay between numerous physical and chemical subprocesses.

In this work, many of these subprocesses have already been in-depth modelled.

The Direct Simulation Monte Carlo (DSMC) approach is frequently referred to as the most effective numerical tool for modelling real engineering problems in a less computationally intensive environment. To model rarefied gas fluxes, the DSMC numerical approach is used. The DSMC method is used to describe the behaviour of large groups of charged particles. Particles occupy space that is divided into cells.

Particles are represented by a small number of superparticles. A weighting factor determines the number of actual particles represented by each super particle. Using the Boltzmann equation, we can simulate the system's behaviour in a self-consistent manner.

The most important feature of DSMC is the decoupling of the movement and collision procedures of the molecules.

In this investigation, Samadii™/sciv (Statistical Contact in Vacuum) package uses to interpret Magnetron Sputtering. For each time step, Samadii™/sciv employs the particle method to determine the force acting on each particle. In the next stage, it uses force and mass to calculate velocity and location. Samadii/sciv calculates the Lorentz force, which is created by the electric field, magnetic field, and particle collisions. The finite element method is used to analyse magnetic field and electric field calculations.

Modelling of Boron Nitride coating intends to improve the PVD process. This model will focus on the process of energy efficiency improvement with the sputtering technique. Based on the product and its characteristics DSMC and other techniques are used to study the BN coating profile. The results of the models are used in experiments to validate the results of the models and to optimize the MS process parameters. The thickness, crystal structure, nano hardness, and adhesion of the BN coating are measured as a result of the experimental BN coatings.

To study the structure of BN coating and understand the correlation between BN phases two packages of software are used: Density functional theory (DFT) with a plane wave basis set is used in CASTEP (Cambridge Serial Total Energy Package) software to determine the electronic characteristics of crystalline solids, surfaces, molecules, and amorphous materials. The elastic, electrical, and phonon properties of the h-BN and c-BN phases will be computed using this software.

The next phase involves determining thermal behaviour from energy against volume using the quasi-harmonic Debye model code approach.

1.2 Scope of The Thesis

- **Chapter 1** presents the introduction, objectives and the aim of this study.
- **Chapter 2** presents the background topics and a literature review relevant to this thesis.
- **Chapter 3** presents the research motivation, research procedure, and methodology.
- **Chapter 4** presents details of magnetic field (MF) and electric field (EF) modeling, Ansys Maxwell 16.0 software technique has been used to model MF and EF and explains the important criteria that should be achieved in these models.
- **Chapter 5** presents the Theoretical and Experimental Study of BN Coating. This chapter can be classified into three parts depending on the subject. In the first part, DSMCs are used to model BN coating. The second part DSMC are used to calculate the temperature, pressure and gas fluxes in the chamber of the PVD system. The third part contains the details of the experiments, the Structure and Characteristics of BN Coatings.
- **Chapter 6** presents the necessary theoretical background for the density functional theory (DFT). In addition, the definition required to calculate the most important physical properties of the material is explained in detail. CASTEP software is used to calculate the structure and properties of the h-BN and c-BN phases. The quasi-harmonic Debye model code method is used for deriving the thermal properties of h-BN and c-BN.
- **Chapter 7** presents the findings and conclusions of this thesis. Possible future work in this field is also described.

CHAPTER 2

BACKGROUND OF THE STUDY AND LITERATURE REVIEW

2.1 Introduction

Thin films are condensed layers with a thickness ranging from a few nanometers to several micrometres that have crystallized or were created through the carefully controlled condensation of atomic, molecular, or ionic species on a substrate (support material) [1,2,3]. Applications for thin films include semiconductors, optical, electronic, telecommunications, biological, energy, food, and biomedical applications [4,5].

It would be impossible to describe all areas where thin films are useful, but integrated circuits (ICS), photovoltaic solar cells, reflecting or anti-reflection coatings, and wear-resistant coatings are a few crucial packages [6]. According to the studies of company BCC, the arena marketplace for thin-film coatings reached nearly \$9.8 billion in 2015 and is predicted to attain \$11.3 billion in 2021 [7]. In addition, technological advances in this vicinity might be pushed through packages inside the fields of energy, aerospace and defence. Trends in nanotechnology and miniaturization in industry and microelectronics are candidate application areas in the coming years. The thin-film deposition is a large gain, the structure of thin film may be managed via manipulation of the atomic scale strategies [8,9]. There are many different thin-film processes, but they can be broadly divided into two types based on the physical characteristics of the species that create the films: liquid-phase (solution) deposition and vapour-phase deposition.

Chemical vapour deposition (CVD) and physical vapour deposition (PVD) are sub-categories of vapour phase deposition. Precursor gases containing the supply material are added inside the reactor and are in contact with the substrate in CVD procedures.

Numerous heterogeneous chemical events (decomposition, desorption, polymerization, etc.) occur close to or on the surface as a result of heat, plasma, or gradient changes, and their structure progressively takes the form of a solid, stable film [10–11]. On the opposite hand, in PVD strategies, film precursors (atoms or ions) are produced both through heating (evaporation) or ion bombardment (sputtering). Both vapour transportation from the source material to the substrate and deposition process (vapour condensation) take place by physiological mechanisms, with no or few chemical reactions involved [12].

Reactive PVD, which is frequently used to deposit chemicals, combines chemical and biological deposition. Precursors frequently come from a metal electrode (through evaporation or sputtering) and the breakdown of a reactive gas (the usage of thermal decomposition, plasma, etc.). PVD techniques and CVD are occasionally carried out at low pressure (below atmospheric pressure) or even in a vacuum, allowing for the environmentally friendly use of supply materials with excellent overall performance and the reduction of impurities and electricity use. The basics of magnet sputtering, one of the famous PVD technology, can be defined in element in this Chapter, because of its significance for this thesis.

2.2 Physical Vapour Deposition -Magnetic Sputtering

An effective vacuum coating method is PVD. PVD has been utilised to increase corrosion resistance and reduce wear. It is necessary for applications that have a practical purpose, such as tools, optical enhancement, ornamental items, moulds, dies, and blades. These are just a handful of the many applications that are already widely used and accepted [13–14]. This method is environmentally benign, and the machinery it uses needs little maintenance. Processes for machining heavily rely on deposition techniques.

One of the most demanding applications, machining tools needs to have properties including hot hardness, high abrasion resistance, toughness, and stiffness [15-16].

PVD may also provide coatings with a wide variety of materials and properties, outstanding adhesion, homogeneous layers, planned structures, graduated properties, controlled morphology, and more [17–18]. Mono-layered, multi-layered, and multi-graduated coating systems, as well as unique alloy compositions and structures, can all be

deposited using PVD methods. The continual fluctuation in coating qualities throughout the film is one of the process's benefits [19,20,21].

One PVD process uses magnetron sputtering (MS). Because phase formation is primarily driven by kinetics rather than thermodynamics in this method, low defect-density films of high melting-point materials can be formed on unheated substrates.

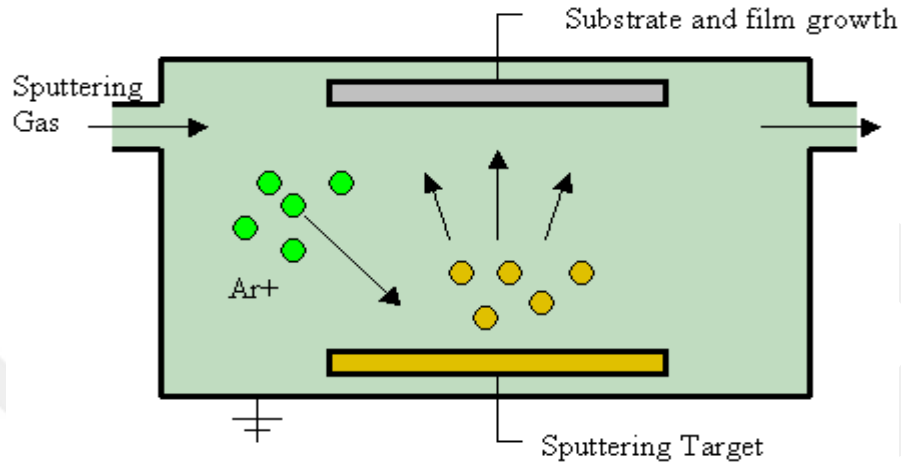


Figure 2.1 PVD - Magnetron sputtering technique

2.2.1 Sputtering

Atoms, molecules, and even clusters can be ejected when an energetic particle (atom or ion) collides with a solid surface. Sputtering is the process of generating atoms and clusters through an ion-solid contact.

According to statistics, each ion produces a certain number of sputtered particles.

These particles have specified energy and geographical dispersion when they depart a target. The target is a cathode containing the source material which is maintained at a negative potential concerning the chamber walls and the substrate in sputter deposition.

Sputter deposition is also a highly effective technique for growing all kinds of thin films with precise crystallographic orientation and micro-structure because of the employment of magnets to confine the discharge closer to the target and the use of reactive gases during deposition. The sputtering yield Y , which is defined as the number of atoms that leave the target per incident ion

$$Y = \text{sputtered particles} / \text{incident particles} \quad (2.1)$$

Nuclear collisions with the target atoms allow the bombardment particle to discharge its energy. These expelled target atoms collide with other atoms if they have enough energy; etc.

The target atoms at the surface can escape if they get enough momentum and move in the right direction to breach the surface barrier., They can sputter when they leave the target [22]. The entire sputtering efficiency, as well as the energy and angular distribution of the sprayed atoms, were theoretically described by Sigmund [23] and Thompson [24].

2.2.2 Glow Discharge

A glow discharge is formed when a gas, usually a rare gas like Ar, is present Ar+ ions are propelled towards the cathode in an electric field in this glow discharge. The energetic ions cause various interactions when they collide. The energetic Ar+ ions, for example, may produce a collision cascade in the target material. Atoms are displaced, and some of them may be able to escape to the Vapor phase from the surface [25].

2.2.3 Plasma and Secondary Electrons Emission

An electron can be expelled from the target surface to the vapour phase by blasting it. The likelihood of producing an electron in a normal sputter process is on the order of 0.1, which is known as the secondary electron emission coefficient. To ionize the Ar-atoms in the plasma, secondary electrons are required.

Electrons transfer their energy to Ar atoms in an inelastic manner by activating the Ar-internal atom's electrons. Because of the mass difference between the electrons and the Ar atoms, this is more likely than contributing to the kinetic energy of Ar.

At radio frequencies (Rf) the electrons oscillating in the glowing space have sufficient energies to cause ionizing collisions, thus reducing the dependence of the discharge on secondary electrons and lowering the breakdown voltage.

A plasma is a partially ionized gas that contains roughly equal amounts of positively and negatively charged particles as well as a varied number of neutral molecules.

The charged particles are most likely electrons and positively charged single ions.

Consequently, the number n_e of electrons divided by the sum of electrons and neutrons ($n_e + n$) indicates the degree of ionization or plasma density [26,27].

Plasma has two primary qualities that can be used to characterize it at the most basic level:

1. It is a quasi-neutral medium, with an overall density of electrons and negative ions equal to that of positively charged ions. The localized imbalance between the two may exist, but only over a very short space, which is determined by plasma properties.
2. It has a collective characteristic; charged particles in plasma interact with one another not just through collisions, but also through long-range electric and magnetic fields that these particles generate.

To demonstrate these concepts, consider a situation in which the density of negatively and positively charged species is disproportionate.

The electric field formed by the charge imbalance will cause Coulomb forces, which will cause charge rearrangement. On a macroscopic scale, plasma thus serves as an electrically neutral medium.

Debye length, D , is the characteristic distance at which a considerable charge separation may exist. It can be written as:

$$\lambda_D = \sqrt{\frac{\epsilon_0 K T_e}{C n_e}} \quad (2.2)$$

K [eV/K] is the Boltzmann constant, T_e [eV] is the electron temperature, C is the elemental electron charge, and n_e is the electron density, where ϵ_0 is the permittivity of the vacuum. In a low-temperature plasma discharge, the thermal velocity of electrons is significantly different from that of ions. The reason for this discrepancy is the formation of a boundary layer at the edge of the plasma known as the plasma sheath. If the target surface is a non-conductive or insulated conductor and is immediately negatively charged concerning the surrounding quasi-neutral plasma bulk [28].

Due to the characteristics of the plasma, a sheath region that is frequently referred to as dark space and is practically isolated from the bulk plasma region forms close to the target (where the negative potential is applied). Within that dark space, the

entire voltage drop occurs between the bulk plasma region and the target (with a negative potential of some hundred volts) [29]. Before striking the target surface there at an angle parallel to the local target surface normal, Ar⁺ ions are first accelerated to energies equivalent to the applied potential [30]. Therefore, an Ar⁺ ion incidence angle of $\theta = 0^\circ$, in general, applies for magnetron sputtering [31]. It has no contribution to plasma maintenance since it cannot be propelled by the sheath (extremely strong repulsion). Thermalized electrons make up the majority of the electrons in the plasma.

After being ejected from the target, the sputtered particles move through the plasma to the substrate.

Collisions with other particles, especially rare gas atoms, are possible throughout the journey.

Each elastic or inelastic collision results in a change in energy and direction. Following the interaction, the atom continues until it is scattered or adsorbed on a surface.

The average distance between two collisions is known as the mean free path. The mean free path can be expressed as:

$$\lambda = \frac{KT}{\sqrt{2}\pi d^2 P} \quad (2.3)$$

Where p is the pressure, d is molecular mass.

2.2.4 Deposition of Reactive Sputtering

Reactive sputter deposition is a technique for depositing films with a composition that differs from the target. Because sputtering from a ceramic target is not favoured due to the target's electrical insulating nature, this approach is employed to deposit ceramic materials. In most cases, a pure metallic target is employed to deposit the thin coating by reactive sputtering.

A compound is deposited at solid surfaces when a reactive gas is added to the sputtering system and reacts with the sputtered target material. A high deposition rate and a stoichiometric film can be achieved this way. Films can also be doped with the necessary amount of gas via reactive sputtering. Because of the difference in secondary

emission coefficient between the ceramic compound and the metal, this hysteresis effect can also be seen in the discharge voltage.

These hysteresis phenomena demonstrate that operating circumstances are not always constant but may change depending on previous operations. In addition to the history dependency, the process's intrinsic instabilities linked to its hysteresis may cause it to drift into unfavourable operating circumstances. As such, long-term operation stability is not clear. The compound synthesis on the target is what is responsible for this hysteresis behaviour [32]. The hysteresis effect for chemical adsorption of the reactive gas at the surfaces was theoretically characterised by Berg et al. and Depla et al. [33,34,35]. As was already said, the reactive gas accelerates through the cathode sheath, causing it to not only chemistry at the target but also implant itself there.

2.3 Boron and Boron Nitride Definitions

Boron (B) is a fascinating material since it has some of the most unusual physical and chemical properties of any element. Elemental B is a refractory, light substance having a melting point of 2177 °C. At room temperature, it is a non-metal that is chemically inert. It is also hard, strong, and effective in absorbing electrons. Boron is divided into isotopes ranging from B₆ to B₁₂, some of which have an extremely short half-life due to instability. There are four major allotropes of crystalline boron: γ, β, α, and T.

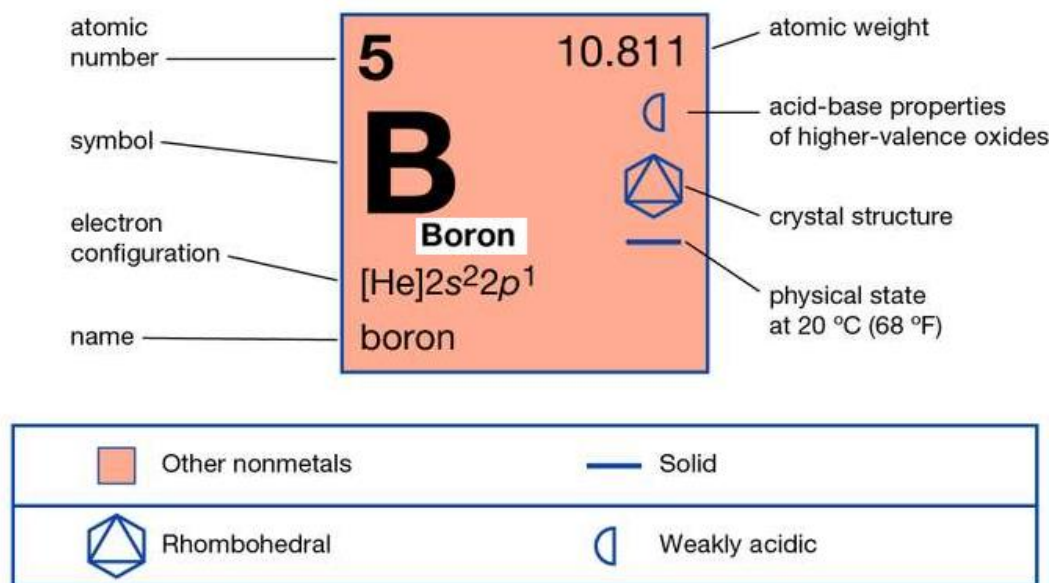


Figure 2.2 Boron definition

Periodic table of the elements

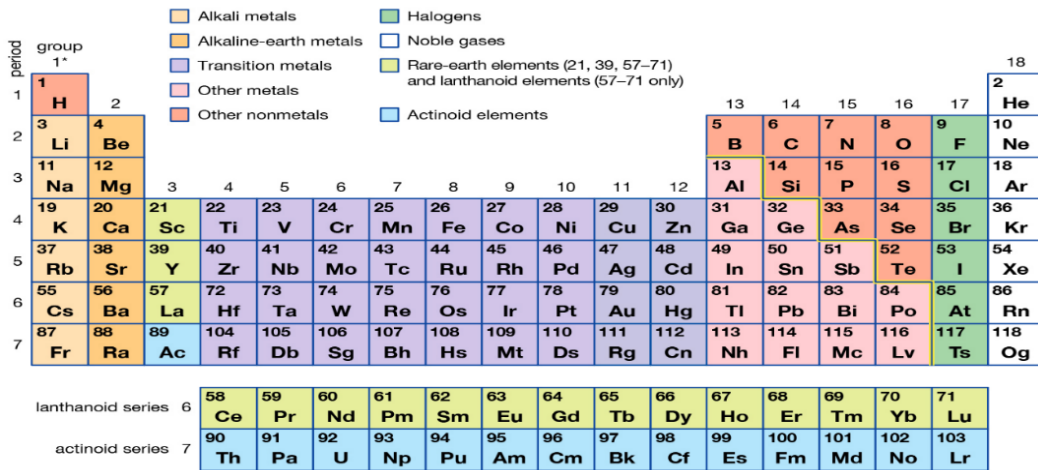


Figure 2.3 Periodic Table

The chemical element B has an atomic number of 5. In the Periodic Table, it's between the III and V groups, as seen in Figure 2.3. It has a 0.117 nm atomic diameter and a molar volume is 4.6 cm³/mol. Boron's electrical arrangement in its ground state is 1s² 2s² 2p¹. By sp² hybridization, boron can form three covalent connections.

It's a metalloid because it possesses both metal and non-metal qualities.

BN is easily produced from BCl₃ (boron trichloride) and NH₃ (ammonia) through the following reaction:

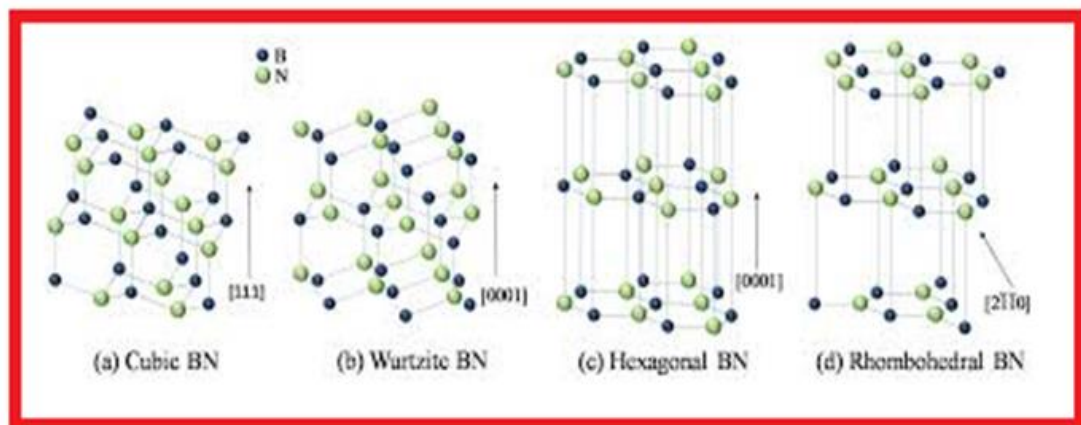
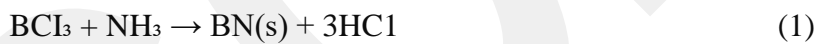


Figure 2.4 Boron Nitride allotropies

Boron nitride (BN) is a synthetic substance that, although its discovered in the early nineteenth century, was not commercialized until the second part of the twentieth century.

Boron nitrides have the chemical symbol BN.

B: N = 1: 1 is the stoichiometric ratio.

Hexagonal (h-BN), rhombohedral (r-BN), cubic (c-BN), and wurtzite (w-BN) crystals are all examples of BN allotropies, as illustrated in Figure 2.4.

The low-density BN crystal lattices h-BN and r-BN are formed of planar layers of B_3N_3 hexagons, with three covalent connections connecting each atom to its three nearest neighbours according to the sp^2 hybridized atomic orbitals [36].

The two high-density polymorphs c-BN and w-BN show four strong covalent bonds between the three-dimensional lattice in which each atom is an sp^3 hybrid and the nearest neighbours atom, forming a tetrahedron around them [36].

- **Cubic boron nitride (c-BN)**

c-BN was initially synthesized in 1957, but commercial manufacturing of c-BN has only begun in the last 15 years. Next to diamonds, cubic boron nitride (c-BN) is the second hardest substance. Cutting tools and forming dies are coated with c-BN coatings.



Experiments and industrial applications demonstrate that tool life is extended and performance is improved.

Because of its superior mechanical and chemical qualities, cubic boron nitride (c-BN) has been used as a significant coating material for cutting tool applications.

Aside from its high thermal conductivity and electrical resistance, it does not react with ferrous metal or oxygen at high temperatures.

Chemical stability towards ferrous metals and oxygen at high temperatures like $1300^{\circ}C$ is an area where c-BN outperforms diamond [37-38].

c-BN is employed in the powder metallurgy or PVD coating of tool steels, the coating of die steels in sheet metal forming, and direct applications to the end product when high wear resistance is required [39,40-41].

Its antimicrobial properties also open up possibilities for biological applications [16]. Experimental studies and FE simulations on micro-milling of Ti-6Al-4V alloy with fine grain uncoated and c-BN coated are presented in the research of Özel [42].

For uncoated and c-BN coated micro-tools, the effects of machining parameters on surface roughness, burr development, and tool wear are examined.

For uncoated and c-BN coated micro-tools, finite element modelling is used to forecast forces, temperatures, and wear rates.

The c-BN coated carbide tool outperformed the uncoated carbide tool in terms of tool wear and cutting temperature, according to this study.

- **Hexagonal boron nitride (h-BN)**

Balmain [43] created hexagonal h-BN for the first time. Hexagonal BN has a lamellar crystalline structure, with strong covalent bonding between molecules inside each layer and virtually weak van der Waals forces connecting between layers [44].

When blended at low quantities (as little as 1 wt%) with liquid lubricants — oils, greasers, and fuels – powdered h-BN can dramatically reduce friction and wear. The h-BN is regarded as a "pure" lubricant.

The electrical insulator h-BN is white. The characteristics of the c-BN and h-BN are different, as indicated in Table 2.1.

Table 2.1 Comparison of c-BN and h-BN properties

Properties	c-BN	h-BN
Density (g/cm ³)	3.48	2.34
Thermal Conductivity (W/m.K), 25°C	1300	550 [45]
Melting Temperature (°C)	2973	2600
Oxidation Temperature (°C)	1200	1100 [46]
Hardness	45-55 GPa	Mohs's scale of hardness is 2 [45]

In their study, Narayan and colleagues found that nanocrystalline h-BN could be converted directly into phase-pure c-BN in the air at room temperature and atmospheric

pressure [47]. Nanosecond laser pulses are used to develop a supercooled molten state of BN, which is quenched into a new BN state called QBN, similar to the formation of Q-carbon. QBN is used to obtain high-quality, phase-pure c-BN produced by regulating the nucleation and growth of c-BN [47].

- **Wurtzite boron nitride (w-BN)**

The shock compression of hexagonal BN produces w-BN, a metastable super hard material that is a high-pressure polymorphism of BN that can only be manufactured as micrometre-sized particles [48].

- **Rhombohedral boron nitride – (r-BN)**

r-BN is rarely witnessed in BN polymorphs. r-BN has also an sp^2 bond structure as well as h-BN [49].

- **Explosive boron nitride (e-BN)**

Batsanov et al. were the first to discover e-BN. The approach is explosive, and it works by compressing h-BN powder with a shock wave [50]. At 200-350°C, e-BN is transformed to r-BN. Furthermore, above 400°C, e-BN is transformed to w-BN.

- **Turbostratic boron nitride (t-BN)**

(t-BN) is another boron nitride polymorphism. Turbostratic BN (t-BN) can be described as a highly disordered h-BN by random rotation and displacement of a hexagonal plane around its c-axis. Consequently, the interplanar distance along the c-axis in t-BN depends on the degree of disorder and is larger than in h-BN [51].

Thermal transformation of t-BN into the stable, hexagonal ordered layer lattice structure was increased by heat treatments at 1500–1800 °C for 15min–5h, according to Alkoy et al [52].

- **Amorphous boron nitride (a-BN)**

The sp^2 structure of t-BN is different from the sp^3 structure of a-BN. One of these, known as sp^3 -amorphous BN, resembles diamond-like amorphous carbon. Boron formation is amorphous at low temperatures (about 600-800 °C) [53,54,55]. Stoichiometric thin films of a-BN are transparent and insulating, according to some studies [56].

a-BN has mostly been investigated as an intermediary or starting material for the synthesis of hexagonal BN (h-BN) or cubic BN (c-BN). a-BN can be made in a variety of ways, including high-energy ball milling of h-BN in air and N_2 gas [57],

explosive reactions of borazines with metals at high temperatures [58-59] and solid-state reactions of nitrogen-containing materials like urea or melamine with boric acid in the air or N₂ atmospheres [60].

2.4 Literature Review

Much research examines how to improve the PVD technology by increasing plasma ionization, reducing dark areas, improving target utilization, improving atomic bombardment efficiency, or even raising deposition rate and optimizing gas selection [61-62].

Kamenetskikh et al, Under conditions of coating exposure in the plasma with a low energy (100 eV) electron beam, two variants of BN coating deposition were compared: RF magnetron sputtering of h-BN target and DC pulsed sputtering of B target. By varying the electron beam current, it is possible to control the ratio of ion fluence to the number of atoms in the coating in the range of 2–24 A and optimize the conditions of c-BN phase formation. The maximum c-BN phase content in coatings produced by sputtering B and h-BN targets was 83% and 58% with intrinsic stresses of 13 and 5 GPa [63].

Kaftanoğlu et al. developed a (PVD) system for covering tools and dies with film (BN). Different coatings were applied to different types of substrates. quality test with coating thickness, nano hardness, scratch, AFM, SEM and FTIR measurements. The coatings improve hardness, reduce friction and increase resistance to high temperatures. BN coating applied for cutting tools leads to extended tool life in the laboratory and industrial applications [64-65].

Molecular dynamics (MD), density functional theory (DFT), and Monte Carlo (MC) simulation are only a few of the mathematical modelling and numerical simulation techniques now in use.

Newton's equations of motion are primarily understood through MD [66], and DFT is frequently used to compute and forecast material properties for material development [67,68]. Because they use repeated random samples of experiments that are somewhat comparable to provide statistically meaningful numerical data, MC is fre-

quently used for systems that are overly complicated [69]. Direct Monte Carlo simulation (DSMC) was used in the current investigation to examine how BN targets behave in MS coatings.

To compare the sputtering yield values for BN and BNSiO₂ in the energy range of 100 eV to 550 eV, Ranjan et al. used two grid ion optics and a beam incidence angle varying from normal to 85°. With 1.2 Sccm of Xenon gas flow and a base pressure of 5.5×10^{-8} mbar in the main vacuum chamber, the operating pressure for ion source firing was 1.65×10^{-4} mbar. Both materials exhibit an increase in yield at a 55° angle. Yields are often poor below 250 eV and reach their peak around 500 eV and at a 55° angle. It was found that the yield shape profile is non-symmetric at oblique incidence and symmetric at normal incidence [70].

The velocity profiles, pressure profiles, density profiles, and concentration distribution of the process gas species (Ar and N₂) across the sputtering chamber were predicted using the Fluent-ANSYS analytical tool by Kapopara et al [71].

The gas flow in the PVD reactor was examined by Bobzin, the findings reveal that the placement of the gas inlet port and substrate has a significant impact on gas distribution inside the chamber and over the substrate, where the reactive gas will react and form a coating. TiN coatings in the sputtering system were modelled using Computational Fluid Dynamic CFD software. To characterize the plasma reactor CC800/9 in an industrial setting, a CFD model was created. It is feasible to replicate the neutral gas flow of argon and nitrogen using the model that has already been established.

FLUENT-ANSYS® was the program used. The Navier–Stokes equations and the Boltzmann equation are used to explain gas flow and kinetics, respectively. The results for the transition regime's gas flow were quite different. The model was able to provide a precise physical description using Boltzmann's equations [72].

CHAPTER 3

RESEARCH METHODOLOGY

3.1 Modelling of Magnetron Sputtering of BN Coating

Reactive magnetron sputtering is a well-known thin-film deposition method. This technique's fundamentals are conceptually simple and can be summarized in a few lines. However, the complex interplay of various physical and chemical sub-processes lies behind this simple thing. Many of these sub-processes have already been thoroughly modelled in this study. Each of these models is characterized by the use of very specific scales.

Kanta et al used Artificial neural networks (ANN) to predict atmospheric plasma spraying (APS) process parameters to manufacture a coating with the desired structural characteristics. Deposition yield and porosity were the coating structural characteristics [73]. Therefore in this study, we try to use ANN to predict the MS coating properties. The data for all experiments about BN coating in the lab are collected. The number of experiments is 160, unfortunately, these experiments are not enough. Therefore this approach has been cancelled. The ANN method needs at least 400 experiments to make predictions for MS characteristics and then make optimization for results.

RSD2013 - Reactive Sputter Deposition: This software models the reactive sputtering process of a single sputtering target in (pulsed) DC mode with one reactive gas added. RSD2013 models the hysteresis of the process. The software has been developed by Koen Strijckmans[74]

SiMTra - Simulation of the Metal Transport: SiMTra is a binary collision Monte Carlo program that allows the user to simulate the transport of sputtered particles through the gas phase flux during sputtering [75]. The two packages of Ghent university can be used with a metal target and DC power supply. The type of target in this research

is a semiconductor and the applied power on the target plate is Rf. Therefore these packages are not efficient to model BN coating.

The model begins with magnetic fields, progresses to electric fields, plasma, particle transport, solid particle interaction, and chemical interactions between active gas and target plate particles, and concludes with thin-film growth as shown in Figure 3.1. There is a significant push to model the entire magnetron deposition process to replace trial and error experiments. Modelling magnetron sputtering necessitates precise magnetic and electric field values. Using finite element models (FEM), this can be accomplished with high precision for the most complex magnetic configurations. The ANSYS Maxwell FEM package is used to simulate both magnetic and electric fields in this study.

The sputtering system's Knudsen number ranges from 0.1 to 10, rarefied gas flow conditions must be considered. As a result, Direct Simulation Monte Carlo (DSMC) appears to be the best approach for dealing with this issue. Samadii™/sciv (Statistical Contact in Vacuum) package [76] uses to interpret Magnetron Sputtering in this study.

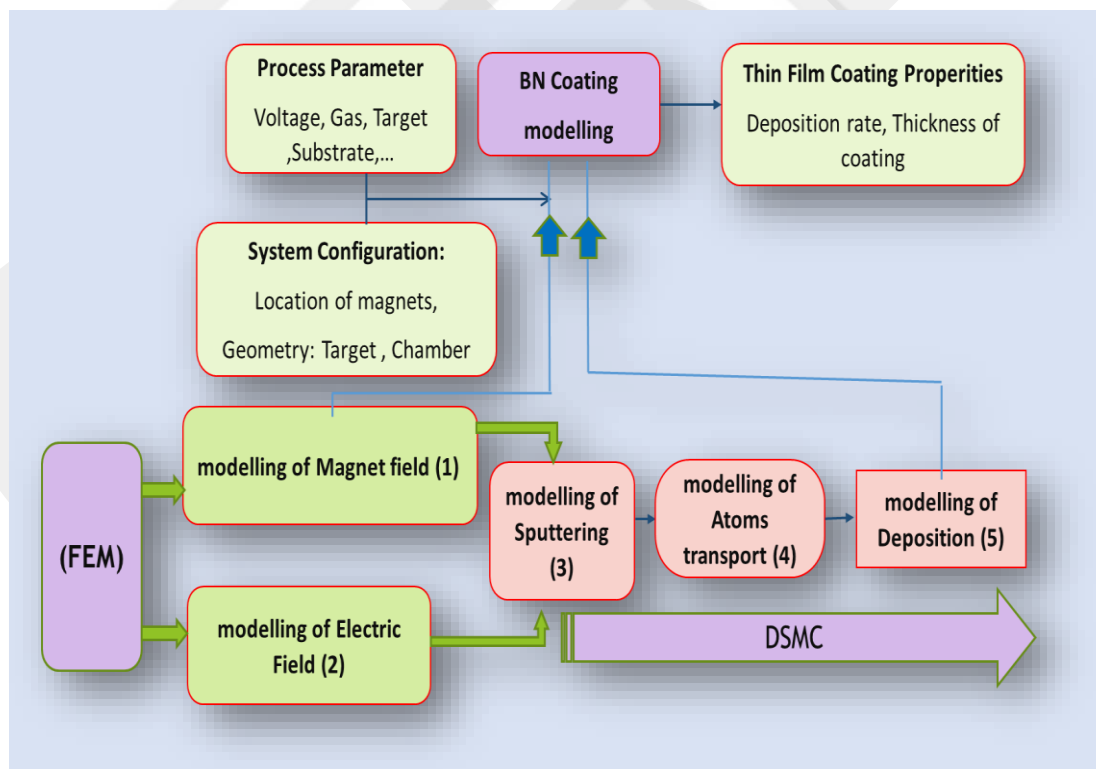


Figure 3.1 Steps of magnetron sputtering model

3.1.1 Direct Simulation Monte Carlo (DSMC) Method

Bird's DSMC method is the dominant numerical method for solving engineering problems involving rarefied gas flow [77]. The degree of gas rarefaction is classified using the dimensionless Knudsen number (Kn)

$$Kn = \lambda / L \quad (3.1)$$

where λ is molecular mean free path length and L is physical length scale.

Based on Kn, gas flow can be classified into four regimes [78,79,80] as shown in Table 2.2

Table 2.2 Classified gas flow regimes depend on Kn

Regime	Kn
Continuum flow	$Kn < 0.001$
Slip flow	$0.001 < Kn < 0.1$
Transition flow	$0.1 < Kn < 10$
Free molecule flow	$Kn > 10$

The conventional Navier-Stokes equation, which is based on the continuum assumption, is only applicable to flows when $Kn < 0.1$ with slip boundary conditions at a solid wall. Even with high order slip boundary conditions, the solution of Navier-Stokes' equation produces very large errors when $Kn > 0.1$ [80]. Multiple statistical mechanics models were developed to evaluate rarefied flows at high Knudsen numbers.

The Direct Simulation Monte Carlo (DSMC) approach is frequently referred to as the most effective numerical tool for modelling real engineering problems in a less computationally intensive environment. The DSMC method is stochastic modelling of the Boltzmann equation.

To model rarefied gas fluxes, the DSMC numerical approach is used. The DSMC method is used to describe the behaviour of large groups of charged particles. Particles occupy space that is divided into cells. Particles are represented by a small number of superparticles. A weighting factor determines the number of actual particles represented by each super particle. Using the Boltzmann equation, we can simulate the system's behaviour in a self-consistent manner.

The most important feature of DSMC is the decoupling of the movement and collision procedures of the molecules. First, all molecules are moved for the given time step. Their new location is found, at this step, collisions with boundaries are also investigated and accordingly, molecules that are found out of bounds are either reflected (wall), re-positioned at the opposite side (periodic conditions) or removed (open boundaries). A new sort in cells is performed. Next intermolecular collisions are performed, considering only molecules within the same cell. At each time step, the number of molecules (number density) and their molecular velocities are summed and stored for each cell. Every few time steps (defined by the user) an averaging is taking place (time-averaging). From these summed and averaged values of number density and velocities all the macroscopic values such as bulk velocity, temperature, pressure, stress tensors, heat fluxes, etc. can be extracted.

Samadii™/sciv package uses to interpret Magnetron Sputtering. For each time step, Samadii™/sciv employs the particle method to determine the force acting on each particle. In the next stage, it uses force and mass to calculate velocity and location. Samadii™/sciv calculates the Lorentz force, which is created by the electric field, magnetic field, and particle collisions. The Samadii™/sciv program will be utilized to model the BN coating in this investigation. Its most representative feature is that calculates probabilistic collision using the concept of (SUPER-PARTICLE) also known as the Direct Simulation Monte Carlo Method (DSMC).

3.1.2 The Internal Parameters of The PVD Coating Model

- Substrate dimension and geometry.
- Target dimension.
- Definition of the material properties type of material for both substrate and target.
- Definition of the target to substrate distance T-S.
- Amount and type of power applied
- Substrate rotation with direction.
- Definition of the deposition angle.

3.2 Modelling of BN Coating Structure and Properties

In this study modelling the polymorphic transition mechanisms from the hexagonal boron nitride (white graphite), a soft solid lubricant to cubic boron nitride (borazine), a super abrasive is done. According to the literature, the phase transition from h-BN to c-BN is driven by high temperature and pressure [81]. Therefore, two software are used to study this allotrope transform:

- **2D field analysis of pressure, temperature and gases properties in the chamber by using DSMC**

DSMC is used to study the gases' properties, pressure and temperature distribution in the MS system in XY coordinate. Samadii™/sciv software uses to interpret the transformation of the BN allotrope. How do the previous properties affect the BN phases?

- **Study the BN crystalline structure by using density functional theory (DFT) and Quasi Harmonic Debye Model**

CASTEP (Cambridge Serial Total Energy Package) software uses density functional theory with a plane wave basis set to calculate the electronic properties of crystalline solids, surfaces, molecules, and amorphous materials. This software will be used to calculate the elastic, electronic and phonon properties of the h-BN and c-BN phases. The Quasi Harmonic Debye Model is used to study the thermal properties of h-BN and c-BN.

3.3 The Basic Information of Computer That Used to Submit Simulation

- LAPTOP-OBKIOUVU
- Processor: 11th Gen Intel(R) Core (TM) i7-11370H @ 3.30 GHz.
- Installed Ram: 16.0 GB (15.7 GB usable)
- System type: 64-bit operating system, x64-based processor
- Edition: Windows 10 Home, Linux
- GPU: NVIDIA GeForce RTX 3070 Laptop GPU
- Intel(R) Iris(R) Xe Graphics

3.4 Experimental Facilities for Magnetron Sputtering

3.4.1 PVD Magnetron Sputtering System

The facilities of the BOREN Center of Competence for Boron Coatings at the Metal Forming Center of Excellence at ATILIM university were used to prepare all of the coating experiments. PVD Magnetron Sputtering system was manufactured by the VAKSIS company. PVD Magnetron Sputtering system contains Vacuum Chamber, Control Panel, Gases and Computer as shown in Figure 3.2. A detailed description of the deposition process tests is presented below. A high vacuum is used in PVD technology. A thin film of BN coating will be deposited in this study using the reactive MS process. The target plate comprises h-BN, a single-crystal structure with a purity of 99.9%. D2 steel is the substrate type. The substrate geometry is 30 mm in diameter with 7 mm thickness.

Two gases, namely inert gas Ar and reactive gas N₂, are used. The radiofrequency (RF) power supply is applied to the target plate. The target geometry is 250 × 100 × 5 mm. An unbalanced magnetron, two magnetic poles and a cooling system are found behind this plate. The magnetic field traps electrons and increases the efficiency of the process. The total pressure of the two gases is maintained at 0.005 Torr. The substrate temperature is 300 °C, and the deposition time is 6 h. A plasma cleaning process is applied to the substrate before the deposition process under 250 W RF power with 0.05 Torr pressure and an Ar flow rate of 50 sccm for 15 min.



Figure 3.2 Parts of PVD magnetron sputtering system

3.4.2 Substrate preparation

Substrate preparation plays an important part in the coating adhesion and the coating quality (durability). The substrate has to be properly prepared to achieve maximum bond strength. For the D2 substrate after heat treatment and polishing, an ultrasonic cleaning machine is used for high-quality cleaning as shown in Figure 3.3. In the ultrasonic cleaning machine, the temperature is set to 65 °C. Duration is adjusted to 20 minutes. Samples are passed through the distilled water and rinsed in the last stage.



Figure 3.3 Ultrasonic cleaning machine

It is critical to comprehend and grasp all process steps involved in the magnetic sputtering technique preparation process to get better thin layer deposition.

Cleaning the substrate is required before the deposition to ensure better adherence between the coating and the substrate. Because contamination sources occur from bad surface conditions or system-related sources, it is vital to clean the entire vacuum system to prevent contamination.

3.4.3 Experiment of Magnetron Sputtering Steps

First step: Prepare the vacuum chamber, which entails gradually increasing the temperature while also activating the vacuum pumps to lower the pressure inside the chamber, as illustrated in Figure 3.4.



Figure 3.4 PVD coating system

Second step: Coating takes place. Coating occurs in the second stage.

The depositing substance is projected onto the substrate's surface. It is possible to employ a variety of materials. Then, in the vacuum chamber, an inert gas is supplied, which is accelerated by applying a high voltage (Rf) in the direction of the magnetic between the target (coating material) and the substrate (workpiece), resulting in the

release of atomic-sized particles from the target. Argon has been used with reactive gases such as nitrogen.

Third step: The temperature and pressure inside the vacuum chamber have returned to normal. Knowing which variables can be controlled when a coating is being deposited is essential. Examples of these factors include the number of pumps, the number and kind of targets, substrate geometry, reactor occupancy rate, pressure, gas type, gas flow, temperature, and current density. The rate of film deposition and adhesion, however, will be impacted by changes in the parameters. Particle size and film thickness variations can therefore have an impact on coating characteristics such as hardness, Young's modulus, morphology, microstructure, and chemical composition [82].

Good plasma etching and excellent substrate surface cleaning ensure effective adhesion [83].

3.4.4 Experimental Determination of Coating Thickness

Coating thickness is measured using the Filmmetrics F₂₀ thin film analyzer as shown in Figure 3.5. The F₂₀ analyzer has a thickness range of 15 nm – 70 μm and the Wavelength Range is 380-1050 nm. By either reflecting or transmitting light through the sample and then evaluating this light across a range of wavelengths, the F₂₀ analyses thin-film properties.

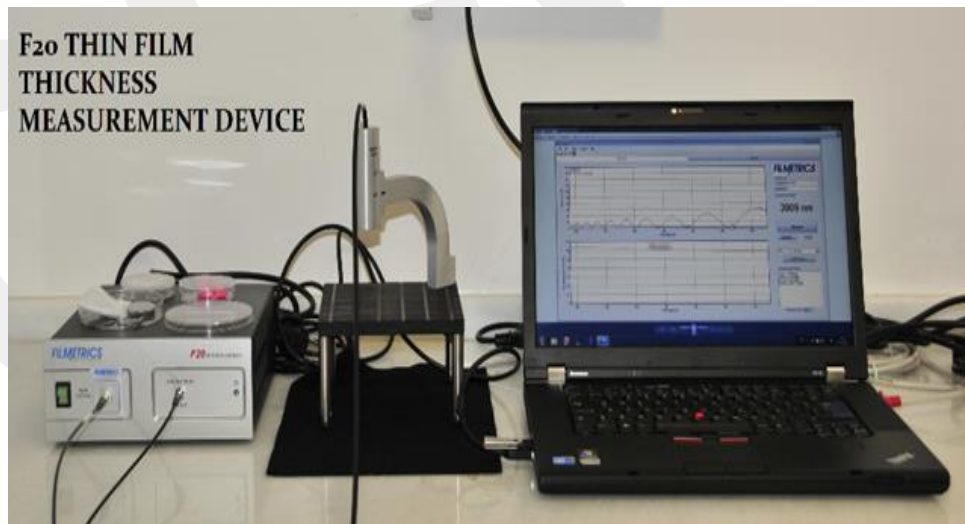


Figure 3.5 F₂₀ thin film thickness measurement device

3.4.5 Experimental Determination of Coating Characterization

The characterization of coated samples is investigated using Fourier Transform Infrared Spectroscopy (FTIR) as shown in Figure 3.6. To explore the crystal structure of a BN thin film, the adsorption mode is applied.

(FTIR) is a method for acquiring an infrared spectrum of a solid, liquid, or gas's absorption or emission. An FTIR spectrometer simultaneously collects high-resolution spectral data over a wide spectral range. Compared to a dispersive spectrometer, which can only detect intensity over a restricted range of wavelengths at once, this gives it a significant advantage.

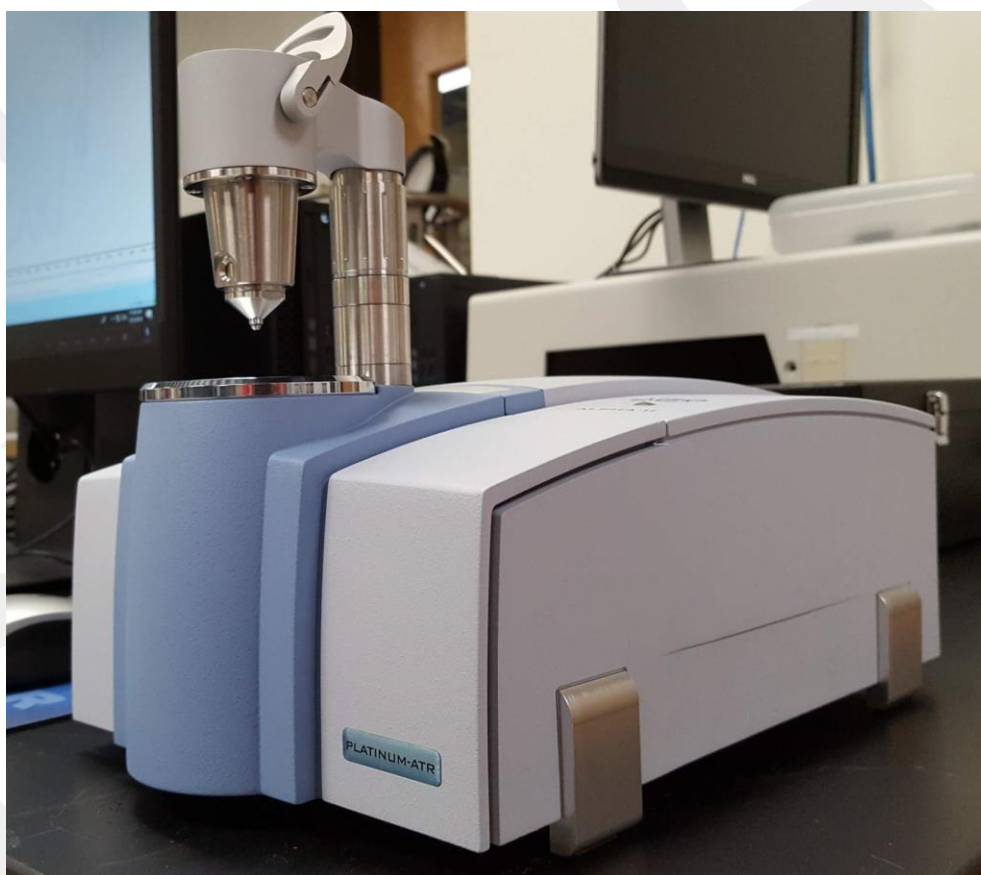


Figure 3.6 Fourier-transform infrared spectroscopy device

3.5 Research Motivation

Modelling of Boron Nitride coating intends to improve the Physical vapour deposition (PVD) process. This model will focus on the process of energy efficiency improvement with the sputtering technique. Based on the product and its characteristics DSMC and other techniques will be used to study the BN coating profile.

To reduce manufacturing times, the process parameters must be optimised. The deposition rate must be regulated to improve the plasma density and energy available during the process.

The purpose of the modelling is an optimization of the deposition rate, coating uniformity, modelling crystal structure, modelling coating thickness and coating homogeneity. Improve the characteristics of coating, hardness and adhesion.

The deposition rate depends on the sputtering process, maximum power density, magnetics and coating zone geometry. Coating homogeneity depends on the gas distribution, Magnetic, Deposition angle and Film density.

CHAPTER 4

MODELLING OF MAGNETIC AND ELECTRIC FIELDS

4.1 Introduction

The magnetic field traps electrons and increases the efficiency of the process. For the generation of a magnetic field permanent magnet alloys like NdFeB, Al-Ni-Co and NdFeB₃₅ are used, which have a magnetic field strength. The magnetron is used for sputtering of 250 mm length of the planar target with a width of 100 mm and thickness of 5mm. The magnetron consists of an inner magnet S-pole and an outer magnet N-pole.

Sputtering occurs when a target material is bombarded with high-energy ions. Ionization of gas in an ion source, extraction, and post-acceleration through one or more electric fields to obtain final energy before hitting the target.

The negative potential (bias) is held on the target to be hit by the energetic ions.

When a gas (e.g., Ar) is introduced into the system, the electric field ionizes some of the gas atoms, resulting in a discharge, as described in Chapter 2 (p.7) An electron can be expelled from the target surface to the vapour phase by blasting it. To ionize the Ar-atoms in the plasma, secondary electrons are required.

Electrons transfer their energy to Ar atoms in an inelastic manner by activating the Ar-internal atom's electrons.

At radio frequencies (Rf) the electrons oscillating in the glowing space have sufficient energies to cause ionizing collisions, thus reducing the dependence of the discharge on secondary electrons and lowering the breakdown voltage.

Ansys Maxwell 16.0 software technique has been used to model the magnetic and electric fields.

4.2 Type of Magnetic Fields

There are different types of magnets for sputtering applications. Planar, cylindrical with an axial magnetic field, or rotating around a set magnetic meeting are all possibilities. Thornton [84,85] Gil and Kay [86] likely invented the primary with cylindrical geometry and the axial magnetic field for thin film deposition on an industrial scale. The development of rotatable tubular magnetics for high-deposition rate coating of bigger surfaces and enhanced target utilization [87].

The magnetron configuration of our greatest interest is the planar magnetron, which is widely used for thin film deposition in both laboratory and industrial applications [88,89]. Permanent magnets, electromagnets, or a mixture of both can be used to generate a magnetic field in a planar design, usually placed behind the target. The primary benefit of a planar magnetron is that it produces uniformly coated substrates because the sputtered material has a strong forward direction parallel to the anode.

In this configuration, the substrate is typically far from the target and the plasma is held too effectively on the target surface.

As a result, it would be difficult to customise the film structure and extend the plasma towards the substrate, which is necessary for successful ion bombardment of the growing film. The magnetic strengths (fluxes) across the pole faces of the outer and inner poles are equal in a balanced magnetron (see Figure 4.1a).

The outside ring of magnets in an unbalanced magnetron, on the other hand, is stronger than the core pole, or vice versa.

In these cases, some magnetic field lines are directed towards the substrate, and electrons can follow these field lines.

As a result, the plasma can flow outwards towards the substrate, improving charged particle transport to the forming film [90]. Two such unbalanced layouts are shown in Figures 4.1b and c.

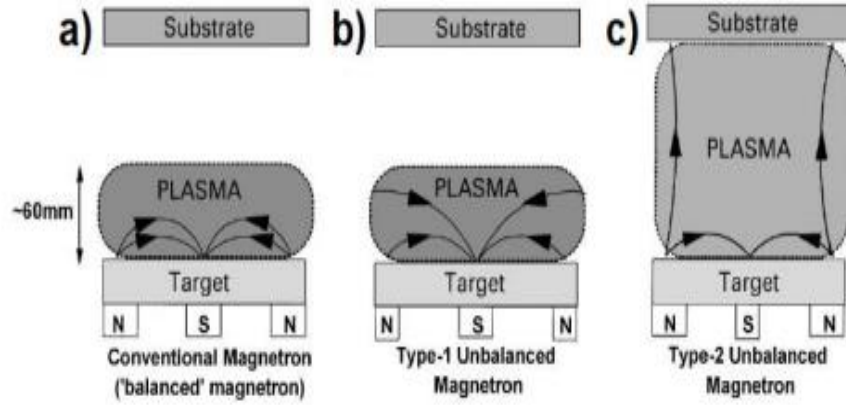


Figure 4.1 Schematic diagram of plasma confinement for balanced and unbalanced magnetrons [90].

4.2.1 Modelling of the Magnetic Field in MS System

Ansys Maxwell 16.0 software technique has been used to model the magnetic field (MF). Ansys Maxwell 16.0 solver works by solving the Maxwell equation to discretize the nodes of each space using the Finite Element Method. There are three solvers available in Maxwell to model magnetic fields.

These solvers are Magnetostatic, Eddy Current, and Transient Magnetic. The type of solver used in this study is magnetostatic. The magnetic field, following the Maxwell Equations, it can be written:

$$\nabla \times \vec{H} = \vec{J} + \frac{\delta \vec{D}}{\delta t} \quad (4.1)$$

$$\nabla \cdot \vec{B} = 0 \quad (4.2)$$

Where \vec{H} is the magnetic field strength, \vec{B} is the magnetic flux density,

\vec{J} is the current density, and $(\frac{\delta \vec{D}}{\delta t})$ is the electric displacement current density.

Relative Permeability and Bulk Conductivity of materials are used as input parameters to find the magnetic field as shown in Table 4.1.

Table 4.1 Boundary condition of the magnetic field

Solver	Material	Relative Permeability [91]	Bulk Conductivity (siemens/m)
Magnetostatic	NdFeB35	1.0997	625000
	h-BN	0.999	4.98
	Ar	1.0003	0
	N2	1.00057	0

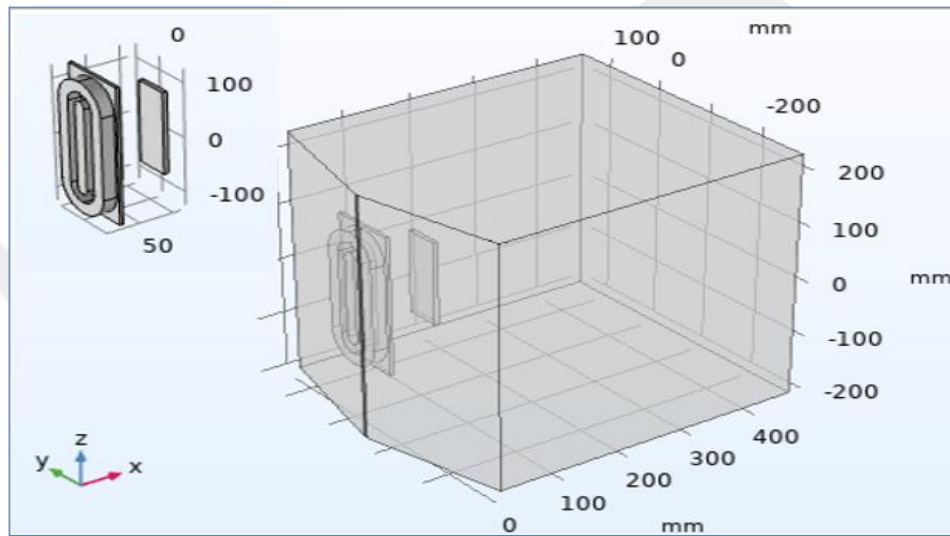


Figure 4.2 Geometry of magnetron sputtering system

The fine mesh was applied to reduce the error analysis result to 1% as shown in Figure 4.3.

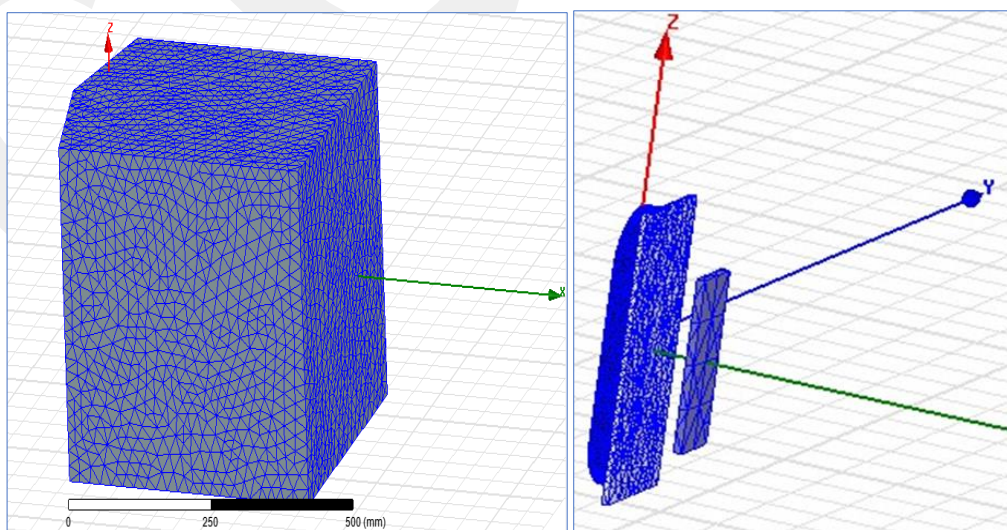
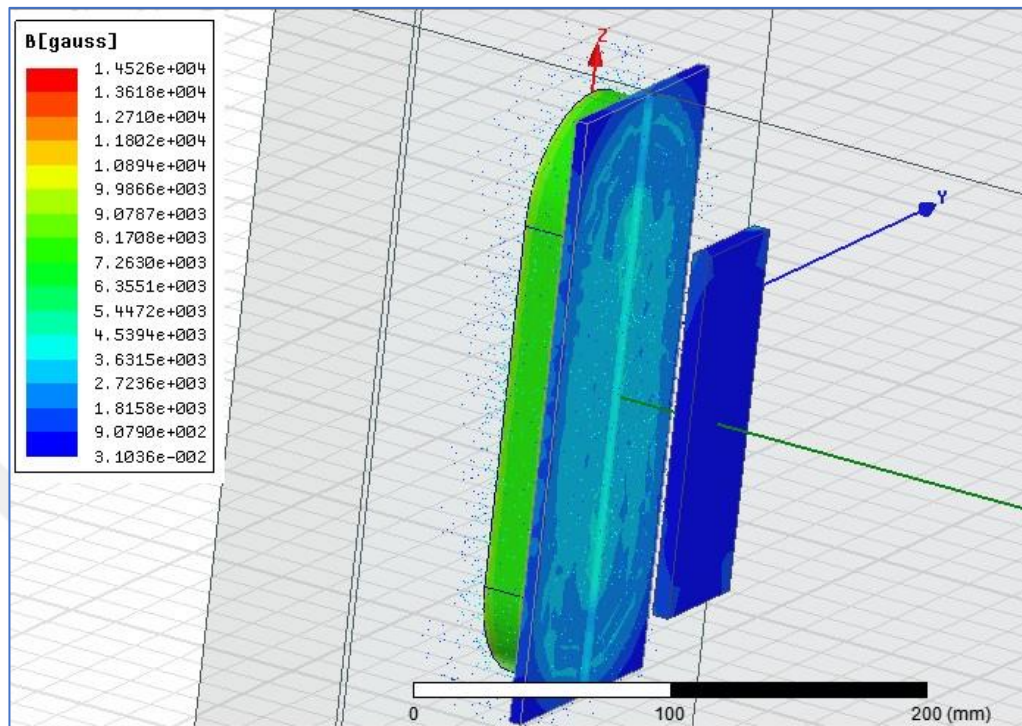
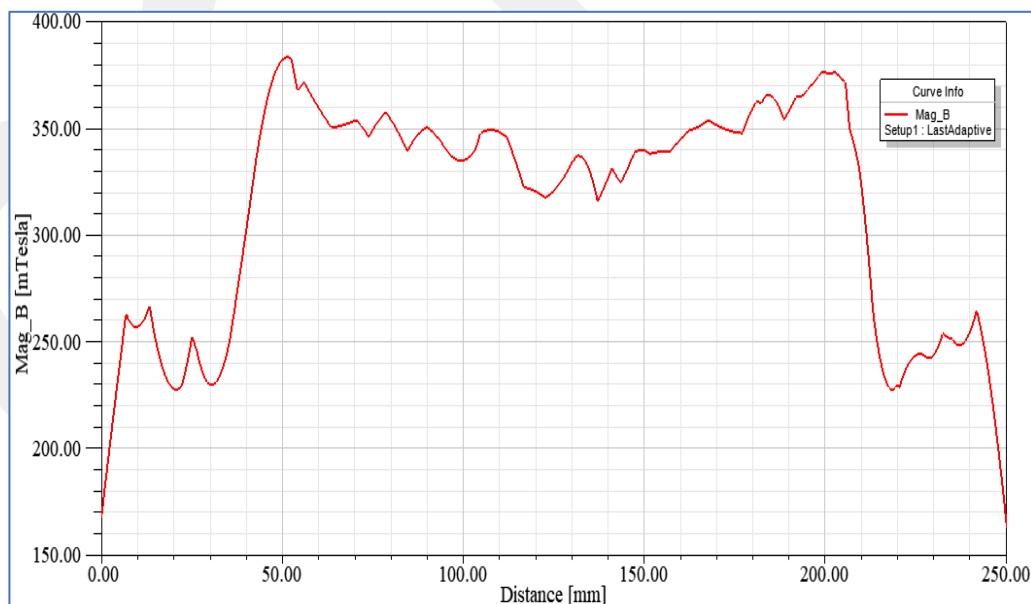


Figure 4.3 Mesh of magnetic field modelling

In MS the most important magnetic flux density distribution is above the target plate. The maximum magnetic flux density on the target plate is ~ 0.38 T as shown in Figure 4.4. The magnitude and direction of Magnetic field strength are shown in Figure 4.5.



(a)



(b)

Figure 4.4 Magnetic flux density distribution :(a) Magnetic flux density distribution in the MS system and (b) Magnetic flux density distribution on the target plate.

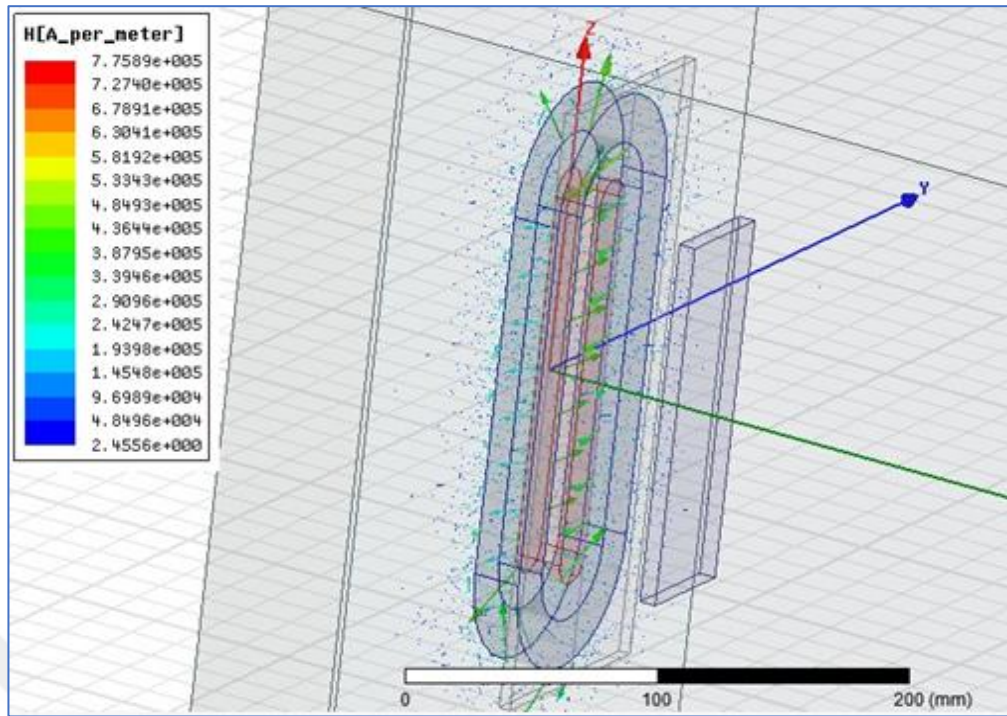


Figure 4.5 The Magnitude and direction of Magnetic field strength in the MS system.

4.3 Modelling of the Electric Field in MS System

Ansyz Maxwell 16.0 software technique has been used to model the electric field (EF). There are three solvers available in Maxwell to model electric fields. These solvers are Electrostatic, AC Conduction, and DC Conduction. The type of solver used in this study is Electrostatic. Relative Permittivity and Bulk Conductivity of materials are used as input parameters as shown in Table 4.2.

Table 4.2 The relative permittivity and Bulk Conductivity of different materials in the MS system

Solver	Material	Relative Permittivity	Bulk Conductivity (siemens/m)
Electrostatic	NdFeB35	1	625000
	h-BN	4.3	4.98
	Steel-D2	1	2000000
	Ar	1.000513 [91]	0
	N ₂	1.000580 [91]	0

4.3.1 Modelling of Electric Field for Different Substrate Bias Voltages

The calculation of EF is based on two excitations of the voltage. The voltage of the target plate and the substrate bias voltage. The voltage of the target is -300 V and the substrate voltages are 0,100 and 250 V as shown in Table 4.3. The type of substrate is D2 steel.

Table 4.3 The boundary condition of the electric field

No.	Name of Model	Target material	Substrate material	T-S (mm)	Power Supply (W)	Substrate Voltage (v)
1	Model A1	h-BN	1xD2	80	900	0
2	Model B1	h-BN	1xD2	80	900	100
3	Model C1	h-BN	1xD2	80	900	250

T-S: Distance between Target and Substrate.
The result of voltage and energy variation between the target plate and the substrate of Model-A1 are shown in Figures 4.6,4.7 respectively.

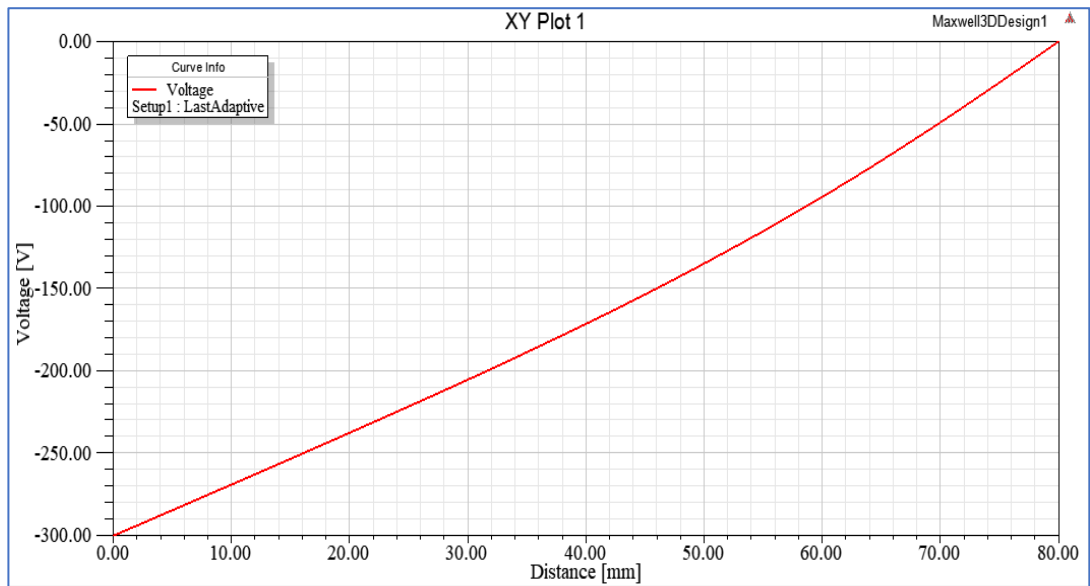


Figure 4.6 The variation of voltages between the target and the substrate of Model -A1.

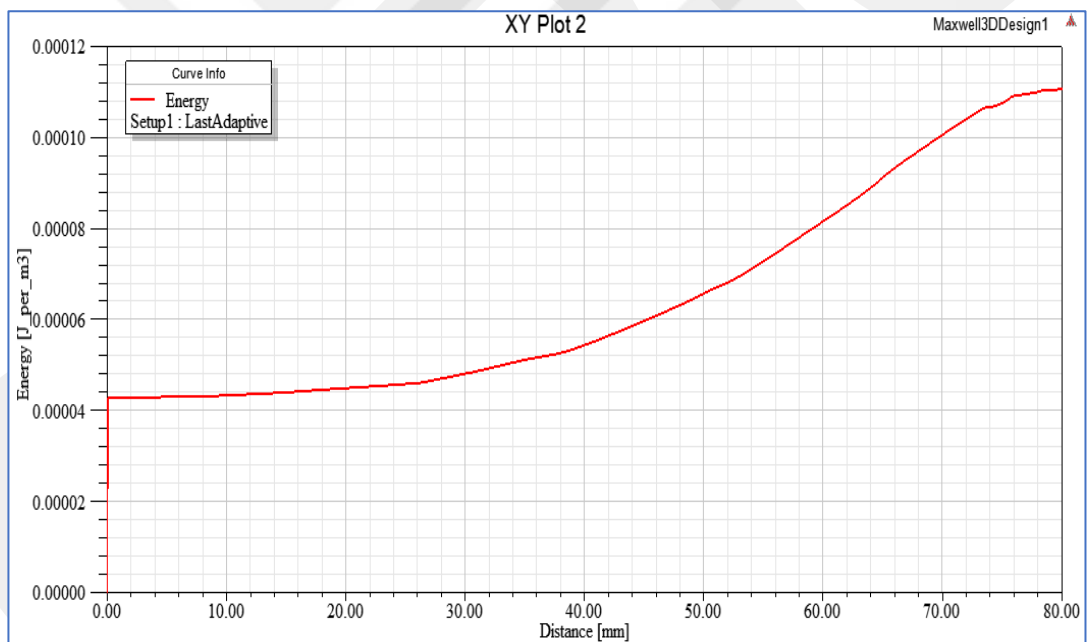


Figure 4.7 The change of energy between the target and the substrate Model -A1

The voltage distribution in the MS system when the bias voltage of the substrate is 0 V is shown in Figure 4.8.

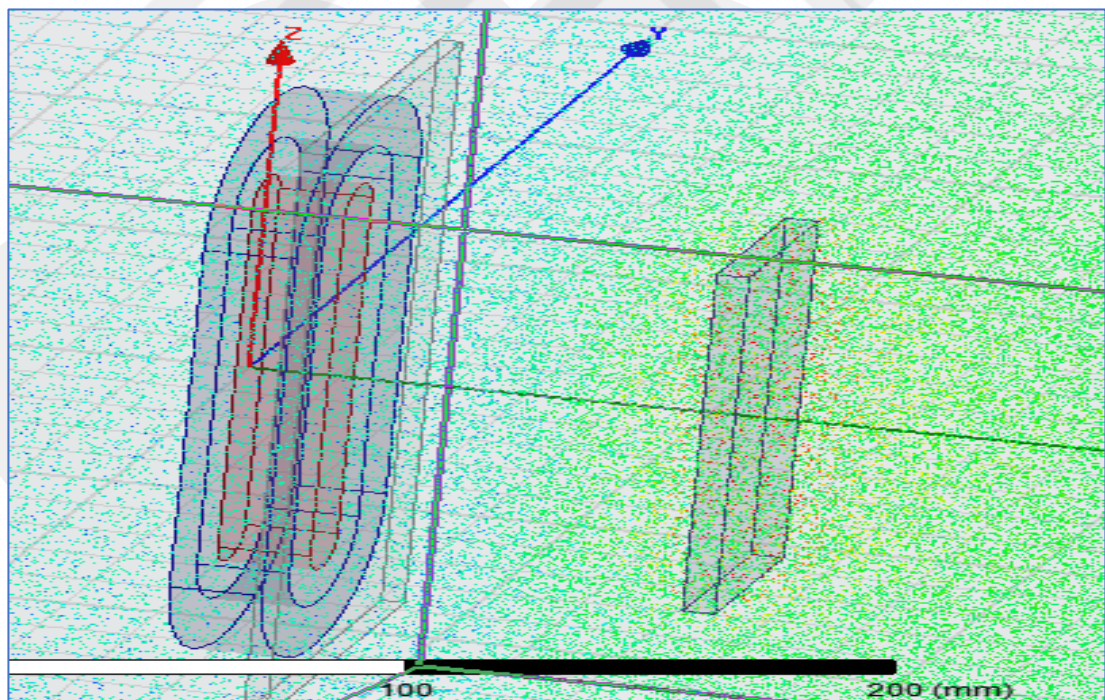
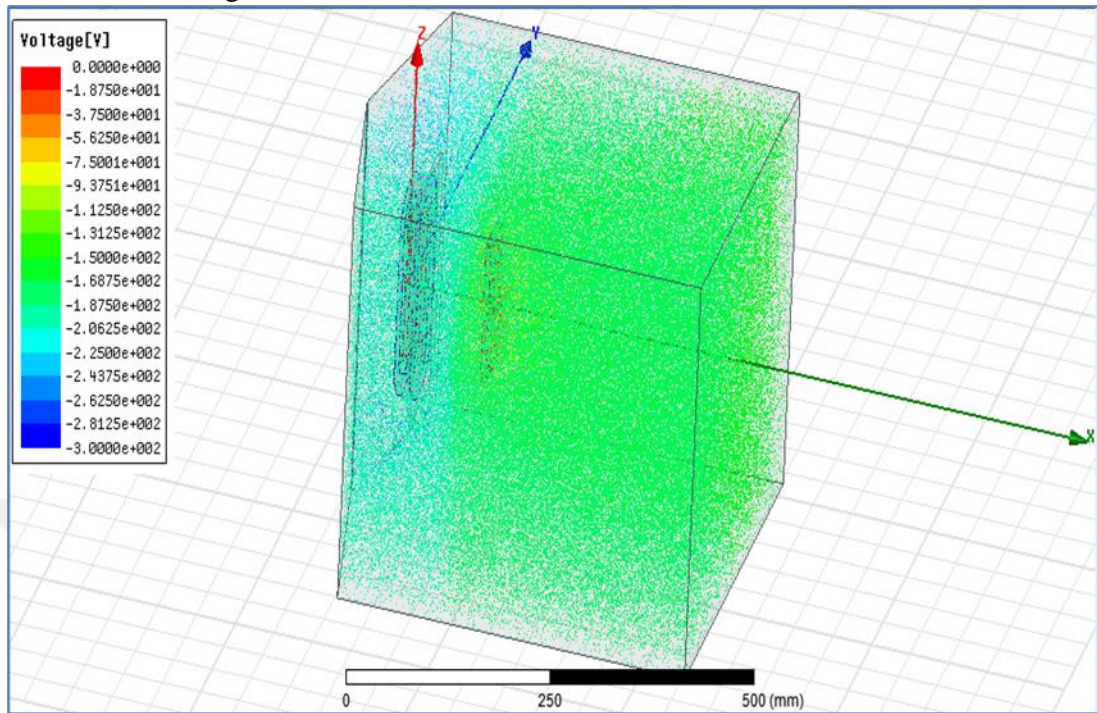


Figure 4.8 The voltage distribution in the MS system. The bias voltage is 0 V

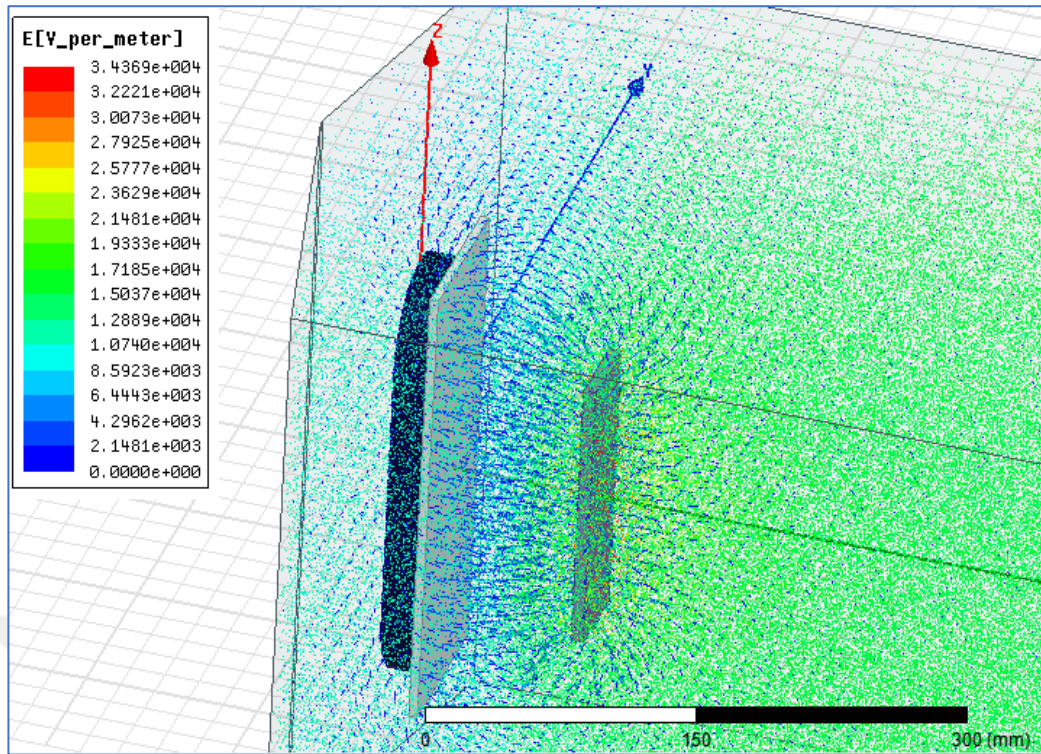


Figure 4.9 The magnitude and direction of the electric field strength of Model-A1.

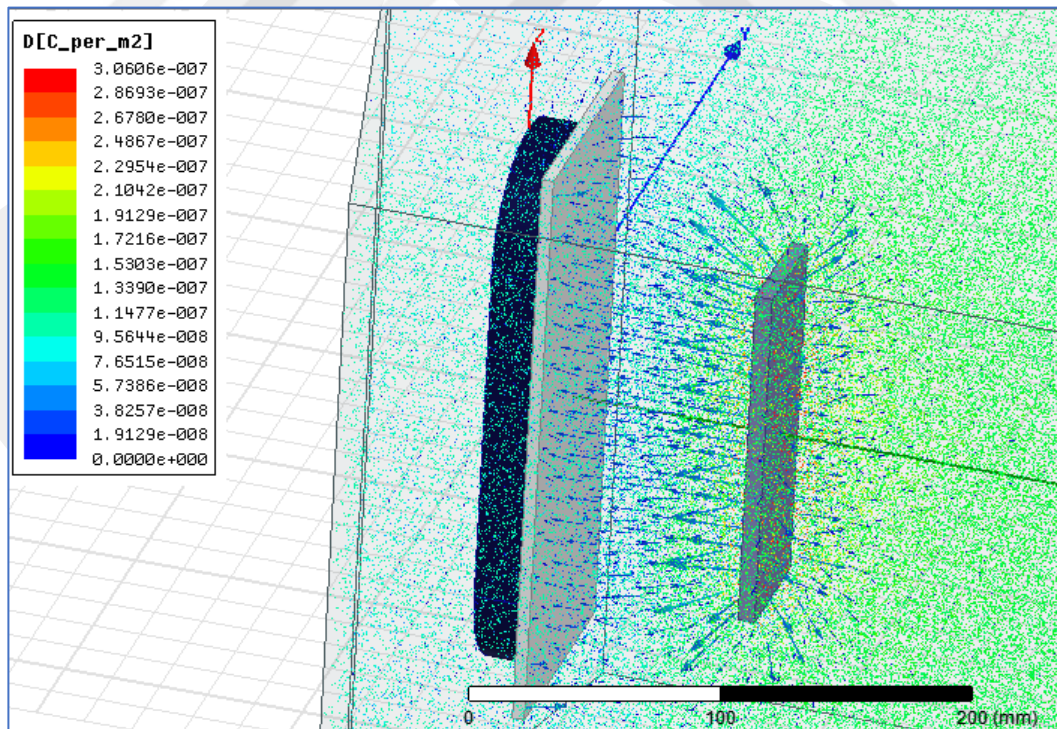
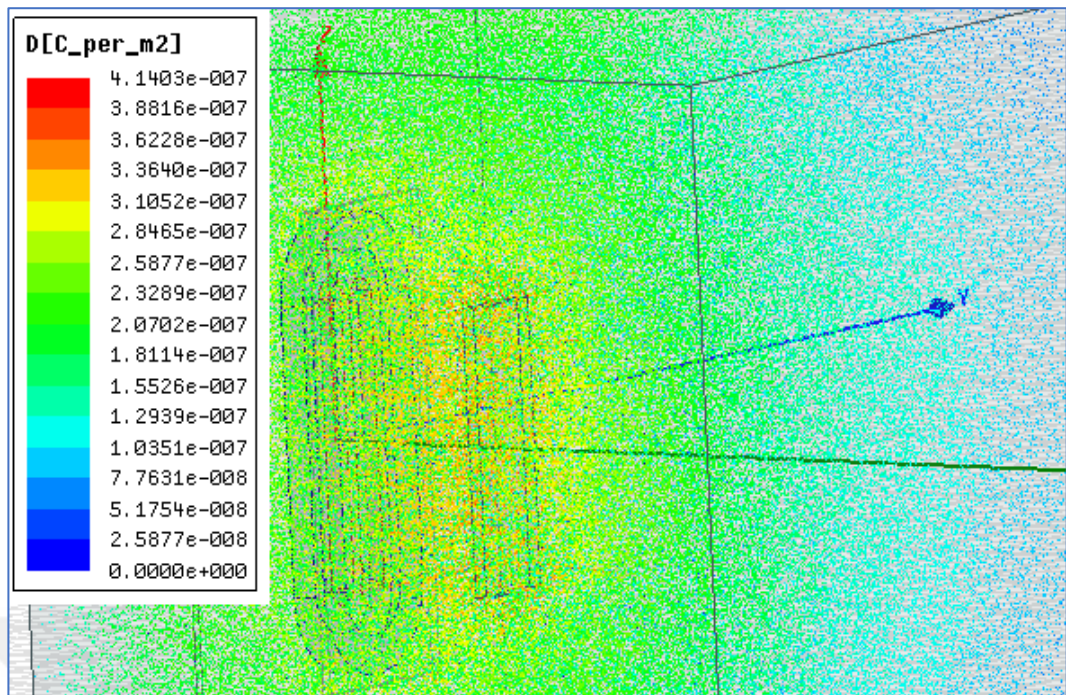
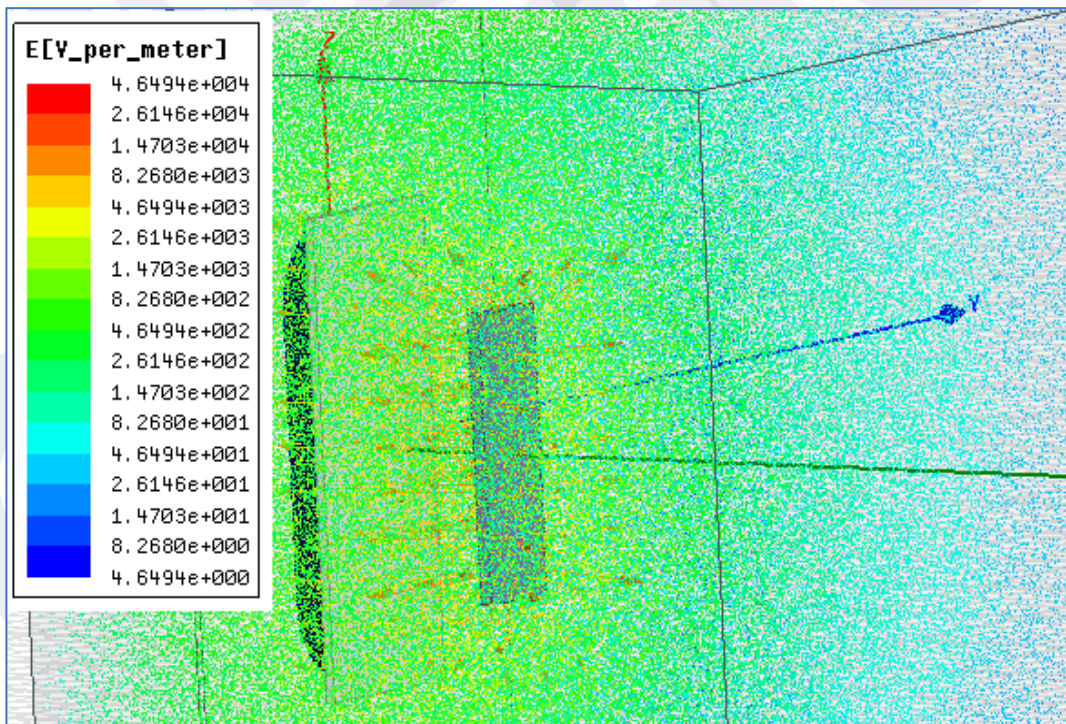


Figure 4.10 The magnitude and direction of electric flux density Model-A1.



(a)



(b)

Figure 4.11 The electric field result of Model-C1. (a) The electric field strength, (b) The electric flux density.

The results of the Electric field for different excitations of the substrate bias voltages are shown in Table 4.4.

Table 4.4 The result of the electric field for different excitations of the substrate bias voltage.

Name of the model	T-S distance (mm)	Substrate voltage (V)	E _{max.} (V/m)	D _{max.} (C/m ²)	Max. energy density (J/m ³)
Model-A1	80	0	3.43469e4	3.0606e-7	8.2273e-3
Model-B1		100	4.0511e4	3.6075e-7	1.2392e-2
Model-C1		250	4.6494e4	4.1403e-7	1.6969e-2

E: Electric field strength.

D: Electric flux density.

T-S: Distance between target and substrate.

4.3.2 Modelling of Electric Field for Different Applied Power Supply on the Target Plate

At the same MS condition but with different power supply 900,1200 and 1500 W with two substrate voltages 0,250 V respectively. In the first step, six models are built to understand the effect of the power supply on the coating. In the next step, the power supply of 1100 W with bias substrate voltage 0 V is modelled (Model-G1).

The result is summarized in Table 4.5.

Table 4.5 The result of the electric field for different power supplies and with bias substrate voltage 0 and 250 V.

Name of the model	T-S (mm)	Rf- Power supply (W)	Target plate voltage (V)	Sub. volt (V)	E _{max.} (V/m)	D _{max.} (C/m ²)	Max. energy density (J/m ³)
Model-A1	80	900	-300	0	3.43469e4	3.0606e-7	8.2273e-3
Model-A2		1200	-346.4	0	4.8977e4	4.3614e-7	1.5239e-2
Model-A3		1500	-388	0	5.4857e4	4.8850e-7	1.9118e-2
Model-C1	80	900	-300	250	4.6494e4	4.1403e-7	1.6969e-2
Model-C2		1200	-346.4	250	4.9466e4	4.4049e-7	1.6095e-2
Model-C3		1500	-388	250	3.3552e4	2.9878e-7	7.0390e-3
Model-G1	80	1100	-317.54	0	4.4895e4	3.9979e-7	1.2805e-2

4.3.3 Modelling Influence of the Substrate position on the EF Profile

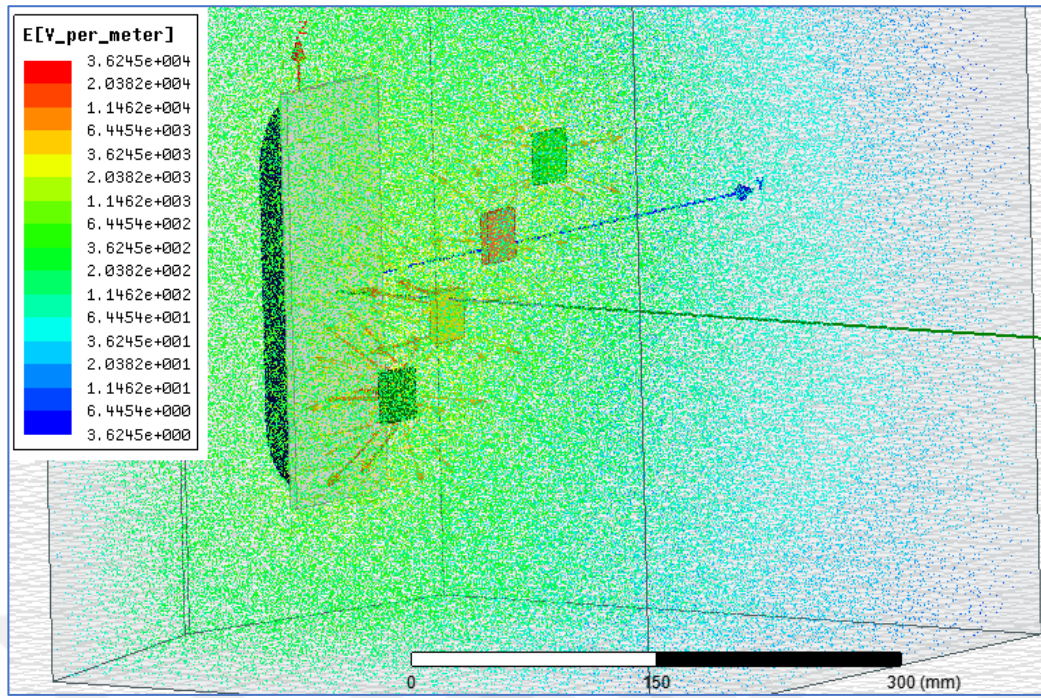
Two models were built to study the effect of substrate position on the EF calculation. The first model (model-E) builds with four small substrates to find EF as shown in Table 4.6. The geometry of the substrate is 30*30*7 mm. The substrate's material is D2 steel. They fixed at different positions in the chamber. In the second model (model-E1), the input parameters of model-E1 are applied with one substrate. The substrate geometry is 50*150*7 mm. The purpose of this model is to study the effect of distance between the target plate and substrate. The centre point of the target plate is (25,0,0). The electric field result of these samples is found, as shown in Table 4.7. For more details see Figures 4.12, 4.13 and 4.14.

Table 4.6 The input parameters of modelling EF for model-E and model-E1

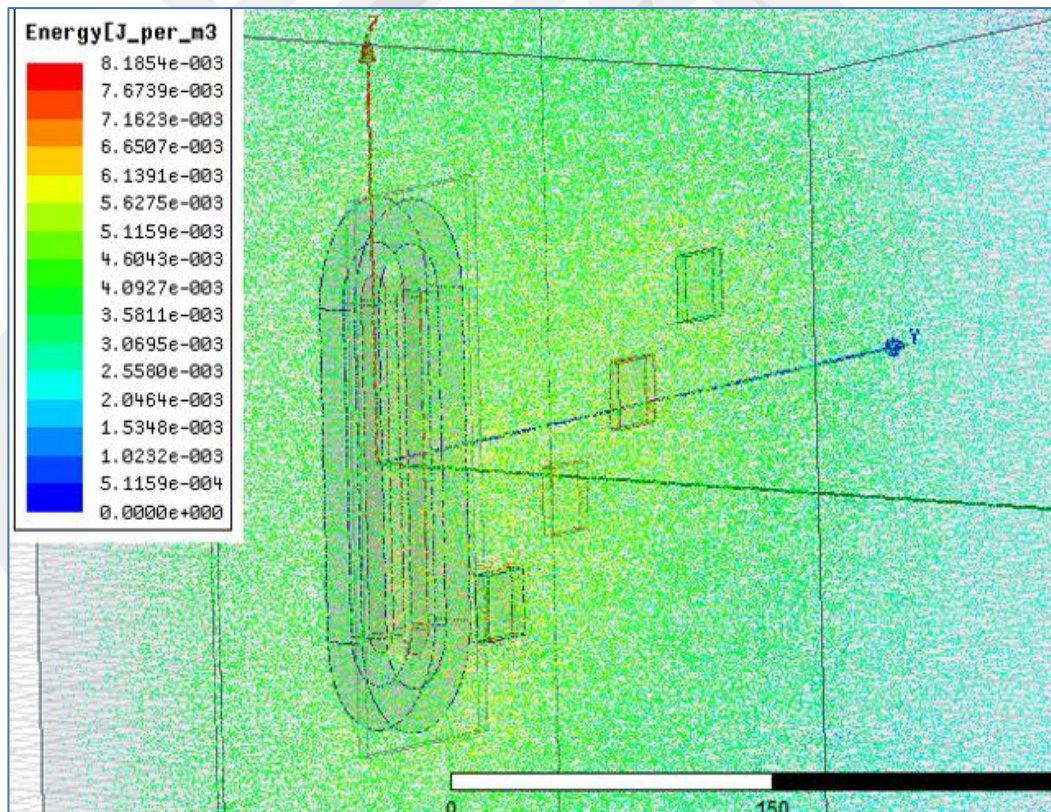
Name of the model	Name of substrate	Sub.Center (X, Y, Z)	Rf-Power supply(W)	Target voltage (V)	Substrate Volt (V)
Model-E	Sub.1	(65,0,-60)	900	-300	0
	Sub.2	(105,0,-10)			
	Sub.3	(145,0,40)			
	Sub.4	(185,0,90)			
Model-E1	Sub.1	(65,0,0)			

Table 4.7 The result of the electric field for multi-substrates with different positions in the chamber

Name of model	Power supply (W)	Target voltage (V)	Subs. voltage (V)	E _{max.} (V/m)	D _{max.} (C/m ²)	Max. energy density (J/m ³)
Model-E	900	-300	0	3.6245e4	3.2276e-7	8.1854e-3
Model-E1	900	-300	0	4.1566e4	3.7014e-7	1.1372e-2



(a)



(b)

Figure 4.12 The electric field result of Model-E. (a) The electric field strength, and (b) The electric energy.

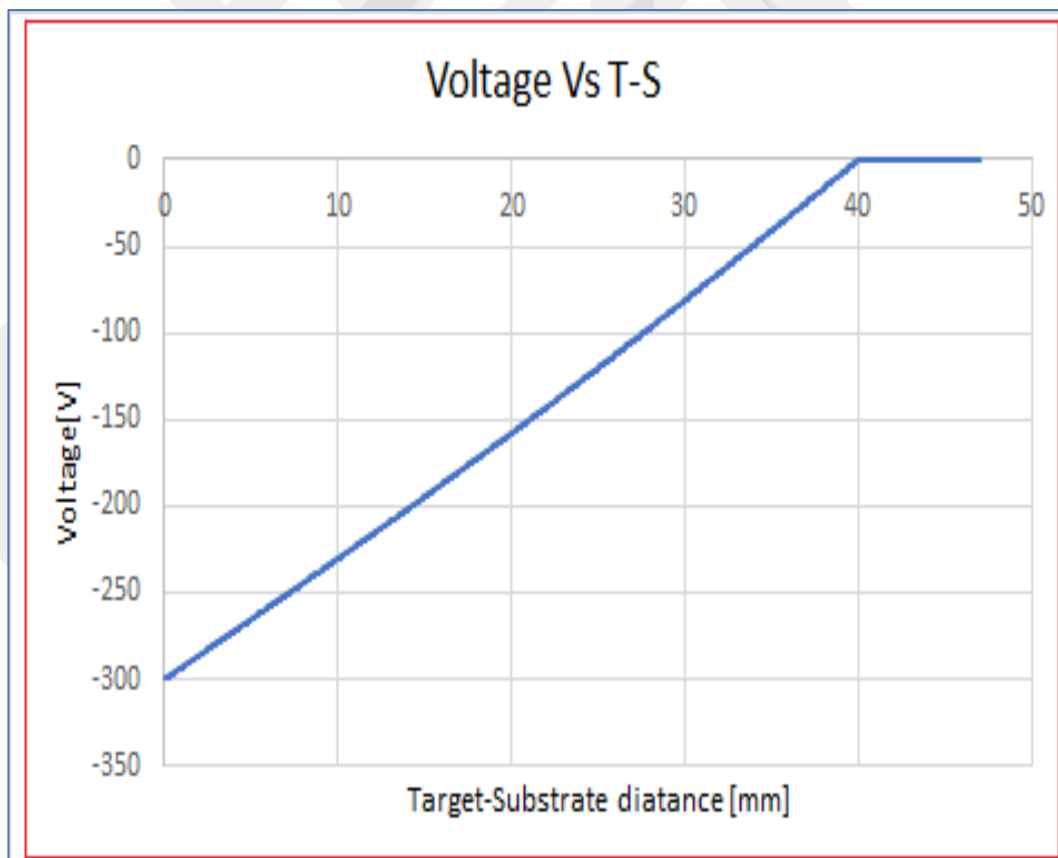
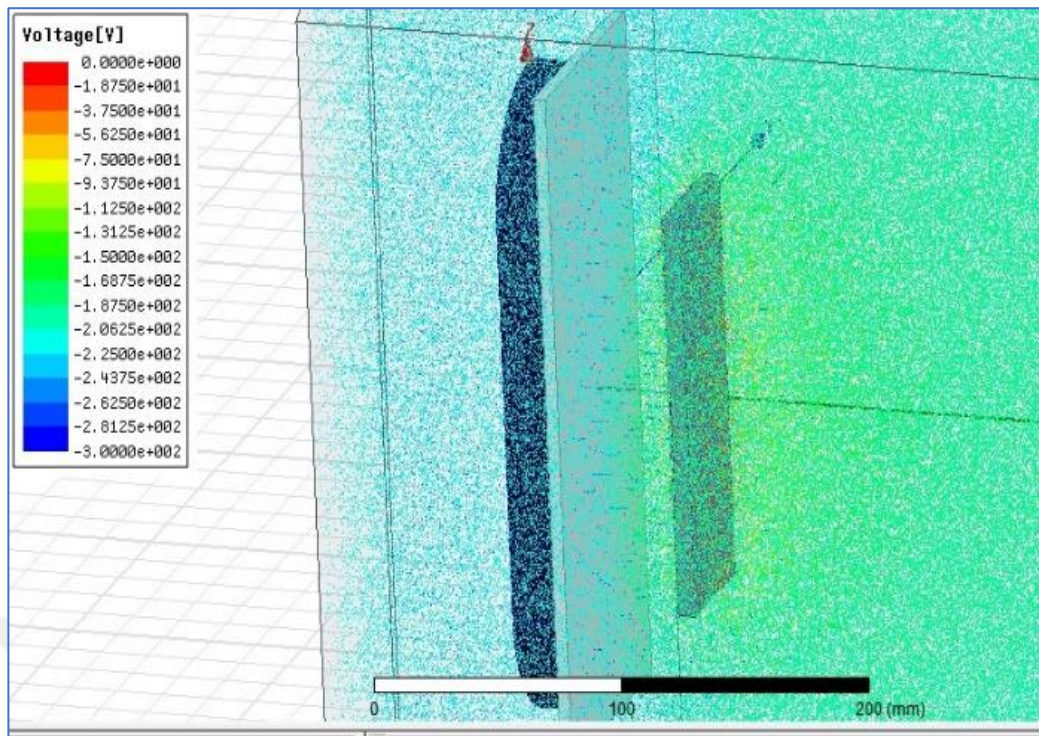


Figure 4.13 Voltage distribution between target plate and substrate (model-E1)

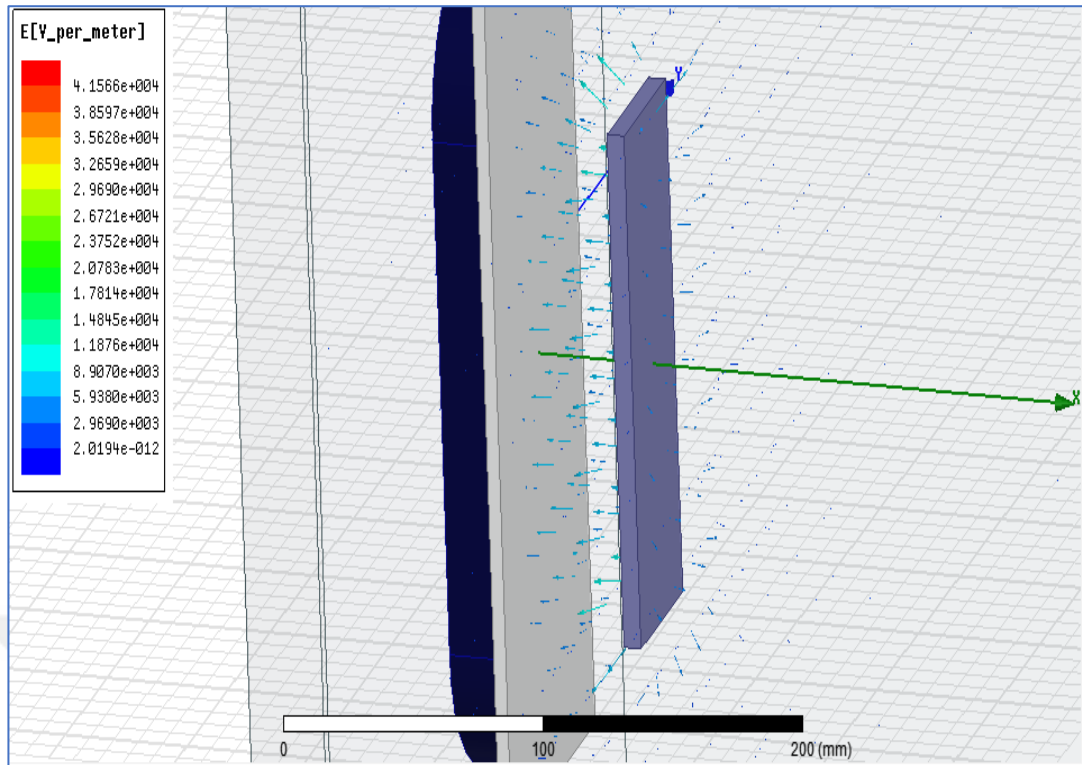
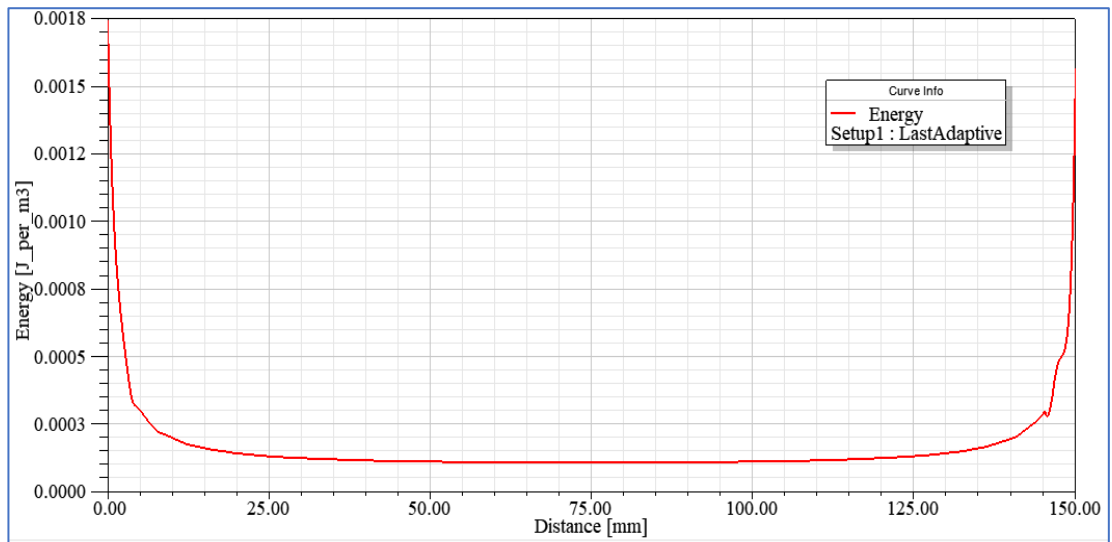
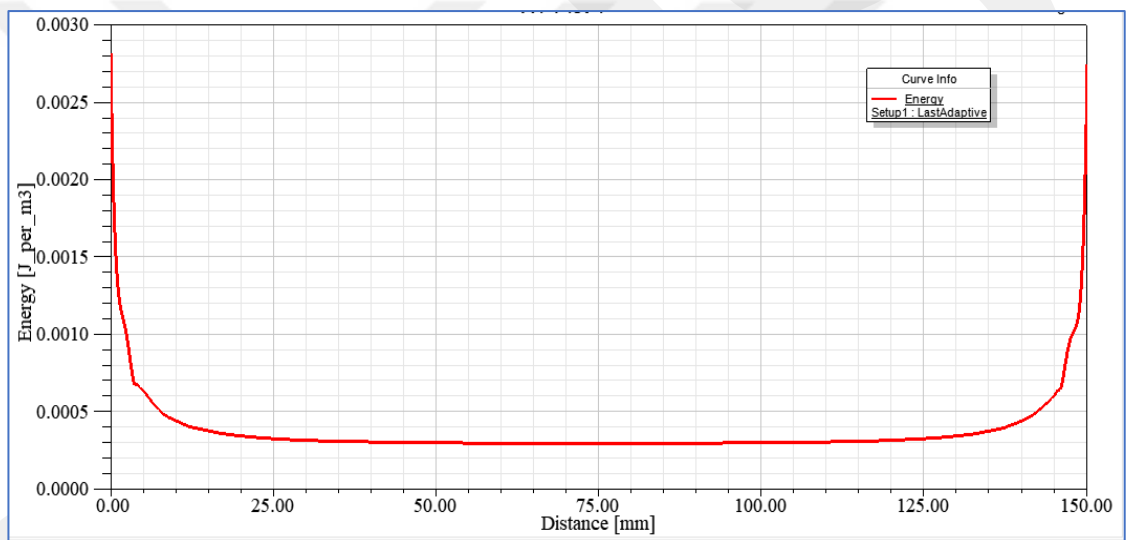


Figure 4.14 Modelling of Magnitude and direction of Electric Field (model-E1).

To study the effect of (T-S) distance on the EF, We will compare the EF result between model-A1 and model-E1, both of them have the same boundary condition with two different distances between the target plate and substrate. The distances are 80 and 40 mm respectively. Figures 4.15 and 4.16 show the result of energy density and electric field strength on the substrate respectively. The maximum energy density and electric field strength are on the edge of the substrate. Decreasing the T-S distance from 80 to 40 mm will increase the energy density from 0.00012 J/m^3 in the centre of the substrate to 0.0003 J/m^3 .



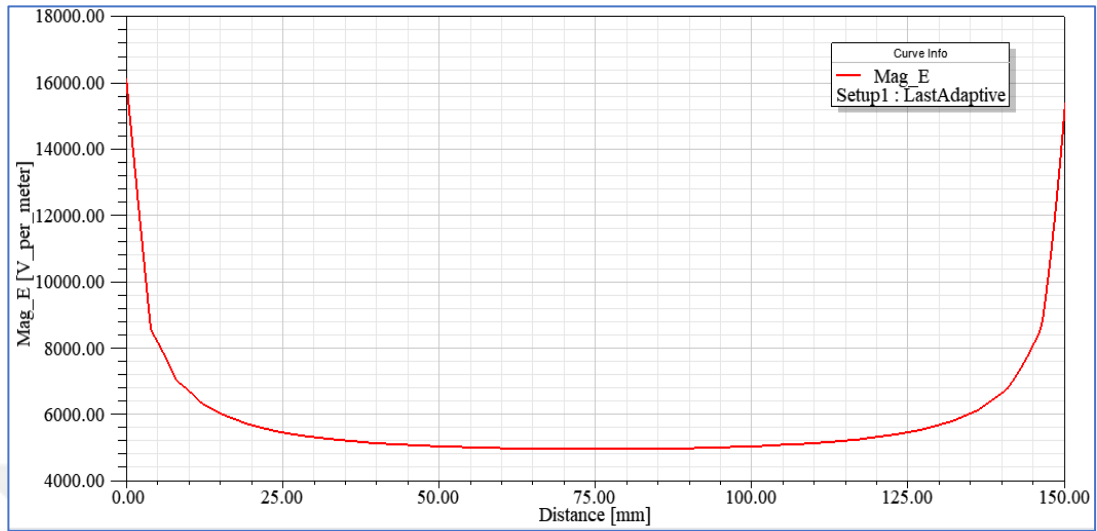
(a)



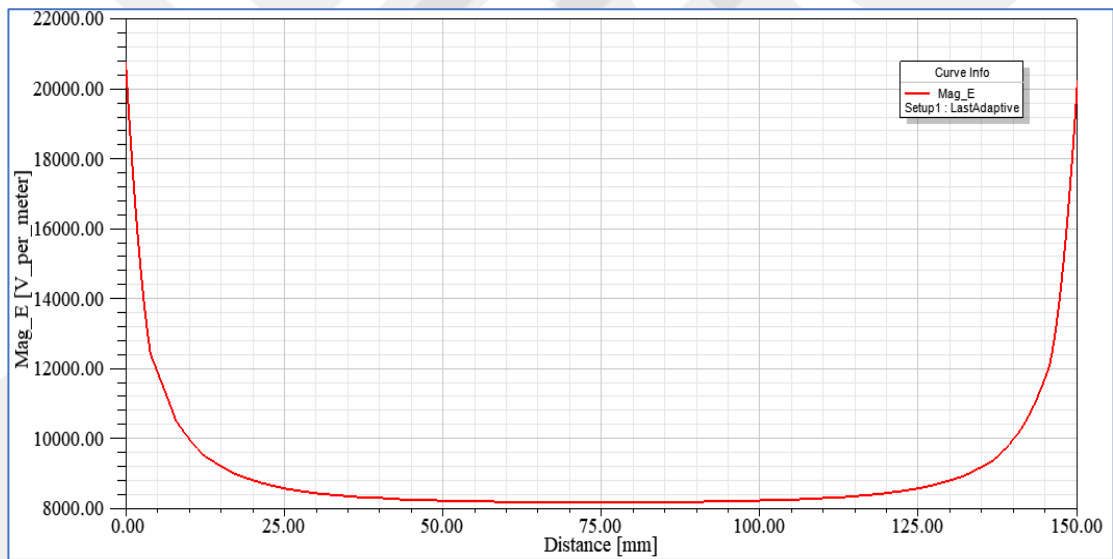
(b)

Figure 4.15 Energy density analysis on the substrate surface. (a) T-S distance is 80 mm and (b) T-S distance is 40 mm.

The electric field strength increased from 4800 V/m to 8200 V/m as shown in Figure 26.



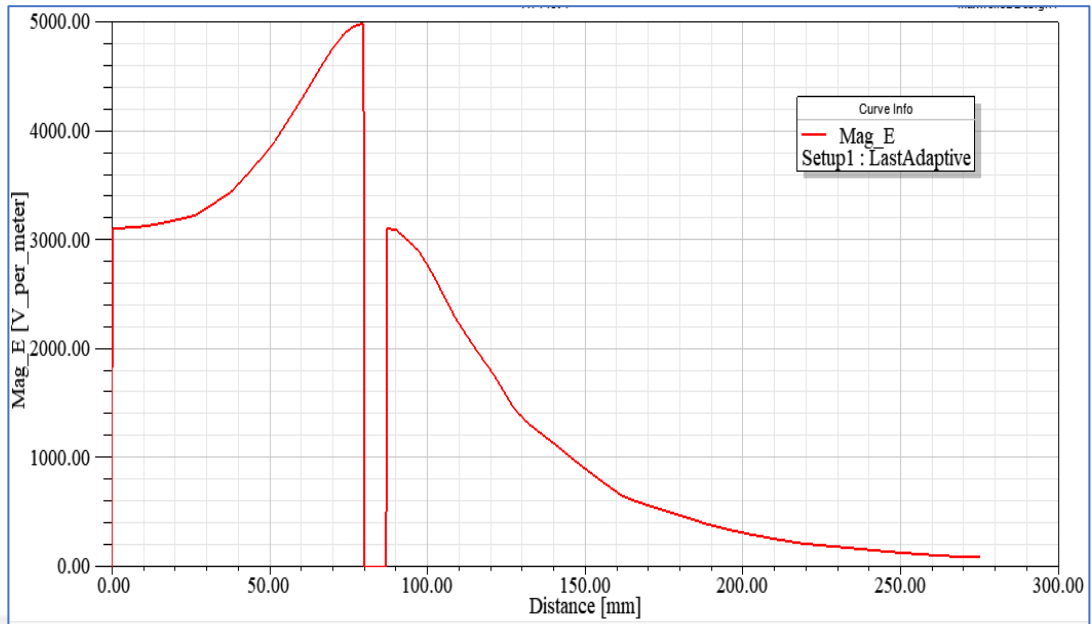
(a)



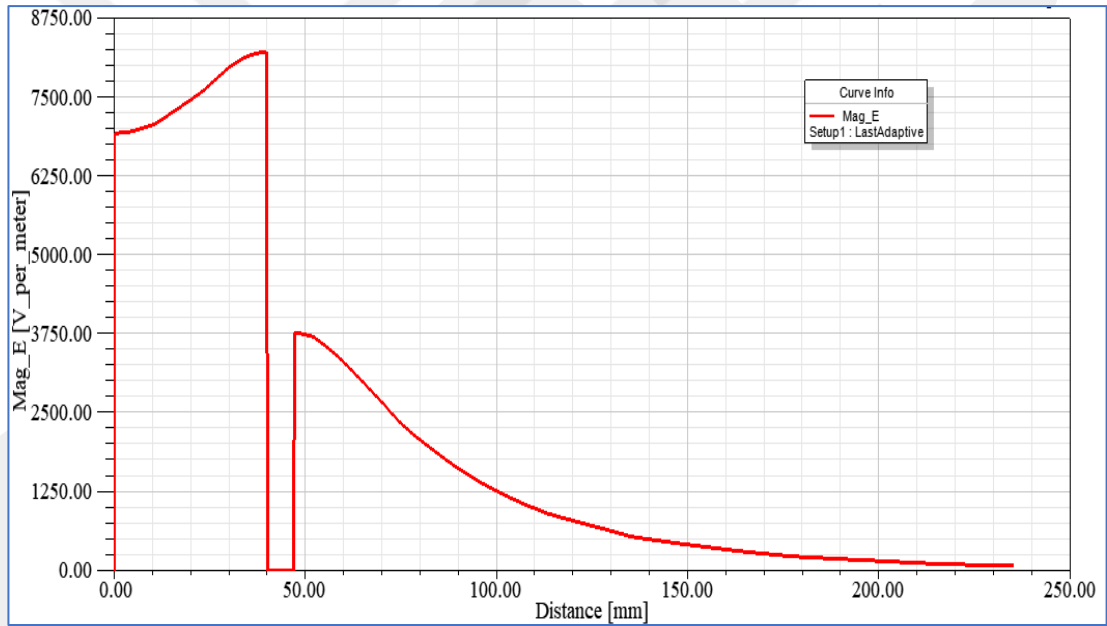
(b)

Figure 4.16 Electric field strength analysis on the substrate surface. (a) T-S distance is 80 mm and (b) T-S distance is 40 mm.

Figure 4.17, Shows the distribution of electric field strength between target and substrate. Decreasing the distance from 80 mm to 40 mm will increase the maximum electric field strength from 5000 V/m to 8250 V/m.



(a)



(b)

Figure 4.17 Electric field strength analysis along the path between the centre of the target plate passes through the centre of the substrate. (a) T-S distance is 80 mm and (b) T-S distance is 40 mm.

4.3.4 Modelling Influence of the Substrate Material on the EF Profile

One model builds with five small substrates. The geometry of the substrate is 30*30*7 mm. Five types of materials are used. These types are D2, Aluminum, Ti, TiN, and glass as shown in Table 4.8. The purpose of the model, study the effect of substrate materials on the EF profile. The boundary condition is shown in Table 4.9.

Table 4.8 The relative permittivity and Bulk Conductivity of different substrate materials in the MS system

Solver	Material	Relative Permittivity	Bulk Conductivity (siemens/m)
Electrostatic	NdFeB ₃₅	1	625000
	h-BN	4.3	4.98
	Steel	1	2000000
	Ar	1.000513	0
	N ₂	1.000580	0
	glass	3.7 – 10 [92]	0
	Ti	86 – 173 [92]	1820000
	TiN	1	8670000
AL	1	38000	

Table 4.9 The input parameters of modelling EF for different substrates material

Name of the model	Name of substrate	Type of material	Sub.Center Point (x,y,z)	Rf-Power supply (W)	Target voltage (V)	Sub. Voltage (V)
Model-F	Sub.1	1xAl	(105,0,-110)	900	-300	0
	Sub.2	1xD2	(105,0,-50)			
	Sub.3	1xTi	(105,0,-10)			
	Sub.4	1xTiN	(105,0,40)			
	Sub.5	1xglass	(105,0,90)			

The result of EF is shown in Figures 4.18 and 4.19, Table 4.10 summarized the result.

Table 4.10 The result of the electric field for multi-substrates with a different type of material

Name of the model	T-S (mm)	Rf-Power supply (W)	Target plate voltage (V)	Sub. volt (V)	E _{max.} (V/m)	D _{max.} (C/m ²)	Max. energy density (J/m ³)
Model-F	80	900	-300	0	3.5653e4	3.1749e-7	8.1404e-3

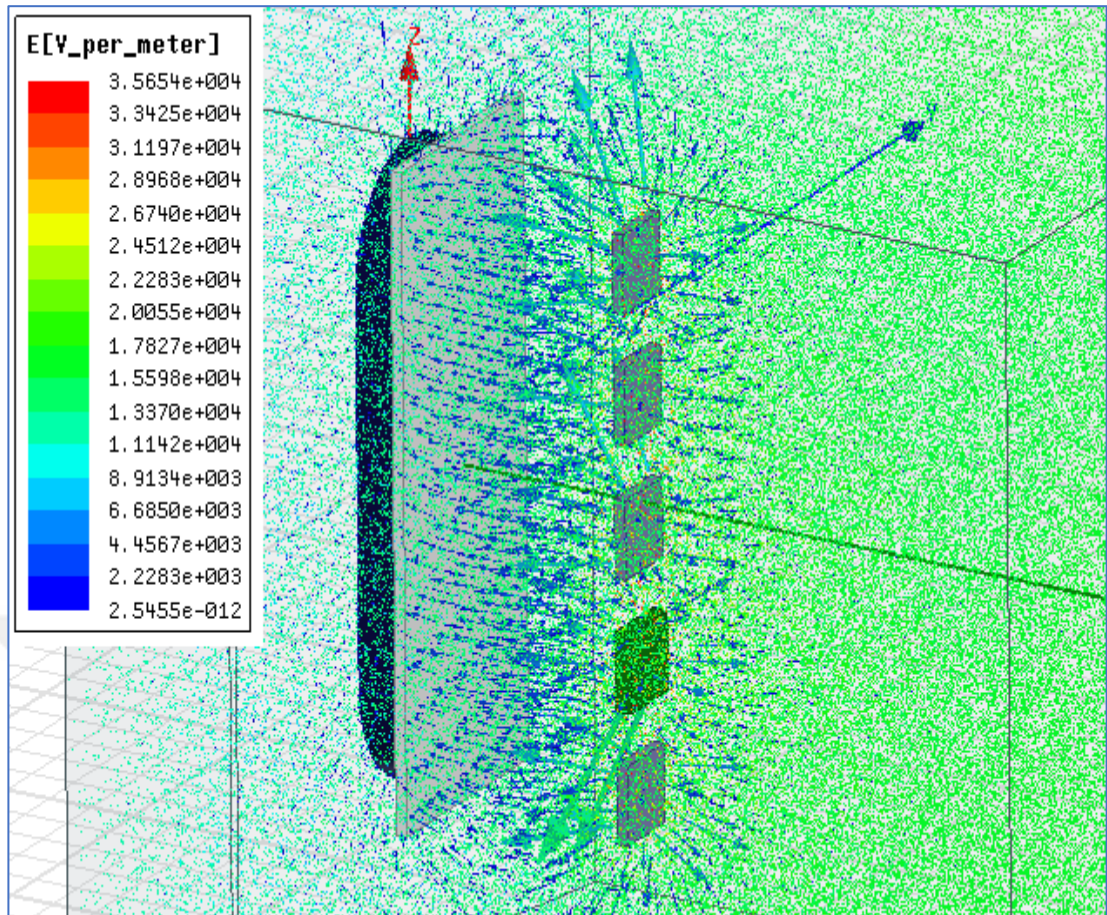
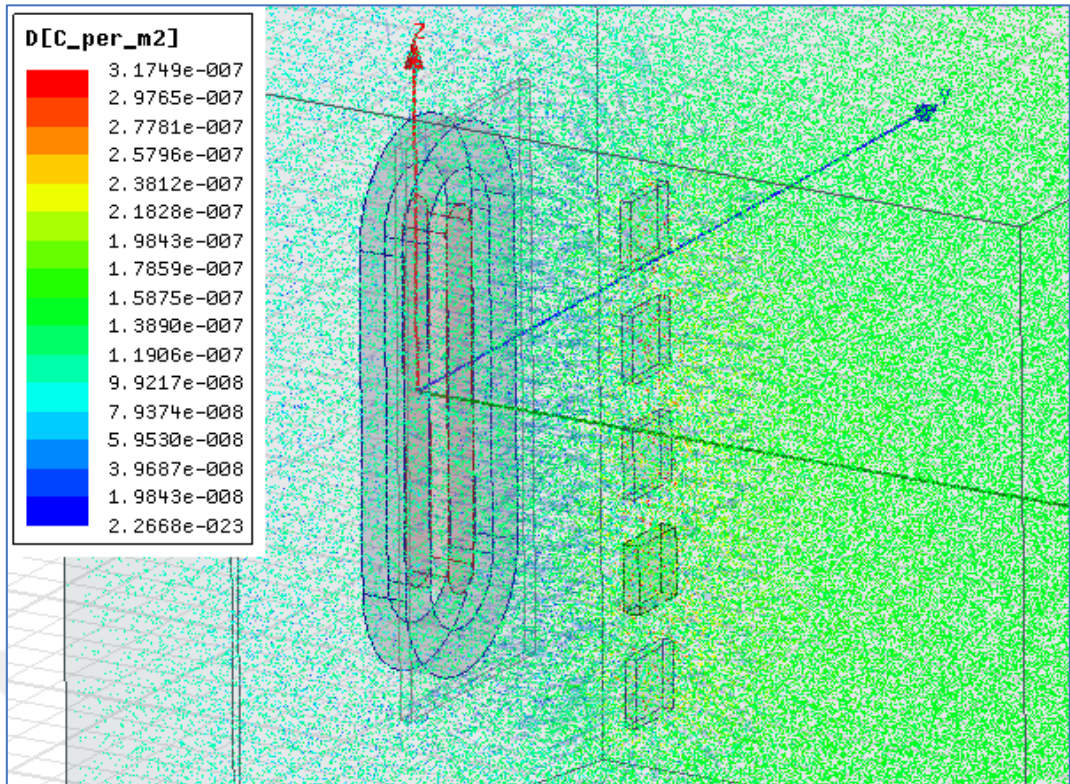
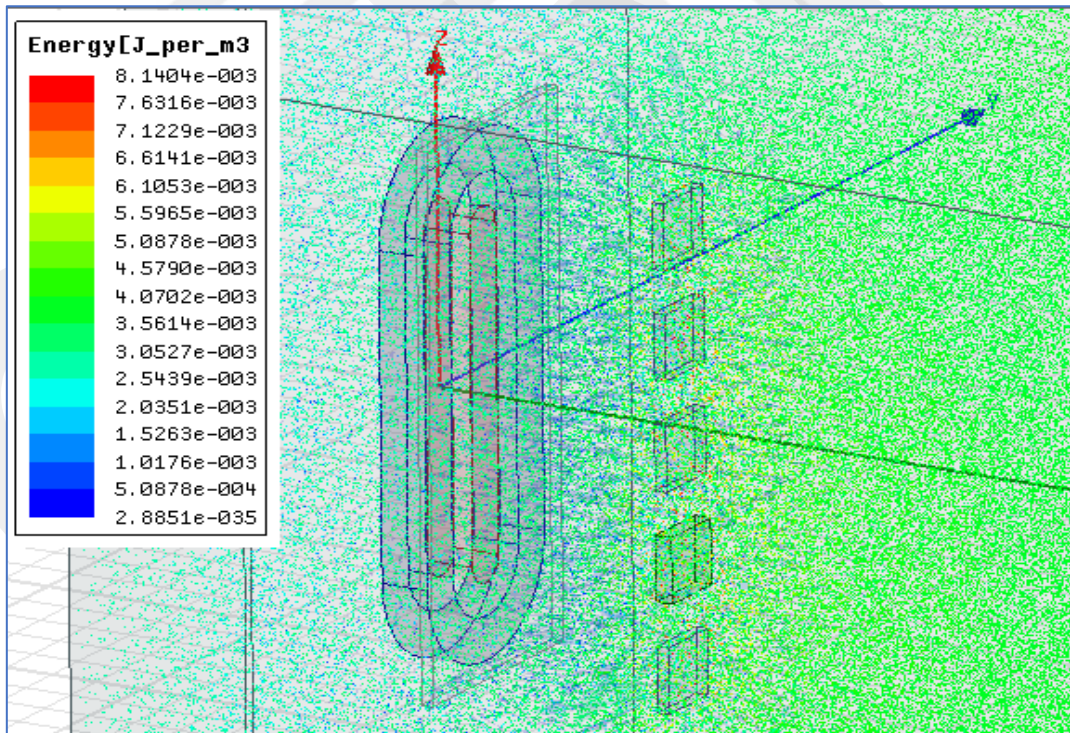


Figure 4.18 The electric field strength of Model-F



(a)



(b)

Figure 4.19 The electric field result of Model-F,(a) The electric flux density and (b) The electric energy.

CHAPTER 5

THEORETICAL AND EXPERIMENTAL STUDY OF BN COATING

5.1 Introduction

Samadii™/sciv (Statistical Contact in Vacuum) package uses to interpret Magnetron Sputtering. For each time step, Samadii™/sciv employs the particle method to determine the force acting on each particle.

In the next stage, it uses force and mass to calculate particles' velocity and location. Samadii/sciv calculates the Lorentz force, which is created by the electric field, magnetic field, and particle collisions. Its most notable feature is that it uses the theory of (SUPER-PARTICLE), also known as the Direct Simulation Monte Carlo Method (DSMC), to calculate probabilistic collisions.

5.2 Theoretical Modelling of BN Coating

The Samadii™/sciv program will be utilized to model the BN coating in this investigation. The input parameters of the BN coating model are summarised in Table 5.1.

Table 5.1 Boundary condition of MS of BN coating

No.	Model-Name	Target material	Substrate		T-S (mm)	T(°C)	Rpm	Magnetron	Substrate Voltage (v)	Time (hr)
			Material	Geometry (mm)						
1	Model-A1	h-BN	1xD2	150*50*7	80	300	Off	900w,40/8 sccm Ar/N ₂	0	6

T-S: The distance between target and substrate.

5.2.1 Geometry and Mesh

The target geometry is 250*100*5 mm. The centre point of the target is (25,0,0).

The substrate geometry is 150*50*7 mm as shown in Figure 5.1. The centre point (position) of the substrate is (105,0,0). Mesh Import from COMSOL- Multiphysics to Samadii/sciv software.

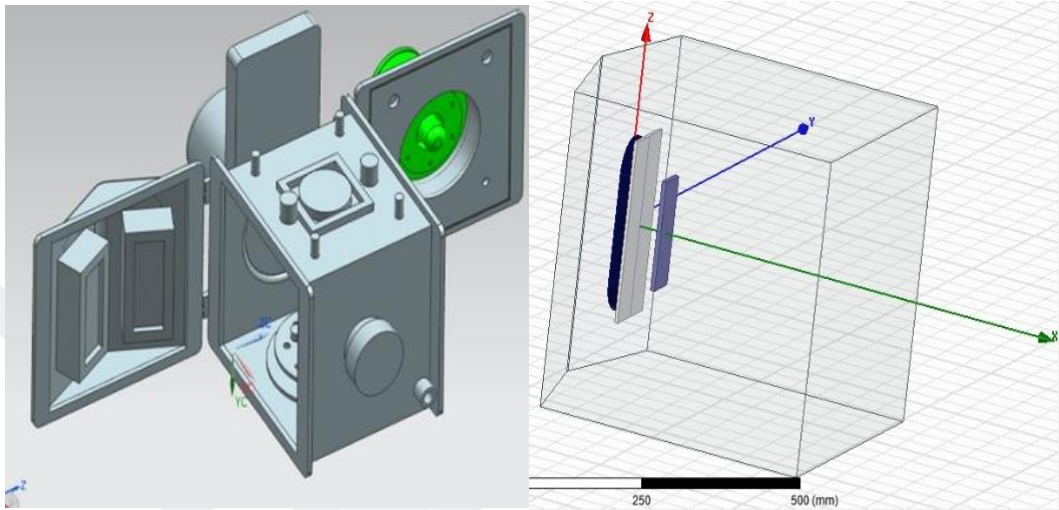


Figure 5.1 Geometry of magnetron sputtering system for modelling

- Mesh will create in COMSOL- Multiphysics.
- Save the file as mphtxt
- Change the file from mphtxt to dll type file.
- Import mesh from COMSOL- Multiphysics to Samadii/ sciv software as shown in Figure 5.2.

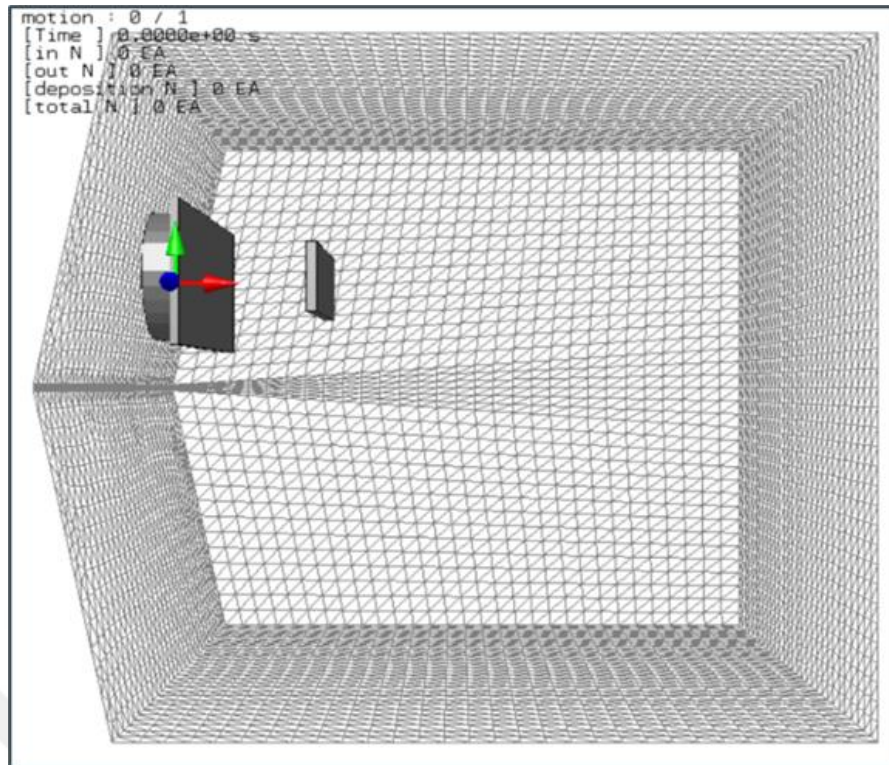


Figure 5.2 Mesh of magnetron sputtering system for modelling

5.2.2. Material Define: Ar, N₂, BN, 2N

- Define the molecular mass, density, and ionic charge as shown in Figure 5.3.
- In Samadii/sciv library there is a definition for four types of materials O₂, H₂, N₂, and Ar.

The figure displays three screenshots of a software interface for material definition, showing the configuration of different materials.

Top Left: samadii:material [beta] (Ar)

- default material enable:
- default material: [dropdown]
- name: Ar
- molecular mass [x1.0E-27 kg]: 66.3
- [g/mol]: 0.0
- viscosity coefficient [x1.0E-5 Ns/m²]: 2.117
- viscosity index: 0.81
- reference diameter [x1.0E-10 m]: 4.17
- symmetry factor: 1
- density [kg/m³]: 1.661
- ionic charge: 1
- wall adsorption coefficient (WAC): 1
- variable wall adsorption coefficient:
- degree of freedom:
 - total: 0
 - rotation: 0
- collision number:
 - rotation: 0
 - vibration C1: 0
 - vibration C2: 0
- characteristic temp. [K]:
 - rotation: 0
 - vibration: 0
 - dissociation: 0
 - ionization: 0
 - reference: 273
- color: [green]

Top Right: samadii:material [beta] (BN)

- default material enable:
- default material: [dropdown]
- name: BN
- molecular mass [x1.0E-27 kg]: 46.5348837
- [g/mol]: 0.0
- viscosity coefficient [x1.0E-5 Ns/m²]: 3.5
- viscosity index: 0.76
- reference diameter [x1.0E-10 m]: 6.5
- symmetry factor: 2
- density [kg/m³]: 2300
- ionic charge: 0
- wall adsorption coefficient (WAC): 1
- variable wall adsorption coefficient:
- degree of freedom:
 - total: 0
 - rotation: 0
- collision number:
 - rotation: 0
 - vibration C1: 0
 - vibration C2: 0
- characteristic temp. [K]:
 - rotation: 0
 - vibration: 0
 - dissociation: 0
 - ionization: 0
 - reference: 273
- color: [white]

Bottom Right: samadii:material [beta] (N2)

- default material enable:
- default material: [dropdown]
- name: N2
- molecular mass [x1.0E-27 kg]: 46.5448504
- [g/mol]: 0.0
- viscosity coefficient [x1.0E-5 Ns/m²]: 1.656
- viscosity index: 0.74
- reference diameter [x1.0E-10 m]: 4.17
- symmetry factor: 1
- density [kg/m³]: 1.2506
- ionic charge: -3
- wall adsorption coefficient (WAC): 1
- variable wall adsorption coefficient:
- degree of freedom:
 - total: 0
 - rotation: 0
- collision number:
 - rotation: 0
 - vibration C1: 0
 - vibration C2: 0
- characteristic temp. [K]:
 - rotation: 2.88
 - vibration: 3371
 - dissociation: 113500
 - ionization: 181000
 - reference: 273
- color: [red]

Working Path (Center):

- 0:GeForce RTX 3070
- Ar
- N2
- BN
- 2N
- assemble
 - add new elm
 - add new vlm
 - draw assm
 - regen
 - inlet-Ar.elm
 - inlet-N2.elm
 - target.elm
 - substrate-00.elm
 - substrate-01.elm
 - substrate-02.elm
 - substrate-03.elm
 - substrate-04.elm
 - substrate-05.elm
 - pole.elm
 - chamber.vlm
- motion
 - edit motion
 - test motion
 - wall growth
- boundary
 - boundary setup
- particle
 - create
 - extract from file
 - inlet-particle
- run info
 - edit run-info
- field import
 - electric field
 - efield 0

Figure 5.3 Materials definition

5.2.3 Assemble

Boundary condition type:

- Define the magnetic poles and chamber as constrained wall
- Define the target plate (BN) as a sputtering target

sputtering Target – change from collided particles to the defined particles and generate new particles.

Define the Sputtering yield data for BN as a function of incident ion energy Ar^+ . The energy dependence of the sputtering yield under a normal angle (0°) and oblique angle (45°) ion incidence are applied [93]. The sputtering yield:70 [ev] means applying the sputtering data to only over 70 ev particles.

- Define particle inlet for MS system for both gases Ar and N_2 . The velocity of gas will be calculated by dividing the flow rate by the area of the cross-section. The area of the cross-section is 33.19 mm^2 .
- Define the substrate surfaces as deposition walls. The boundary conditions are shown in Figures 5.4 and 5.5.

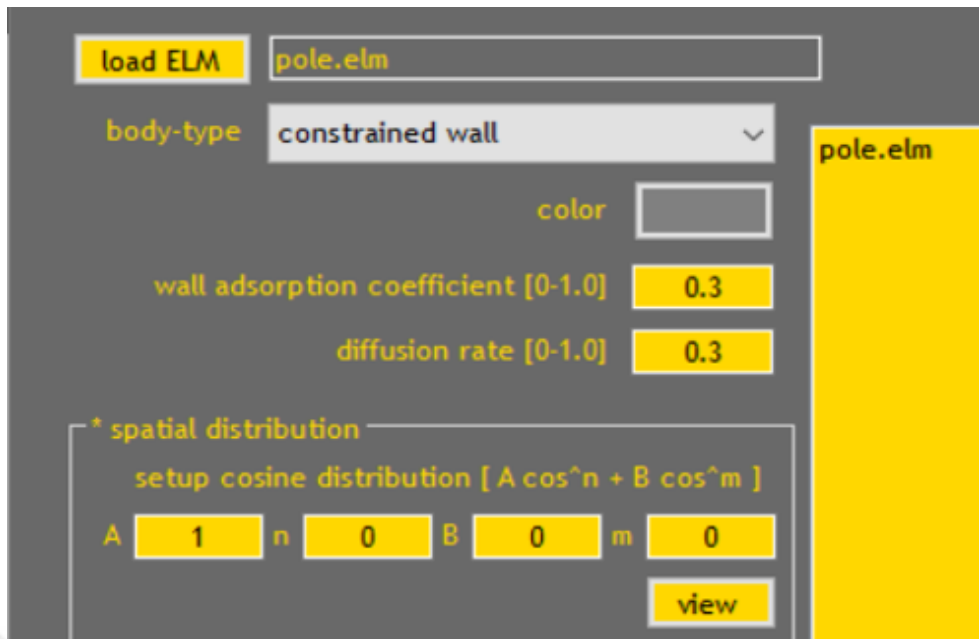
- **Processes (1):** Wall adsorption= [wall adsorption of material* wall adsorption of the body] *100%

The Wall adsorption coefficient is a number that sets the percentage of particles that collide with the body attached to the body.

Wall adsorption = $[0.8*1] *100\%=80\%$ of collision particles of BN with substrate surface will be deposited.

The remained particles of (BN) after the process (1) those get the speed with temperature (get enough energy) will deposit on the substrate.

- **Processes (2):** Diffusion rate: The percentage of wall collision particles will be affected by the wall temperature and cosine distribution. For example, when diffusion rate = 0.8 that means 80% of wall collision particles get wall temperature energy and the remaining 20% go under specular reflection.



(a)



(b)

Figure 5.4 The boundary condition of MS system: (a) constrained wall and (b) sputtering target

load ELM inlet-Ar.elm

body-type particle-inlet

color

wall adsorption coefficient [0-1.0] 0.2

diffusion rate [0-1.0] 1

* spatial distribution

setup cosine distribution [$A \cos^n + B \cos^m$]

A 1 n 0 B 0 m 0

view

import spatial distribution

* spatial distribution format view view

load (none)

* thermal condition

temperature [K] 576

import thermal analysis result

* thermal data at any position [x,y,z,temperature] [mm, K]

load (none)

* input condition

material Ar

flow rate 40 sccm

velocity [m/s]

pressure 0 Pa

(a)

load ELM substrate-01.elm

body-type deposition

color

wall adsorption coefficient [0-1.0] 0.8

diffusion rate [0-1.0] 0.8

* spatial distribution

setup cosine distribution [$A \cos^n + B \cos^m$]

A 1 n 0 B 0 m 0

view

(b)

Figure 5.5 The boundary condition of the MS system: (a) particle inlet and (b) deposition.

Note: The deposition rate can be applied only on 2D therefore the substrate departs into a 2D surface as shown in Figure 5.6.

- Substrate-00.elm
- Substrate-01.elm
- Substrate-02.elm
- Substrate-03.elm
- Substrate-04.elm
- Substrate-05.elm

After defining the boundary conditions for all parts in the MS model, choose draw to assemble and regen to fixed assemble with this boundary.

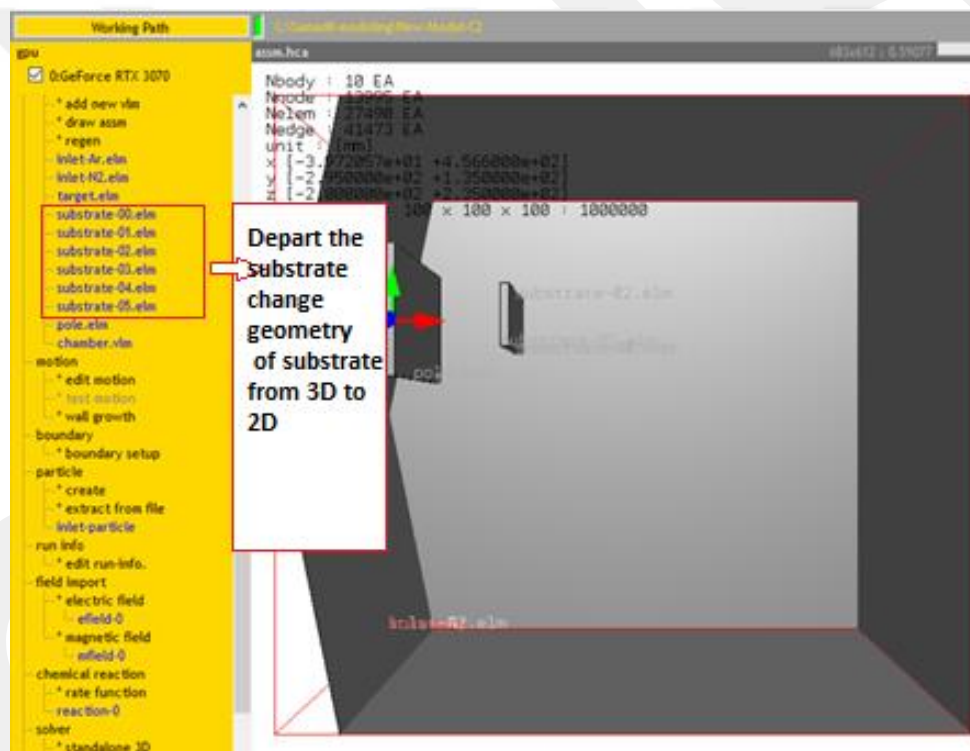


Figure 5.6 Depart the substrate on 2D surfaces

5.2.4 Boundary Setup

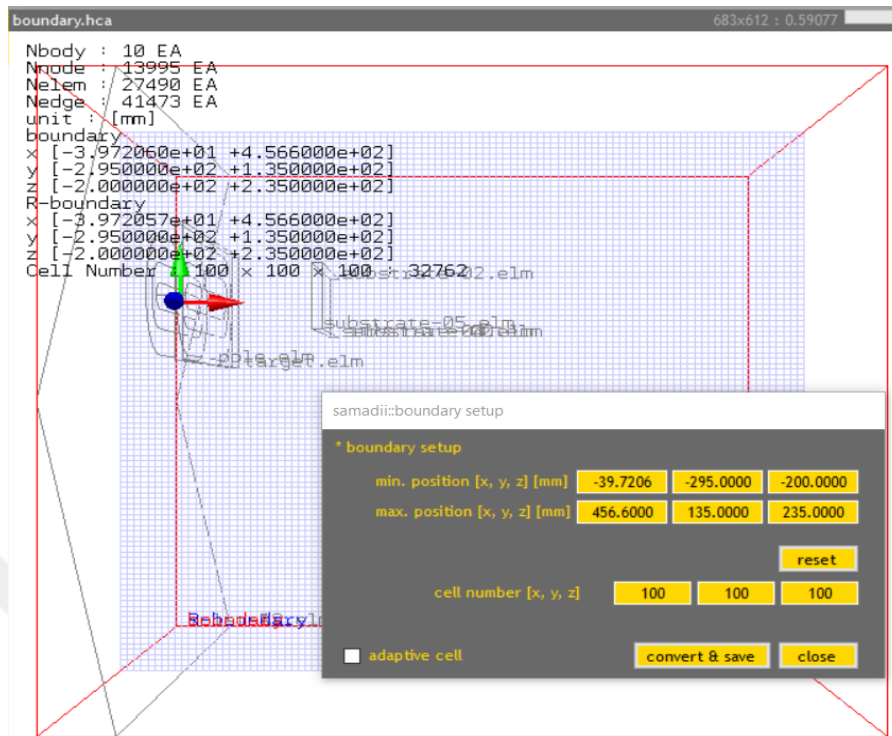


Figure 5.7 Boundary condition of modelling

5.2.5 Creation of Particles

Change the defined flow rate to particle number.

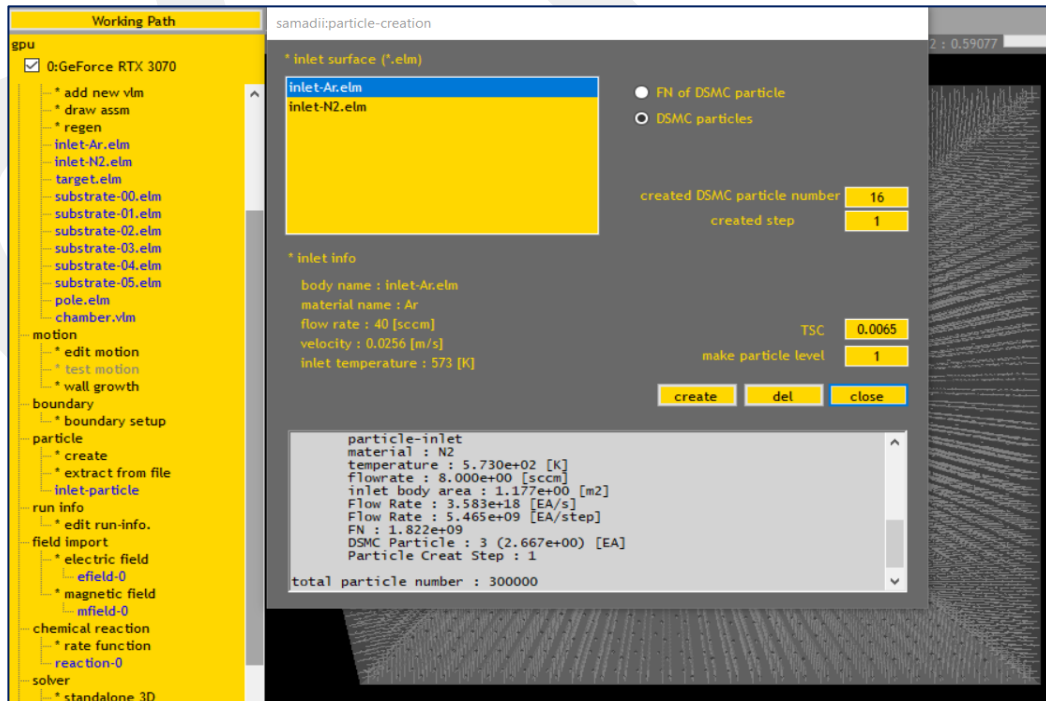
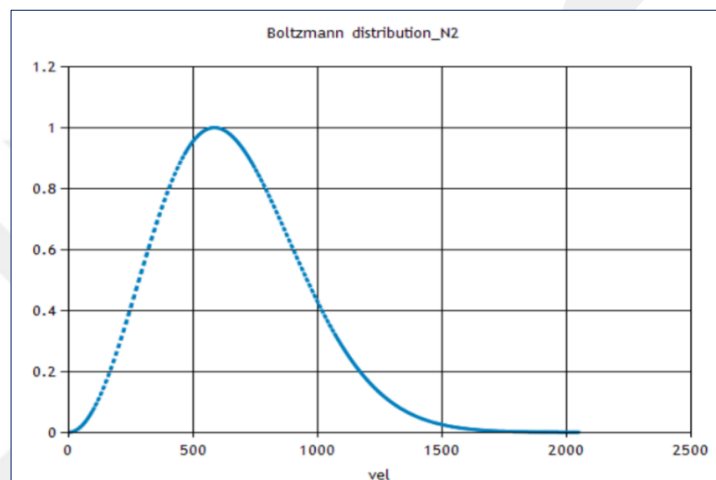


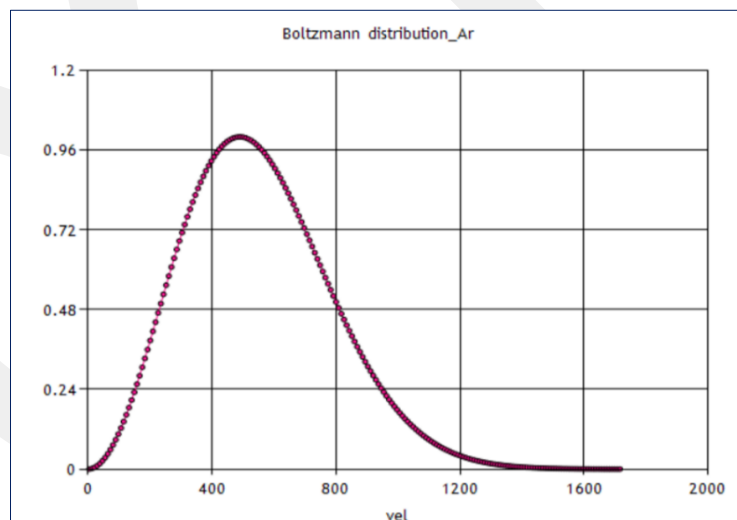
Figure 5.8 Creation of particles

FN of DSMC particle: define the number of molecules represented by one particle (FN). DSMC particle: define the number of representative particles to be generated during the 1-time step. TSC (Time Scale Constant): Define the time step.

Make particle level: the number of how many particles are used to represent the graph (Maxwell-Boltzmann distribution, cosine distribution, and spatial distribution) by DSMC particles. Define the preparation particle number (level 1 = 300,000 [EA], maximum 5,000,000 [EA]). The process will change the defined flow rate to particle number as shown in Figure 5.9.



(a)



(b)

Figure 5.9 Boltzman Distribution (probability density Vs velocity) for Ar and N₂ in (Model-A1)

Maxwell-Boltzman Distribution:

$$f(v) = \sqrt{\frac{2}{\pi}} \left(\frac{m}{K_B T}\right)^3 * v^2 e^{\frac{-mv^2}{2K_B T}} \quad (5.1)$$

The typical speed is: $v_p = \sqrt{\frac{2K_B T}{m}} \quad (5.2)$

Root mean square speed $v_{rms} = \sqrt{\frac{3K_B T}{m}} \quad (5.3)$

K_B : Boltzman constant.

T: Temperature, m: mass.

5.2.6 Electric Field and Magnetic Field Import

The electric and magnetic field will import from Ansys Maxwell (Chapter 4) to Samadii Software.

Export 3D mesh position data in Samadii/sciv to Ansys Maxwell file then export solution as shown in Figure 5.10. Submit this solution in Samadii/sciv.

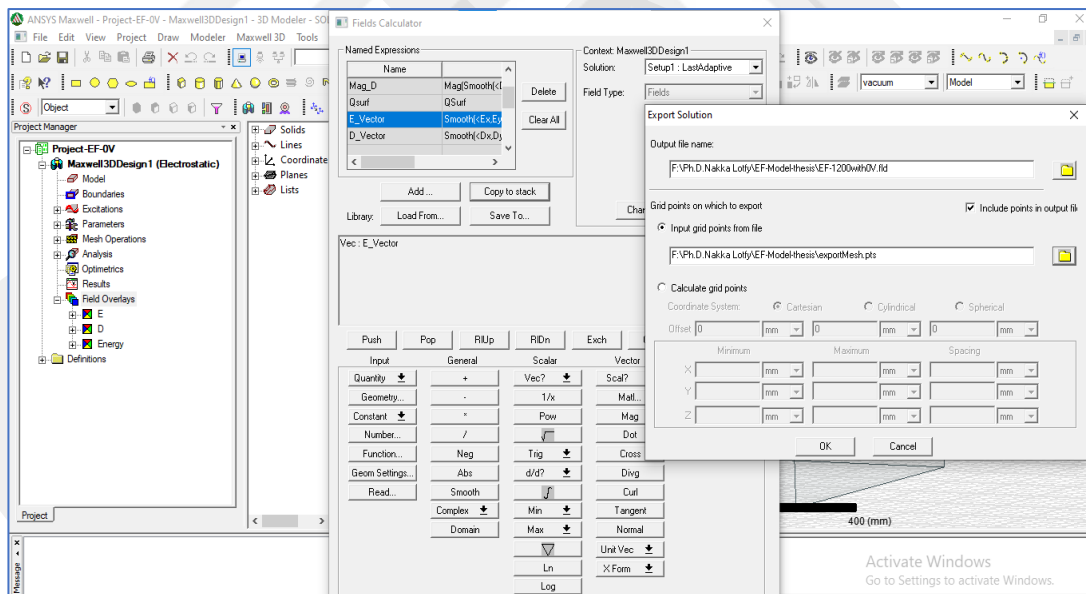


Figure 5.10 Export of the electric and magnetic field from Ansys Maxwell

Import Bx, By, Bz [T] Magnetic data file and Ex, Ey, Ez [v/m] Electric data file from Ansys to Samadii software.

The field frequency and phase are defined. The frequency is 13.65 MHz, and the phase is 0° as shown in Figure 5.11.

$$\text{Electric field: } E = E_r \cos(2\pi f t - \varphi) \quad (5.4)$$

$$\text{Magnetic field: } B = B_r \cos(2\pi f t - \varphi) \quad (5.5)$$

f : frequency, φ : phase

The converted result is indicated in Figures 5.12 and 5.13.

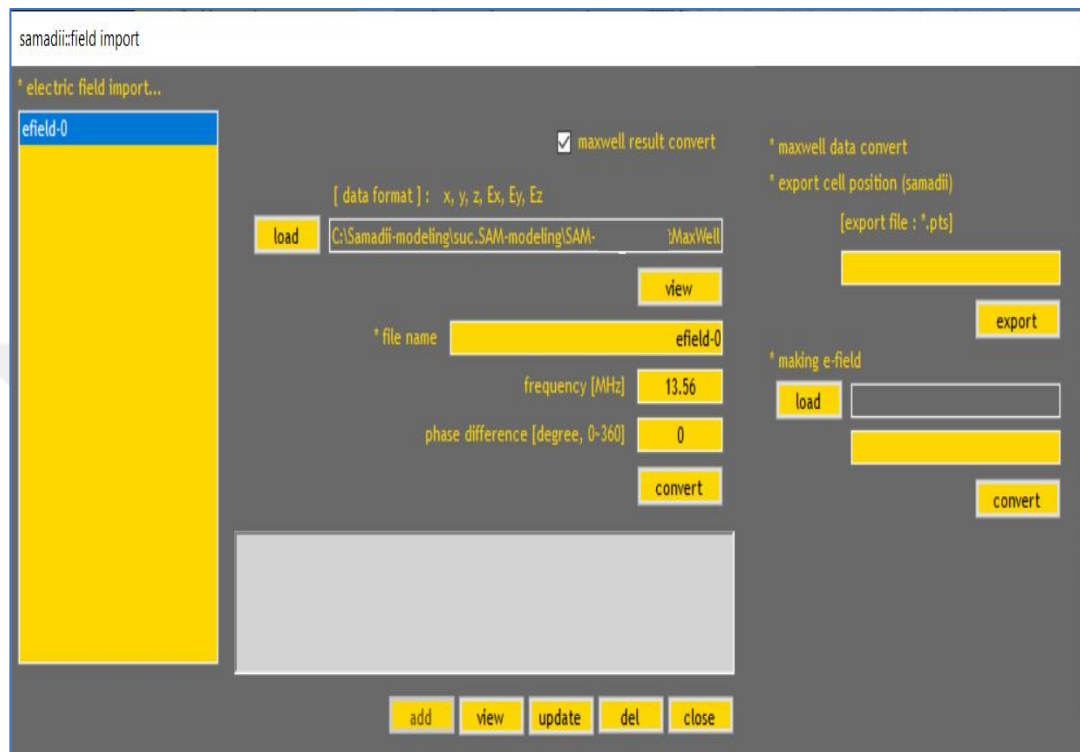


Figure 5.11 Import of electric and magnetic fields

Lorenz force

$$F = q(E + V \times B) \quad (5.6)$$

F: external force (N)

B: Magnetic field (T)

E: Electric field (v/m)

V: ion speed (m/s)

q: quantity of electric charge (C)

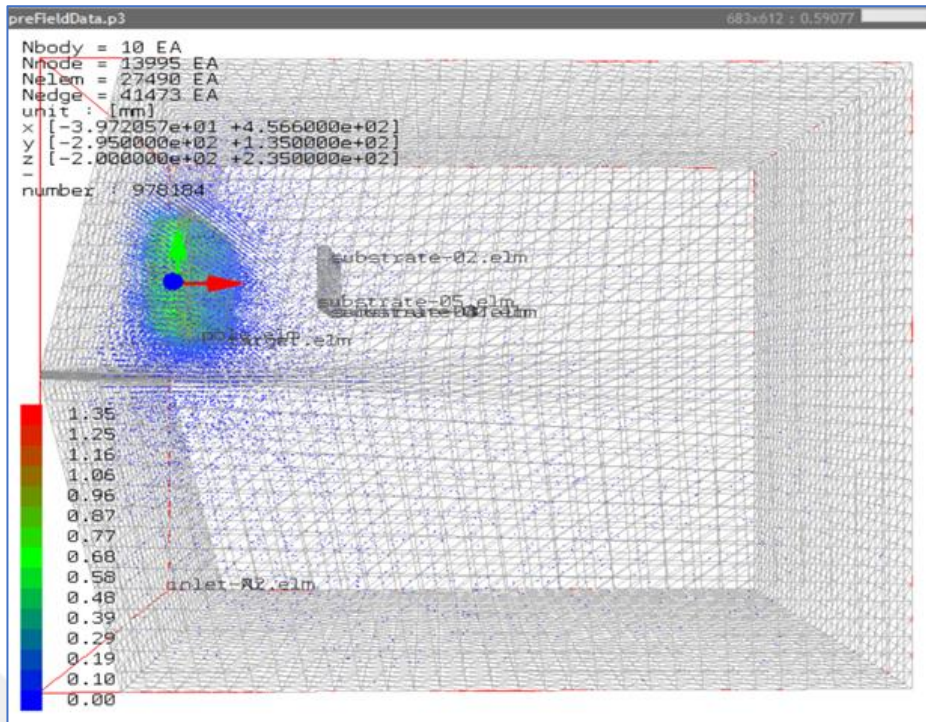


Figure 5.12 Convert maxwell magnetic field data to Samadii/sciv magnetic field

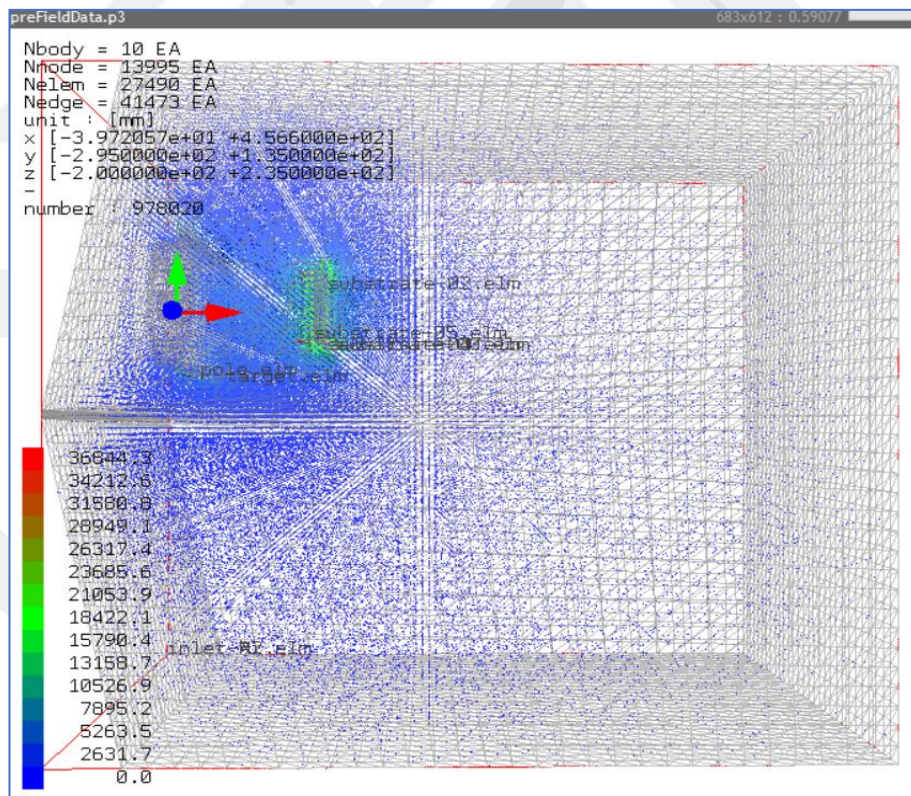


Figure 5.13 Convert maxwell electric field to Samadii/sciv electric field (Model-A1)

5.2.7 Chemical Reaction

TCE (Total Collision Energy) uses for chemical reactions.

TCE is a probability chemical reaction method using the Arrhenius equation and total collision energy when particles collide with each other.

Arrhenius equation:

$$\text{Forward: } kf = \Lambda f T \eta f e \left(-\frac{Ea}{RT} \right) \quad (5.7)$$

$$\text{Backwards: } kr = \Lambda b T \eta b \quad (5.8)$$

K: The rate of chemical reaction, Ea : Activation energy, R: universal gas constant, T: temperature.

Λf , Λb : forward, backward frequency factor - ηf , ηb : forward, backward temperature exponent.

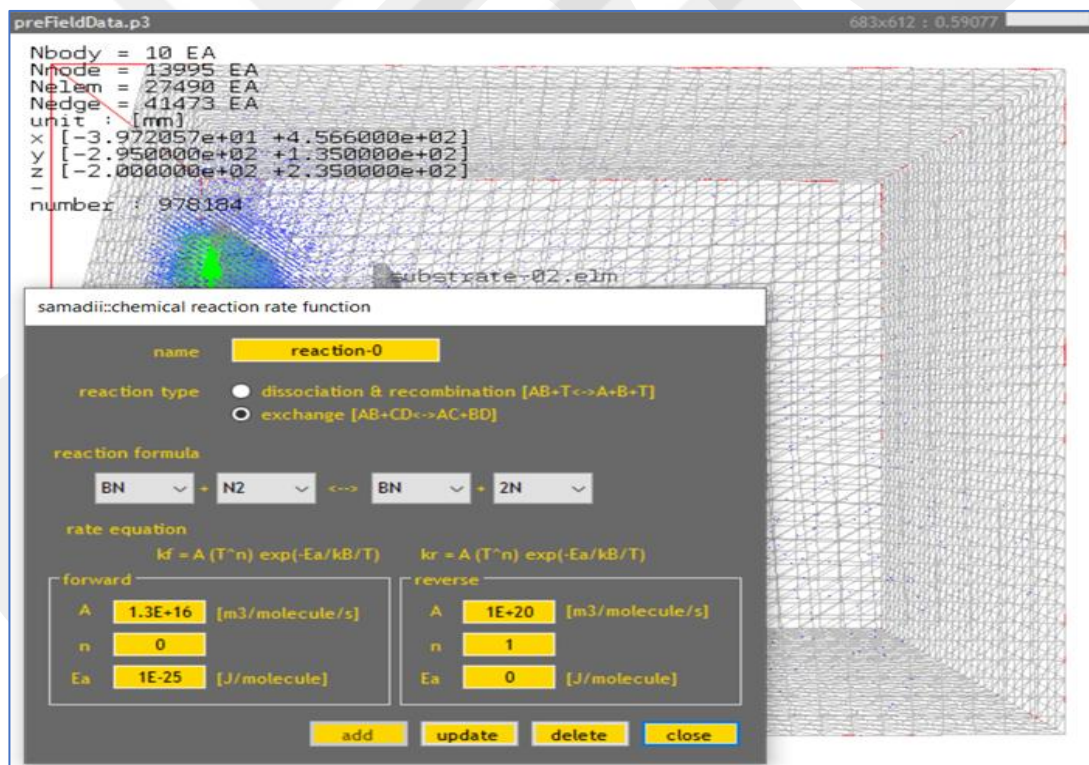


Figure 5.14 Arrhenius equation of the chemical reaction

5.2.8 Run Information and The Launch of Model

The collision model is defined as a collisional mean defining whether a collision between particles. In this model we used the application of artificial base condition, the base temperature and pressure (input value) is defined. The maximum collision number in a cell is calculated from Equation (5.9)

$$(N_{col.})_{\max} = \frac{N\bar{N}F_N(\sigma*Cr)_{\max} \Delta t}{2V_c} \quad (5.9)$$

$(N_{col.})_{\max}$: Maximum collision number.

N: Particle number.

\bar{N} : Average particle number.

$(\sigma * Cr)_{\max}$: Collision cross-section * maximum relative velocity.

Δt : TSC*(the time it took for the fastest molecular to travel the unit cell).

V_c : Volume of the cell.

$$\bar{N} = \frac{P_{\text{base}}*V_c}{K_B*T_{\text{base}}} \quad (5.10)$$

P_{base} : The base pressure and T_{base} : The base temperature.

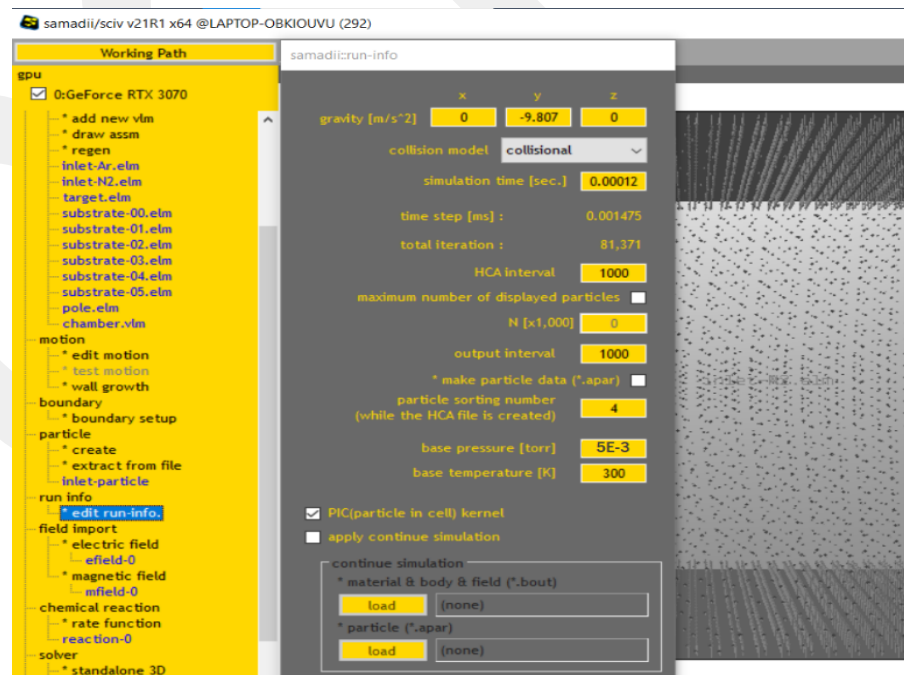


Figure 5.15 Run information of MS model

$$\text{Collision determination } p_{coll} = \frac{\sigma_{cr}c_r}{\{\sigma_{cr}c_r\}_{\max}} < R_f \quad (5.11)$$

R_f : Random value (0~1)

The variable hard sphere (VHS) method is used to calculate the diameter of collision as shown in Equation (5-12).

$$d = d_{ref} \left[\left(\frac{2K_B^*T_{ref}}{m_r C_r^2 (C_r^*)^2} \right)^{(w-1/2)} \frac{1}{\Gamma(5/2-\omega)} \right]^{1/2} \quad (5.12)$$

$$m_r = \frac{m_1 m_2}{m_1 + m_2} \quad (5.12a)$$

$$d_{ref} = \left(\frac{30 \left(m K_B T_{ref} / \pi \right)^{1/2}}{4(5-2\omega)(7-2\omega)\mu_{ref}} \right)^{1/2} \quad (5.12b)$$

d_{ref} : DAMC standard molecular diameter.

ω : Viscosity index.

T_{ref} : DSMC standard molecular temperature.

Γ : Gamma function.

m_r : Reduced mass.

c_r, c_r^* : Relative speed before and after the collision.

Input the time of simulation and HCA, Find the number of iterations required to complete the model as shown in Figure 5.15.

In this model: The time of simulation is 1.2e-4 s.

5.2.9. Solver Module

Check the applied module, and the simulation status before launching the model as shown in Figure 5.16.

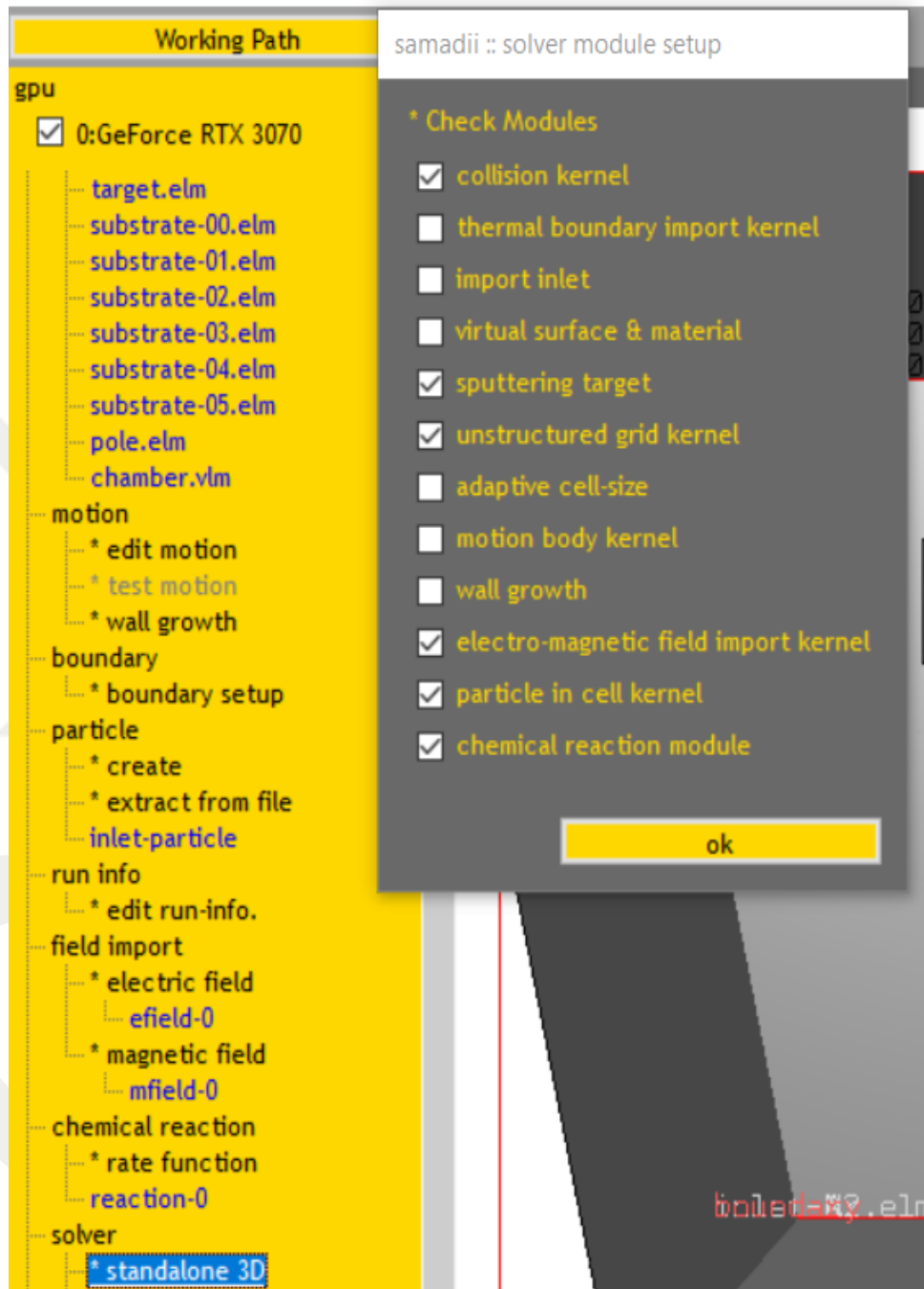


Figure 5.16 The applied module of the MS model

5.2.10 Progress of BN Coating Model

In the out file, it is possible to check the progress of your model and display the result by the HyperCube8 program as shown in Figure 5.17.

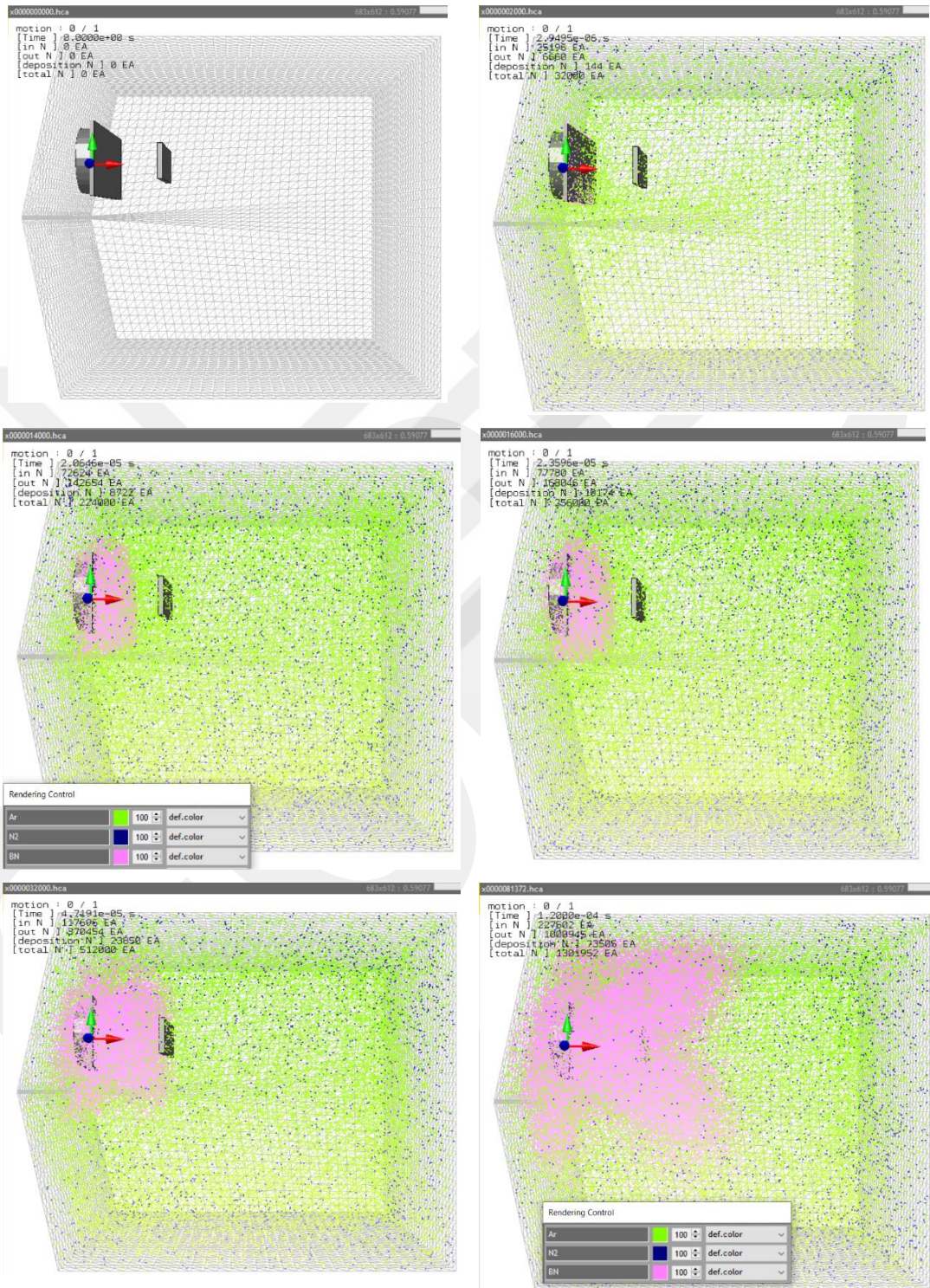


Figure 5.17 Progress of modelling of BN coating -Model-A1

5.2.11 The Result

5.2.11.1 Deposition Efficiency of Coating

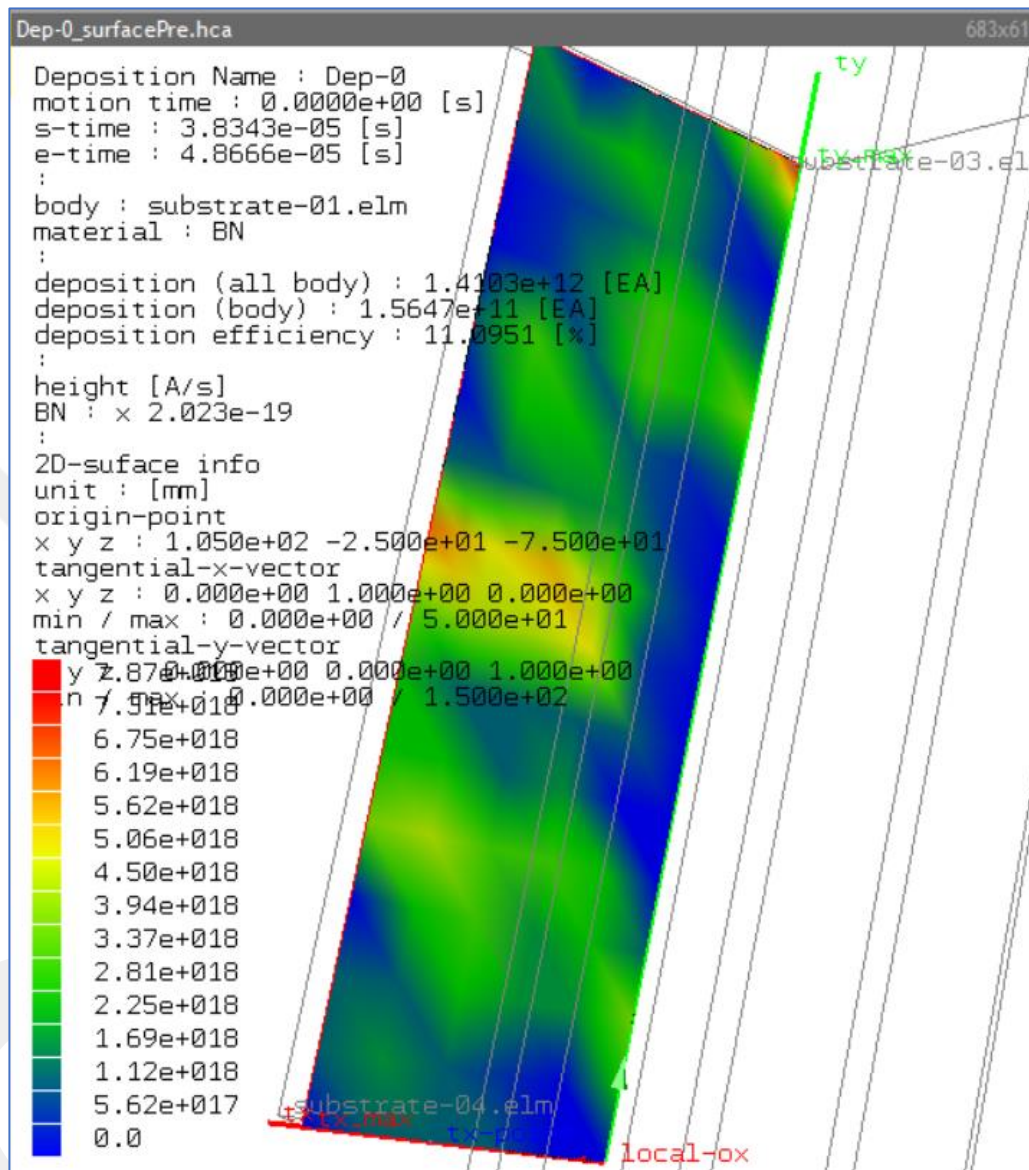


Figure 5.18 Deposition efficiency of Model-A1 ($t=4.8e-5$ s)

5.2.11.2 Deposition Analysis (Deposition Rate and Thickness of coating)

In Samadii software, It is possible to find cumulative deposition thickness [#m²]. Calculating the deposition thickness based on an arbitrary point. Creates a circle with a certain size around the measurement point and calculates the number of particles inside the circle as the deposition rate. The time of simulation is 4.8e-5 s.

Calculate the average thickness within the 2D area. Set the area-plot division to 1,1. It calculates the section as one area.

To change the deposition rate unit [#m².s] to [nm/s], we will use Equation (5.13)

$$[\text{Deposition rate (\#/m}^2\text{.s)} * \text{Volume (m}^3)]_{\text{BN}} * 1\text{E}9 \text{ (nm/m)} = \text{(nm/s)} \quad (5.13)$$

Example: Find the thickness of the coating of Model-A1 in nm unit at t=4.8e-5 s in Figure 5.19.

$$[2.02\text{E}18 \text{ (\#/m}^2\text{.s)} * (46.5\text{E-}27/2300) \text{ (m}^3)]_{\text{BN}} * 1\text{E}9 \text{ (nm/m)} = 0.04084 \text{ nm/s}$$

$$0.04084 \text{ (nm/s)} * 6 \text{ (hr)} * 3600 \text{ (s)} = 882.1252 \text{ nm}$$

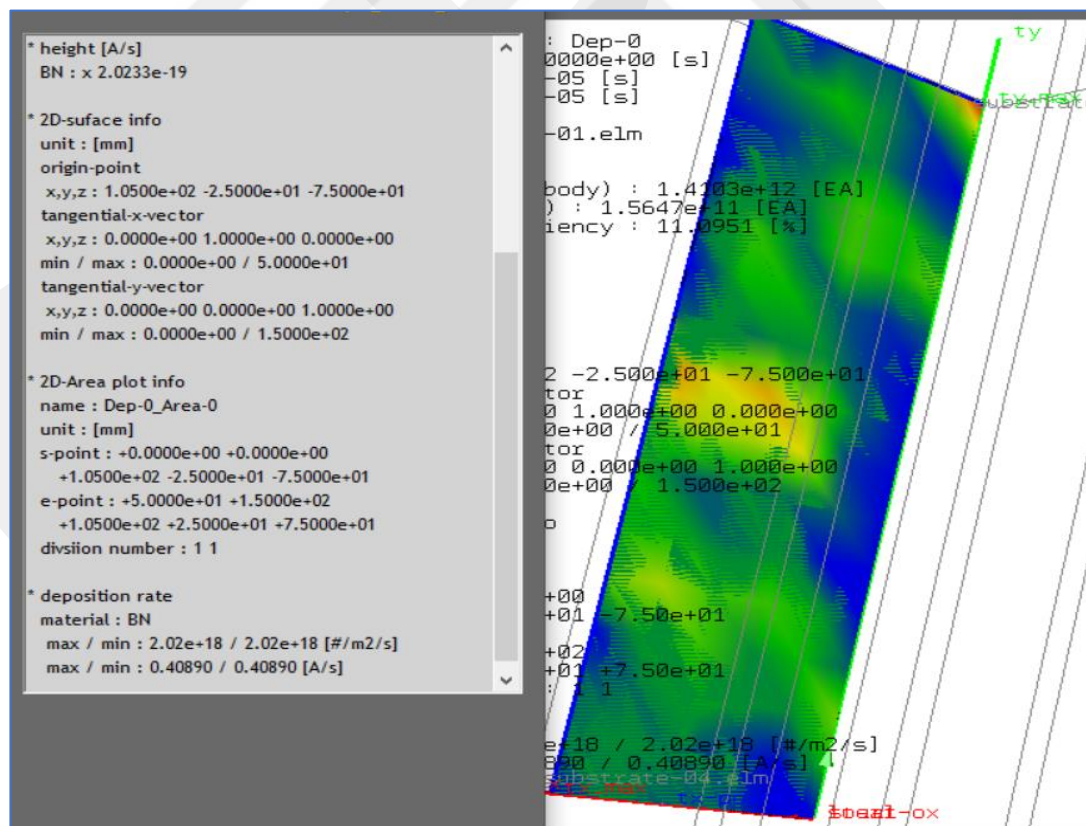


Figure 5.19 The average deposition rate with a 2D-area plot of Model-A1 (t=4.8e-5s)

To find the deposition efficiency of BN modelling, the time of the model will extend to arrive approximately at the steady-state situation. The time of the model will be 1.2×10^{-4} . This time will give a good idea about what will happen with the progress of the model. The deposition rate results in the model will be divided into two areas: a) Area 1 (deposition rate of the thin film-nano film). The time of it is 4.8×10^{-5} s, b) Area 2 (deposition rate of the microfilm). The time of this section is 1.2×10^{-4} s as shown in Figure 5.20.

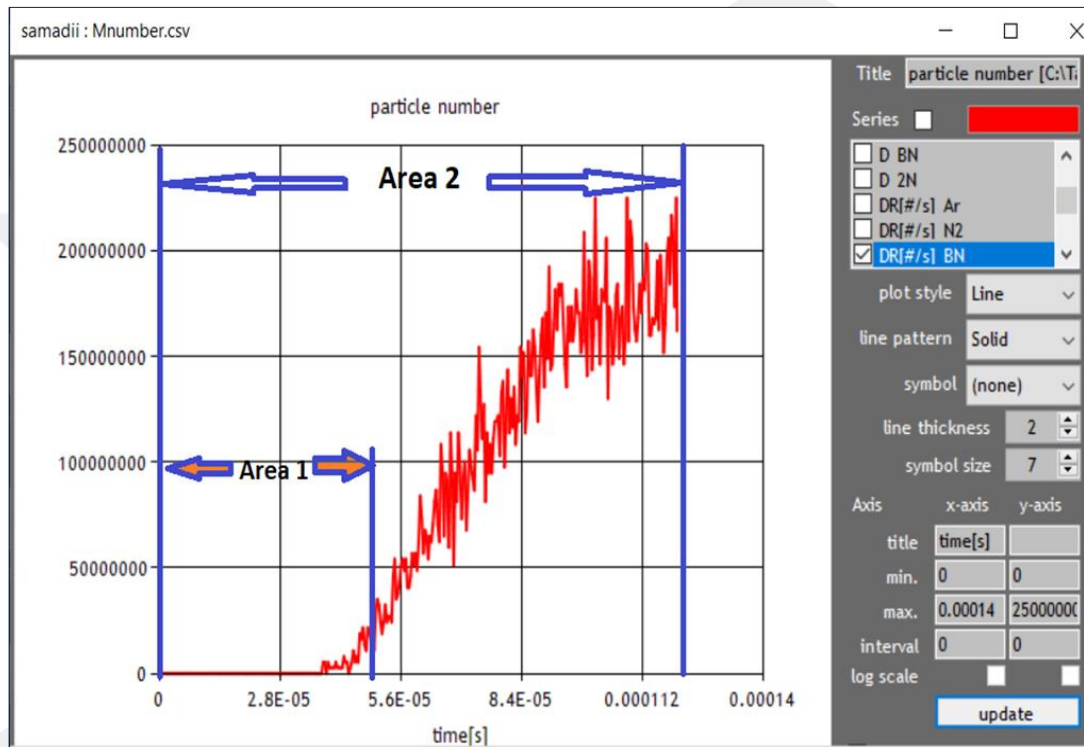


Figure 5.20 The deposition rate for nanofilm and microfilm of Model-A1

When the simulation is running, various log files are created for example history file (record the progress of the model), a number file (record the number of particles in the area of simulation), and a Boltzman Distribution file. The result of these files can be opened by HyperCube Plot. From the Number file as shown in Figures 5.21 and 5.22, it is possible to find :

- (N): Number of particles (#).
- (D): Number of deposited particles at the deposition surface.
- (DR): Deposition Rate (#/s).
- (K): Number of escaped particles without deposition (#).
- (KR): Escaped Rate (#/s).

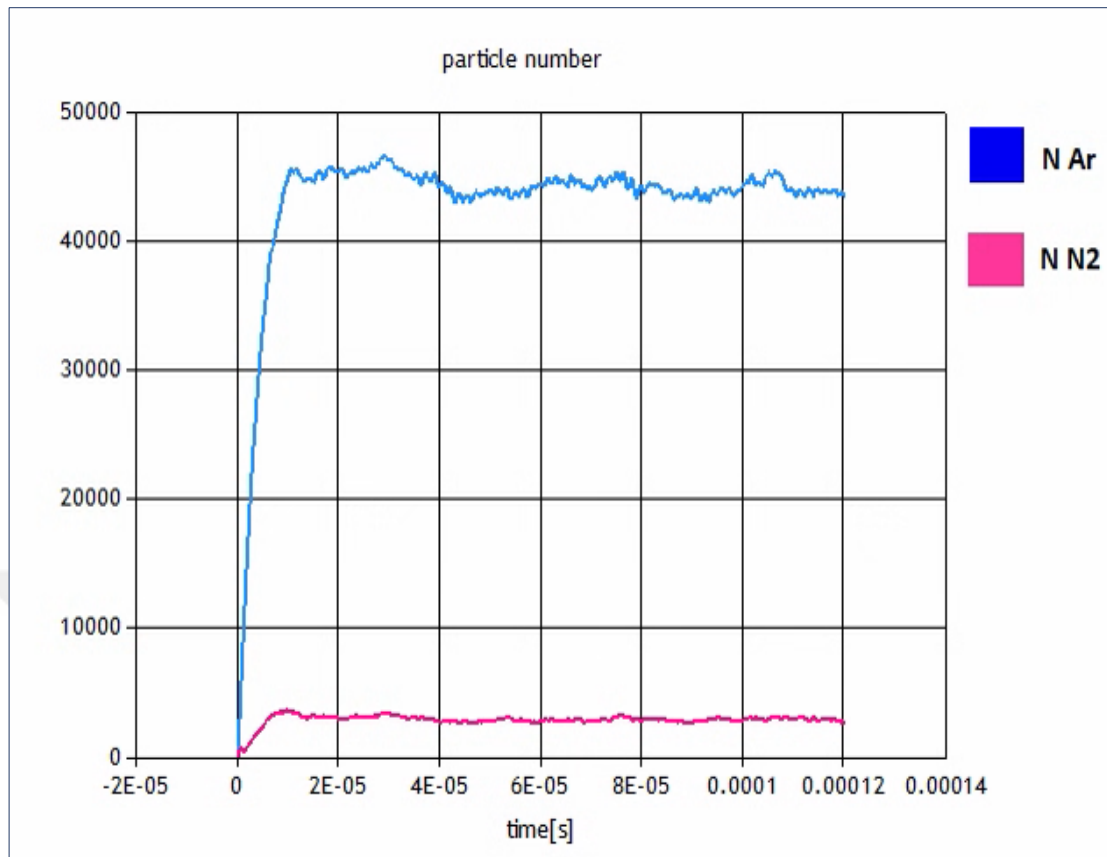
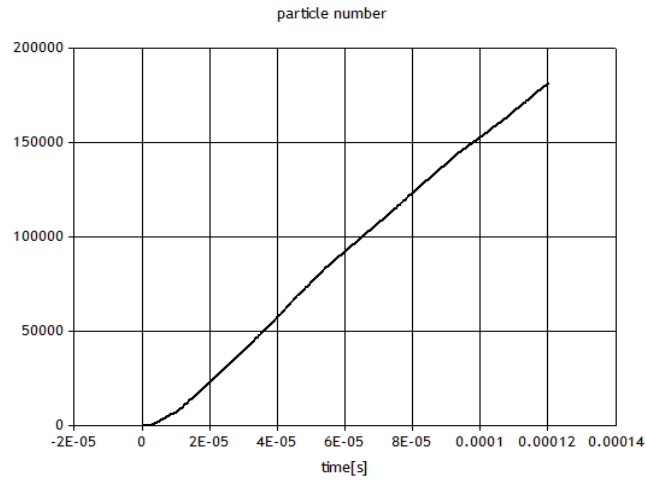
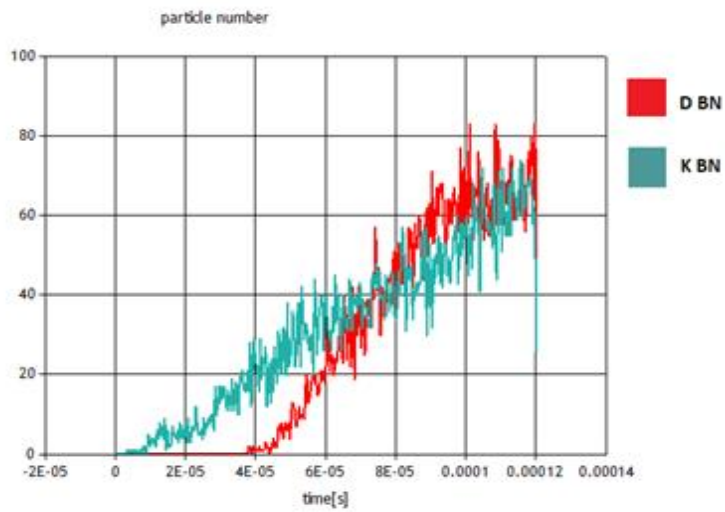


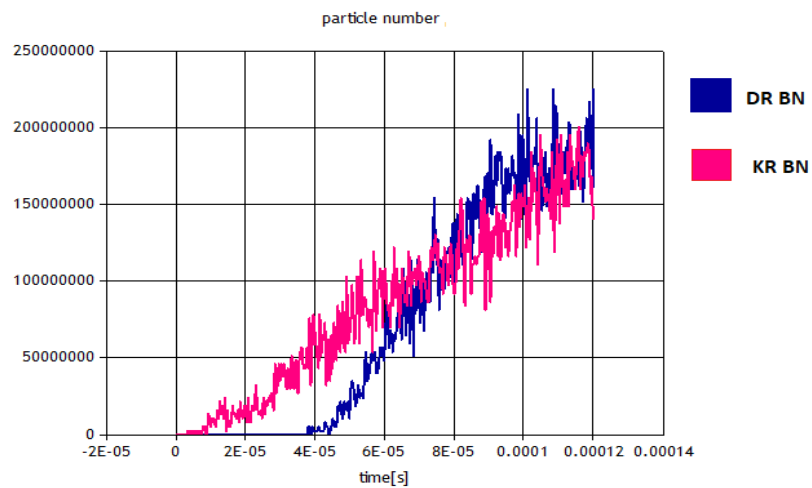
Figure 5.21 The Ar and N₂ particles (#/s) in Model-A1



(a) Number of sputtering (BN) particles



(b) Number of deposition and escaped (non-deposition) BN particles



(c) The deposition rate and Escaped rate (non-deposition) of BN particles

Figure 5.22 The Details of BN Particles of Model-A1

With the progress of the model, it is possible to find the details of the coating profile for all the steps. For example efficiency of deposition, deposition rate, and thickness of the coating as shown in Figures 5.23 and 5.24.

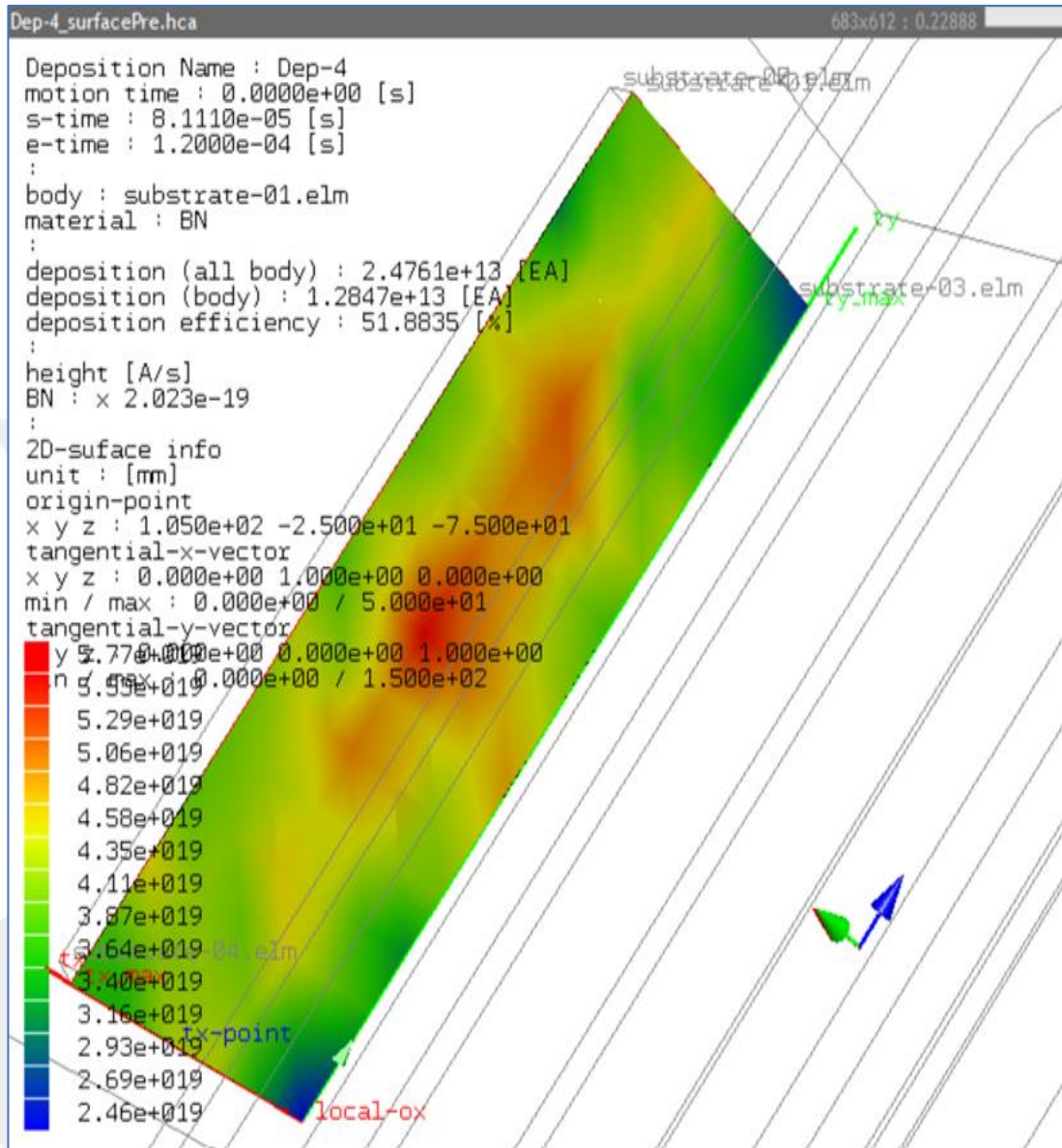


Figure 5.23 Deposition Efficiency of Model-A1 at Time= 1.2e-4s

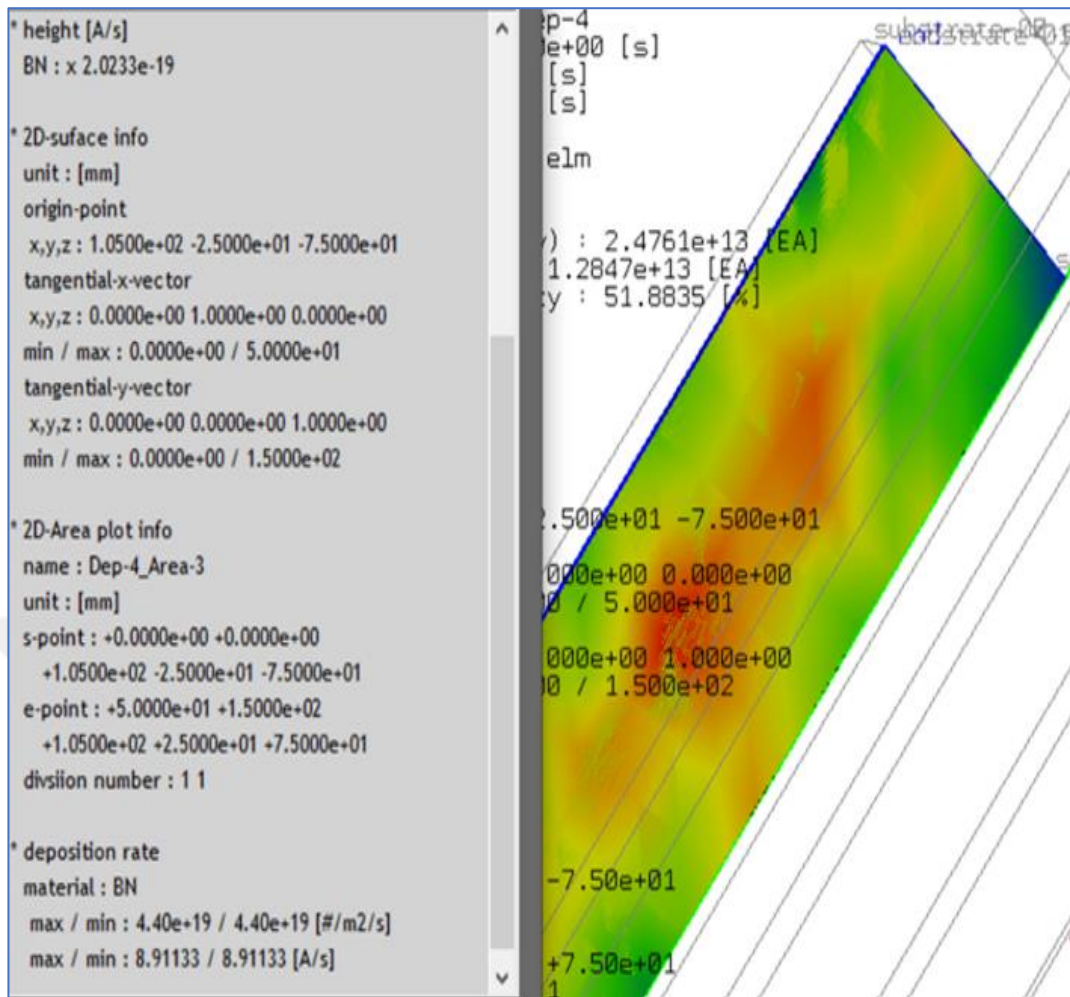


Figure 5.24 The average deposition rate with a 2D-area plot of Model-A (t=1.2e-4s)

5.2.11.3 Deposition Uniformity

Uniformity is a common application that can be used to compare deposition properties of films in the same condition.

By using a 2D line, the start point of the line is (20,150) and the endpoint is (0,0). The line will be divided into 100 points. The thickness will be calculated for all these points. The uniformity Equation (5.14) is :

$$\text{Uniformity \%} = \frac{(h_{\max} - h_{\min})}{(h_{\max} + h_{\min})} * 100\% \quad (5.14)$$

The uniformity of coating is 85.7% as shown in Figure 5.25.

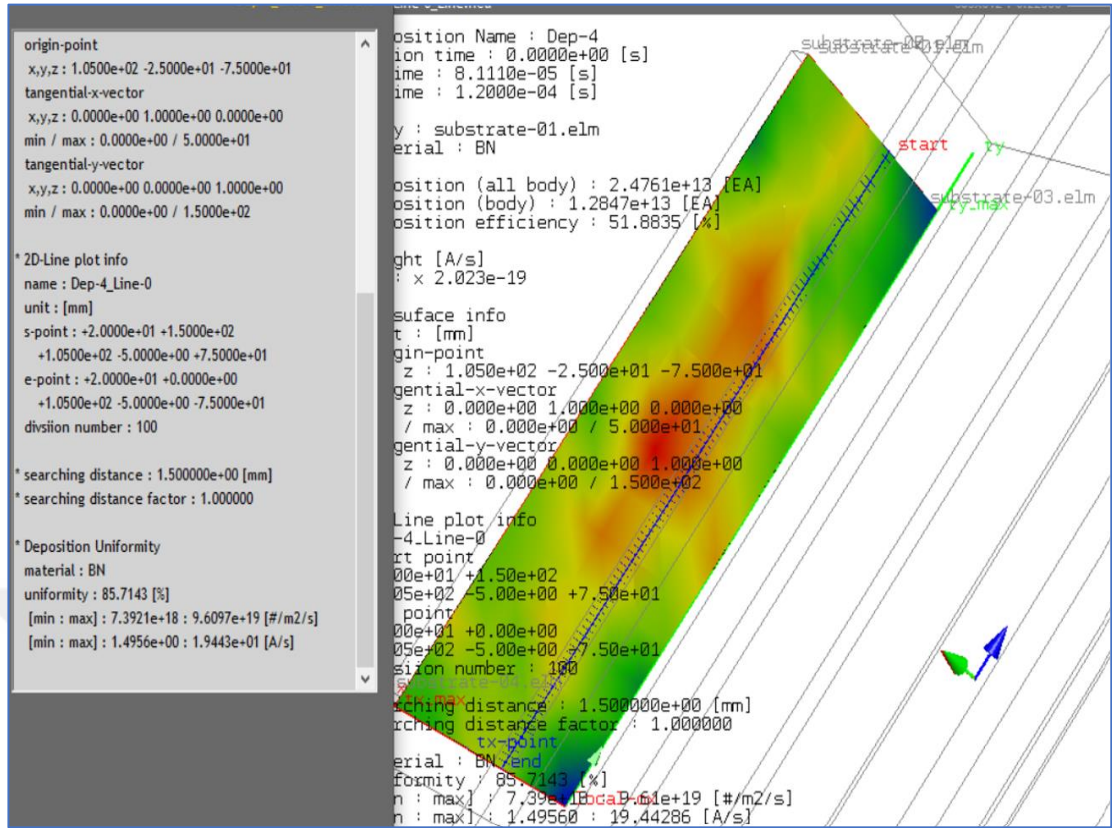


Figure 5.25 The uniformity with the 2D-line plot of Model-A1 at time=1.2e-4s

5.2.12 Validation of Model-A1 Result Compared with The Experiment Result

The thickness of coating calculated by the DSMC model is compared with experimental results (Run 153) [*]. The strong agreement between the outcomes demonstrates the model's capacity to predict the coating thickness accurately, as shown in Table 5.2.

Table 5.2 The result of BN coating thickness for Model-A1 compared with the experiment.

No.	Model-Name	Sub. Material	T (°C)	Rpm	Magnetron	Sub. Voltage (v)	Exp. Thickness (nm)	Model. Thickness (nm)	Error%
1	Model-A1	1xD2	300	Off	900w,40/8scc m Ar/N ₂	0	861.0286	882.1252	2.4

[*] Run 153 has the same boundary condition as model A1. The facilities of the BOREN Center of Competence for Boron Coatings at the Metal Forming Center of Excellence at ATILIM university were used to prepare this experiment.

5.3 Modelling Influence of The Input Parameter on The Coating Profile

In this part, we will investigate the behaviour of PVD under different input parameters. These parameters are substrate bias voltage, power supply, the volumetric flow rate of gases, the distance between target and substrate and the study of the effect of substrate material type on deposition rate.

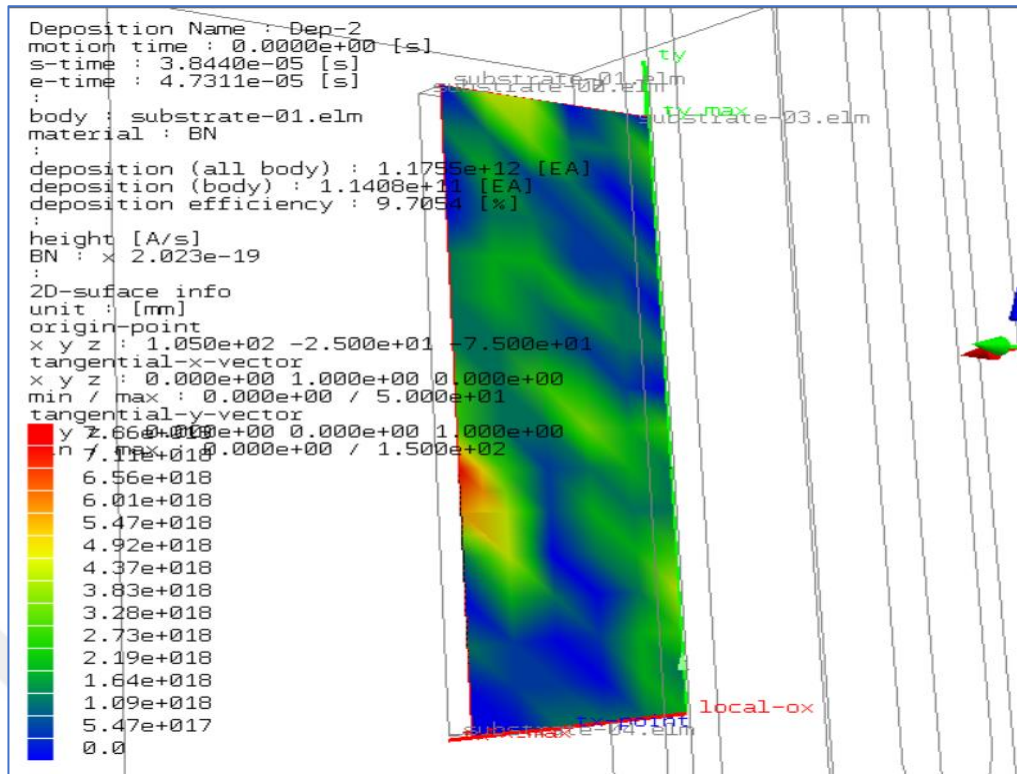
5.3.1 Modelling The Influence of The Substrate Voltage On The Deposition Profile

Study the effect of the substrate voltage variable on the coating. The substrate voltages are 0,100 and 250V. The result of the electric field for different excitations of the applied voltage is shown in (Chapter 4, Table 4.5,p.39). The boundary conditions are shown in Table 5.3. The effect of the substrate voltage (100 and 250 V) on the deposition efficiency and deposition rate at times $4.8e-5$ s and $1.2e-4$ s are shown in Figures 5.26,27,28,29,30 and 31 respectively.

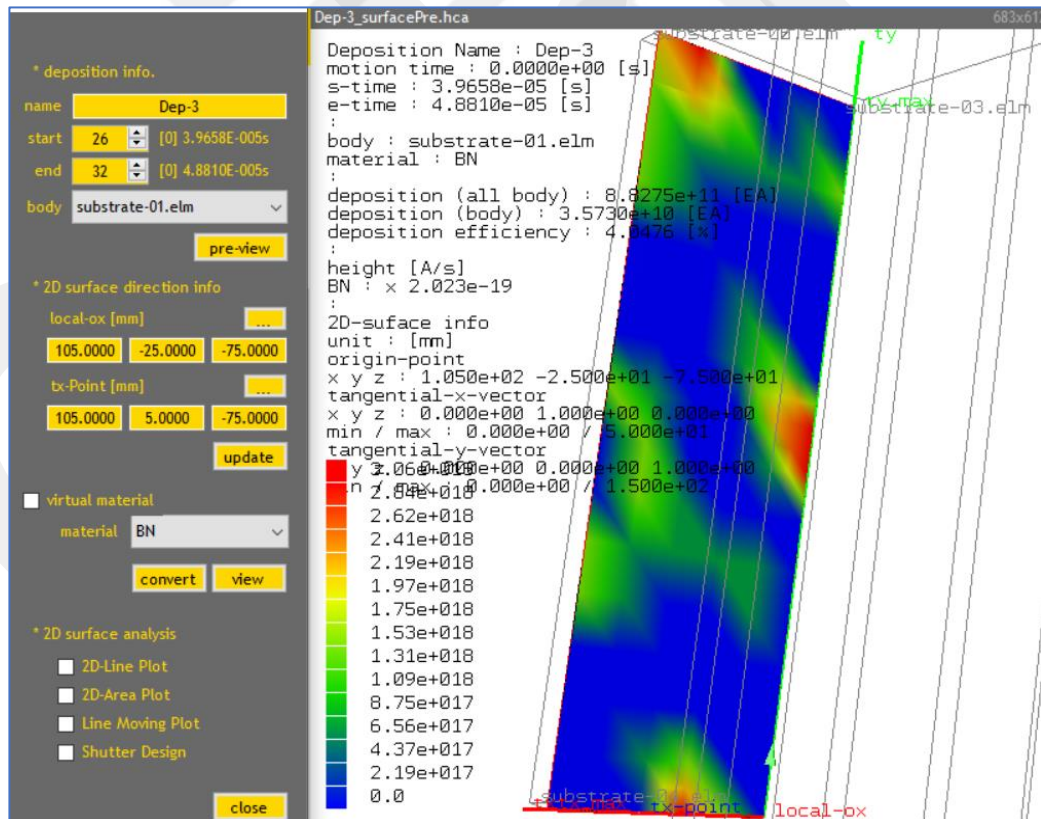
Table 5.3 Boundary Condition of MS Modelling and experiments for different substrate bias voltages

No.	Model-Name	Exp. Name [*]	Target	Substrate Material	Substrate Geometry (mm)	T-S distance (mm)	T(°C)	Magnetron	Subs. Voltage (v)	Time (hr)
1	Model-A1	Run 153	h-BN	1xD2	150*50*7	80	300	900w,40/8sccm Ar/N ₂	0	6
2	Model-B1	Run 154	h-BN	1xD2	150*50*7	80	300	900w,40/8sccm Ar/N ₂	100	6
3	Model-C1	Run 152	h-BN	1xD2	150*50*7	80	300	900w,40/8sccm Ar/N ₂	250	6

[*] The facilities of the BOREN Center of Competence for Boron Coatings at the Metal Forming Center of Excellence at ATILIM university were used to prepare this experiment.

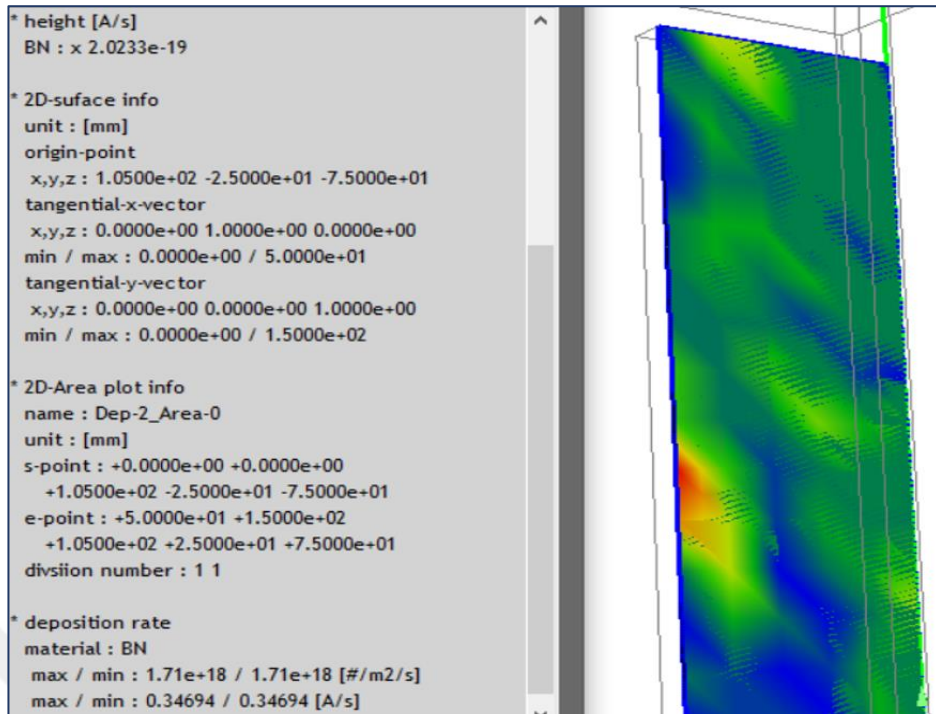


(a) Model-B1 (The substrate voltage=100 V)

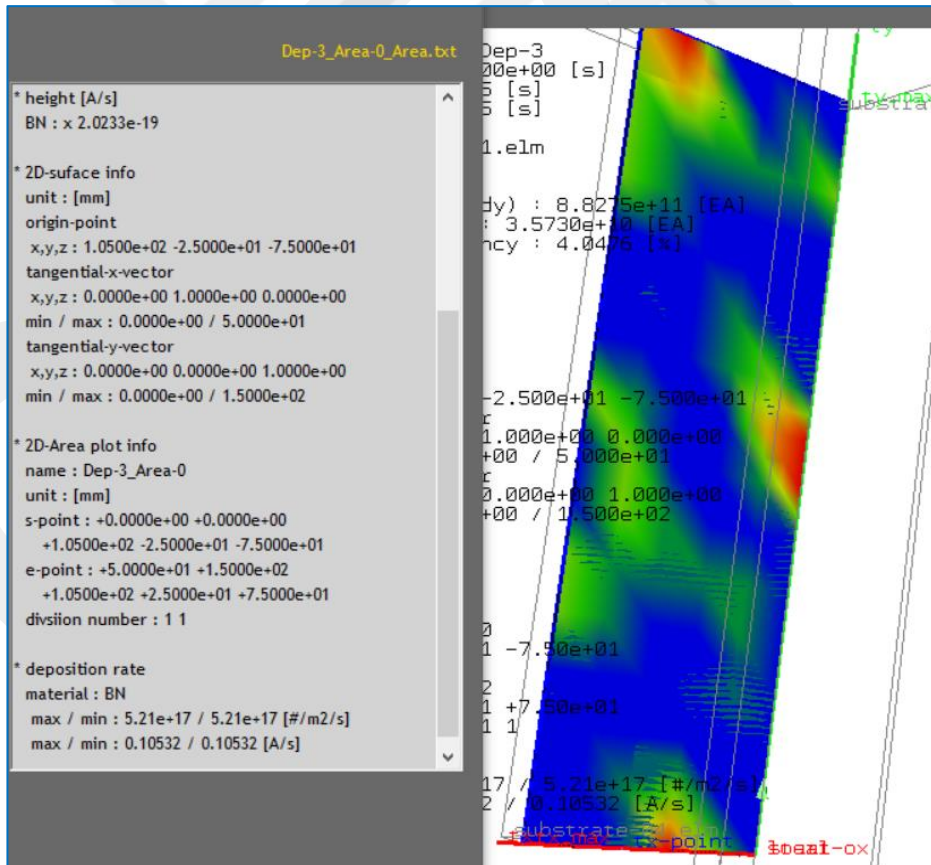


(b) Model-C1 (The substrate voltage=250 V)

Figure 5.26 Influence of the substrate voltage on the deposition efficiency($t=4.8e-5$ s)



(a) Substrate voltage=100V



(b) Substrate voltage=250V

Figure 5.27 Influence of the substrate voltage on the deposition rate ($t=4.8e-5s$)

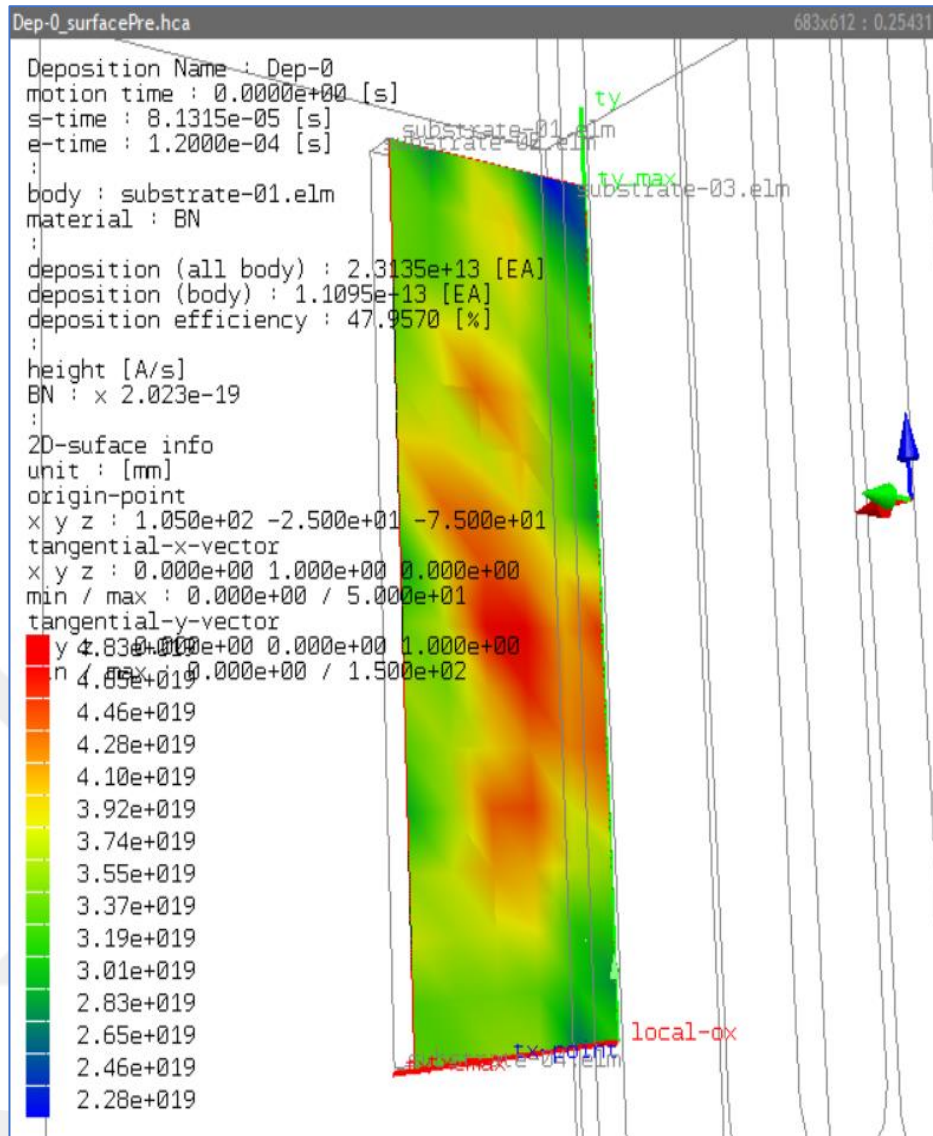


Figure 5.28 The deposition efficiency of BN particles when bias voltage=100 V at time=1.2e-4

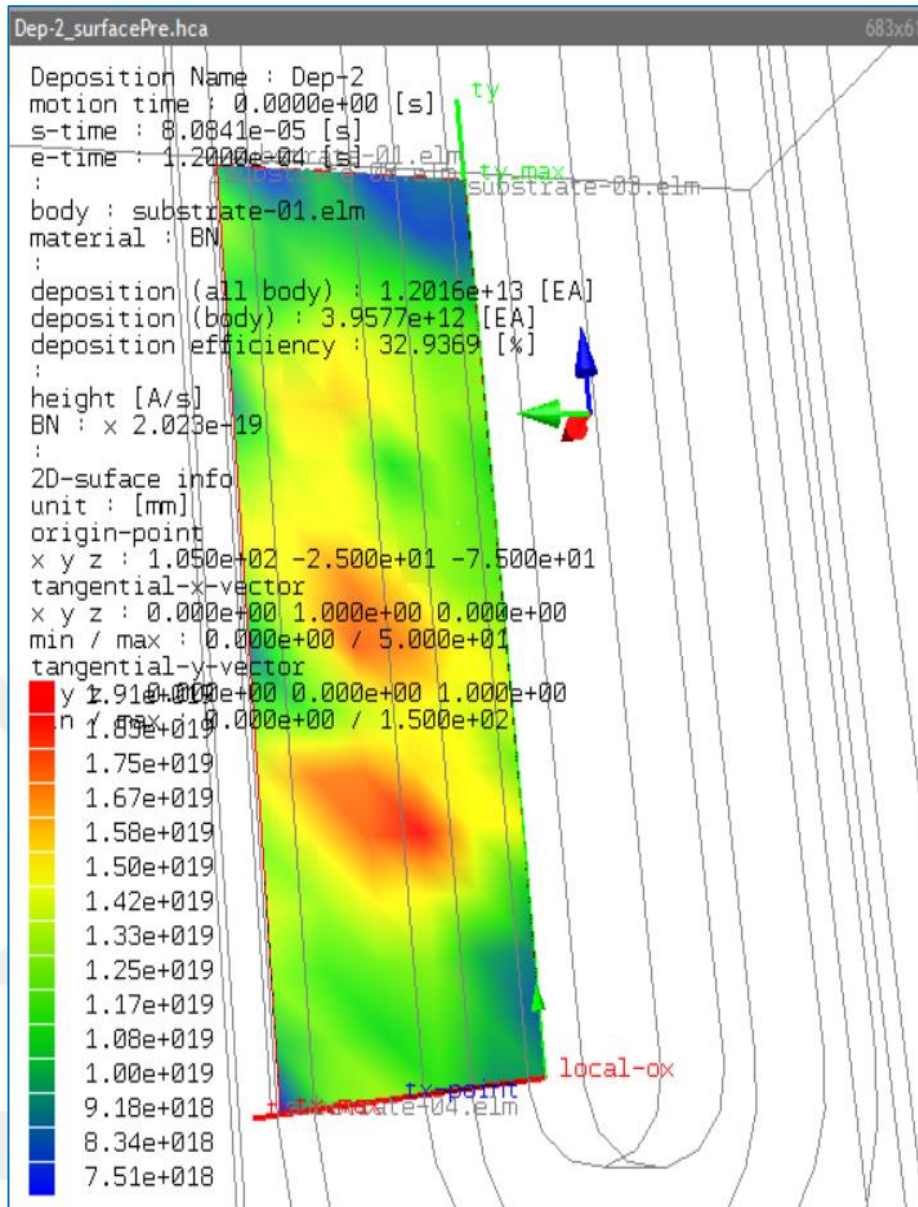
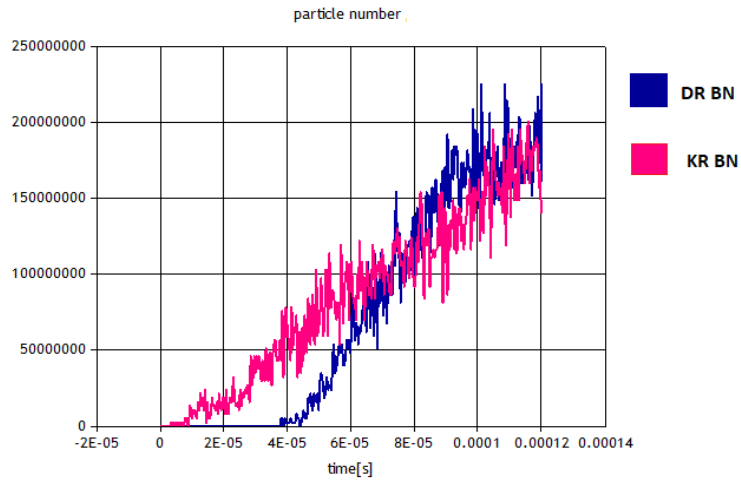
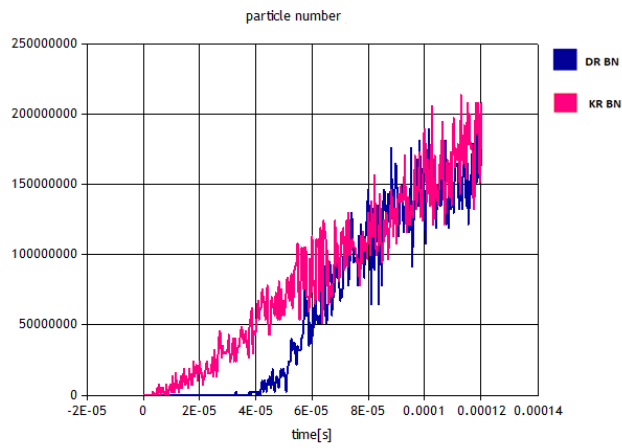


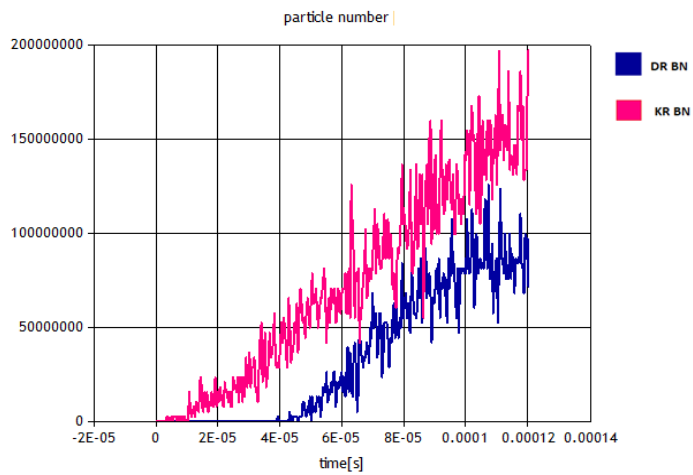
Figure 5.29 The deposition efficiency of BN particles when bias voltage= 250 V at time=1.2e-4



(a) The deposition rate and Escaped rate of BN particles when substrate voltage=0 V



(b) The deposition rate and Escaped rate of BN particles when substrate voltage=100V



(c) The deposition rate and Escaped rate of BN particles when substrate voltage=250V

Figure 5.32 The deposition rate and escaped rate of BN particles with different substrate voltages

The effect of variable bias substrate voltages on the deposition rate of BN particles is shown in Figure 5.33.

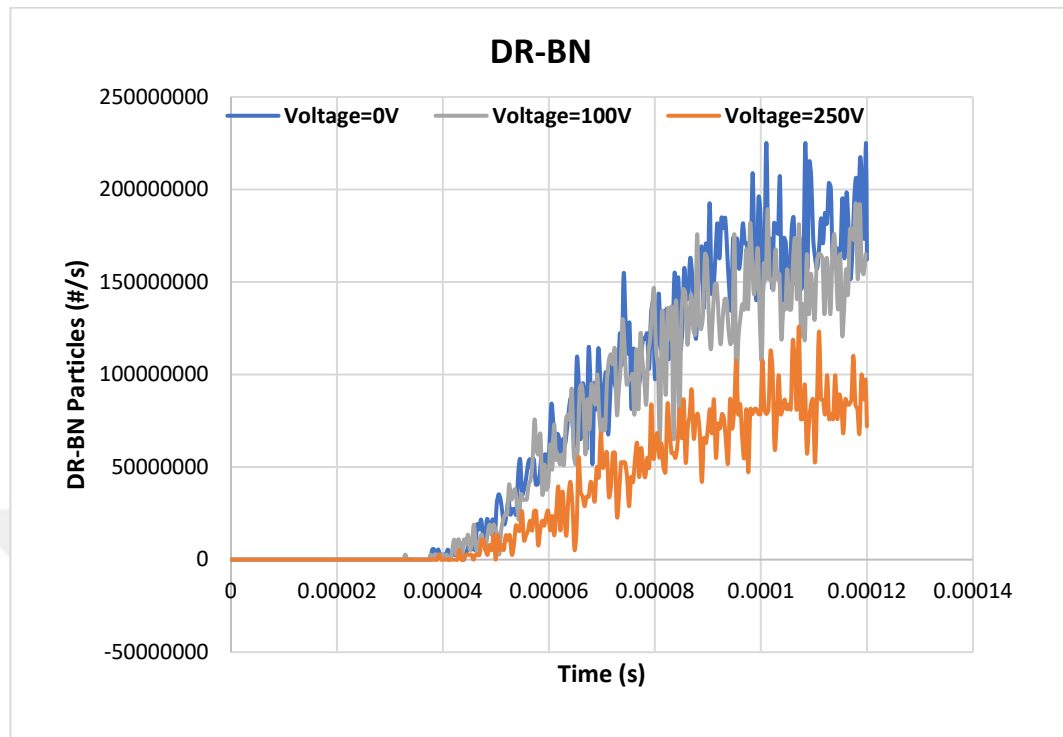


Figure 5.33 Compare the deposition rate of the different substrate bias voltage

5.3.1.1 The Correlation Between Different Substrate Bias Voltage and Thickness of The Coating for Experiment and Model.

The results from the models are compared with experiments in this investigation. The model and experimental results demonstrate a good correlation. The result of the models provides an effective approximation with experiment results [*] for substrate voltages 0 and 100 V with errors of 2.4% and 7%, respectively. Moreover, the result of the substrate voltage (250 V) is remarkably close to the experiment with an error of 0.7%, as shown in Figure 5.34.

[*] The details of the experiment's result are shown in Appendix B

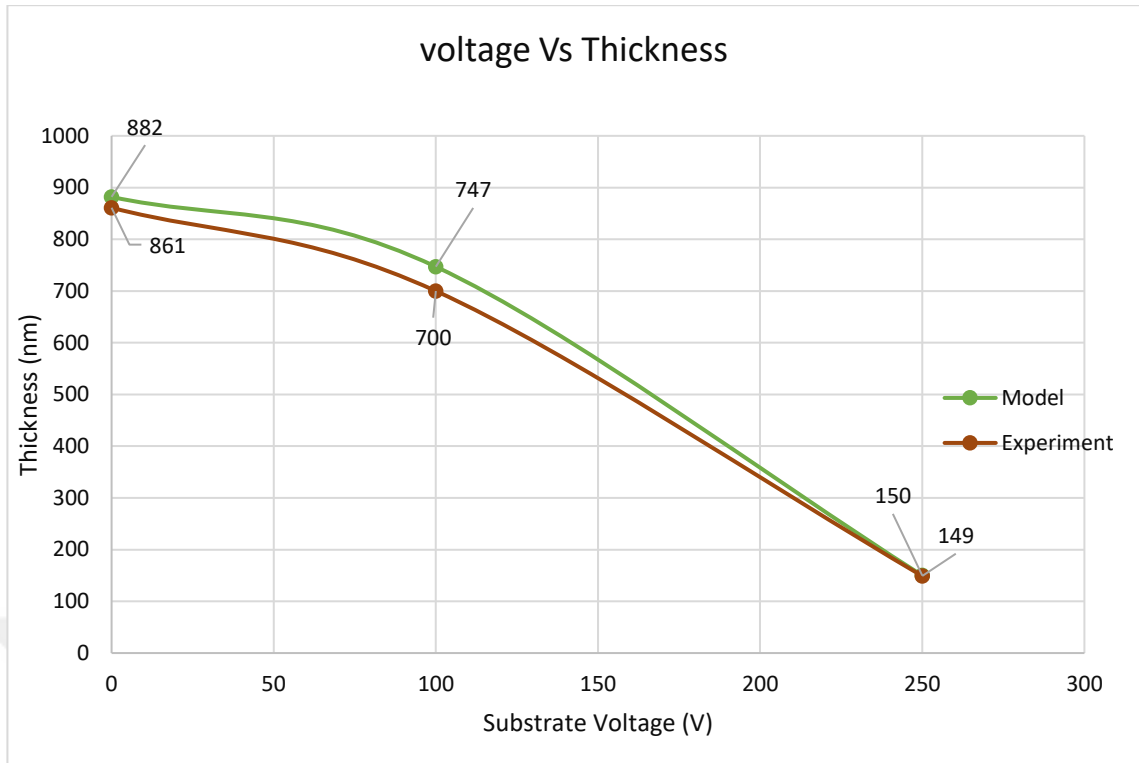


Figure 5.34 The substrate bias voltage vs. Thickness for models and experiments

5.3.2 Modelling The Influence of The Power Supply on The Deposition Profile

At the same MS condition but with different power supply, 900,1200 and 1500W with two substrate voltages 0 and 250 V respectively as shown in Table 5.4. The type of target plate is h-BN. Six models are built to understand the effect of power supply on coating parameters. The result of the electric field for different excitations of the applied voltage and power supply are shown in (Chapter 4, Table 4.5,p.39)

Table 5.4 **Boundary** Condition of MS Modelling with different power supply and substrate voltage 0 and 250 V.

No.	Model-Name	Substrate Material	Substrate Geometry (mm)	T-S Distance (mm)	T (°C)	Rpm	Magnetron	Sub. Voltage (v)	Time (hr)
1	Model-A1	1xD2	150*50*7	80	300	Off	900w, 40/8sccm Ar/N ₂	0	6
2	Model-A2	1xD2	150*50*7	80	300	Off	1200w, 40/8sccm Ar/N ₂	0	6
3	Model-A3	1xD2	150*50*7	80	300	Off	1500w, 40/8sccm Ar/N ₂	0	6
1	Model-C1	1xD2	150*50*7	80	300	Off	900w, 40/8sccm Ar/N ₂	250	6
2	Model-C2	1xD2	150*50*7	80	300	Off	1200w, 40/8sccm Ar/N ₂	250	6
3	Model-C3	1xD2	150*50*7	80	300	Off	1500w, 40/8sccm Ar/N ₂	250	6

The result of the six models is shown in Table 5.5. From the models, it is clear that the relation between the power supply and the thickness of BN coating is not proportional. The thickness increase when the power increase from 900W to 1200W but it is decreased at the power of 1500 W when the substrate voltage is 0 V. As well as when comparing this result with the same condition but the substrate voltage is 250 V the models show that the coating thickness decrease when the power supply increase.

Table 5.5 The MS Models result -Effect of power supply on the thickness of BN coating

No.	Model-Name	Substrate Material	T(°C)	Rpm	Magnetron	Substrate Voltage(v)	Deposition Rate (#/m ² .s)	Thickness (nm)
1	Model-A1	1xD2	300	Off	900w,40/8sccm Ar/N ₂	0	2.02 e18	882.1252
2	Model-A2	1xD2	300	Off	1200w,40/8sccm Ar/N ₂	0	2.41 e18	1052.4365
3	Model-A3	1xD2	300	Off	1500w,40/8sccm Ar/N ₂	0	2.26 e18	986.9322
1	Model-C1	1xD2	300	Off	900w,40/8sccm Ar/N ₂	250	5.21 e17	150.3713
2	Model-C2	1xD2	300	Off	1200w,40/8sccm Ar/N ₂	250	4.29 e17	123.8182
3	Model-C3	1xD2	300	Off	1500w,40/8sccm Ar/N ₂	250	4.20 e17	121.2206

The deposition rate result when substrate voltage 0 V with power supply 900,1200 and 1500 V are shown in Figure 5.35.

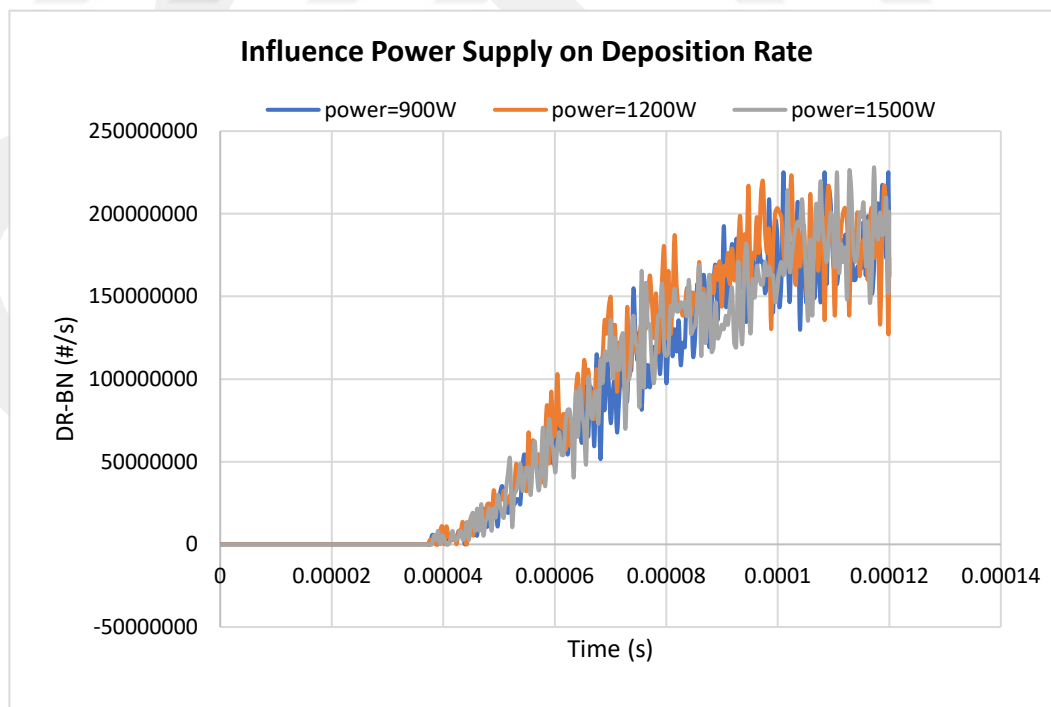


Figure 5.35 Influence of the power supply on the deposition rate when substrate voltage is (0V)

With the progress of coating, the deposition efficiency result for three models at power supply 900,1200 and 1500W with substrate voltage(0V) are close to each other. The highest efficiency on power is 1200V. It is 52% as shown in Figure 5.36. In Figure 5.37, the power 1500W gives the best uniformity of 89%.

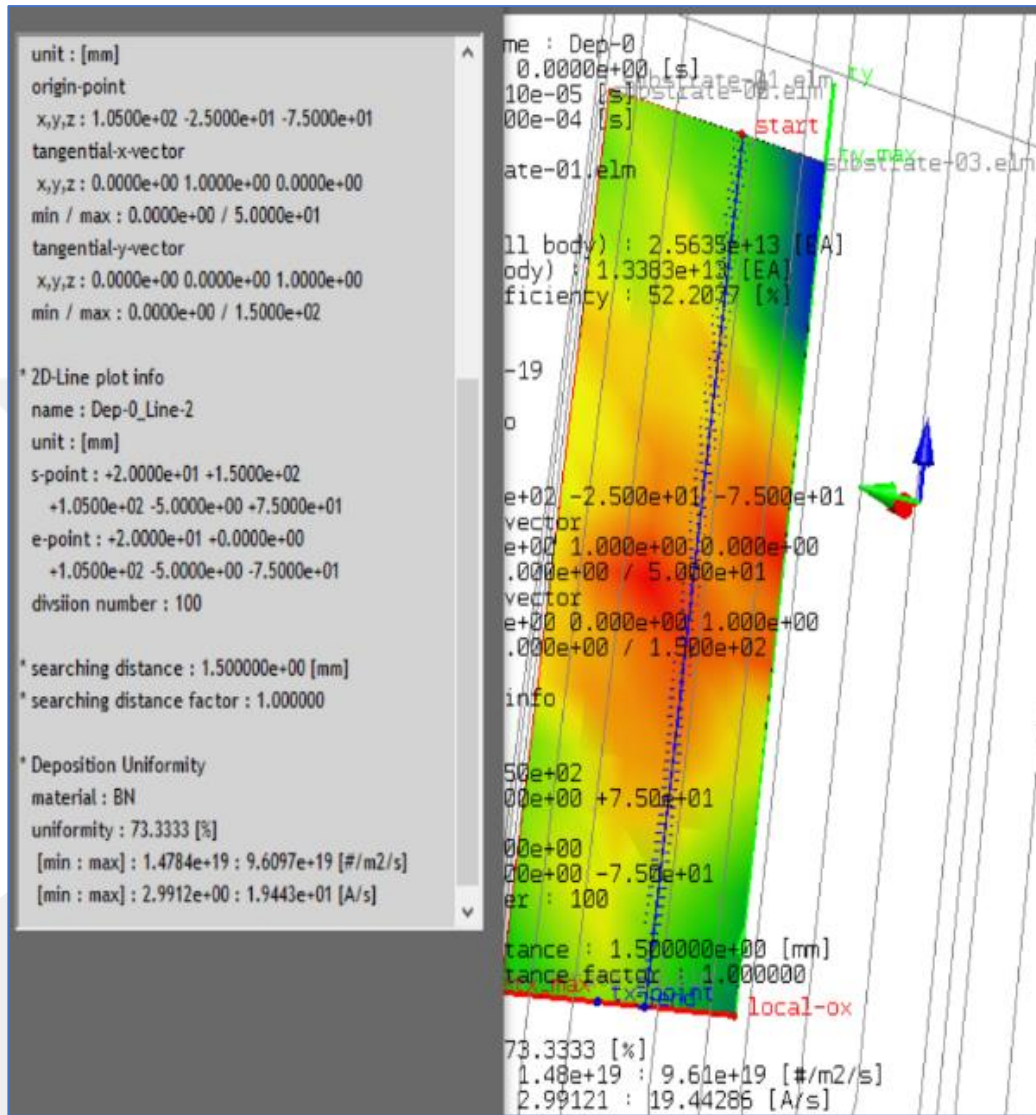


Figure 5.36 The deposition efficiency and uniformity when power supply=1200 W and substrate voltage (0V).

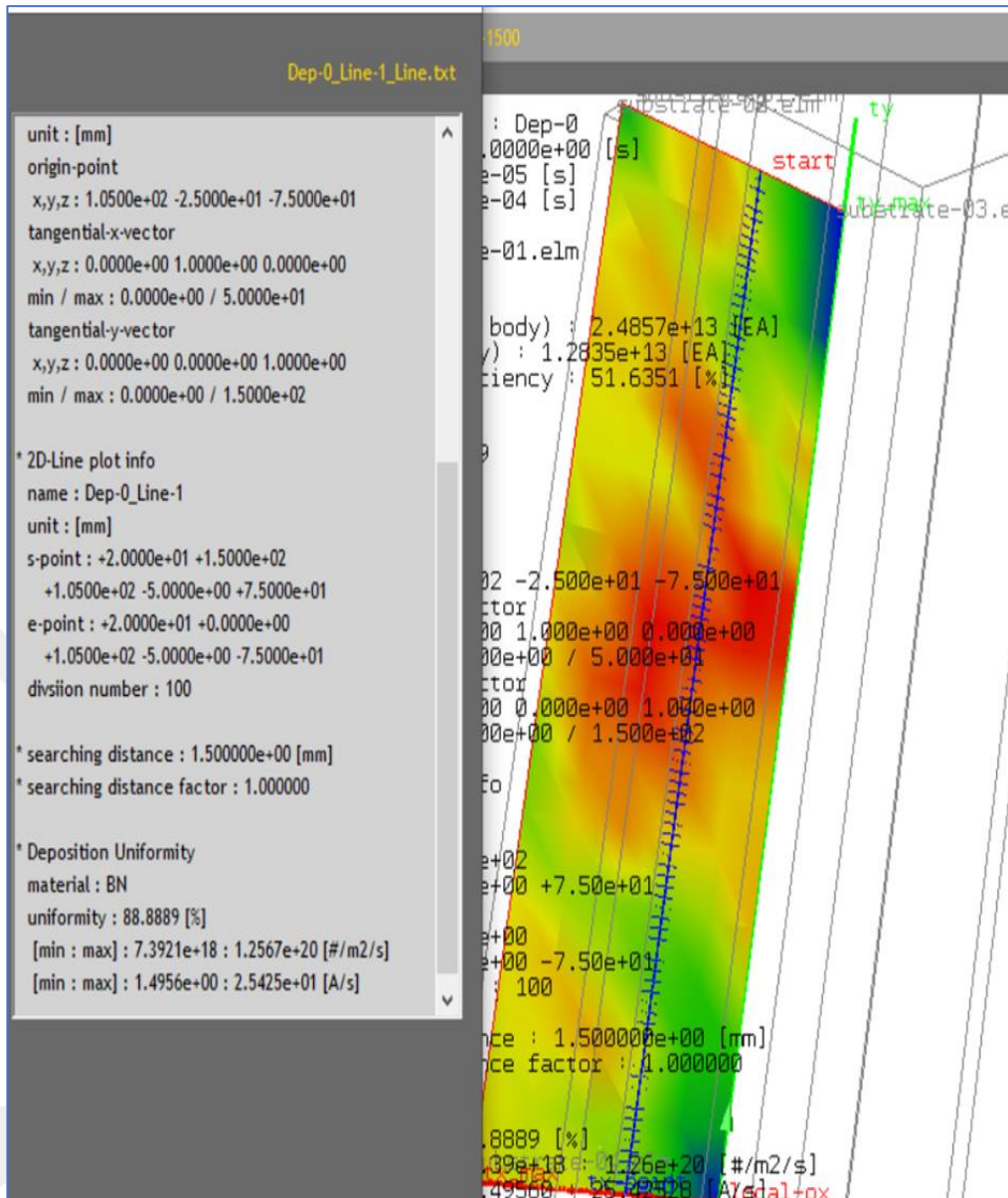


Figure 5.37 The deposition efficiency and uniformity when power supply=1500 W and substrate voltage (0

From Figure 5.38, We note that there is no wide difference in the deposition rate of BN particles at power 900,1200, and 1500 W when the bias substrate voltage is 250 V. The deposition efficiency for all of them is close to 33%. This small difference in the deposition rate caused the small difference in the thickness of the coating as shown in Table 5.5.

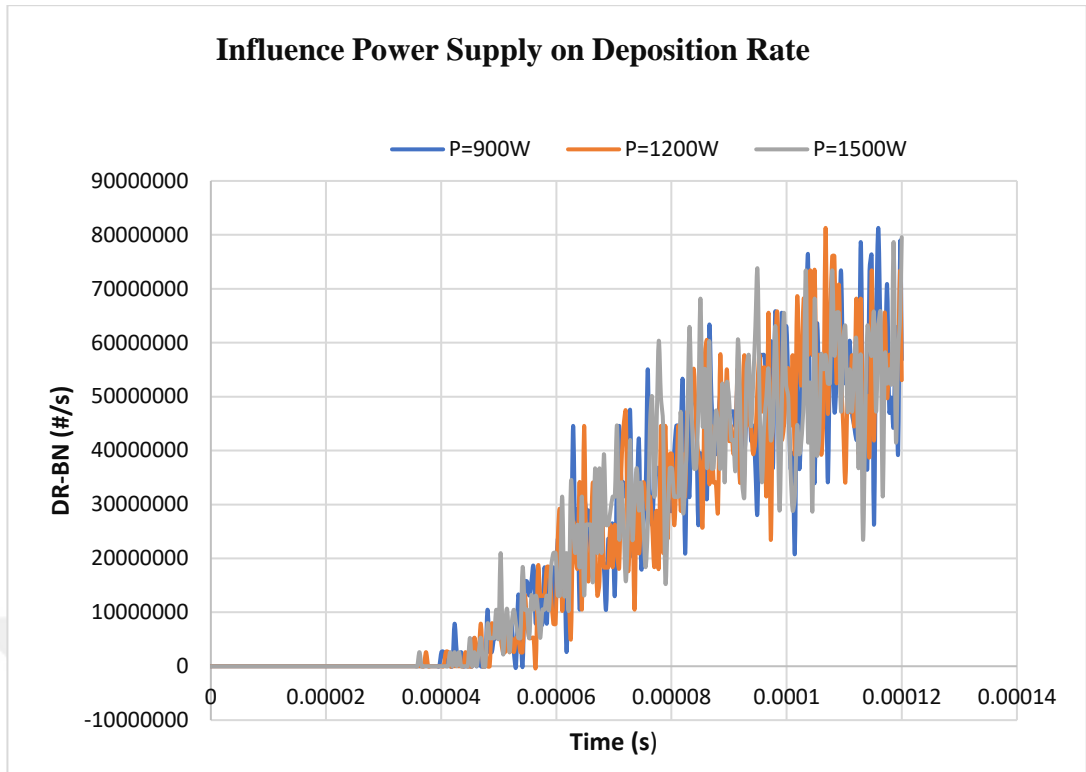


Figure 5.38 Influence of the power supply on the deposition rate at substrate voltage (250 V)

5.3.3 Modelling Influence of The Variable Volumetric Gas Flow Rate on The Deposition Profile

Three models build to study the effect of the volumetric flow rate of gas on deposition profiles. The volumetric flow rate for both gases Ar and N₂ will be changed. This change of flow rate will have the same Ar to ratio N₂. The Ar: N₂ ratios are 40:8,80:16 and 10:2. The details are shown in Table 5.6.

Table 5.6 The Boundary condition of MS Models with variation of gas flow rate.

No	Model-Name	Target	Sub. Material	Substrate Geometry (mm)	T-S Distance (mm)	T (°C)	Rpm	Magnetron	Sub. Voltage (v)	Time (hr)
1	Model-D1 (Model-A1)	h-BN	1xD2	150*50*7	80	300	Off	900w, 40/8sccm Ar/N ₂	0	6
2	Model-D2	h-BN	1xD2	150*50*7	80	300	Off	900w, 10/2sccm Ar/N ₂	0	6
3	Model-D3	h-BN	1xD2	150*50*7	80	300	Off	900w, 80/16sccm Ar/N ₂	0	6

The results of deposition rate for both Model-D2 and Model-D3 with Ar: N₂ are 80:16 and 10:2 shown in Figures 5.39 and 5.40 respectively.

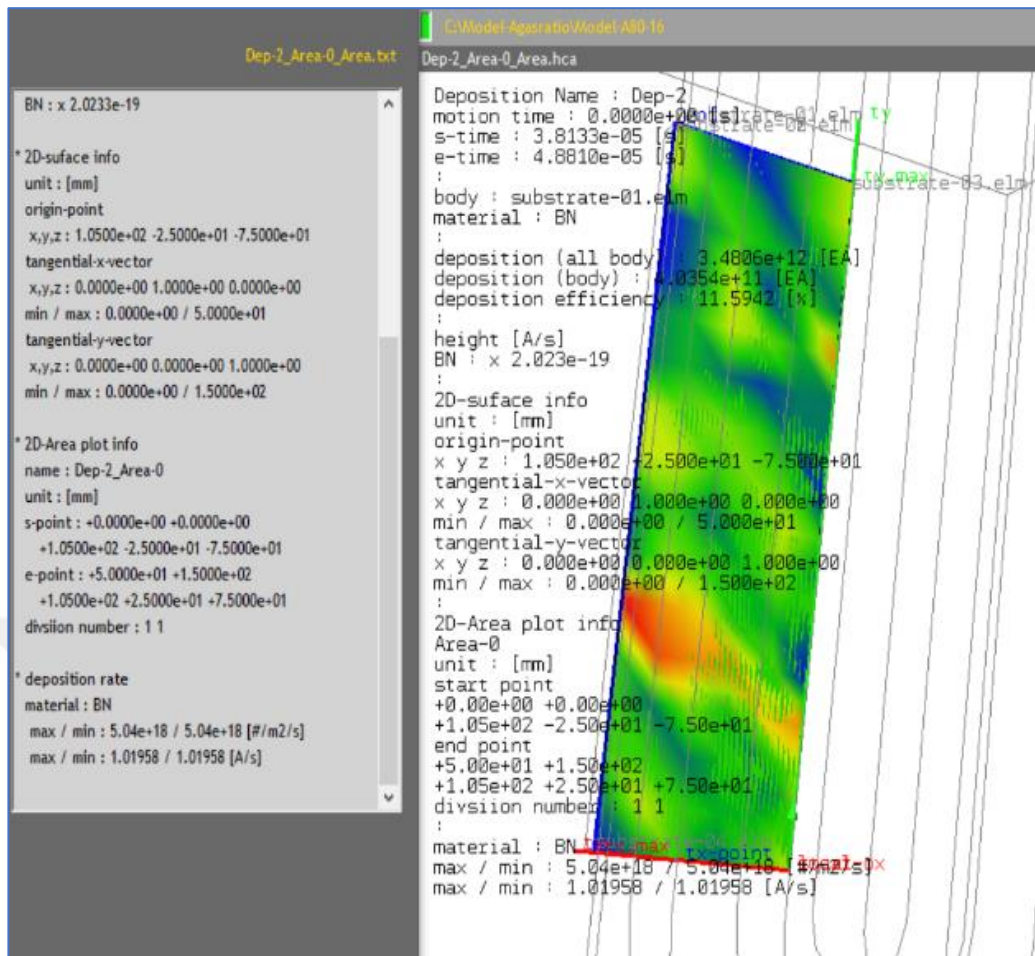


Figure 5.39 Influence of the variable volumetric gas when Ar: N₂ =80:16 sccm on the deposition rate at time=4.8e-5s

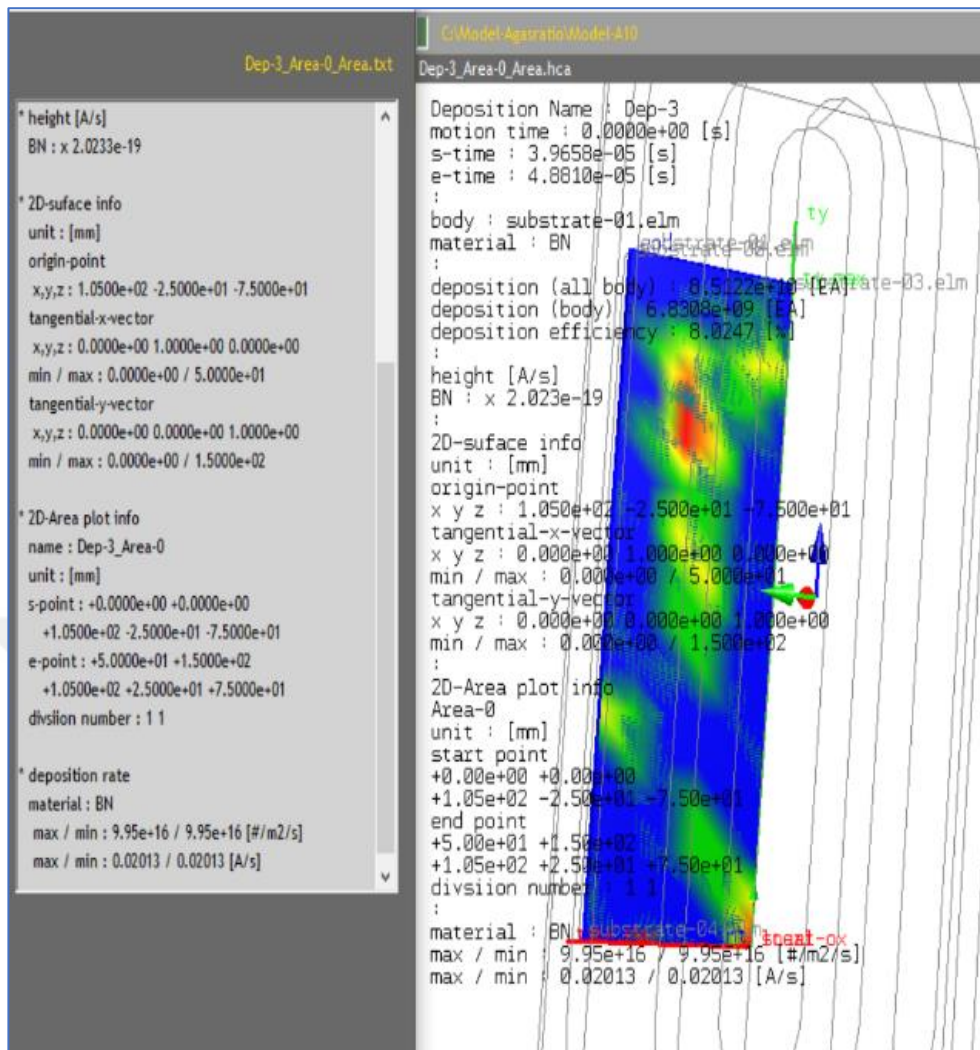


Figure 5.40 Influence of the variable volumetric gas when Ar: N₂ =10:2 sccm on the deposition rate at time=4.8e-5s

From these models, we note that the number of sputtering BN particles is high when Ar: N₂ is equal to 40:8 and 80:16. The number of sputtering BN particles when Ar: N₂ is 10:2 is low compared with two previous models as shown in Figure 5.41. The deposition efficiency of 40:8 and 80:16 models at steady state (t=1.2e-4s) are 52% and 49% respectively. The highest deposition efficiency when Ar: N₂ (10:2) is 53%.

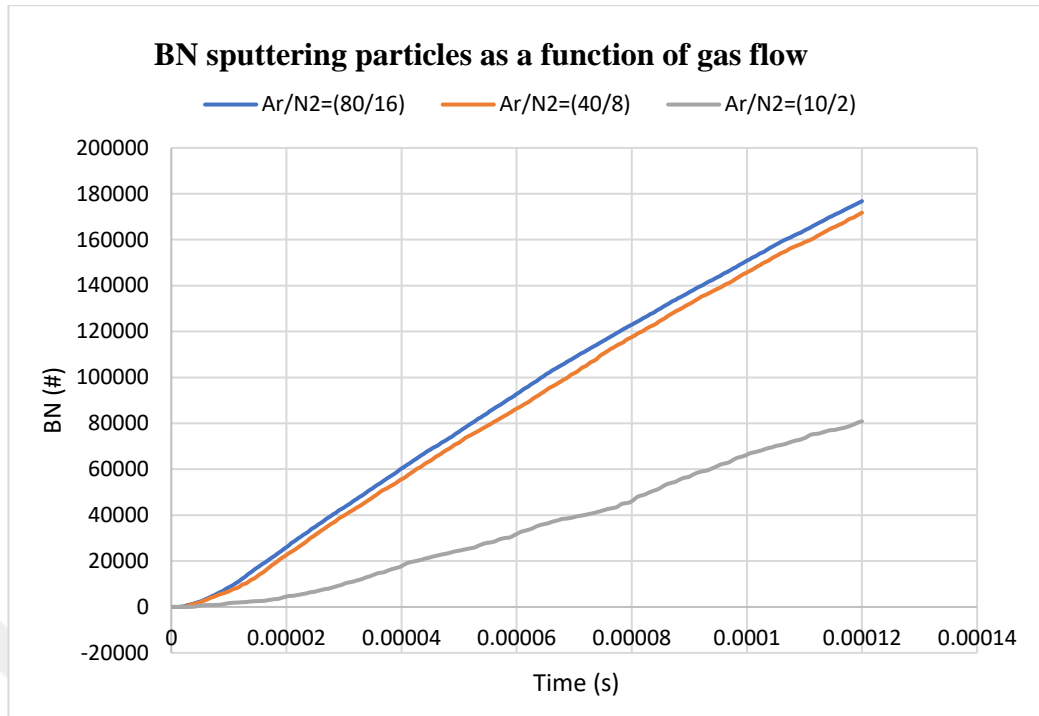


Figure 5.41 BN sputtering particles (#/s) on the different volumetric flow rates of Ar and N₂

The deposition rate of the three models is shown in Figure 5.42 and the thickness of the coating results is shown in Table 5.7.

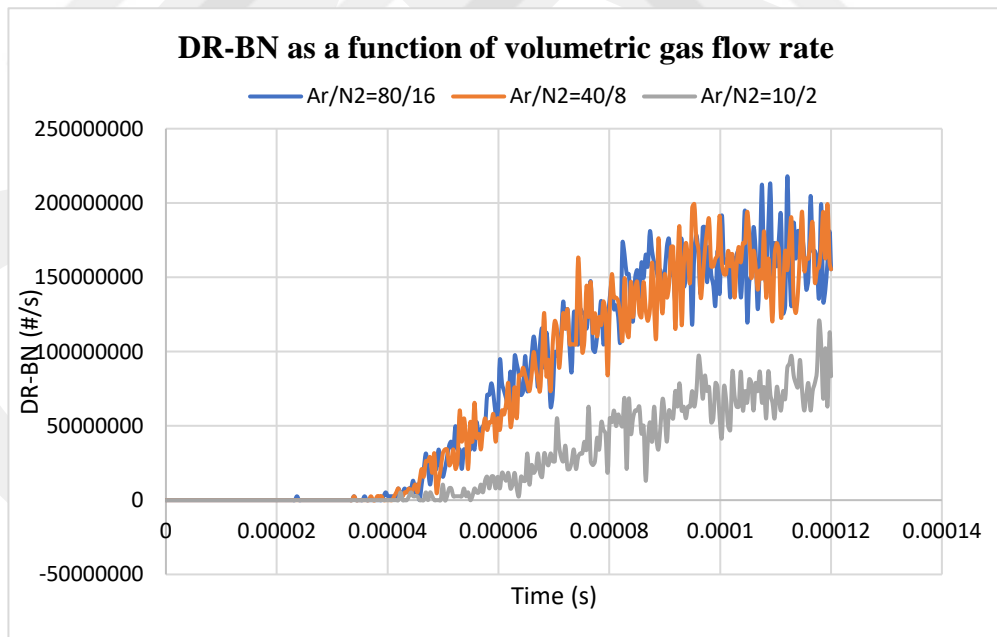


Figure 5.42 Deposition rate of BN particles on different volumetric flow rates of Ar and N₂

Table 5.7 The result of MS Models with the variation of gas flow rate

No.	Model-Name	Sub. Material	T(°C)	Rpm	Magnetron	Substrate Voltage(v)	Dep. rate (#/m ² .s)	Thickness(nm)
1	Model-D1 (Model-A1)	1xD2	300	Off	900w,40/8sccm Ar/N ₂	0	2.02 e18	882.1252
2	Model-D2	1xD2	300	Off	900w,10/2sccm Ar/N ₂	0	9.95e16	43.4512
3	Model-D3	1xD2	300	Off	900w,80/16sccm Ar/N ₂	0	5.04 e18	2200.9461

5.3.4 Modelling Influence of The substrate -Position on The Deposition Profile

Two models were built to study the effect of substrate position on the deposition profile.

In the first model (model-E), four small substrates were fixed in four positions in the chamber as shown in Figure 5.43. The geometry of the substrate is 30*30*7 mm.

In the second model (model-E1), only one substrate is used. The geometry of the substrate is 50*150*7 mm. This model was built to study the effect of target substrate distance on the deposition profile. The distance is 40 mm.

The result of the electric field for the two models is shown in (Chapter 4, Table 4.7, P.40). The boundary condition is shown in Table 5.8.

Table 5.8 The Boundary condition of MS Models with different T-S distances

No	Model-Name	Target	Sub. Material	Sub.Name	Substrate centre	T (°C)	Magnetron	Sub. Voltage (v)
1	Model-E	h-BN	4xD2	Sub.1	(65,0,-50)	300	900w, 40/8sccm Ar/N ₂	0
				Sub.2	(105,0,-10)			
				Sub.3	(145,0,40)			
				Sub.4	(185,0,90)			
2	Model-E1	h-BN	1 xD2	Sub.	(65,0,0)			

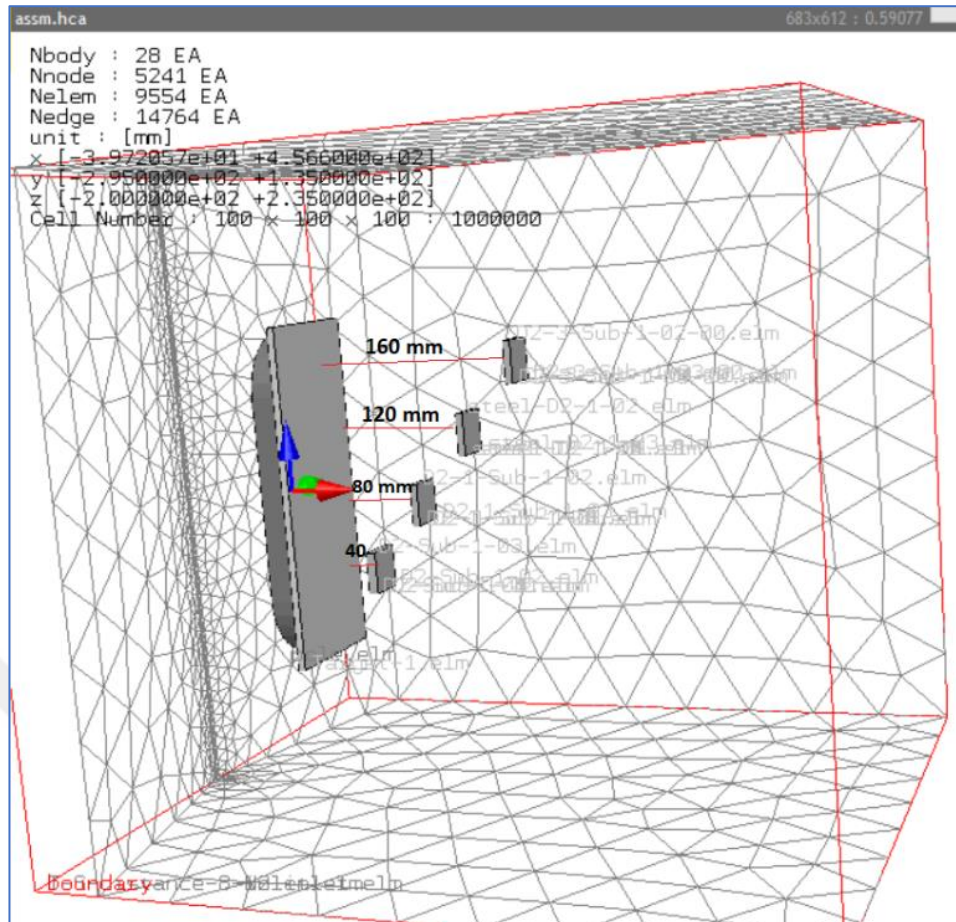
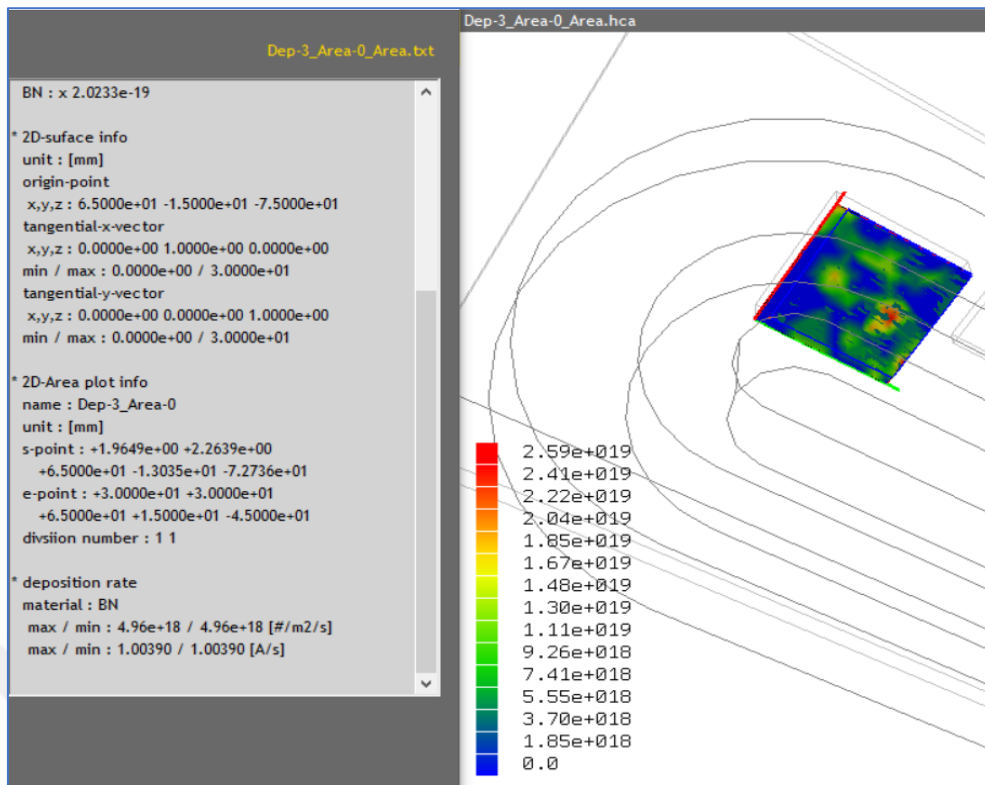
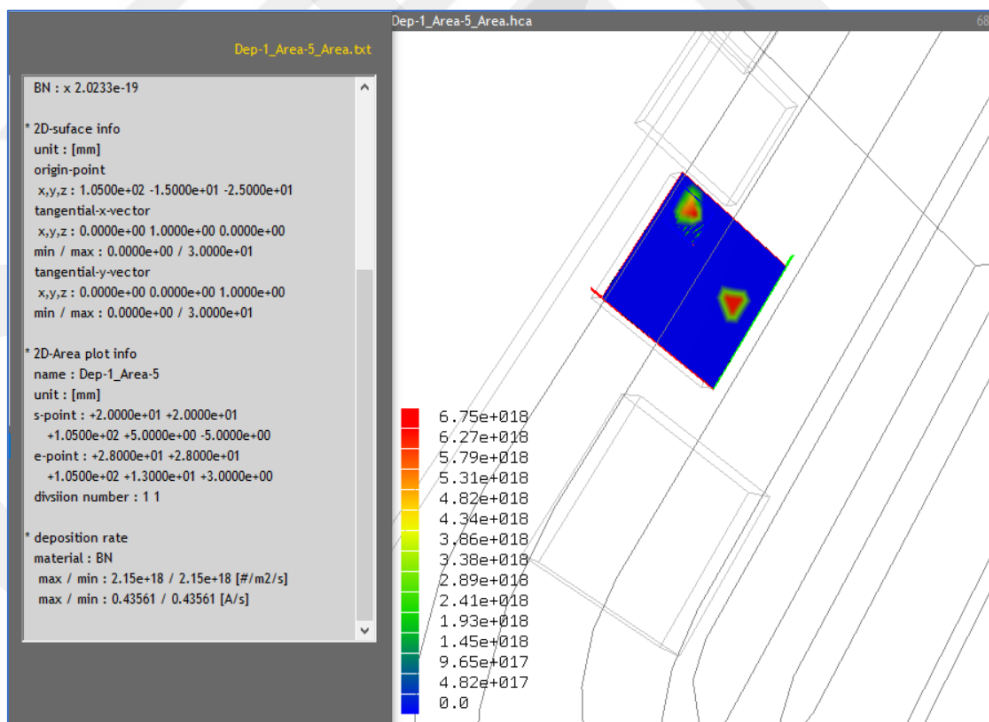


Figure 5.43 Geometry of BN modelling with different T-S distances

The maximum thickness of the coating is at substrate 1, while the thickness at substrate 4 is 0 nm as shown in Figures 5.44 and 5.45. The result of Model-E shows a large difference in the thickness of the coating with the change of the substrate position as shown in Figure 5.46.

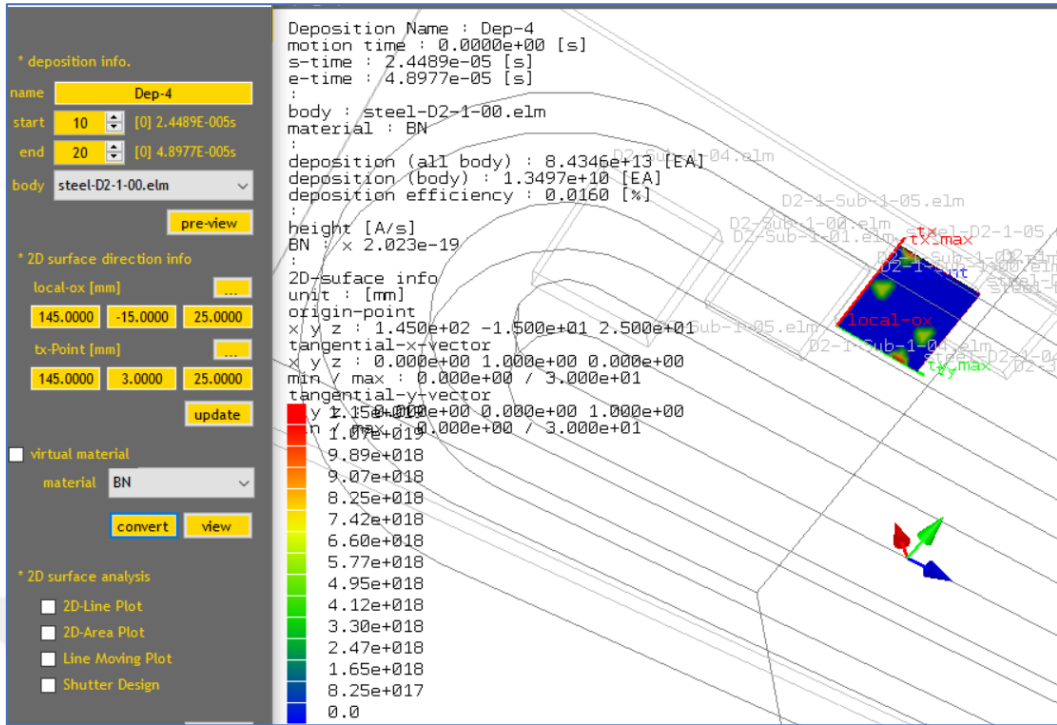


(a) Substrate 1

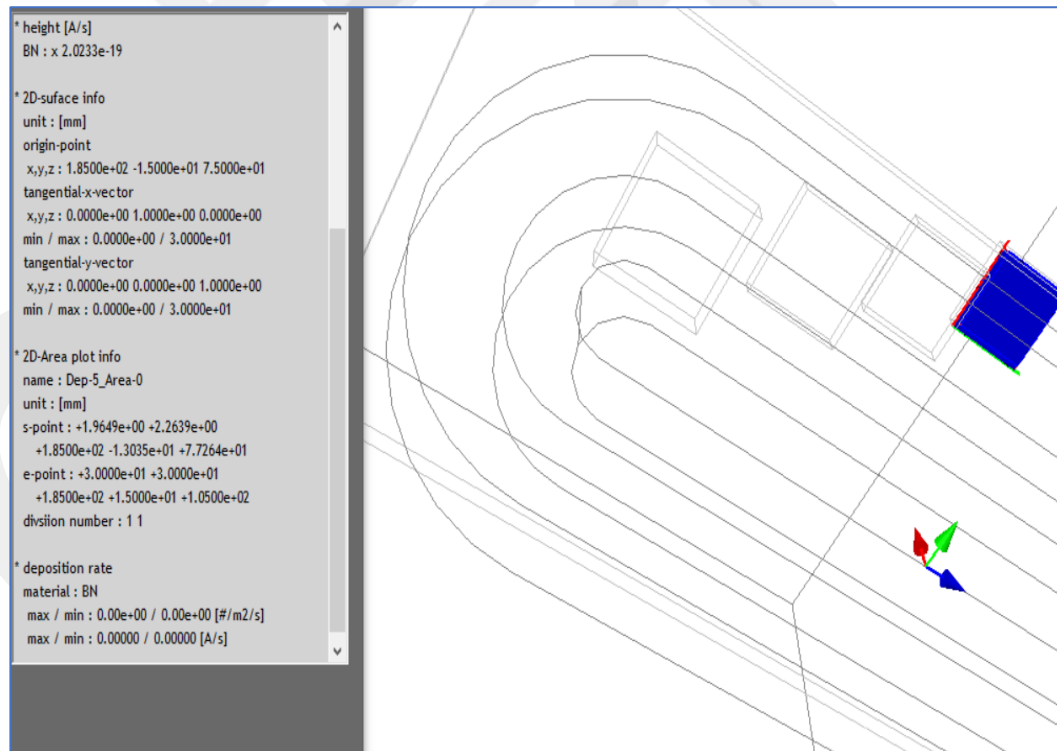


(b) Substrate 2

Figure 5.44 Deposition rate of BN coating of model-E (Sub.1 and Sub.2)



(a) Substrate 3



(b) Substrate 4

Figure 5.45 Deposition rate of BN coating model-E (Sub.3 and Sub.4)

Figure 5.46, shows the effect of the substrate position on the coating thickness. The centre point of the target plate is (25,0,0). The result of Model-E is summarized in Table 5.9.

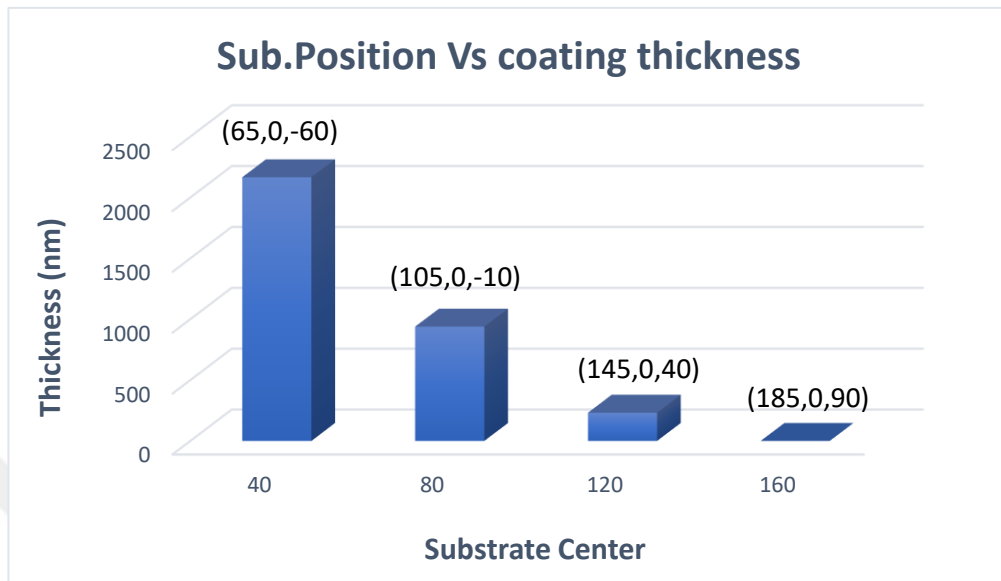


Figure 5.46 Thickness of BN coating Vs Substrate position (the centre point of the substrate) Model-E

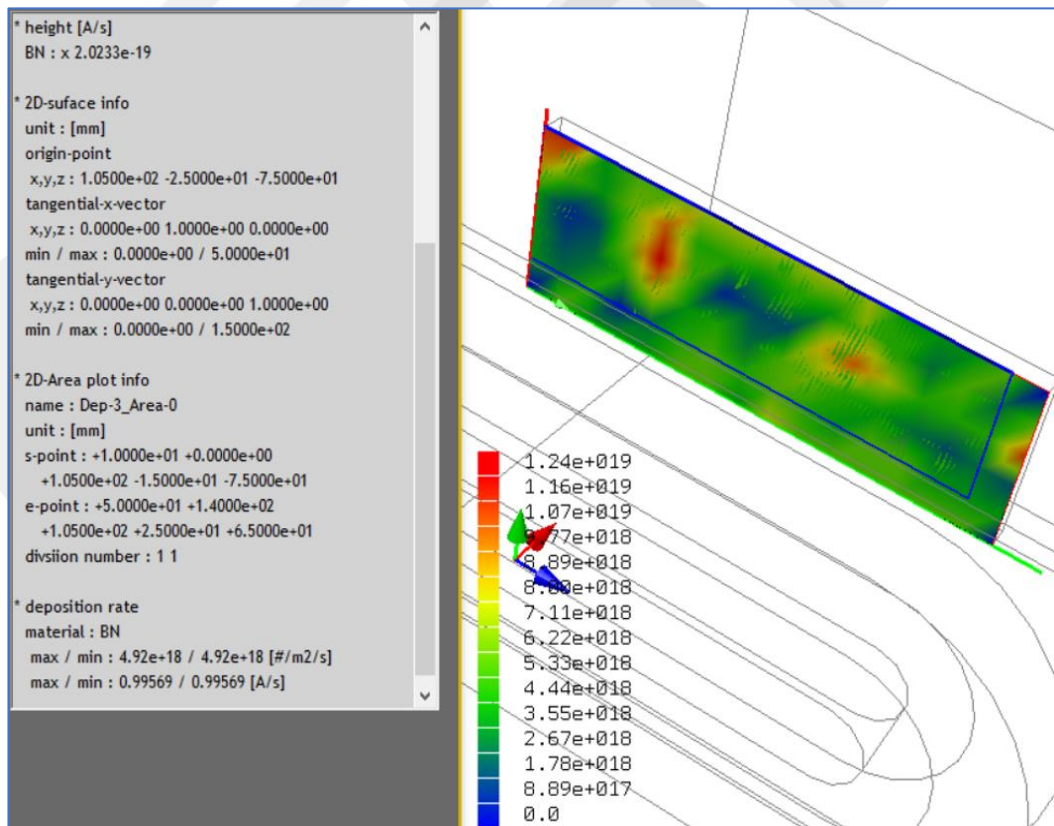


Figure 5.47 Deposition rate of BN particles (Model-E1), T-S distance 40 mm

Table 5.9 The result of MS Models with different T-S distance

No.	Model-Name	Sub. Material	Sub. Name	T (°C)	Rpm	Magnetron	Substrate Voltage(v)	Deposition Rate (#/m2.s)	Thickness (nm)
1	Model-E	4xD2	Sub.1	300	Off	900w, 40/8sccm Ar/N ₂	0	4.96e18	2166
			Sub.2					2.15e18	938.9
			Sub.3					5.32e17	232.3
			Sub.4					0	0
2	Model-E1	1xD2	Sub.					4.92e18	2149

5.3.5 Modelling Influence of The Substrate Materials on The Deposition Profile

One model builds with five small substrates. The geometry of the substrate is 30*30*7 mm. Five types of materials are used. These types are D2, Aluminum, Ti, TiN, and glass. The material of the target plate is (h-BN). The result of the electric field for multi-substrates with a different type of material is explained in (Chapter 4, Table 4.10,p.47). The purpose of the model, study the effect of substrate materials on deposition profile. The boundary condition is shown in Table 5.10. This model contains 34 surfaces due to departing all the substrate geometry to the 2D surface as shown in Figure 5.48. The centre point of the target plate is (25,0,0).

Table 5.10 The Boundary condition of MS Models with different T-S distances

No	Model-Name	Substrate	Sub. Geometry (mm)	Sub.Center Point (x,y,z)	T-S mm	T (°C)	Rpm	Magnetron	Sub. Voltage (v)	Time (hr)
1	Model-F	1xAl	30*30*7	(105,0,-110)	80	300	Off	900w,40/8 sccm Ar/N ₂	0	6
		1xD2		(105,0,-50)						
		1xTi		(105,0,-10)						
		1xTiN		(105,0,40)						
		1xglass		(105,0,90)						

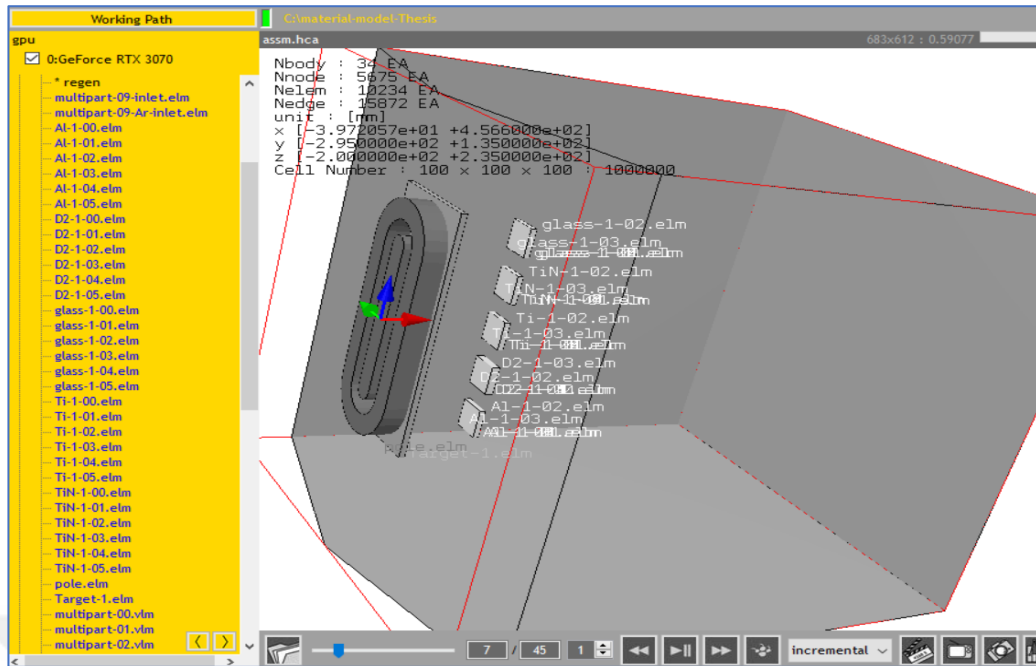


Figure 5.48 The 2D faces of Model-F

With the progress of the magnetron sputtering model, the particles of BN are sputtering. The active gas N_2 is ionized to $2N$ due to a chemical reaction with the BN target as shown in Figure 5.49. The result of Model-F is summarized in Table 5.11.

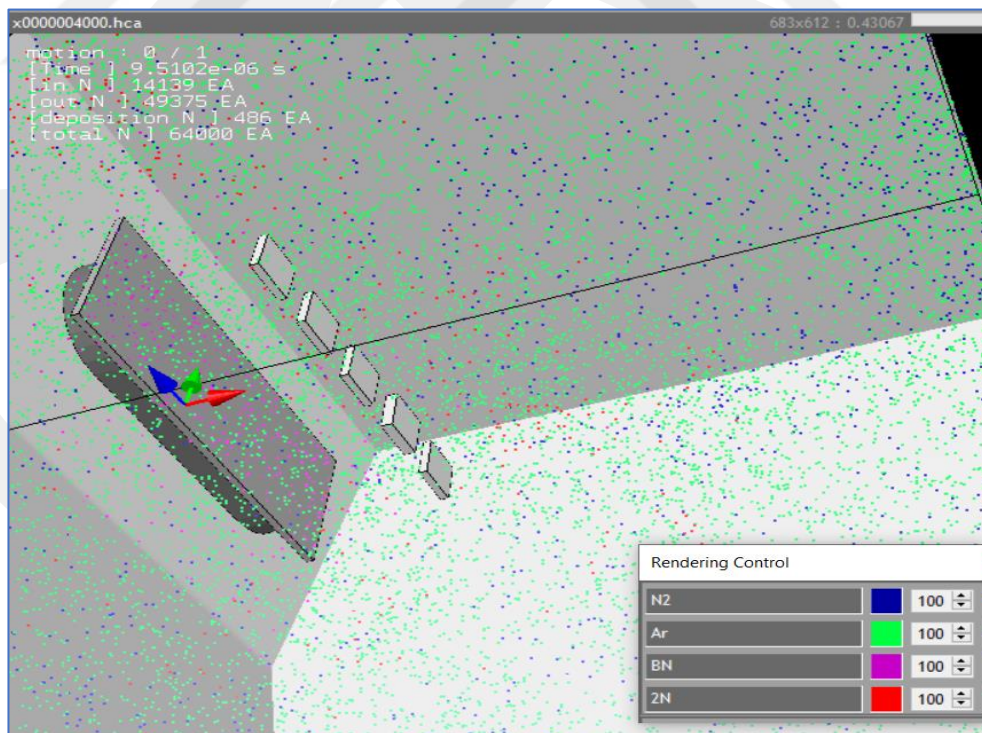


Figure 5.49 The chemical reaction between the BN target plate and N_2 gas caused to produce of $2N$ (Model-F)

Table 5.11 The result of the MS Model with a different type of substrate material

No.	Model-Name	Sub. Material	T-S mm	T (°C)	Rpm	Magnetron	Substrate Voltage (v)	Deposition Rate (#/m2.s)	Thickness (nm)
1	Model-F	1xAl	80	300	Off	900w,40/8 sccm Ar/N ₂	0	1.6e18	698.7
		1xD2						2.10e18	917
		1xTi						1.96e18	855.9
		1xTiN						2.62e18	1144.2
		1xglass						1.7e18	751

5.4 2D Field Analysis of BN Coating Model

The 2D-Analysis (X-Y coordinates) of properties in the chamber of the MS system is done. These properties are gas density and flux, pressure and temperature. This analysis aims to study the effect of the input parameters of coating on the pressure and temperature distribution in the chamber. Then understand how the pressure and temperature change the character of the BN particles that arrive at the substrate.

This analysis may help to understand the transformation mechanism of the h-BN phase to c-BN.

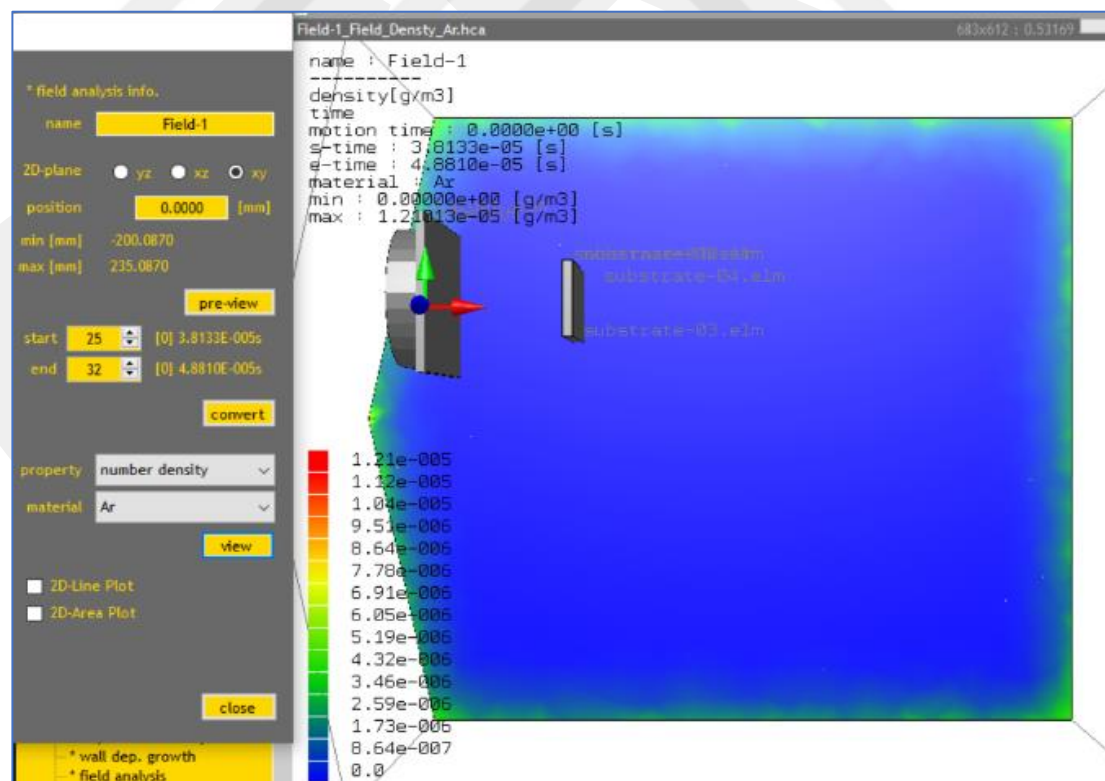


Figure 5.50 Density analysis of Ar in model-A1

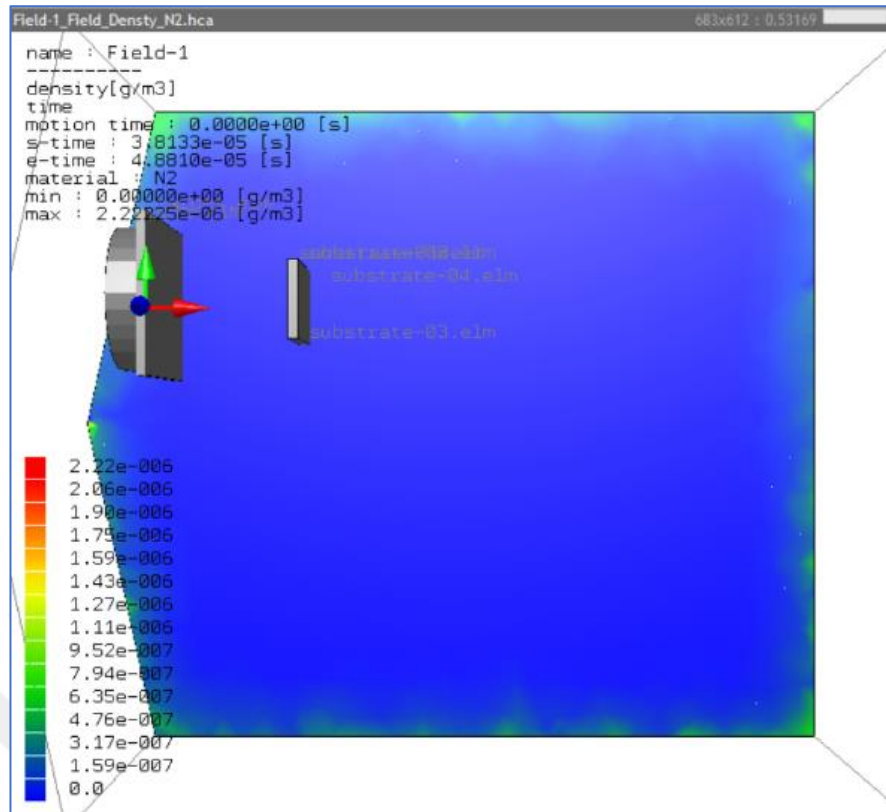


Figure 5.51 Density analysis of N₂ in model-A1

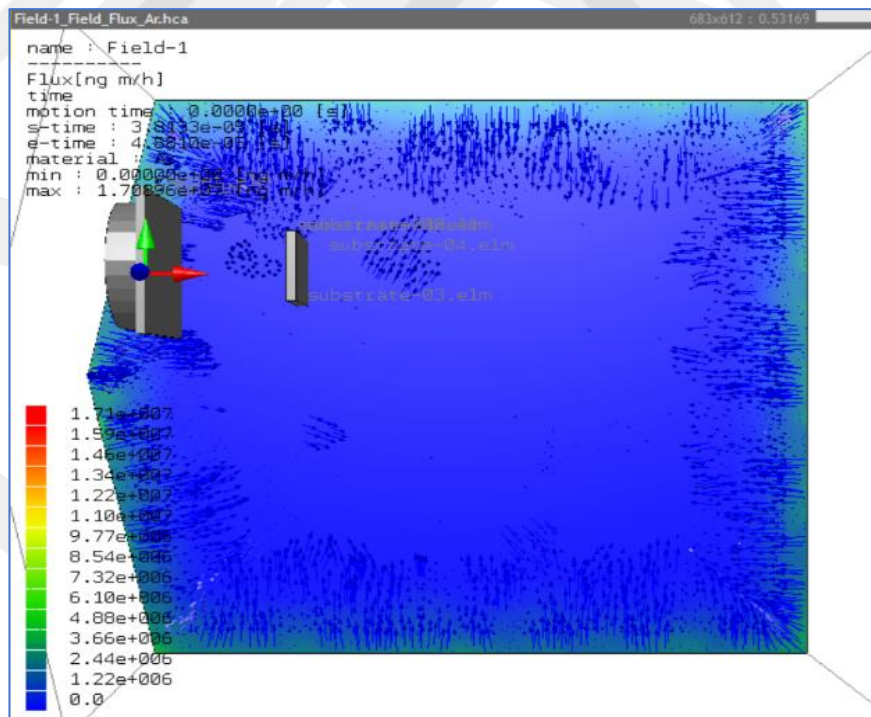


Figure 5.52 Flux analysis of Ar in model-A1

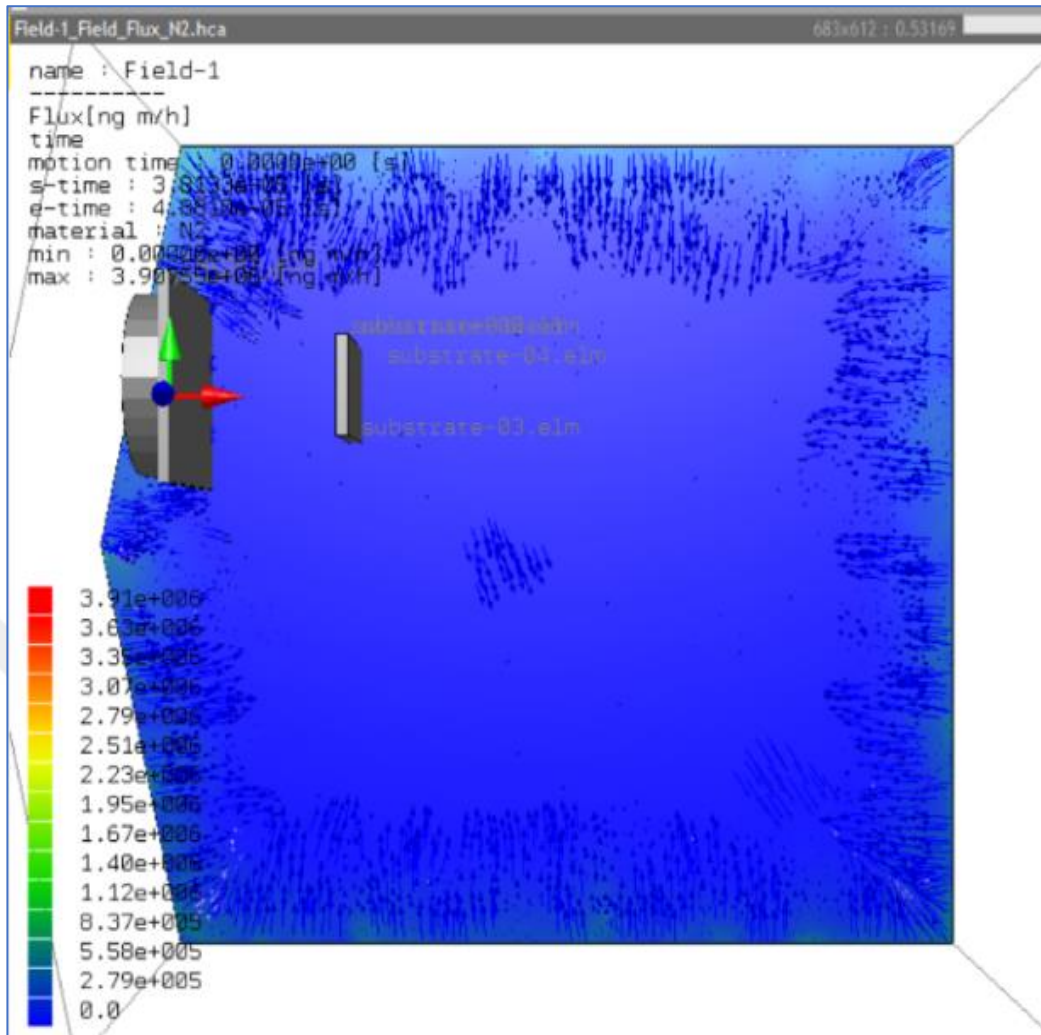
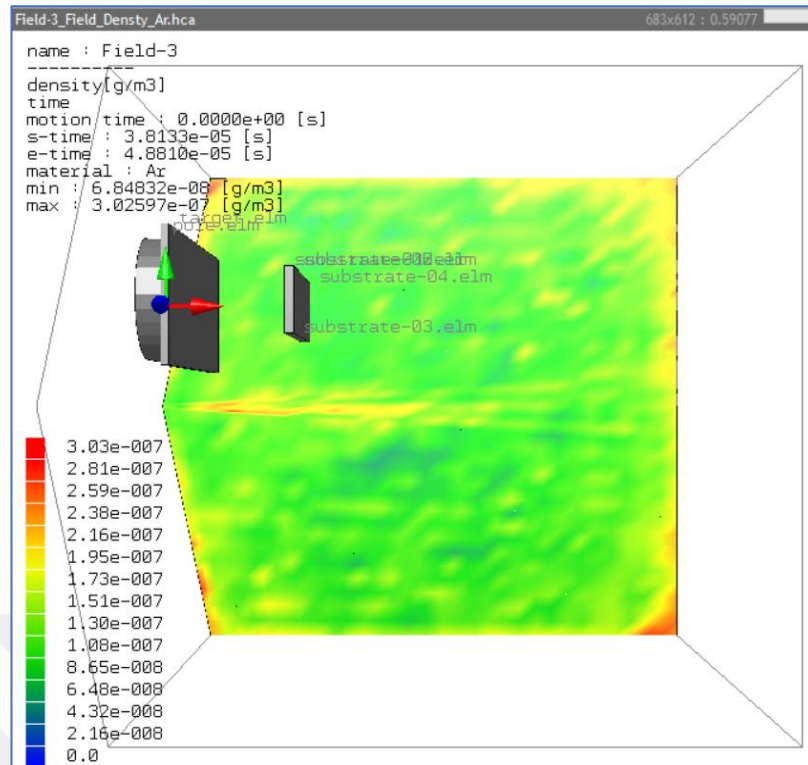
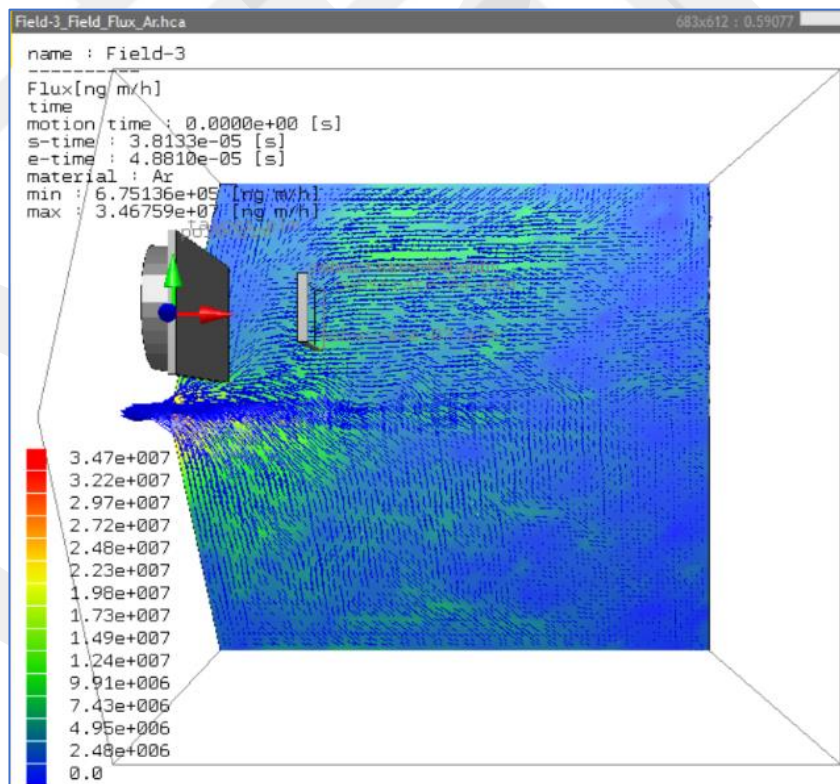


Figure 5.53 Flux analysis of N₂ in model-A1



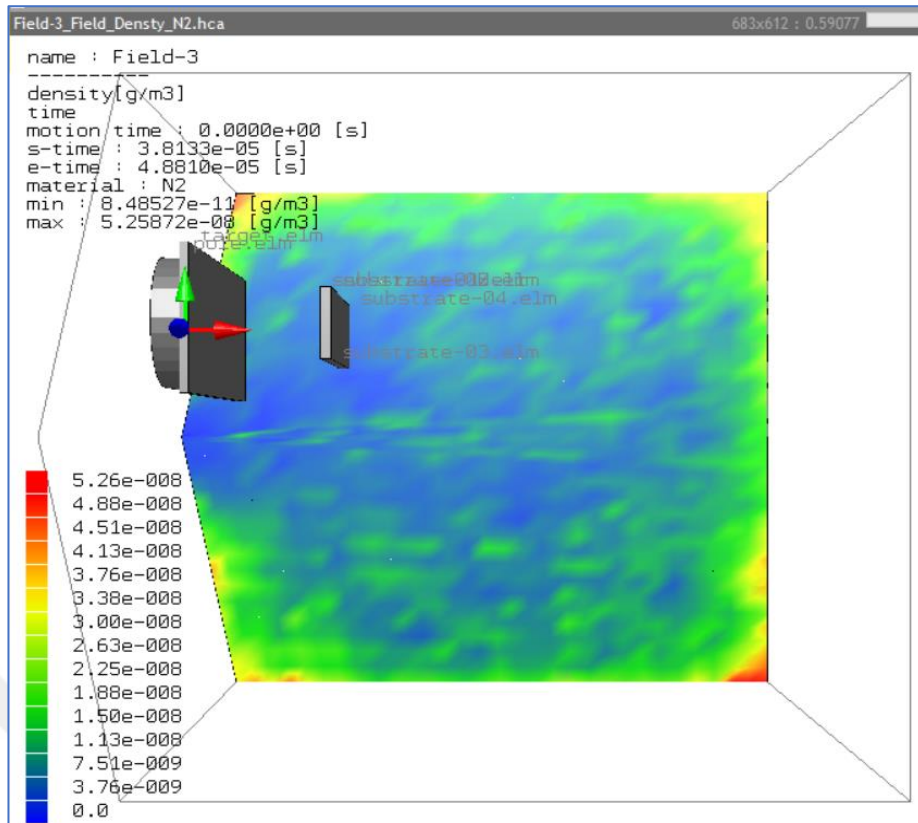
(a)



(b)

Figure 5.54 Density and flux analysis of Ar in Model-C1,(a) Ar density and

(b) Ar flux



(a)

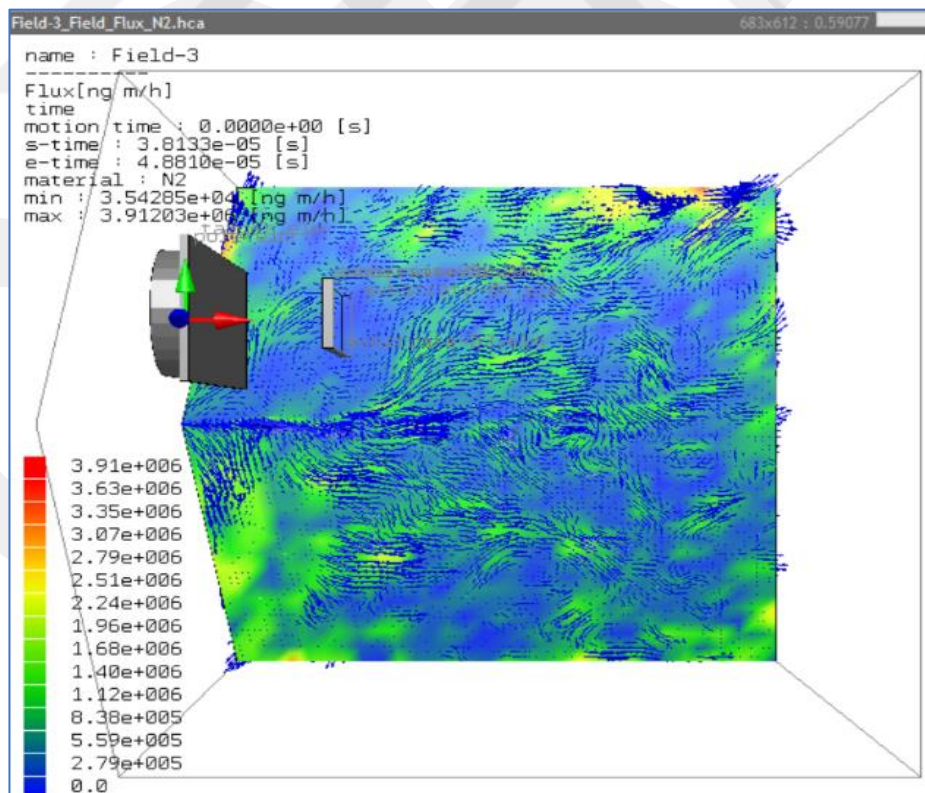


Figure 5.55 Density and Flux analysis of N₂ in model-C1,(a) N₂ density and (b) N₂ flux

From Figures 5.56, 5.57 and 5.58, When comparing the pressure and the temperature of model-A1 and model-C1 (When the bias voltage is 0 and 250 V), increasing the bias voltage of the substrate leads to an increase in pressure and temperature. The FTIR analysis of the experiment result (Run-152) shows that the h-BN transform to c-BN.

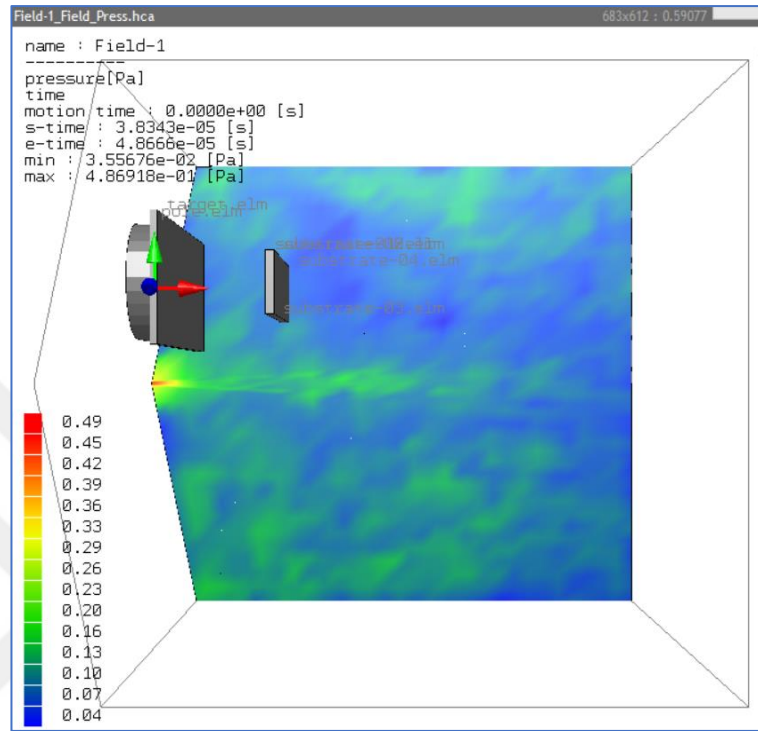


Figure 5.56 The pressure of model-A1

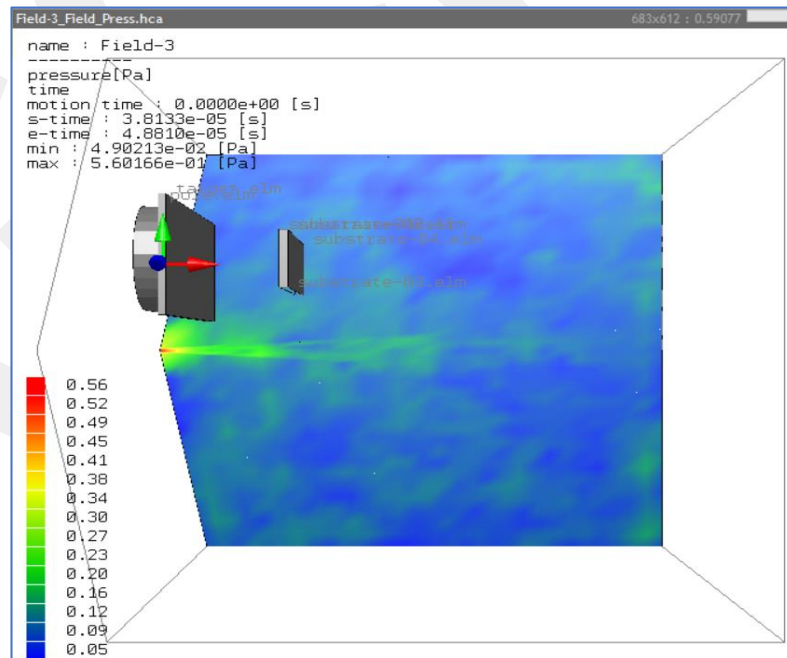
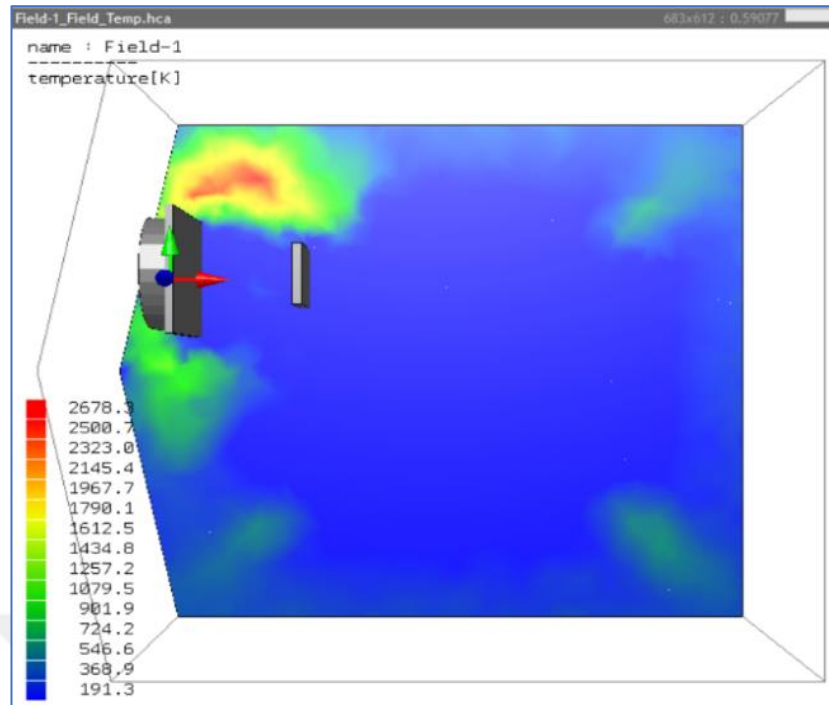
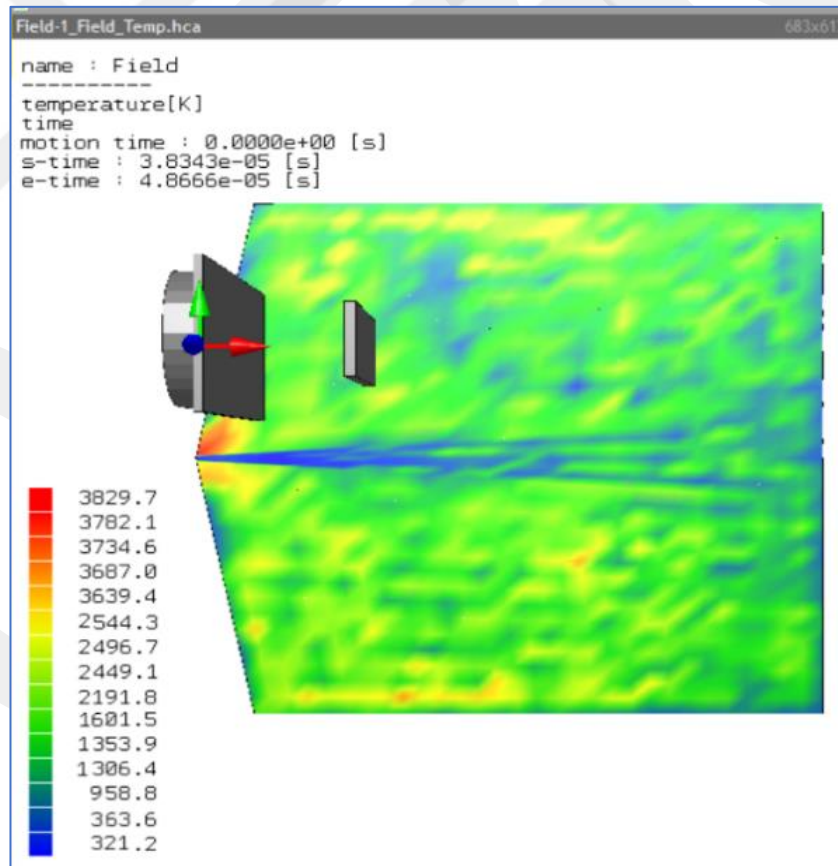


Figure 5.57 The pressure of mod



(a)



(b)

Figure 5.58 Influence of bias substrate voltage on temperature distribution in the chamber,(a) model-A1 and (b) model-C1

5.5 Optimization of BN Coating

5.5.1 Modelling Optimization of BN Coating

From the previous models, We can say that the maximum deposition rate at power supply is 1200 W and substrate voltage 0V as shown in model-A2. In the study of the effect of the volumetric gas flow rate of Ar and N₂, the maximum deposition rate when Ar: N₂ is 80:16 sccm as shown in model-D3. Therefore we will combine these boundary conditions as input parameters to optimize the BN coating thickness as shown in Table 5.12. The result of the model shows a high deposition rate, see Figure 5.59.

Table 5.12 The input parameters of the BN coating optimization -(Model-G)

No	Model-Name	Target	Sub. Material	Sub. Geometry (mm)	T-S Distance (mm)	T (°C)	Rpm	Magnetron	Substrate Voltage (v)	Time (hr)
1	Model-G	h-BN	1xD2	50*50*7	80	300	Off	1200w,80/16 sccm Ar/N ₂	0	6

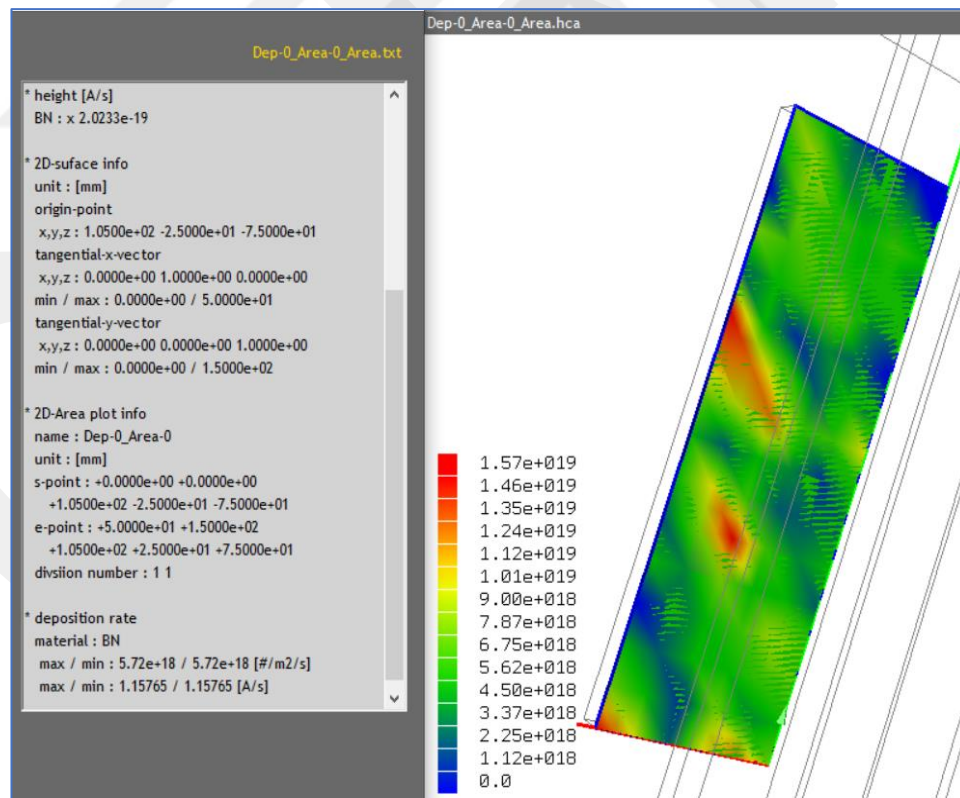


Figure 5.59 The result of the BN coating model (Model-G) at optimization boundary conditions.

Table 5.13 The result of the BN coating optimization (model-G)

No.	Model-Name	Sub. Material	T (°C)	Rpm	Magnetron	Substrate Voltage(v)	Dep. rate (#/m ² .s)	Thickness (nm)
1	Model-G	1xD2	300	Off	1200w,80/16 sccm Ar/N ₂	0	5.72e18	2498

Due to some technical issues in the MS system in the facilities of the BOREN Center of Competence for Boron Coatings, the maximum Rf-power supply that can be applied is 1100 W.

Therefore, we will build a new model (Model-G1) with this new parameter and check the result before Preparing the coating experiment as shown in Table 5.14. The electric field for this model is summarized in (Chapter 4, Table 4.5, P.39).

The result of Model-G1 is summarized in Table 5.15.

Table 5.14 The input parameters of the BN coating optimization -(Model-G1)

No	Model-Name	Target	Sub. Material	Sub. Geometry (mm)	T-S Distance (mm)	T(°C)	Rpm	Magnetron	Substrate Voltage (v)	Time (hr)
1	Model-G1	h-BN	1xD2	50*50*7	80	300	Off	1100w, 80/16 sccm Ar/N ₂	0	6

Table 5.15 The result of the BN coating optimization model-G1

No.	Model Name	Target	Sub. Material	T(°C)	Rpm	Magnetron	Substrate Voltage (v)	Dep. rate (#/m ² .s)	Thickness (nm)
1	Model-G1	h-BN	1xD2	300	Off	1100w,80/16 sccm Ar/N ₂	0	4.21e18	1840

From table 5.15, The thickness of the coating is 1840 nm (model-G1). The power supply is 1100 W. The 2D analysis of the maximum temperature and pressure of the model-G1 analysis is 3700 C and 0.95 Torr.

The 2D analysis shows that there is a correlation between the change in pressure and temperature with the change of characteristics of BN particles. Increasing the maximum temperature in the chamber will increase the chance to transform h-BN to c-BN, therefore we will apply the model-G1 parameters as a step to combine a high deposition rate and high-density polymorphs (c-BN).

5.5.2 Magnetron Sputtering Experiment-Optimization of BN Coating

- **Run 203**

A detailed description of the experiment (RUN 203) is presented below, the main parameters are listed in Table 5.14. A high vacuum is used in PVD technology. D2 steel is the type of substrate, and the substrate geometry is 30 mm in diameter with 7 mm thickness. Four substrates are used in different positions. The result of the closest substrate to the target will be compared with the substrate result in Model-G1 (both of them have the same parameters). The radio frequency (RF) power supply is applied to the target plate. The gas flow rates of Ar and N₂ are 80 and 16 sccm, respectively. The total pressure of the two gases is maintained at 0.005 Torr. The power supply is 1100 W. The substrate bias voltages are 0 V. The vacuum temperature is 300 °C, and the deposition time is 6 hr. A plasma cleaning process is applied to the substrate before the deposition process. F₂₀ Filmmetrics is used to measure the thickness of BN coatings. For each BN-coated substrate, ten measurements are taken and the averages are computed.

- **RUN 209**

The same boundary conditions are applied in the two experiments Run 203 and Run 209 with a different target to substrate distance (TSD). The target to substrates distances are 100,200,230 and 290 mm for experiment Run 203, While for experiment Run 209 are 50 and 290 mm. . Two substrates with angels angles of 0° and ~42° from the target plate centre are applied in Run 209 as shown in figure 5.60.

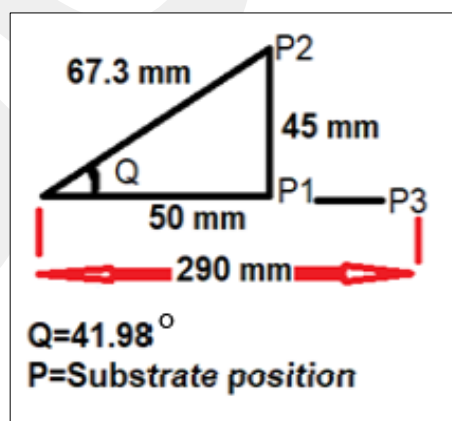


Figure 5.60 The substrate position in experiment Run 209

Theoretical and experimental studies of BN coating show that the TSD has an impact on thickness. For a D2 substrate, the coating thickness is 1900.7 nm and 3296.5 nm, respectively, when the TSD is 100 mm and 50 mm. The coating's increased thickness is 1395.8 nm. When compared to P1, the deposition rate for angle 42° D2 substrate at P2 is higher in experiment Run 209. (figure 5.60). The coating has a thickness of 3518 nm. The distribution of the magnetic field on the target plate is the cause of these variations (See Chapter 4, Figure 4.4, P.32).

According to figures 5.61 and 5.62, the difference in coating thickness and BN phase for substrates with varied TSD with an angle of 0° is caused by changes in the kinetic energy of BN particles and the electric field as a function of TSD.

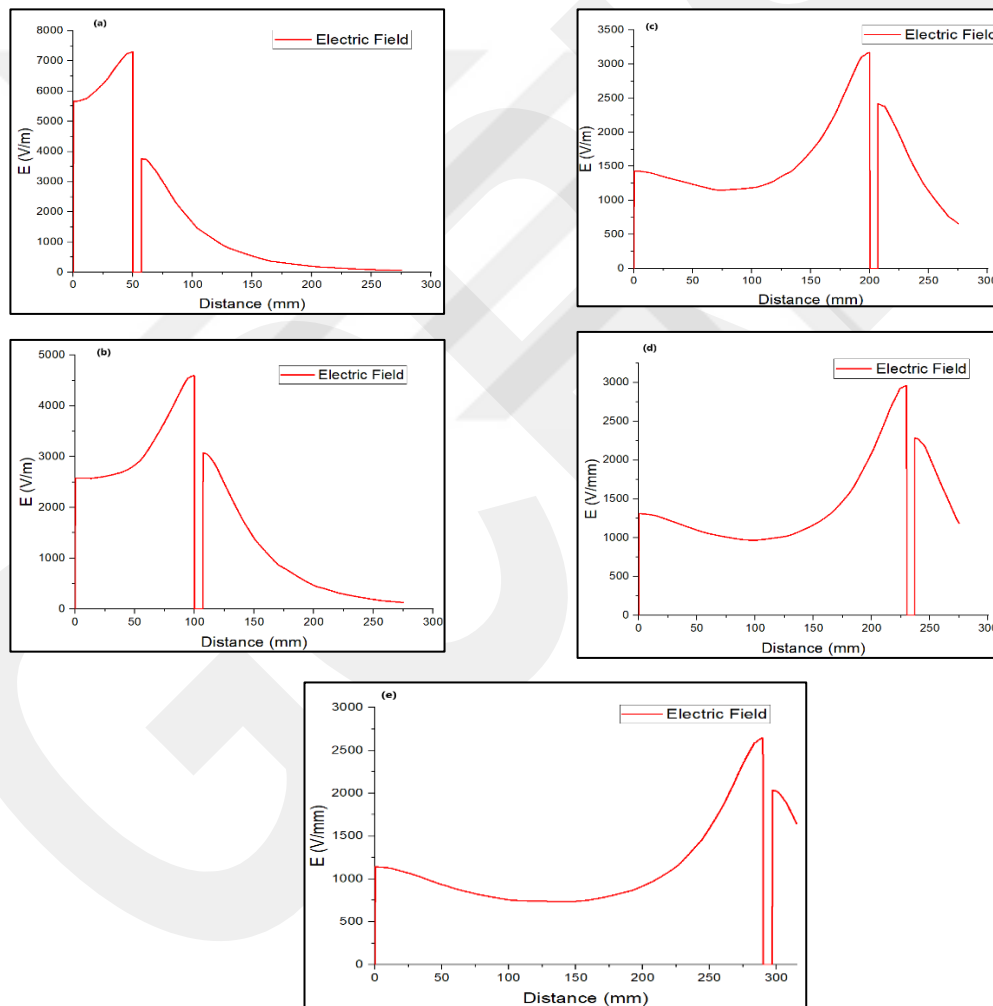


Figure 5.61 Distribution of the EF between the target and the substrate with different (TSD),(a) 40 mm,(b) 100 mm,(c) 200 mm,(d) 230 mm and (e) 290 mm (Theoretical analysis of BN coating Models)

The electric field strength on the surfaces of the substrates is calculated. The maximum electric field strength is on the edge of the substrate. The EF becomes stable from 25 mm of the substrate's edge. Decreasing the T-S distance from 100 to 50 mm will increase the EF in the substrate's centre from 5270 V/m to ~8700 V/m as shown in Figure 5.62.

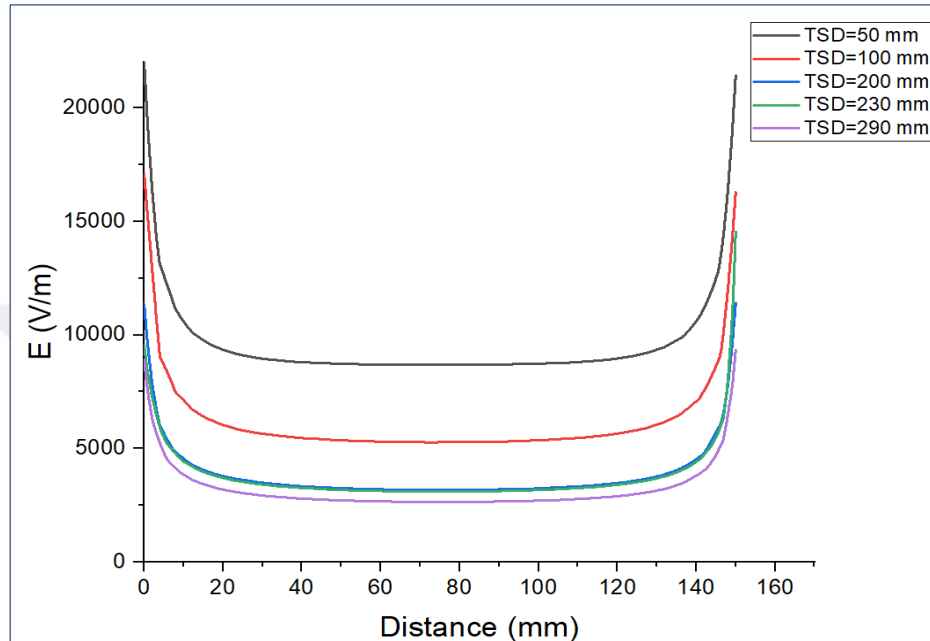


Figure 5.62 Electric field strength analysis on the substrate surface as a function of TSD (Theoretical analysis of BN coating Models)

The coating thickness of RUN203-D2-4 is 200.41 nm. The coating thickness of RUN209-D2-3 is 188.45 nm. The coating thickness is decreased by 11.96 nm. The result for both substrates is closed (The substrates have the same TSD).

- **Run 217**

This experiment will submit by using a bias substrate voltage of 180 V . We try to increase the hardness of the substrate. D2 steel is the type of substrate. From the model and experiment the deposition rate decrease with increasing the bias substrate voltage. Therefore, we will try to increase the deposition by increasing the amount of volumetric gas flow rate. The gas flow rates of Ar and N₂ are 90 and 18 sccm, respectively. The total pressure of the two gases is maintained at 0.005 Torr. The power supply is 1100 W. The vacuum temperature is 300 °C, and the deposition time is 6 hr. The target to substrate distances is 50 and 290 mm.

5.5.2.1 FTIR Measurement Results

The FTIR analysis for all substrates in experiments Run 203, Run 209 and Run 217 are found. When comparing the Substrate D2-1 in Exp. Run 203 with D2-1 in Exp. Run 209, The same parameters with TSD 100 and 50 mm respectively. The surface morphology test by FTIR indicates that the h-BN coating deposition layer is affected when the TSD is changing. The FTIR result shows that the low-density BN crystal lattices (h-BN) transform into high-density polymorphs cubic BN (c-BN) when TSD is 50 and 100 mm.

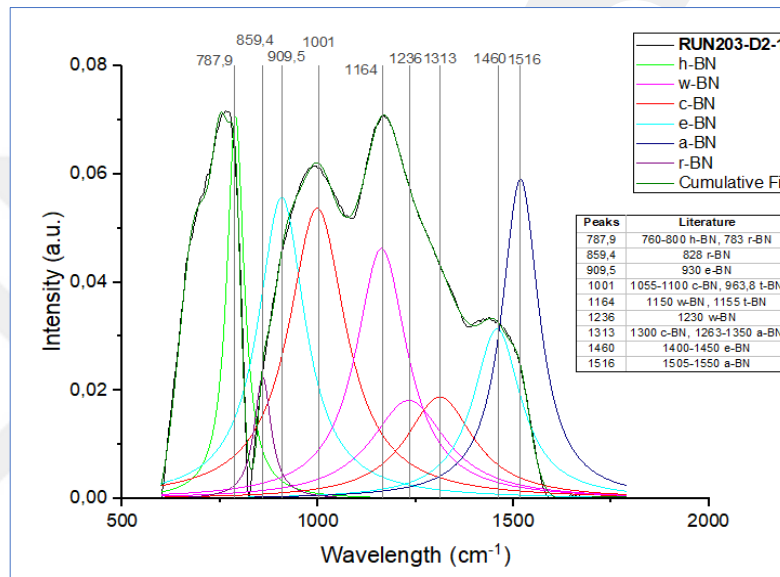


Figure 5.63 FTIR analysis of D2-1 in experiment Run 203 (TSD =100 mm)

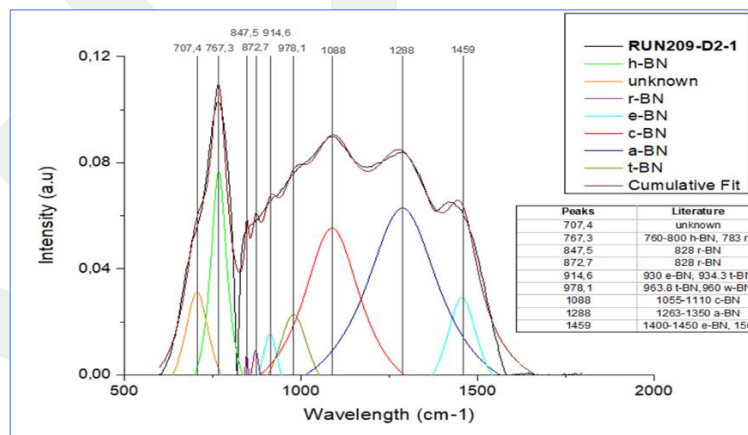


Figure 5.64 FTIR analysis of D2-1 in experiment Run 209 (TSD =50 mm)

The h-BN allotrope transforms into other phases like Turbostratic BN (t-BN), Rhombohedral BN (r-BN) Explosive boron nitride (e-BN) and Amorphous boron nitride (a-

BN). When comparing the result of four substrates, The closest substrate (D2-1) to the target plate-BN transforms to c-BN while this allotrope type doesn't available on the substrate (D2-4) when the T-S distance is 290 mm (The details of this experiment are in Appendix B).

For experiments (203 & 209) all the substrates have the same boundary condition, the difference is T-S distances. This indicates that the first transformation of the h-BN allotrope occurs in the vacuum and the last transformation occurs at the moment of collision of the BN particles with the sample. Two factors affect the collision, first the kinetic energy of BN particles, shortening the distance between the particles and substrate allowed it to keep its energy. The second is the electric energy of the substrate. The electric energy is affected by bias substrate voltage, power supply and the (T-S) distance. The couple's energy will change the h-BN allotrope. That means the coating thickness and allotrope is affected by the distance between the target - substrate and substrate energy.

FTIR analysis for substrate (D2-1) in experiment Run 217 is found, see Figure 5.65.

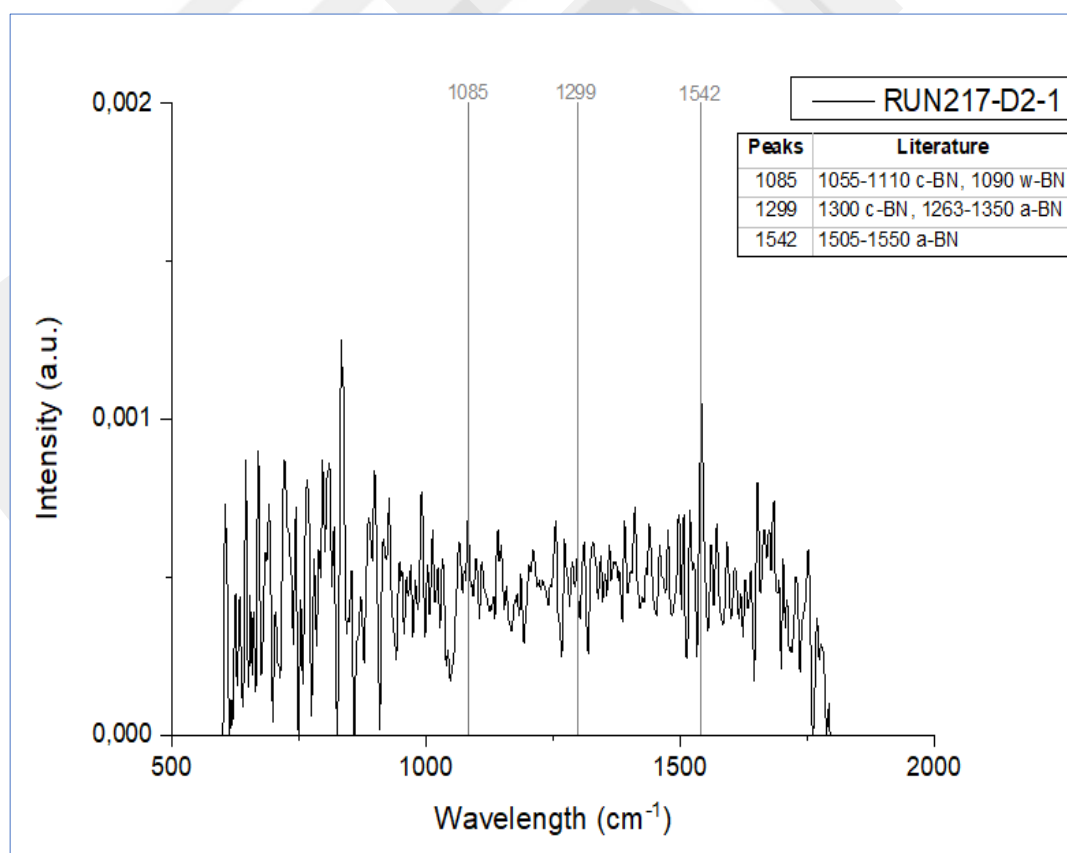


Figure 5.65 FTIR analysis of D2-1 in experiment Run 217 (TSD =50 mm)

5.5.2.2 Adhesion, Hardness and Friction Measurement Results for Run 203, Run 209 and Run 217

- **Run 203 & Run 209:** The BN coating quality was measured with the scratch test. Adhesion of BN coatings is measured by the Revetest® device. The BN-coated surface is tested by scratching it with a diamond tip at a constant speed. A Rockwell diamond tip with a radius of 200 μm was used for the scratch test. The Rockwell-type indenter creates a scratch on the sample's surface with increasing force. The load applied during the scratch test starts from 0.5 N and goes up to 150 N. The scratch length on the sample is 3mm, and the diamond tip advanced at a speed of 6mm/min as shown in Figure 5.66. The residual depth and penetration depth are measured during the test as shown in Figure 5.67. The result of adhesion measurement shows that the farthest substrate to the target plate (TSD is 290 mm) has the highest adhesion to the other. The scratch tip began to scratch out the coated surface at 58.43 N. The scratch tip began on the substrates when TSD are 50,100,200 and 230 mm are 23.76,19.2, 3.72 and 3.70 N respectively.

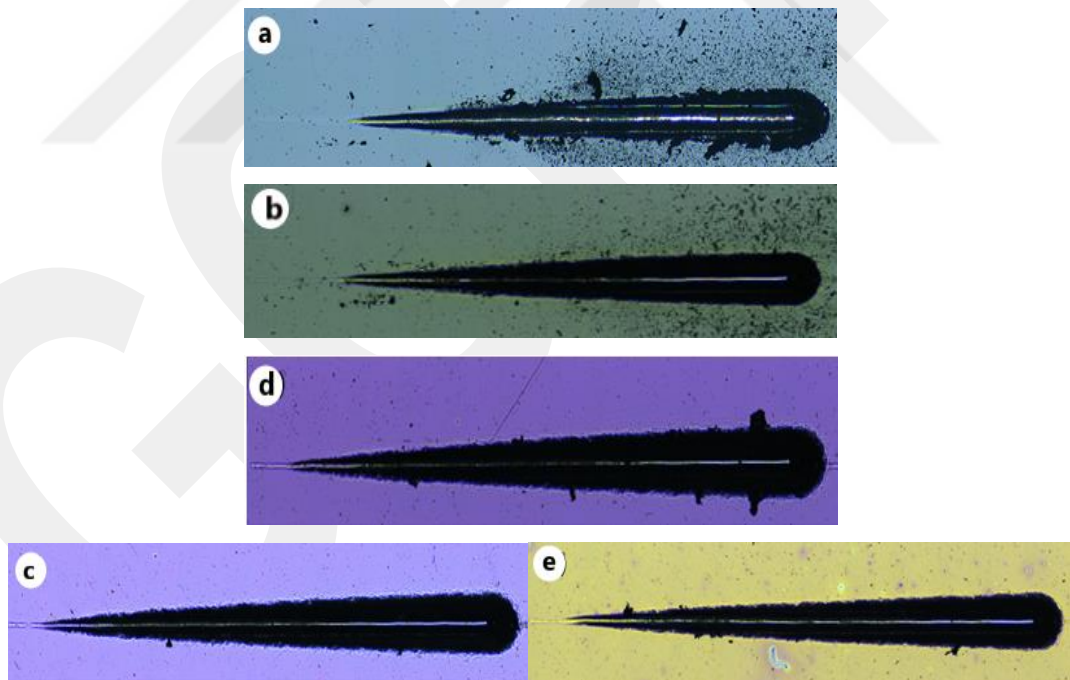


Figure 5.66 Image of Adhesion measurement for substrates as a function of TSD, a.50 mm,b.100 mm ,c.200 mm ,d.230 mm and e.290 mm for experiment 203 & 209.

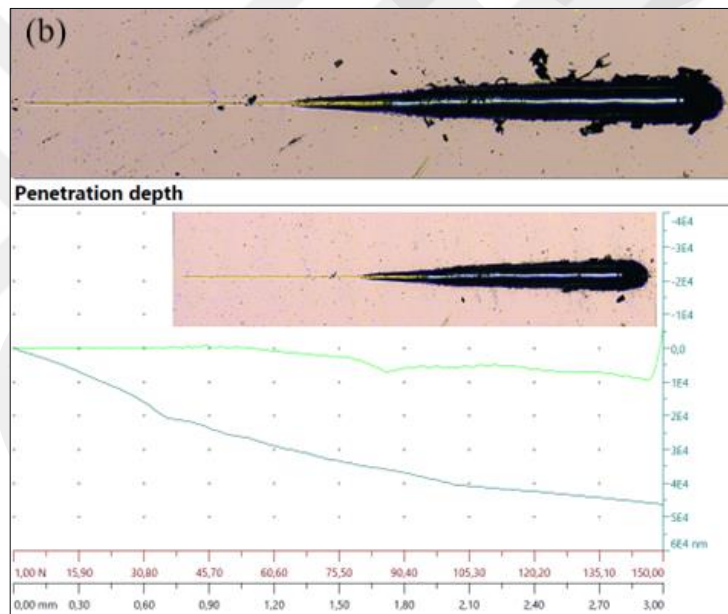
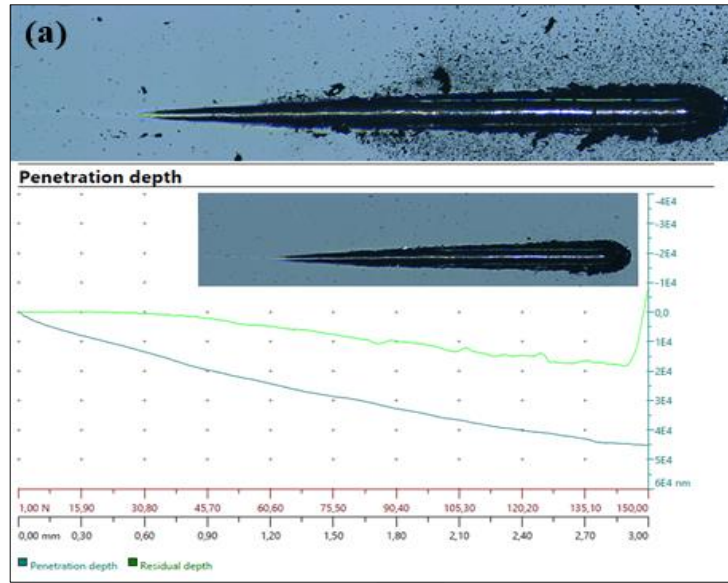


Figure 5.67 The scratch measurement, the residual depth and penetration depth of the substrates, a. TSD is 50 mm and b. TSD is 290 mm for the experiment (209).

Nano-Hardness measurements (NHM) were performed with the CSM Nano-Indentation Testing Device. The NHM shows that the farthest substrate from the target plate has the highest hardness as shown in Figure 5.68. The result of the average measurement of friction coefficient for substrates is very close to each other and it is (0.81-0.85).

- **Run 217:** The Adhison of substrate D2-1(TSD =50 mm) is increased to 75.55 N. The adhesion of substrate D2-3 (TSD=290 mm) is 52.15N.

The hardness measurement, when the applied force is 250 mN for substrates with TSD 50 and 290 mm is 8.5 and 9.8 GPa. The hardness measurement, when the applied force is 5 mN for substrates with TSD 50 and 290 mm is 9 and 11.2 GPa. The hardness of the BN coating increased compared with the previous experiments (Run 203 and Run 209) as shown in 5.68, but the thickness of the coating decreased. The thickness of the coating is < 50 nm.

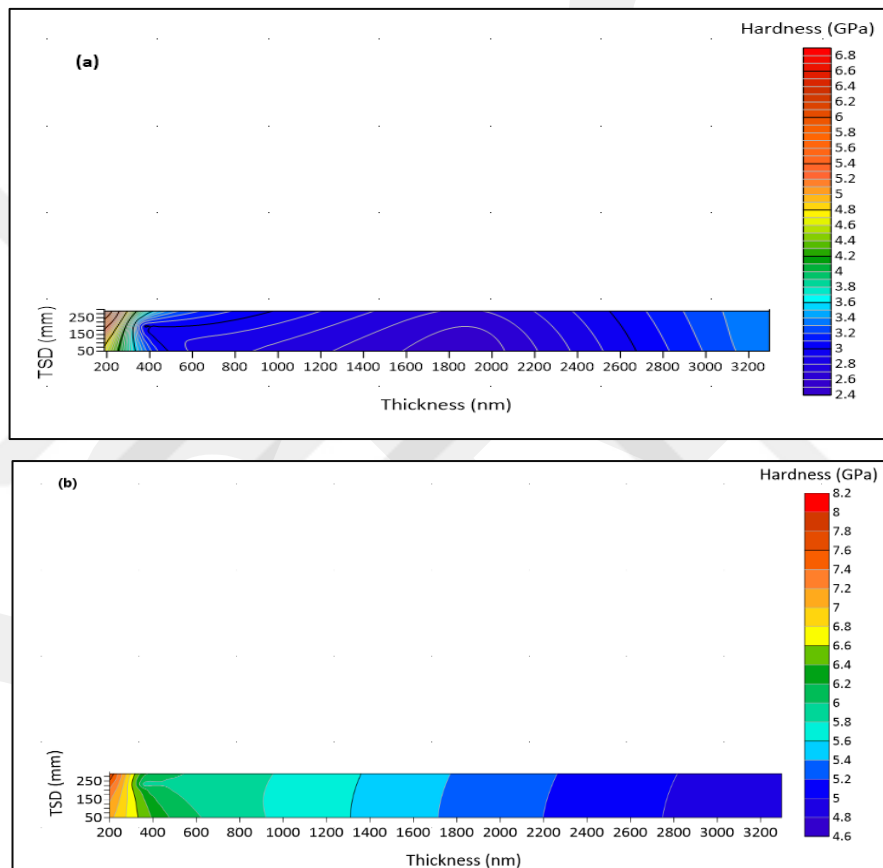


Figure 5.68 Result of hardness measurement (Run 203 & Run 209) as a function of TSD and thickness with different applied loads,(a) The applied load is 5 mN and (b) The applied load is 250 mN.

- **What is the progress?**

To find the advantages achieved from the new parameter that is applied in experiment Run 209, the result of our experiments will be compared with the result from the literature review. Hacaloğlu study, two groups of experiments classified as BN coating by Inductively Coupled Plasma (ICP) and without using ICP (reference experiment) [94], for the same bias substrate voltage but different boundary conditions, (different power supply, volumetric gas flow rate and TSD).

BN coating without using spindle mechanism, substrate voltage is 0 V. The power supply is 900 W. The volumetric gas flow rate ratio Ar/N₂ is 40/8 [94]. Compare with experiment Run 209, Decreasing the TSD, and increasing the volumetric flow rate of Ar and N₂ gases with power supply led to an increased deposition rate of coating (thickness of coating) and coating adhesion results. In both the reference experiment (without using ICP) and the 500W ICP power applied experiment, scratches started immediately. In the 1500W ICP power applied experiment, scratch started at almost 44N for 0V [94]. Increase the power supply effect on the BN phases and the hardness of the coating. The hardness in the reference experiment is 1.3 GPa when the applied load is 250 N and 0.6 GPa when the applied load is 5N While the hardness in experiment Run 209 is 4.8 and 3.4 GPa as shown in Table 5.16.

Table 5.16 Compares the characteristic of the BN coating experiment Run 209 with the experiment from a literature review [94]

			Hardness (GPa)	
Exp. literature	Exp. state	Thickness (nm)	250 mN	5 mN
	No ICP	3038.4	1.3	0.6
	500 W (ICP)	2177.1	3.1	1.3
	1500 W (ICP)	1551.3	5.4	3.4
Run 209	No ICP	3296.5	4.8	3.4

5.6 The Results

5.6.1 The Correlation of BN Coating Models and Experiments

Table 5.17 The boundary conditions and results of BN coating models and experiments.

The input parameters								The result (output)		
No.	Model Name	Sub.	T (°C)	P (Torr)	Magnetron	Substrate Voltage (v)	Time (hr)	Exp. Thickness (nm)	Model Thickness (nm)	Error %
1	Model-A1	1xD2	300	0.005	900w,40/8 sccm Ar/N ₂	0	6	861.0286	882.1252	2.4
2	Model-B1	1xD2	300	0.005	900w,40/8 sccm Ar/N ₂	100	6	699.93	746.7495	6.69
3	Model-C1	1xD2	300	0.005	900w,40/8 sccm Ar/N ₂	250	6	149.4073	150.3713	0.65
4	Model-A2	1xD2	300	0.005	1200w,40/8 sccm Ar/N ₂	0	6		1052.4365	
5	Model-A3	1xD2	300	0.005	1500w,40/8 sccm Ar/N ₂	0	6		986.9322	
6	Model-C2	1xD2	300	0.005	1200w,40/8 sccm Ar/N ₂	250	6		123.8182	
7	Model-C2	1xD2	300	0.005	1500w,40/8 sccm Ar/N ₂	250	6		121.2206	
F8	Model-D2	1xD2	300	0.005	900w,10/2 sccm Ar/N ₂	0	6		43.4512	
9	Model-D3	1xD2	300	0.005	900w,80/16 sccm Ar/N ₂	0	6		2200.9461	
10	Model-E	4xD2	300	0.005	900w,40/8 sccm Ar/N ₂	0	6		2166	
									938.9	
									232.3	
									0	
11	Model-E1	1xD2	300	0.005	900w,40/8 sccm Ar/N ₂	0	6		2149	
12	Model-F	1xD2	300	0.005	900w,40/8 sccm Ar/N ₂	0	6		917	
		1xAl							698.7	
		1xTi							855.9	
		1xTiN							1144.2	
		1xglass							751	
13	Model-G	1xD2	300	0.005	1200w,80/16 sccm Ar/N ₂	0	6		2498	
14	Model-G1	1xD2	300	0.005	1100w,80/16 sccm Ar/N ₂	0	6	1900.7	1840	3.19

Note: The distance between the target and substrate for all the models is 80 mm except model-E.

5.6.2 The Result of 2D Analysis of the BN Coating Model

From 2D -analysis of temperature and pressure, We note that the substrate bias voltage, power supply and gas volumetric flow rate affected temperature and pressure. These two parameters mostly play an important role in the first transformation of the h-BN phase in the chamber.

Table 5.18 2D field analysis of BN coating model

No	Model - Name	Magnetron conditions	Sub. Volt (V)	Ar-Density (g/m ³) Max/Min	N ₂ -Density (g/m ³) Max/Min	Ar-Flux (ng.m/h) Max/Min	N ₂ -Flux (ng.m/h) Max/Min	P (Pa)	T (K)
1	A1	900w,40/8 sccm Ar/N ₂	0	1.21e-5/8.6e-7	2.22e-6/1.59e-7	1.7e7/1.22e6	3.9e6/2.79e5	0.49/0.04	2687/191
2	A2	1200w,40/8 sccm Ar/N ₂	0	2.7e-7/7.9e-8	4.9e-8/2.4e-11	4.2e7/7.82e6	4.27e6/8.6e3	0.72/0.05	3689/262
3	A3	1500w,40/8 sccm Ar/N ₂	0	2.99e-7/7.23e-8	4.7e-8/0	3.36e7/5.38e5	3.17e6/0	0.49/0.05	3121/191
4	B1	900w,40/8 sccm Ar/N ₂	100	3.03e-7/7.3e-8	4.72e-8/5.82e-10	3.06e7/6.5e5	3.79e6/8.88e4	0.81/0.043	3548/314
5	C1	900w,40/8 sccm Ar/N ₂	250	3.03e-7/2.16e-8	5.26e-8/3.76e-9	3.47e7/2.48e6	3.91e6/2.79e5	0.56/0.046	3830/321
6	C2	1200w,40/8 sccm Ar/N ₂	250	2.92e-7/7.66e-8	5.10e-8/0	3.28e7/1.42e6	3.43e6/0	0.81/0.05	2482/543
7	C3	1500w,40/8 sccm Ar/N ₂	250	2.87e-7/7.65e-8	5.89e-8/0	2.92e7/7.16e5	3.49e6/0	0.61/0.06	4102/274
8	D2	900w,10/2 sccm Ar/N ₂	0	1.21e-7/3.27e-8	2.06e-8/0	9.14e6/6.67e4	7.72e5/0	0.099/0.007	1718/132
9	D3	900w,80/16 sccm Ar/N ₂	0	4.49e-7/1.27e-7	9.12e-8/9.99e-11	5.6e7/1.12e6	7.8e6/6.37e4	0.91/0.12	3200/241
10	E	900w,40/8 sccm Ar/N ₂	0	9.57e-7/8.06e-8	2e-8/8.7e-11	1.72e7/4.82e5	4.69e6/1.61e2	0.43/0.02	2426/40
11	E1	900w,40/8 sccm Ar/N ₂	0	1.31e-5/8.7e-7	2.42e-6/1.68e-7	1.9e7/1.42e6	4.1e6/2.88e5	0.49/0.05	2690/200
12	F	900w,40/8 sccm Ar/N ₂	0	1e-6/5e-8	6.6e-8/2.96e-10	2.33e7/4.02e5	1.77e6/3.83e4	0.42/0.06	2400/55
13	G	1200w, 80/16sccm Ar/N ₂	0	5.53e-7/1.27e-7	1.01e-7/7.35e-11	6.44e7/6.04e5	5.87e6/3.93e5	0.98/0.16	3850/238
14	G1	1100w, 80/16sccm Ar/N ₂	0	4.52e-7/1.15e-7	9.1 e-8/8.9e-11	5.33e7/5.03e5	5.67e6/3.53e5	0.95/0.15	3700/230

5.7 The Correlation between Input Parameters and the Coating Profile

The effect of substrate voltage, power supply, gas volumetric flow rate and distance between target and substrate (T-S) on the thickness of the coating is shown in Figures 5.69,5.70,5.71 and 5.72.

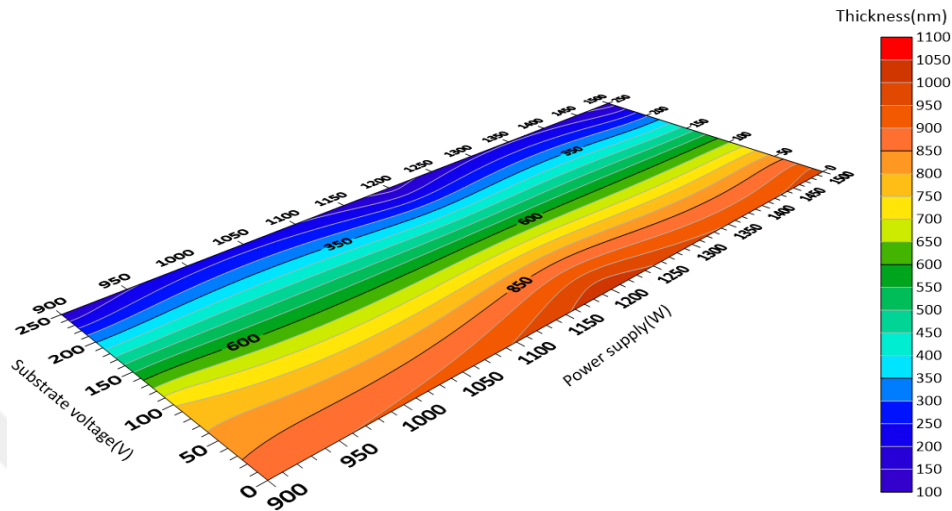


Figure 5.69 The effect of substrate voltage and power supply on the thickness of the coating. The Ar and N₂ flowrate is 40 and 8 sccm respectively.

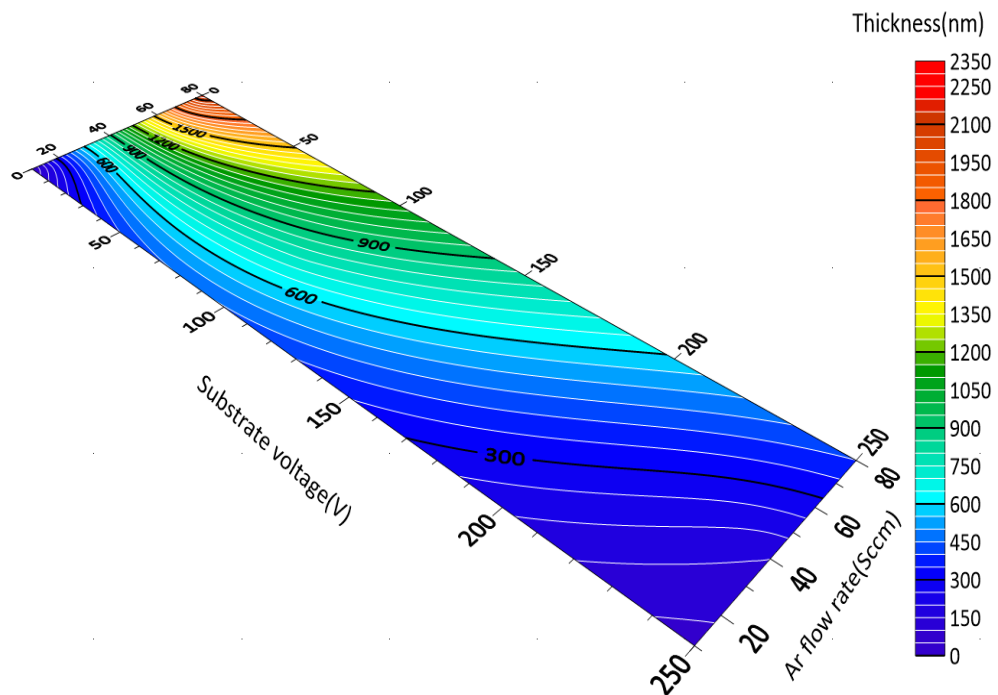


Figure 5.70 The effect of substrate voltage and gas flow rate on the thickness of the coating at the constant power supply, The power supply is 900W.

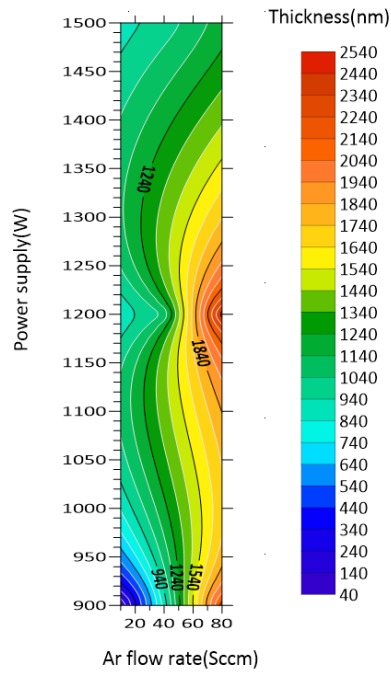


Figure 5.71 The effect of power supply and gas flow rate on the thickness of the BN coating in models at constant substrate bias voltage, The substrate bias voltage is 0V.

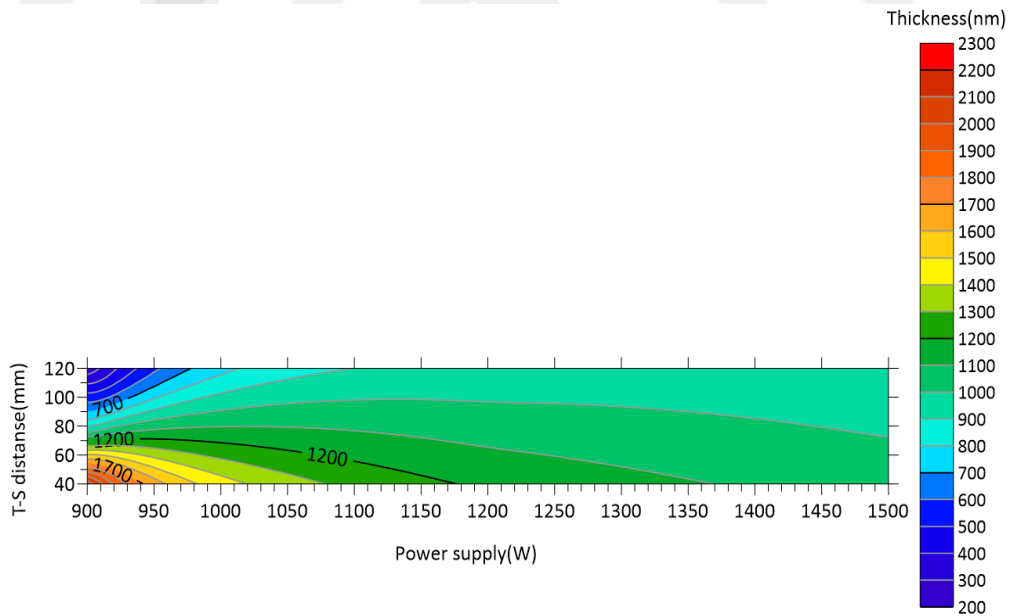


Figure 5.72 The effect of power supply and distance between target and substrate (T-S) on the thickness of the coating at constant substrate bias voltage, The bias voltage is 0V and Ar, N₂ flowrate is 40 and 8 sccm respectively.

5.8 The Correlation between Input Parameters and the pressure, Temperature of MS System

The effects of substrate voltage and power supply on the pressure and temperature in the chamber of the MS system are shown in Figure 5.73.

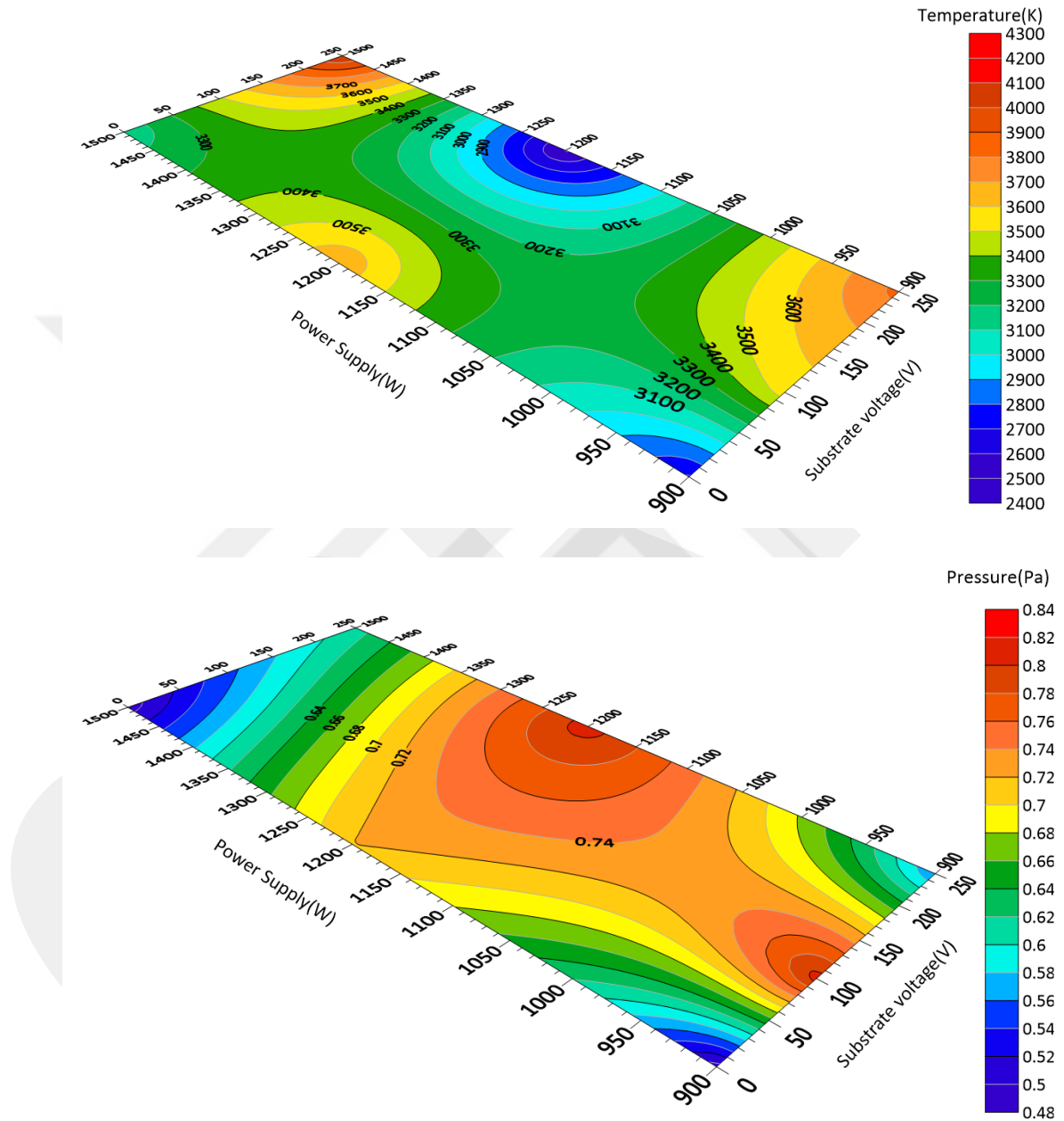


Figure 5.73 The effect of substrate bias voltage and power supply on the pressure and temperature of MS system at constant gas flow rate, The gas flow rate of Ar and N₂ are 40 and 8 sccm.

CHAPTER 6

THE STRUCTURE AND PROPERTIES OF BN ALLOTROPES

6.1 Introduction

To study the structure of BN coating and understand the correlation between BN phases, low-density phase (h-BN) and high-density phase (c-BN), CASTEP (Cambridge Serial Total Energy Package) software uses to understand the background of this correlation. CASTEP uses first-principles quantum mechanics computations. CASTEP uses Density Functional Theory (DFT) and plane-wave pseudopotential methods to investigate the characteristics of crystals and surfaces of semiconductors, ceramics, metals and minerals. Surface chemistry, structural properties, band structure, the density of states, and optical quality are all common applications.

One of the most successful and widely used methods of electronic structure calculations is DFT. DFT is a method for deriving the properties of condensed matter systems from fundamental principles by solving the many-electron Schrödinger equation. In DFT methods, the energy of the system is determined by the electron density instead of the wave function. The primary function of any DFT implementation is the ability to minimize the energy to obtain the electronic ground state of the system.

In this study, CASTEP software is used to calculate the structure and properties of the h-BN and c-BN phases. This chapter provided the necessary theoretical background for the DFT. In addition, the definition required to calculate the most important physical properties of the material is explained in detail.

6.2 Literature Review

Boron nitride (BN) nanoparticles have distinguished characteristics and the potential for usage in a wide range of technologies, among other materials. Among the many potential industries where BN has been effectively applied are photonics, aircraft, and medicine.

Using first-principles calculations within spin DFT, Xu et al. examined the electrical and magnetic characteristics of BN-doped graphene superlattices. The effects of the inserted BN nanodots' geometrical sizes and shapes were examined by the researchers. The BN nanodot's size affects the superlattice's band gap. An inversion symmetry between the valence and conduction bands concerning the Fermi level is seen when the B and N atoms in the BN nanodot are switched [95]. The cubic zincblende form or a brand-new wurtzite form can be immediately transformed from the hexagonal, graphite-like boron nitride under static high pressures. It seems that a catalyst is not necessary. The wurtzite form is favoured at low temperatures, below 300 K, while the zincblende form is chosen at high temperatures, between 2500 and 4000 K. The lowest pressure necessary for the conversions is roughly 115 kbar; somewhat greater pressures on the order of 130 kbar are sufficient for temperatures above and below 2000 K. The dense phase crystallites, despite being small, provide effective x-ray diffraction patterns that can be exploited to determine their crystal structures [96].

Grimsditch as well as others, Brillouin scattering has been used to determine the single-crystal cubic boron nitride's three independent elastic stiffness constants C_{ij} , which are $c_{11}=820$, $c_{12}=190$, and $c_{44}=480$ GPa. The resulting bulk modulus, 400 GPa, from two independent estimations based on x-ray measurements in a diamond anvil cell is reasonably consistent. A value of $dB/dP=3.0$ is found to be the best fit for the x-ray results using the bulk modulus [97].

Cai et al. use the first-principle method to compute the surface energies of the primary phases in the Li-N-B synthesis system to clarify the process for producing cubic boron nitride (c-BN) with catalysts under high pressure and temperature.

Density functional theory is used to calculate the surface energy of low-index surfaces made of lithium boron nitride (Li_3BN_2), c-BN, and hBN at 1700 K and 5.0 GPa, respectively. The surface energies of the major low-index surfaces of cBN are $(111) > (001) > (110)$, those of hBN are $(1010) > (1120) > (0001)$, and those of Li_3BN_2 are

(100) > (110) > (0001) [98]. To evaluate the possibility of using boron nitride (BN) nanoflake for a SO₂ gas capture technique concerning environmental problems with gas pollution, density functional theory (DFT) simulations were made. To do this, a typical model of a hydrogen-capped B₁₂N₁₂ coronene-like surface was taken into consideration. To create the S@BN model and the O@BN model, two beginning positions for SO₂ gas were chosen: first perpendicularly positioning the S side of SO₂ towards the BN surface, then once more placing the O side of SO₂ perpendicular to the BN surface to create the O@BN model. The findings suggested that disregarding the beginning position, the SO₂ molecule's most advantageous sites were strangely parallel to the BN surface. In this instance, the gas molecule was nearly in the centre of the surface, indicating that the surface had the right size for the molecular adsorption process [99].

A first-principle approach based on DFT has been used to analyse the surface energy of the low-index surfaces of cubic boron nitride (c-BN) and hexagonal boron nitride (h-BN), to demonstrate the transition mechanism of c-BN single crystal under high temperature and high pressure (HTHP). Under 1800 K and 5.5 GPa, the surface energies of the h-BN (110), (100), and (0001) facets and the c-BN (110), (100), and (111) facets, respectively, are calculated using the GGA to be 0.200 eV, 0.427 eV, 0.336 eV and 0.210 eV, 0.430 eV, and 0.410 eV.

The surface energy values of the hBN and c-BN facets are, respectively, 0.221 eV, 0.444 eV, 0.354 eV, and 0.250 eV, 0.436 eV, 0.475 eV under 2000 K and 6.0 GPa.

The lattice plane of (100) in hBN is parallel to the plane (100) of cBN, and the relative difference in surface energies between the two facets at 1800 K, 5.5 GPa, and 2000 K, 6.0 GPa, respectively, is only 0.7% and 1.2%. According to the Modified Thomas-Fermi-Dirac (TFDC) electron theory, the direct transition of hBN into c-BN can be induced. Based on the surface energy of hBN and cBN, this implies that c-BN is most likely to be changed by hBN under HTHP [100].

KÖKTEN and others, the energetics and structural features of hexagonal boron nitride sheets doped with silicon and phosphorus were investigated using simulations based on density functional theory. The dopant atoms were substituted as an impurity in the system at either the B or N sites in a neutral charge state. The study, investigation into the effects of cell size on calculated parameters including bond length, charge transfer,

and defect formation energies was extensive. It was found that when silicon or phosphorus atoms are substituted, link lengths increase in comparison to the original sheets [101].

Stagi et al. describe the correlations between structure and defects [102].

According to calculations by Kim et al., the existence of a vacancy defect, which results in a geometric distortion in the hexagonal lattice structure, can affect the electronic structure of monolayer h-BN [103].

DFT is used by Bernardi et al. to explain the characteristics of the electronic energy gap and optical absorption spectra of carbon-boron nitride monolayers [104].

According to He et al., the super hard boron nitride phase known as Z-BN was examined within the context of the DFT using first-principles calculations as a potential intermediate phase between h-BN and zinc-phase BN (c-BN).

The research demonstrates that Z-BN is a transparent insulator with an indirect band gap of approximately 5.27 eV, strong structural stability, and high density equivalent to c-BN. Unexpectedly, it has a Vickers hardness of 55.88 GPa. Because of its low transition pressure point of 3.3 GPa, this new BN phase can be produced experimentally by cold-compressing h-BN [105].

He et al. investigated the structural stability, electronic structure, and optical properties of BN-doped black phosphorescent material systems at various concentrations using a generalized DFT approach. It was discovered that the BN-doped black phosphorescent material was more stable than the B and N atom-doped materials. The structural stability of the system decreases gradually as the doping concentration increases, and the structure with a doping concentration of 25% is the most stable [106].

DFT was utilized by Khan et al. to thoroughly examine the borophene/boron nitride (B / BN) interface and discover a new anode material for lithium-ion batteries (LIB). With a large charge capacity and a low energy barrier, borophenes make good two-dimensional (2D) anode materials, although they are unstable when employed alone. According to the study's findings, the borophene layer's thermal and mechanical stability is greatly increased by properly preparing the interface with the boron nitride substrate. Furthermore, Li diffusion at the interface has a low energy barrier, according to Nudge Elastic Band (NEB) simulations. A B/BN interface is a great option for LIB anode materials because of these advantages [107]. Khan et al. used DFT to analyses

the borophene/boron nitride (B / BN) interaction in detail and find a new anode material for lithium-ion batteries (LIB). Although they are unstable when used alone, borophenes make good two-dimensional (2D) anode materials due to their high charge capacity and low energy barrier. The results of the study show that by appropriately preparing the interface with the boron nitride substrate, the thermal and mechanical stability of the borophene layer is significantly improved. Nudge Elastic Band (NEB) simulations also show that the energy barrier for Li diffusion at the contact is minimal. These benefits make the B/BN interface a fantastic choice for LIB anode materials [107].

DFT was used to examine the dopamine (DPM) adsorption behaviour on BN nanostructures in the gas and solvent phases. According to our findings, the DPM adsorption on the BN nanocage is more powerful than that on other BN nanotubes.

The discoveries so far have been predicted to help adsorb DPM and produce new hybrid molecules [108].

A new pulsed laser annealing (PLA) method was used to grow boron nitride (BN) films with varying proportions of cubic phase content on a (0001) sapphire substrate. A hexagonal boron nitride (h-BN) target is ablated with a pulsed KrF laser ($\lambda = 248$ nm) during a pulsed laser deposition process, followed by a pulsed laser, to synthesize cubic boron nitride (c-BN). The Annie ring (PLA) was used. ($\lambda = 193$ nm) ArF laser. The study discovered that laser power density can modulate c-BN phase content during PLA processing.

As the bulk phase content increased, the optical bandgap of the produced BN films increased, resulting in a correlation between the optical bandgap in the film and the c-BN phase content [109].

The binding and electrical properties of covalent functionalization of $B_{12}N_{12}$ and $B_{16}N_{16}$ clusters with 5-aminolevulinic acid medicines were studied by Soltani et al. using DFT simulations. With the help of the B3LYP technique, they discovered that 5-AVA (NH_2 group) was drug-loaded and could covalently bind to $B_{12}N_{12}$ and $B_{16}N_{16}$ nanoclusters with roughly comparable binding energies of 2.01 and 1.95 eV, respectively. In comparison to the B3PW91 and PBE techniques, the outcome is entirely different. The functionalization of the 5-AVA medicines on the $B_{12}N_{12}$ and $B_{16}N_{16}$ clusters demonstrates their significant impact on the electronic characteristics of the adsorbent. It is

anticipated that BN cluster-containing 5-aminolevulinic acid (5-AVA) pharmaceuticals will be used in biomedical devices and medication delivery systems [110].

Beheshtiana et al. looked at the characteristics of chemically altered BNNT with sulfamide molecules using B3LYP and PBE functionals. Sulfamide was found to diffuse into the tube wall and release an NH_3 molecule.

According to the B3LYP functional, this process releases around 10.4 kcal/mol of energy, with a 4.8 to 10.5% change in the tube's energy gap. Additionally, a modest reduction in the work function may facilitate the emission of field electrons from the BNNT surface. Sulfamide's chemical modification of BNNTs causes very minimal modifications to their electrical characteristics, making it an effective way to clean these tubes [111].

Korkmaza and others, a semiconductor vacuum against point defects, hexagonal boron nitride (h-BN) enable a stable and predictable spin state at ambient temperature.

It is suitable for applications in quantum engineering because of this.

For defining those features, first-principles techniques are a crucial instrument.

The removal of either the void type B atom (VB), the void type N atom (VN), or both the B atom and the N atom (DV) results in three different types of vacancies.

Researchers are interested in hybrid graphene and hexagonal boron nitride (C-BN) nanostructures because of their complementing electronic characteristics [112].

In contrast to hexagonal boron nitride (h-BN), which has a huge band gap, graphene is a semiconductor with a zero band gap. A hybrid zigzag graphene atomic chain doped with boron nitride and a zigzag boron nitride atomic chain doped with carbon pairs were both studied by Thakur et al. for their structural, electrical, and mechanical properties. While ZGRBN has an indirect band gap, ZBNGR has a zero band gap. Through the use of strain and an outside electric field, the second hybrid's band gap is adjusted and converted to metal. During chain compression, it is discovered that the first hybrid uses more braking energy. The significance of hybrid atomic chains in device applications is highlighted by these investigations [113].

often et al. investigate the structural and electronic properties for both unrelaxed and relaxed cases of oxygen-doped cBN(110) surface by DFT calculations. The oxygen atom has been substituted in a neutral charge state on both the B site (OB) and the N

site (ON). Defect formation energies, [unrelaxed (E_{of}) and relaxed (E_f)], and relaxation energies, E_r , have been calculated. It has been found that substitution ON is more probable, moreover, the ON causes an inward relaxation of the first neighbour surface B atom [114].

The majority of theoretical model research is focused on h-BN, c-BN, and w-BN, while some works explore the interaction between h-BN and c-BN, according to the literature survey.

Two theoretical models suggest that hBN is more stable than cBN: generalized gradient approximation and local density approximation calculations [115–117].

Under HTHP circumstances, the research focuses on the conversion of h-BN to c-BN. More research is required because there is no literature addressing the conversion of h-BN to c-BN at high temperatures and high vacuum pressure.

At 1800 K, 5.5 GPa, and 2000 K, 6.0 GPa, respectively, it is discovered that the relative surface energy difference between the lattice plane of (100) in h-BN and plane (100) in c-BN is only 0.7% and 1.2% [100].

It has been suggested that the DFT method's inherent flaws become crucial for the small energy variations in the BN system.

The additional research covers the topics of doped BN, flaws, and BN characteristics, as given in Table 6.1.

Table 6.1 The condensed theoretical modelling investigations of BN by DFT

Subject	Details of study
Doped BN	<p>The significance of geometrical size and shape in the research of BN-doped graphene superlattice [95], Si and P-doped h-BN sheets [101], Using a density generalized theory approach based on the first principles, the structural stability, electronic structure, and optical characteristics of BN-doped black phosphorene systems at different concentrations were investigated [106]. Additionally, the structural, electronic, and mechanical properties of hybrid zigzag graphene atomic chains with boron nitride doped and zigzag boron nitride atomic chains with carbon pairs doped were investigated [113].</p> <p>An oxygen-doped cBN(110) surface was examined for its structural and electrical characteristics in both its relaxed and unrelaxed states using density functional theory computations [114].</p>
Transformation of BN phase	<p>The wurtzite form is favoured at low temperatures, below 300 K, whereas the zinblende form is preferred at high temperatures, between approximately 2500 and 4000 K. Both forms regularly coexist. The minimal pressure needed for the changes is around 115 kbar at 2000 K [96]. A first-principle approach based on density functional theory has been used to examine the surface energy of the low-index surfaces of cubic boron nitride (c-BN) and hexagonal boron nitride (h-BN) to demonstrate the transition mechanism of a c-BN single crystal under high temperature and high pressure (HTHP) [100]. Tuning optoelectronic characteristics by converting h-BN to c-BN [109]. Transform the intermediate phase of boron nitride known as h-BN into the superhard Z-BN phase. Transform h-BN intermediate phase between h-BN and zinc blende BN, a superhard boron nitride phase known as Z-BN is proposed (c-BN) [105]</p>
BN properties	<p>Elastic constants of cubic boron nitride are measured[97].</p> <p>Explain the characteristics of the optical absorption spectrum and electronic energy gap of carbon-boron nitride (CBN) monolayers using DFT [104]. DFT calculations were used to examine the dopamine (DPM) adsorption behaviours on the BN nanostructures in the gas and solvent phases [108], as well as the electronic and optical characteristics of BN nanoclusters functionalized with 5-AVA. It is anticipated that BN cluster-containing 5-aminolevulinic acid (5-AVA) drugs will be used in biomedical devices and medication delivery systems [109].</p>
Application	<p>Studies on the borophene/boron nitride interface for use as an electrode [107] and the potential use of boron nitride (BN) nanoflake for a SO₂ gas capture approach with environmental difficulties with gas pollution [98] have been conducted.</p>
Defect	<p>The relationships between defects and structure [102].</p> <p>The hexagonal lattice structure of monolayer h-BN may deform geometrically as a result of the presence of a vacancy defect, according to simulations in a report[103]. The boron nitride hexagonal (h-BN) structural defect [112].</p>

6.3 Schrödinger Equation

The eigenvalue problem was one of the most significant issues in quantum chemistry when the renowned Schrödinger equation was established in 1926.

For (N-body) systems, the time-independent Schrödinger equation can be written as follows:

$$\hat{H}\Psi = E\Psi \quad (6.1)$$

Where \hat{H} is Hamiltonian energy, Ψ is the wave function (N-body) and E is the total energy of the system.

$$\hat{H} = -\sum_i \frac{\hbar}{2m_e} \nabla_i^2 - \sum_k \frac{\hbar}{2m_k} \nabla_k^2 - \sum_i \sum_k \frac{e^2 Z_k}{r_{ik}} + \sum_{i<j} \frac{e^2}{r_{ij}} + \sum_{k<l} \frac{e^2 Z_k Z_l}{r_{kl}} \quad (6.2)$$

$$\hbar = \frac{h}{2\pi}, \text{ Where } \hbar \text{ is reduced plank constant} \quad (6.3)$$

m_e : is the electron mass, m_k : is the nuclei mass, e is the electron charge, Z is the number of atomic, r is the distance, (i,j) is electron indices and (k,l) are nuclei indices.

The system's overall energy comes from five sources. The kinetic energy of the electron and the nuclei are the first two terms. The three further terms are the attraction between the electron and the electron, the nuclei - nuclei, and the electron with the nuclei. For N-body systems, the Schrödinger equation cannot be precisely solved.

Only approximations will work to solve the equation.

The Born-Oppenheimer (BO) approximation can be utilized to reduce the complexity of the issue. The ability to discriminate between a molecule's electronic and nuclear motions is a prerequisite for the BO approximation. Nuclei-electronic motion coupling is mostly ignored by the BO approximation. Atomic nuclei can be thought of as stationary since they move far more slowly than electrons do in a chemical environment. The electronic Schrödinger equation can be stated in the following way after the BO approximation:

$$(\hat{H}_{el} + V_N)\Psi_{el} = E_{el}\Psi_{el} \quad (6.4)$$

$$\hat{H}_{el} = -\sum_i \frac{\hbar}{2m_e} \nabla_i^2 - \sum_i \sum_k \frac{e^2 Z_k}{r_{ik}} + \sum_{i<j} \frac{e^2}{r_{ij}} \quad (6.5)$$

Where V_N is a constant for nuclear-nuclear repulsion energy, (Ψ_{el}) is the electronic wave function, \hat{H}_{el} and E_{el} the electronic Hamiltonian operator and electronic energy, respectively.

The system's total energy can be calculated from Equation (6.4) by adding the electronic energy and the constant nuclear-nuclear repulsion energy [118].

6.4 Hohenberg- Kohn Theorems

The relationship between electron density and the energy with electronic characteristics of atoms and molecules was established by Pierre Hohenberg and Walter Kohn in 1964. The work of Hohenberg and Kohn served as the forerunner of density functional theory DFT as we know it today [119].

- According to Hohenberg and Kohn, there is a distinct ground-state electron density for every external potential.
- By minimizing the density function relating to the density of electrons, energy can be obtained.

6.5 Kohn–Sham Method

Since around fifty years ago, the Kohn-Sham approach has been applied to solid-state physics. The method has grown in favour among physicists and chemists along with the development of more precise density functionals, particularly because it frequently enables accurate treatments of molecular systems that are not possible with more conventional quantum mechanical techniques [120, 121]. Calculating the ground-state energy requires knowledge of the ground-state density.

It was proposed by Kohn and Sham in 1965 [122] that it is possible to substitute an effective Hamiltonian of non-interacting particles in an effective external potential for the original system's Hamiltonian, producing the same ground-state density [123, 124].

$$E_{KS}[\rho] = T_{KS}[\rho] + \int dr V_{ext}(r)\rho(r) + E_H[\rho] + E_{xc}[\rho] \quad (6.6)$$

Here, T_{KS} is the kinetic energy of the non-interacting system., E_{xc} the exchange-correlation. E_H is the Hartree functional, which describes the electron-electron interaction using the Hartree-Fock method, and it is given by

$$E_H[\rho] = \frac{1}{2} \iint \frac{\rho(r)\rho(r')}{|r-r'|} dr dr' \quad (6.7)$$

The difference is referred to as the exchange-correlation, E_{xc} .

(E_{int}) is an approximated version of the internal interaction of the electrons. Therefore, the differences between the exact and approximate solutions for the kinetic energy, and electron-electron interaction terms were represented via (E_{xc}) which is expressed by:

$$E_{xc}[\rho] = (E_{int}[\rho] - E_H[\rho]) + (T[\rho] - T_{KS}[\rho]) \quad (6.8)$$

In light of this, if the exchange-correlation (E_{xc}) is precisely known beforehand, the Kohn-Sham method could be a potent tool for obtaining an exact ground-state density. The local density approximation (LDA), which is illustrated in Equation 6.9, is one method for analyzing the exchange-correlation function [125].

$$E_{xc}^{LDA} = \int d^3r n(\vec{r}) E_{xc}^{hom}(n(\vec{r})) \quad (6.9)$$

Although LDA assumes density as a constant, there are specific situations when this approximation is incorrect and density change must be taken into account. The extended gradient approximation is another way to the exchange-correlation function (GGA).

GGA depends on the density gradient ($f(n(r), \nabla(n(r)))$) given by equation (6.10).

$$E_{xc}^{GGA} = \int d^3r f(n(\vec{r}), \nabla(n(\vec{r}))) \quad (6.10)$$

Different GGA approaches, such as Perdew-Burke-Ernzerhof (PBE) [127], Perdew-Wang (PW91) [126], and others, accept different values of $f(n(r), \nabla(n(r)))$.

The most used approximations for exchange-correlation functions are LDA and GGA. The LDA + U or GGA + U approach is another choice. Based on an LDA or GGA function type, it has additional parameters to support orbit-dependent interactions. For highly restricted orbitals like d and f, interaction parameters are crucial.

In comparison to the LDA and GGA parameters, the U parameter is better. The association function is yet another function utilized in DFT computations.

The Hartree-Fock term density function is included in the hybrid function, which is orbit-dependent. More than LDA or GGA, the coupling function predicts the excitation energy. One of the most common hybrid functions is B3LYP [128].

6.6 Pseudopotentials

The nucleus and all electronic interactions are included in the DFT calculation. To make the issue more manageable, a pseudopotential method was developed, which ignores the strong Coulomb interaction with the nucleus and the effects of the core electrons in favour of the effective potential operating on the valence electrons.

Due to the modest contribution of core electrons to a material's energy and the overwhelming contribution of valence electrons, pseudopotential approaches have little impact on the accuracy of DFT calculations. The concept behind pseudopotential approaches is the scattering of electrons from the nucleus. Valence electrons are additionally drawn to the nucleus. The valence electron's wavefunction must be orthogonal to the nucleus' wavefunction of the nucleus.

DFT computations were performed using pseudopotential techniques including Norm conserving [129], Ultrasoft [130], and Projector Augmented Wave (PAW) [131]. In all-electron calculations, normalized norm-conserving pseudopotentials yield the same results.

The pseudopotential that upholds the standard, however, is not particularly smooth, and an extremely soft pseudopotential with a smooth function is another pseudopotential technique. Ultra-soft pseudopotentials also provide accurate results. The PAW method has a smaller cut-off radius than the ultrasoft pseudopotential. The DFT calculation is self-consistent. Before we can get any other information, we first need to predict the density. The Kohn-Sham equation can be solved using this density to determine the density and energy of the ground state.

A density is used to determine potential energy. If the initial estimates match the observed densities, the calculation is complete. If the initial estimates do not match the achievement density, a new estimate is created and the previous steps are repeated. electron density.

6.7 Crystal Structure

Atoms are arranged in the periodic table to create crystals. As a result, the crystal has periodic physical characteristics and is translationally invariant. According to the lattice vectors a , b , and c with the angles, between these vectors, seven crystal systems were produced, including the cubic, trigonal, hexagonal, tetragonal, orthorhombic, monoclinic, and triclinic crystal systems [132], as given in Table 6.2. In experimental literature research and on numerous websites, such as the Bilbao Crystallographic Server [132] and the Materials Project [133], the crystal structure of a material can be found. Additionally, the crystals' visualisation was created using the VESTA program.

Table 6.2 The crystal systems, lattice vectors and the lattice angles

crystal systems	lattice vectors	lattice angles
Triclinic	$a \neq b \neq c$	$\alpha \neq \gamma \neq \beta$
Monoclinic	$a \neq b \neq c$	$\alpha = \gamma = 90^\circ \neq \beta$
Orthorhombic	$a \neq b \neq c$	$\alpha = \gamma = \beta = 90^\circ$
Tetragonal	$a = b \neq c$	$\alpha = \gamma = \beta = 90^\circ$
Cubic	$a = b = c$	$\alpha = \gamma = \beta = 90^\circ$
Trigonal	$a = b = c$	$\alpha = \gamma = \beta < 120^\circ, \neq 90^\circ$
Hexagonal	$a = b \neq c$	$\alpha = \beta = 90^\circ, \gamma = 120^\circ$

6.8 Band Theory

It was believed that the energy of electrons may provide details about the characteristics of solids. The energy of each electron in an atom has been determined using free-electron models. This model disregards the exchange and correlation properties of electrons and treats them as non-interacting particles. Although this model works well for metals, it is unable to account for semiconductors' magnetic, superconducting, optical, and electronic capabilities. After that, we must think of a model that can account for these traits more effectively. Equation (6.11) states that electrons can be thought of as existing in a periodic potential, which is created by nuclei and other electrons.

$$\begin{aligned}
 V(\vec{r}) &= V(\vec{r} + \vec{r}_n) \\
 \vec{r}_n &= n_1 \vec{a} + n_2 \vec{b} + n_3 \vec{c}
 \end{aligned}
 \tag{6.11}$$

$\vec{r} \cdot \vec{n}$ is the arbitrary translation vector with $n_1, n_2,$ and n_3 being integers. a, b and c are lattice vectors. The Schrödinger equation with the periodic potential yields, the wavefunctions as plane waves:

$$\begin{aligned}\psi_k(\vec{r}) &= u_k(\vec{r})e^{i\vec{k} \cdot \vec{r}} \\ u_k(\vec{r}) &= u_k(\vec{r} + \vec{r}_n)\end{aligned}\tag{6.12}$$

Bloch's theorem, which describes this periodic potential and the plane-wave solution, is also known as the Bloch state of electrons. The reciprocal lattice can be used to obtain this periodicity as well. Concerning the reciprocal lattice vector \vec{G} , the periodic potential generates the following energy eigenvalues for the Bloch state:

$$E(\vec{k}) = E(\vec{k} + \vec{G})\tag{6.13}$$

The solid electron band structure is an energy band formed by these energy values. For electronic band structures, knowing the k value is sufficient. Some bands are vacant while others are filled with electrons. The band gap is the energy differential between the lowest vacant level and the highest occupied level. The substance is referred to as an insulator if the band gap is substantial. Electrons can flow from the occupied band to the empty band in semiconductors because the band gap is lower than that of the insulator. Consider simply the first Brillouin zone for semiconductors

In semiconductors, the conduction band is the unoccupied band while the valence band is the occupied band. Metal does not distinguish between bands that are occupied and those that are not. The metal's electrical conductivity is the result of the ability of electrons to move from the occupied to the unoccupied band.

The intersection of the occupied and unoccupied bands is known as the Fermi level.

The density of states (DOS) is one more way to visualize band structure.

The percentage of states that a system must assume for each energy is represented by its (DOS).

6.9 Mechanical Properties

Elastic constants (C_{ij}) could be determined to evaluate a crystal's bonding style, ductility, and mechanical stability. For each technical application, understanding a material's mechanical and dynamic behaviour based on its elastic constants is crucial.

These constants provide details regarding the material's stiffness, hardness, and stability. A desirable quality to assure a crystal's durability in any application is its mechanical stability against outside forces. The stress-strain method [135] and the volume-conserving method [134] were both employed to calculate single-crystal parameters. In comparison to the volume-conserving strategy, the stress-strain approach converges more quickly.

Elastic constants are abbreviated as C_{ij} , these elastic constants must satisfy the well-known Born stability requirements [136–138] for a combination to be mechanically stable. Table 6.3 lists the Born stability criteria for the BN crystal phases.

Table 6.3 Criteria of Born stability for various crystal phases

Crystal phase	Stability criteria
Orthorhombic	$C_{ii} > 0, \dots \text{where } (i = 1, 2, \dots, 6)$ $C_{11} + C_{22} - 2C_{12} > 0$ $C_{11} + C_{33} - 2C_{13} > 0$ $C_{22} + C_{33} - 2C_{23} > 0$ $[C_{11} + C_{22} + 2(C_{12} + C_{13} + C_{23})] > 0$
Tetragonal	$C_{ii} > 0, \dots \text{where } (i = 1, 3, 4, 6)$ $C_{11} - C_{12} > 0$ $C_{11} - 2C_{13} + C_{33} > 0$ $2C_{11} + 2C_{12} + 4C_{13} + C_{33} > 0$
Hexagonal & Rhombohedral	$C_{11} > C_{12} $ $2C_{13}^2 < C_{33}(C_{11} + C_{12})$ $C_{44} > 0; C_{66} > 0$ $C_{66} = (C_{11} - C_{12}) / 2$
Cubic	$C_{11} > 0$ $C_{12} > 0$ $C_{44} > 0$ $C_{12} > C_{44}$ $C_{11} + 2C_{12} > 0$ $C_{11} - C_{12} > 0$

The mechanical properties such as bulk modulus (B), shear modulus (G), Young's modulus (E), and B/G can be calculated using these elastic constants. Hardness (Hv), Poisson's ratio (ν), and Pugh's modulus can all be calculated [139].

The bulk and shear modulus are calculated using the Voigt-Reuss-Hill approximations. The Reuss bound is the lower limit of the moduli under the assumption of uniform stress, while the Voigt bound is the upper limit of the moduli under the assumption of uniform strain throughout the crystal. The Hill approximation is frequently employed to generate reliable estimates of the elastic parameters for polycrystalline materials. Poisson's ratio (ν) and Pugh's modulus (G/B) (the latter of which was created by Chen et al. [140]) can be used to determine the brittleness or ductility of a material. If the $G/B > 0.5$ indicates brittleness, otherwise, the material is assumed to be ductile [141,142]. Frantsevich's rule states that $\nu = 0.33$ is the critical value of the Poisson's ratio, with higher values denoting ductility and lower values denoting brittleness [143]. To identify the bonding type of the investigated materials, the G/B ratio and Poisson's ratio (ν) have also been determined. The material has a predominance of covalent bonding if the G/B ratio is approximately 1.1 [139].

A G/B ratio of about 0.6 indicates that ionic bonding predominates in the material [139].

If the normal value is 0.25 for ionic materials and roughly 0.1 for covalent materials. The details of calculated bulk moduli (B), shear moduli (G), Young's moduli (E), Poisson's ratio (ν), Pugh's modulus (G/B) and Vickers hardness (HV) are listed below:

The bulk and shear moduli of the hexagonal phase are:

$$B_V = \frac{2C_{11} + C_{12} + 4C_{13} + C_{33}}{9} \quad (6.14)$$

$$G_V = \frac{C_{11} + C_{12} + 2C_{33} - 4C_{13} + 12C_{44} + 12C_{66}}{30} \quad (6.15)$$

$$B_R = \frac{C_{11} + C_{12} + 2C_{33} - 2C_{13}^2}{C_{11} + C_{12} + 2C_{33} - 4C_{13}} \quad (6.16)$$

$$G_R = \frac{5[C_{11} + C_{12} + 2C_{33} - 2C_{13}^2]C_{44}C_{66}}{6B_V C_{44}C_{66} + 2C_{11} + C_{12} + 2C_{33} - 2C_{13}C_{44} + C_{66}} \quad (6.17)$$

The bulk and shear moduli of the cubic phase are:

$$B_V = \frac{C_{11} + 2C_{12}}{3} \quad (6.18)$$

$$G_V = \frac{C_{11} - C_{12} + 3C_{44}}{5} \quad (6.19)$$

$$B_R = B_v \quad (6.20)$$

$$G_R = \frac{5C_{11} - C_{12}C_{44}}{4C_{44} + 3C_{11} - C_{12}} \quad (6.21)$$

The B and G values were calculated by taking the average of the B_v (Voigt), B_R (Reuss), and G_v values, as well as the G_R values.

$$B = \frac{B_R + B_v}{2} \quad (6.22)$$

$$G = \frac{G_R + G_v}{2} \quad (6.23)$$

Young's modulus can be calculated using Equation (6.24) for all crystal structures.

$$E = \frac{9GB}{G + 3B} \quad (6.24)$$

Another polycrystalline property, Poisson's ratio (ν) and Pugh's modulus:

$$\nu = \frac{1}{2} \left[\frac{(B - \frac{2}{3}G)}{(B + \frac{2}{3}G)} \right] \quad (6.25)$$

$$\text{Pugh's modulus} = B / G \quad (6.26)$$

The hardness (H_v) is calculated from [144]:

$$H_v = 2(K^2 G)^{0.585} - 3 \quad (6.27)$$

$$K = \frac{G}{B}$$

6.10 Calculations of the h-BN Structure and Properties

6.10.1 Build crystals structure of h-BN

To create the h-BN structure, some adjustment was needed. The crystal group is 194 P63/MMC. The lattice lengths are 2.516, 2.516 and 7.258 Å. The angles' degree is $\alpha = \beta = 90$ and $\gamma = 120$, Then the atoms of B and N were added to the structure as shown in Figure 6.1.

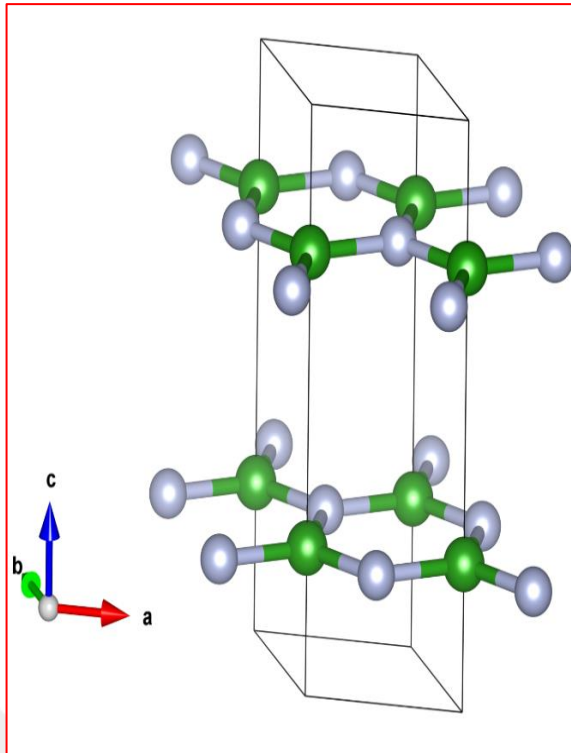


Figure 6.1 The crystal structure of h-BN, The grey atoms (N) and the green atoms (B).

6.10.2 Geometry Optimization

With the use of the geometry optimization assignment, a three-dimensional periodic system's geometry can be improved to produce a stable structure.

The interaction between electrons and ions was described by the norm-conserving pseudopotential. The contact, exchange, and correlation potentials were described using the Perdew-Burke-Ernzerhof (PBE) function with generalized gradient approximation (GGA). To establish the appropriate cut-off energy and K-point, we do numerous tests. The energy cut-off is 800 eV, and the K-point is set at 18x18 x 6. The algorithm Broyden-Fletcher-Goldfarb-Shannon (BFGS) is used in geometry optimization and properties calculation.

6.10.3 Elastic Constants

Elastic constants (C_{ij}) could be determined to indicate the bonding style, ductility (or brittleness), and mechanical stability of a crystal. The tensor of elastic constants can be obtained using elastic calculations, which offer all the essential data.

After complete geometry optimization, this calculation will be sent.

The findings of the stress-strain approach used to determine the elastic constants are shown in Table 6.4. Compounds meet the Born stability criterion for mechanical stability, as inferred from Table 6.4 [136]. The mechanical properties, including bulk modulus (B), shear modulus (G), Young's modulus (E), Poisson's ratio (ν), and hardness (Hv), have been calculated using these elastic constants and are shown in table 5. The listed results in Table 5 are compared with studies in the literature on the elastic properties of h-BN.

Table 6.4 The elastic constant (C_{ij}) (GPa) of h-BN

C_{11}	C_{33}	C_{44}	C_{12}	C_{13}	C_{66}
637.67	48.25	0.394	117.62	-34.94	260.03

Check the stability of the elastic constant. For the Hexagonal crystal system:

$$C_{11} > |C_{12}|$$

$$2C_{13}^2 < C_{33}(C_{11} + C_{12})$$

$$C_{44} > 0; C_{66} > 0$$

$$C_{66} = (C_{11} - C_{12}) / 2$$

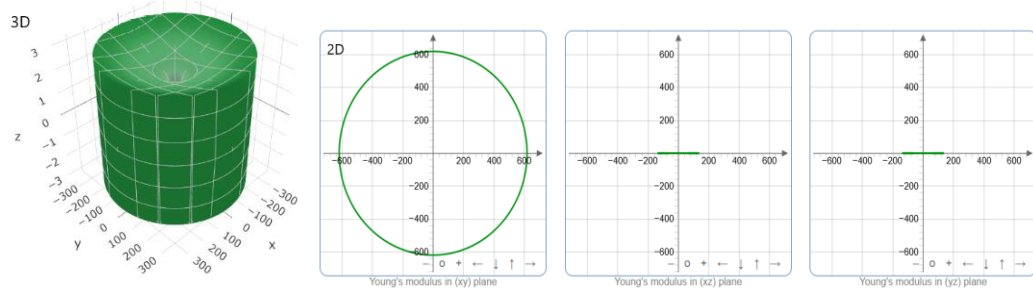
Table 6.5 Calculation of bulk modulus (B), shear modulus (G), Young's modulus (E), and Poisson's ratio (ν) for h-BN

Scheme	(B) Bulk modulus (GPa)	(G) Shear modulus (GPa)	(Y) Young modulus (GPa)	(ν) Poisson ratio
Voigt	146.95	130.7	302.59	0.156
Ruess	-48.69	0.98	2.98	0.512
Hill	49.12	65.88	136.59	0.334
Exp.	37 [52]			
DFT [53]	102.76	74.43	179.86	0.20829

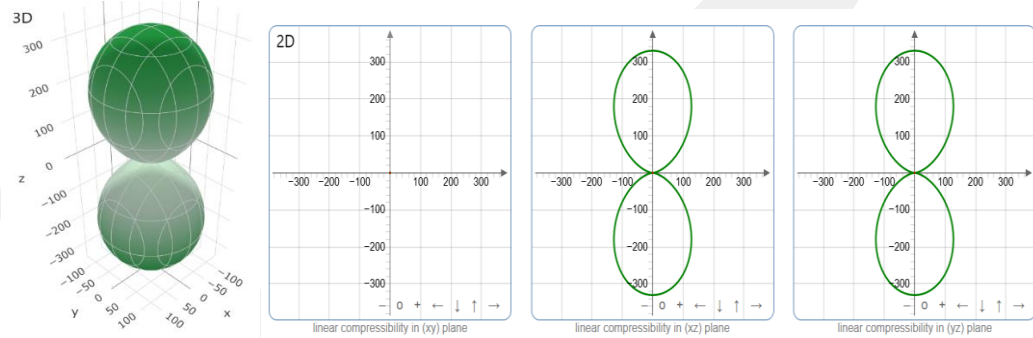
The B/G ratio could be used to determine the bonding type of the materials. Pugh's modulus= $B/G=0.74 > 0.5$ indicating the h- has covalent bonding dominantly.

Two-dimensional (2D) and three-dimensional (3D) visualizations illustrate the anisotropic elastic characteristics of h-BN. To calculate the direction-dependent Young's modulus, linear compressibility, shear modulus, and Poisson's ratio, the elastic constants were used in the ELATE program [147]. Figure 6.2 illustrates the results for the h-BN molecule.

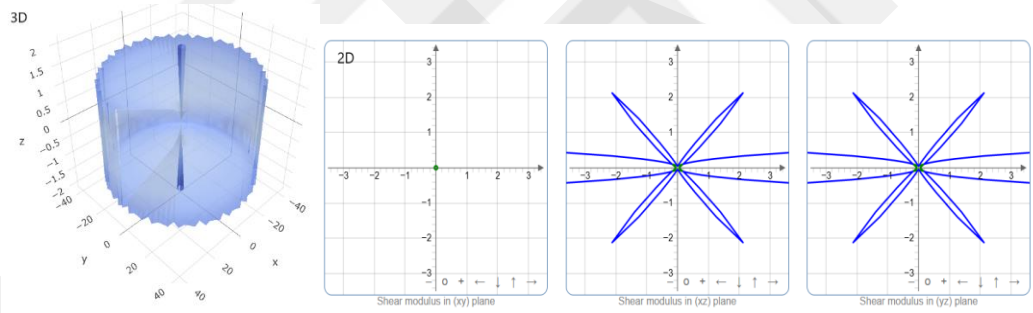
(a) Young's modulus



(b) linear compressibility



(c) Shear modulus



(d) Poisson's ratio

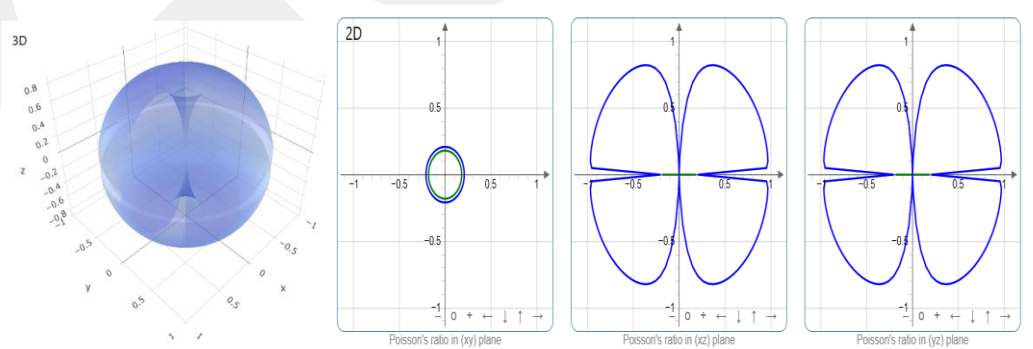


Figure 6.2 Direction-dependent of (h-BN) (a) Young modulus, (b) linear compressibility, (c) Shear modulus, and (d) Poisson's ratio

6.10.4 Electronic Properties

- **Band structures** are crucial properties of semiconductor materials since they dictate the majority of the electrical and optical capabilities that make these materials valuable in technology. The function type is GGA with (PBE). The calculation results are shown in Figure 6.3. The evaluated band gap is 4.461 eV, indicating that this is a semiconductor material with a wide bandgap. The experimental determination of the h-BN band gap is 5 eV [103].

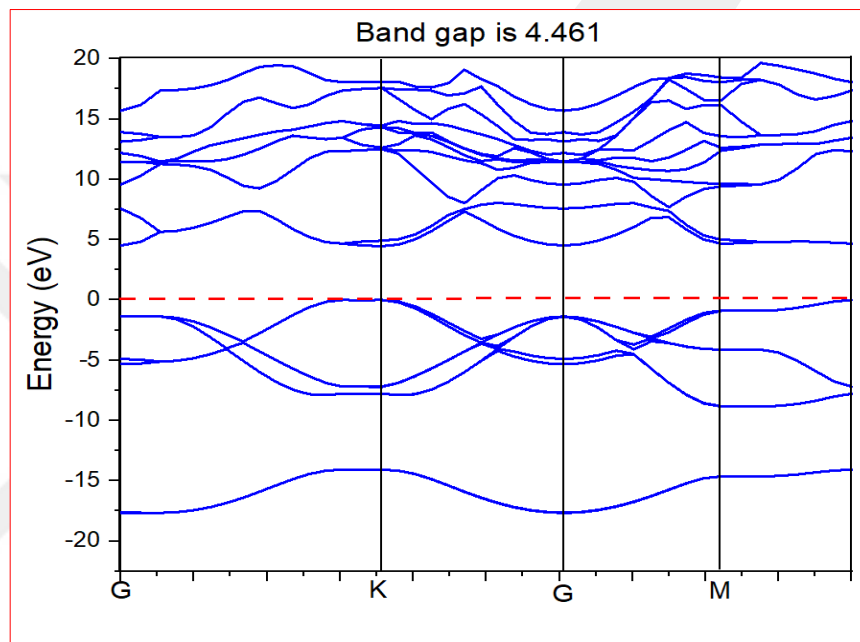


Figure 6.3 Calculation of band structures

- **The Density of States (DOS):** The electronic properties of the structures were also analysed using the density of states (DOS), as shown in Figure 6.4, which reflects the number of electronic states accessible for occupancy per energy level.

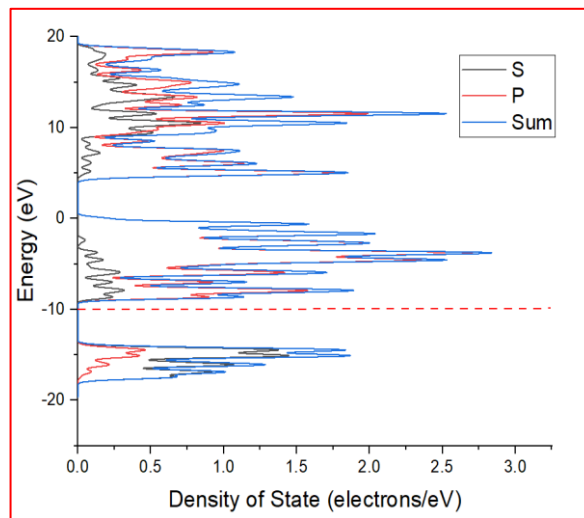


Figure 6.4 Calculated Density of State of h-BN

6.10.5 Optical properties

The dielectric constant, which represents a compound's ability to hold an electrical charge, is one of its most important optical properties.

Real and imaginary components make up the complex dielectric function. The imaginary component refers to energy absorption in a material, whereas the real component refers to the compound's ability to hold an electric charge.

Knowing the energy dependence of these components can help predict the behaviour of a material when it is exposed to a given light. BN was subjected to DFT simulations to disclose its varied optical characteristics [148-149].

The spectra of dielectric function components ($\varepsilon = \varepsilon_{real} + \varepsilon_{image}$) were displayed in the (0 -25) eV range as shown in Figure 6.5.

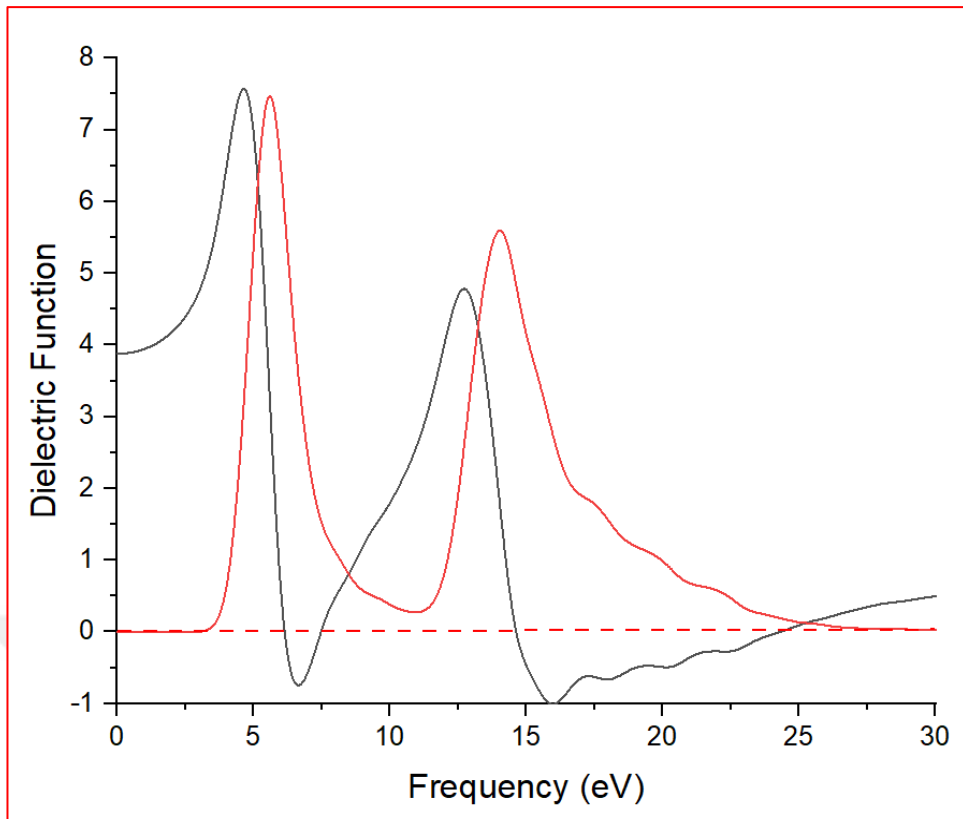


Figure 6.5 Calculation of dielectric function of h-BN, (real and imaginary components)

6.10.6 Phonons

The significance of the phonon of lattice dynamics is illustrated by the large number of physical properties that can be clarified utilizing phonons: infrared, Raman, and neutron phonons. The calculation result is shown in Figures 6.6 and 6.7.

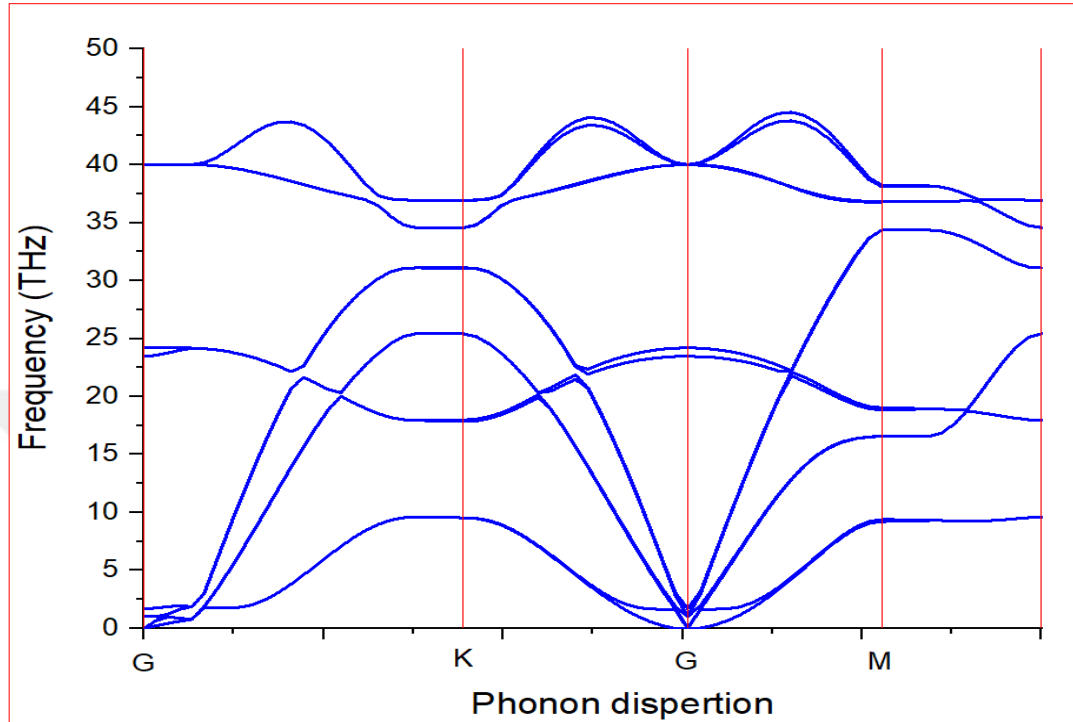


Figure 6.6 Phonon of h-BN

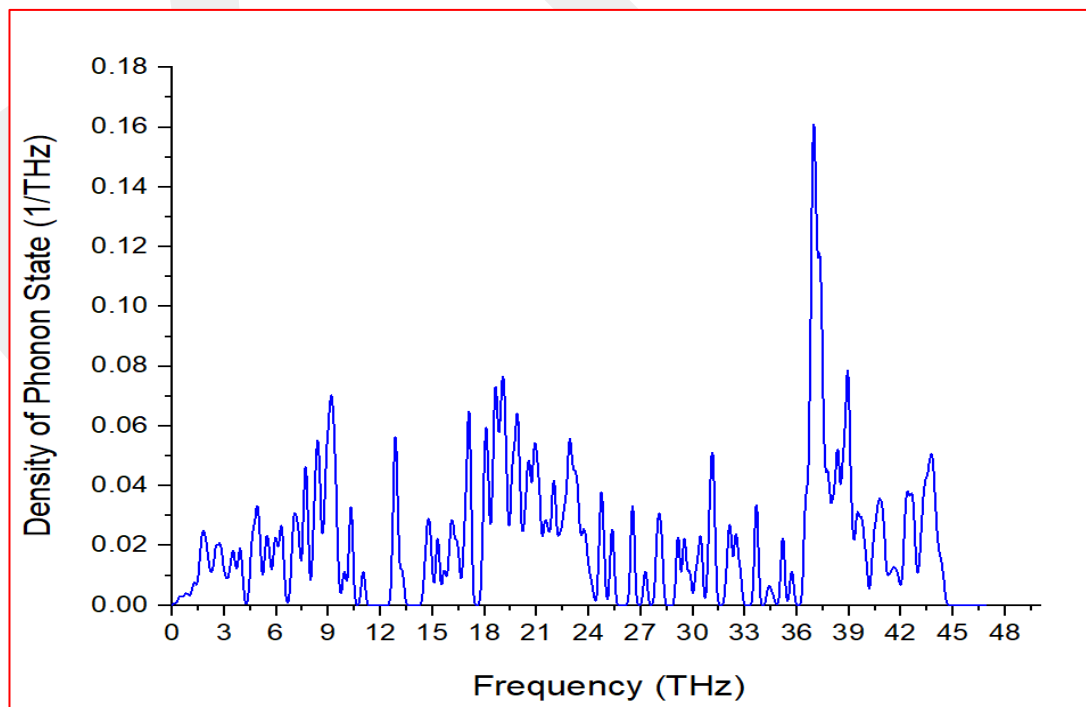


Figure 6.7 Density of Phonon State of h-BN

6.11 Calculations of The c-BN Structure and Properties

6.11.1 Build crystals structure of c-BN

To create the c-BN structure, some adjustment was needed. The crystal group is 216 F43m and the lattice type is cubic. The lattice lengths are $a=b=c= 3.631 \text{ \AA}$. The angles' degree is $\alpha = \beta = \gamma = 90$. Then the atoms of B and N were added to the structure as shown in Figure 6.8.

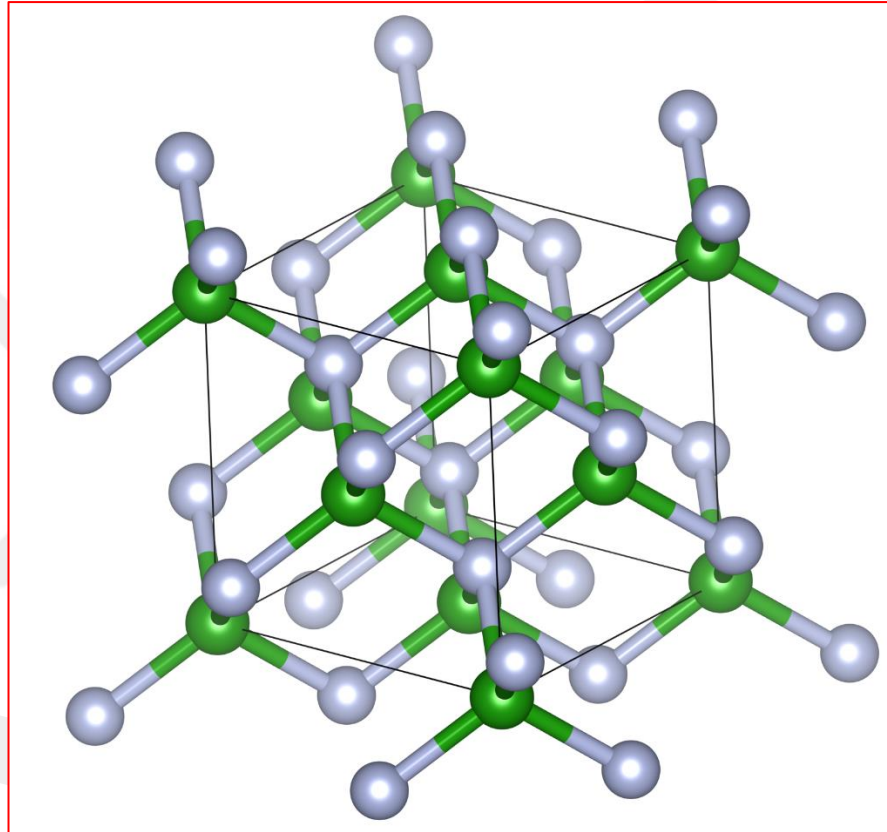


Figure 6.8 The crystal structure of c-BN, The grey atoms (N) and the green atoms (B).

6.11.2 Geometry Optimization

With the use of the Geometry Optimization assignment, a three-dimensional periodic system's geometry can be improved to produce a stable structure.

The interaction between electrons and ions was described by the norm-conserving pseudopotential. The contact, exchange, and correlation potentials were described using the Perdew-Burke-Ernzerhof (PBE) function with generalised gradient approximation (GGA). The energy cut-off is 550 eV, and the K-point is set at 8x8 x8.

Geometry optimization and property calculation both use the Broyden-Fletcher-Goldfarb-Shannon (BFGS) algorithm.

6.11.3 Elastic Constants

The tensor of elastic constants can be obtained using elastic calculations, which offer all the essential data. After complete geometry optimization, this calculation will be submitted. Table 6.6 displays the outcome of the elastic constant.

The measurements are made using Brillouin scattering, and the three independent elastic stiffness constants C_{ij} of single-crystal cubic boron nitride have been measured [97]. The findings are compared to the Grimsditch investigation.

The mechanical properties, including bulk modulus (B), shear modulus (G), Young's modulus (E), Poisson's ratio (ν), and hardness (Hv), have been calculated using these elastic constants and are shown in table 6.7.

Table 6.6 The elastic constant (C_{ij}) (GPa) of c-BN

Reference	C_{11}	C_{12}	C_{44}
This study	759.14	142.88	432.76
Exp. [4]	820	190	480

Check the stability of the elastic constant. For the Cubic crystal system:

$$C_{11} - C_{12} > 0$$

$$C_{11} + 2C_{12} > 0$$

$$C_{44} > 0$$

c-BN satisfies all of the mechanical stability criteria, indicating their elastic stability.

Table 6.7 Calculation of bulk modulus (B), shear modulus (G), Young's modulus (E), and Poisson's ratio (ν) for c-BN

Ref.	Scheme	(B) Bulk modulus (GPa)	(G) Shear modulus (GPa)	(Y) Young modulus (GPa)	(ν) Poisson ratio
This study	Voigt	348.29	382.91	840.65	0.0977
	Ruess	348.29	372.49	823.80	0.10580
	Hill	348.29	377.70	832.26	0.10175
Exp.		400 [97]			

B/G ratio and Poisson's ratio could be used to determine the brittleness or ductility of the material and determine the bonding type of the materials.

Pugh's modulus= $B/G = 0.92 > 0.5$ and Poisson's ratio is $0.10 < 0.33$ indicating

the c-BN is a brittleness material and has covalent bonding dominantly.

The hardness (H) is calculated from:

$$H_v = 2(K^2G)^{0.585} - 3$$

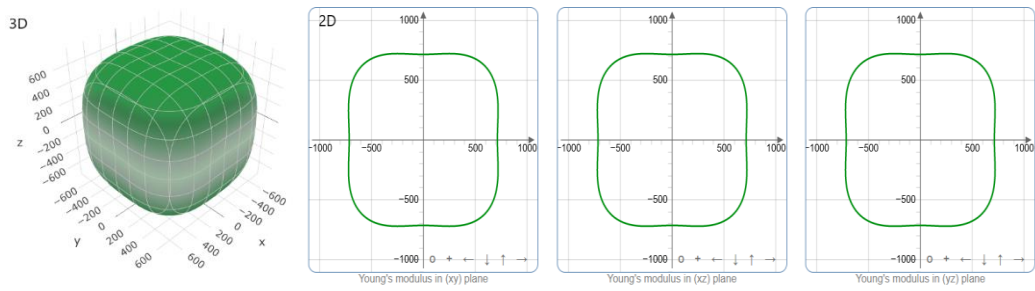
$$K = \frac{G}{B}$$

$$H=67.77 \text{ GPa}$$

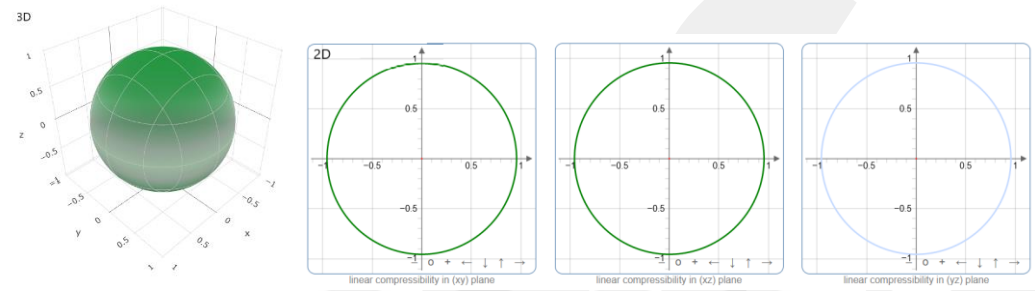
In both 2D and 3D, the anisotropic elastic characteristics of c-BN have been seen.

The ELATE programme [54] has been used to get direction-dependent young's modulus, linear compressibility, shear modulus, and Poisson's ratio using the estimated elastic constants. Figure 6.9 shows the outcomes for the h-BN molecule.

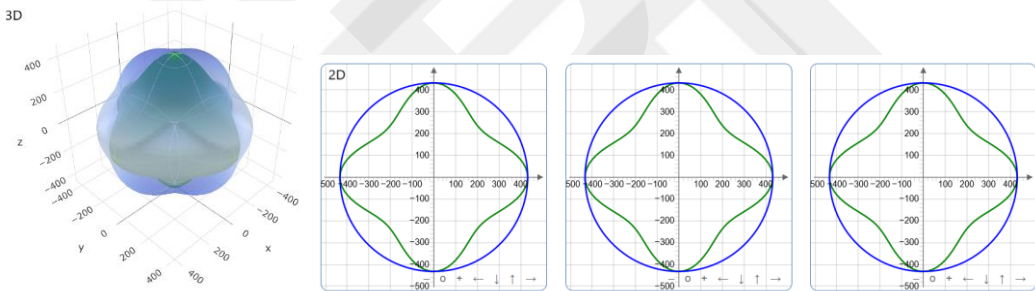
(a) Young's modulus



(b) linear compressibility



(c) Shear modulus



(d) Poisson's ratio

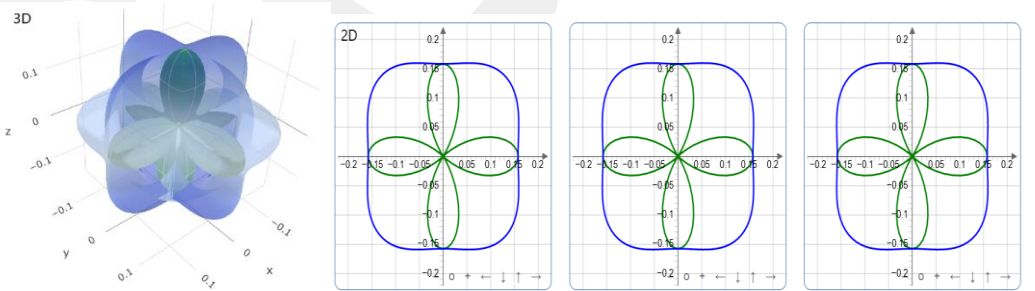


Figure 6.9 Direction-dependent of (c-BN) (a) Young modulus, (b) linear compressibility, (c) Shear modulus, and (d) Poisson's ratio

6.11.4 Electronic Properties of (c-BN)

Band structures and Density of States (DOS): Two exchange-correlation functions are used to calculate band structure and DOS. The function types are GGA and hybrid (HSE06). The GGA with the density gradient (PBE) method is applied. The calculation results are shown in Figures 6.10 and 6.11. The evaluated band gap is 4.517 and 6.546 eV. Experimentally determined values of band gap for c-BN is 6.4 eV [150]. From the CASTEP calculation, the best result is by the HSE06 function.

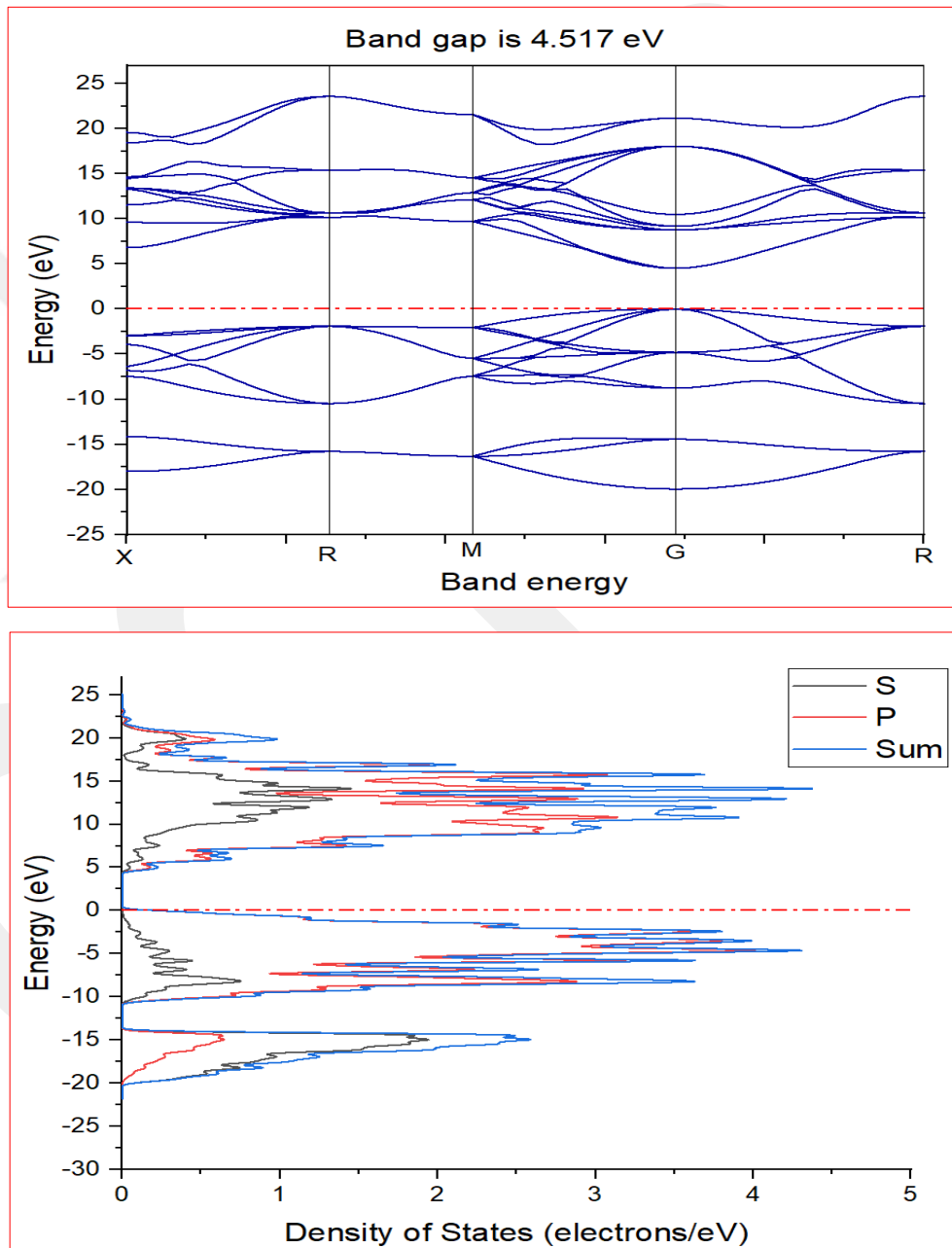


Figure 6.10 Calculation of (c-BN) band structures and density of state by GGA functional

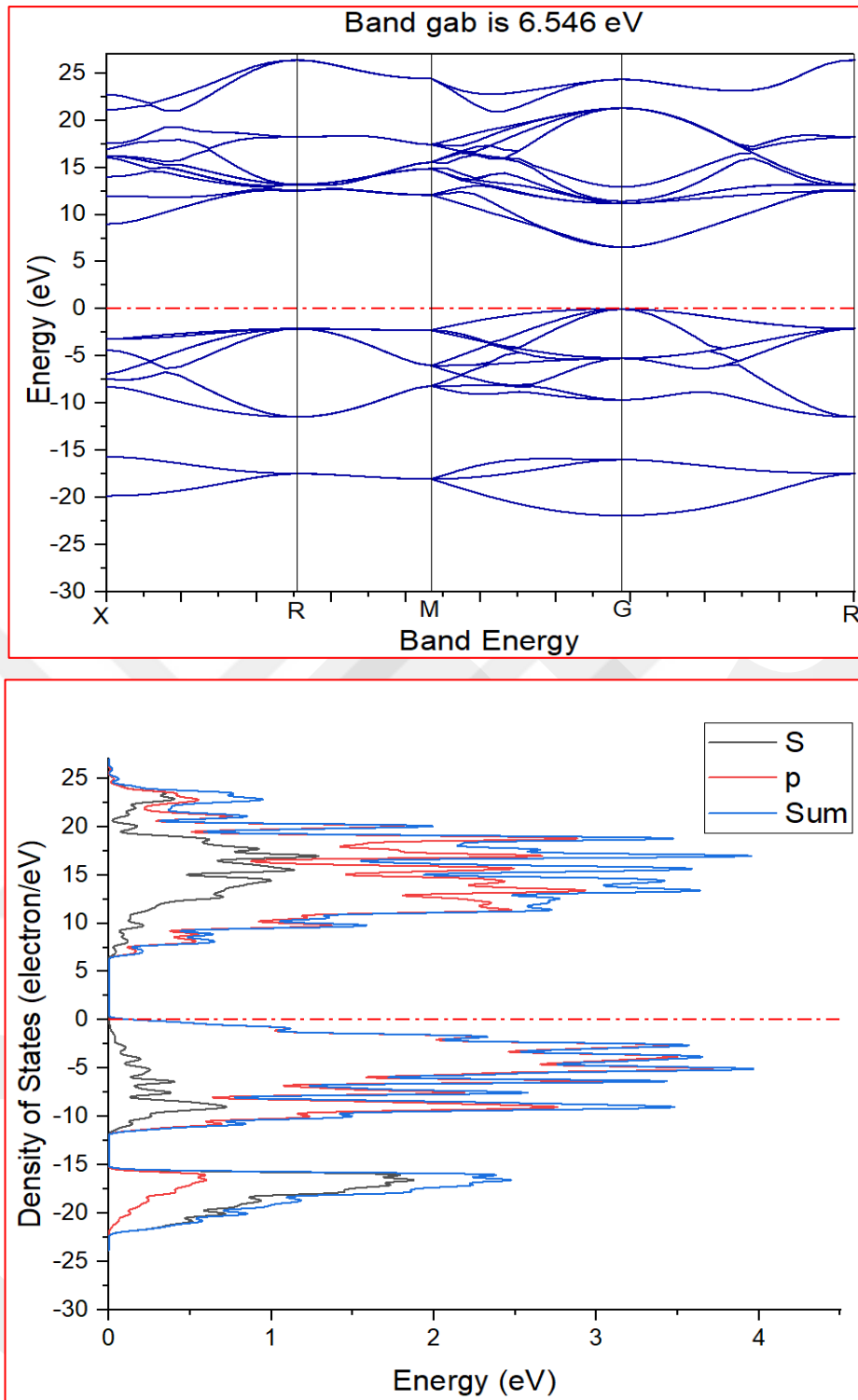


Figure 6.11 Calculation of (c-BN) band structures and density of state by HSE06 functional.

6.11.5 Optical properties:

The calculation results are shown in Figure 6.12.

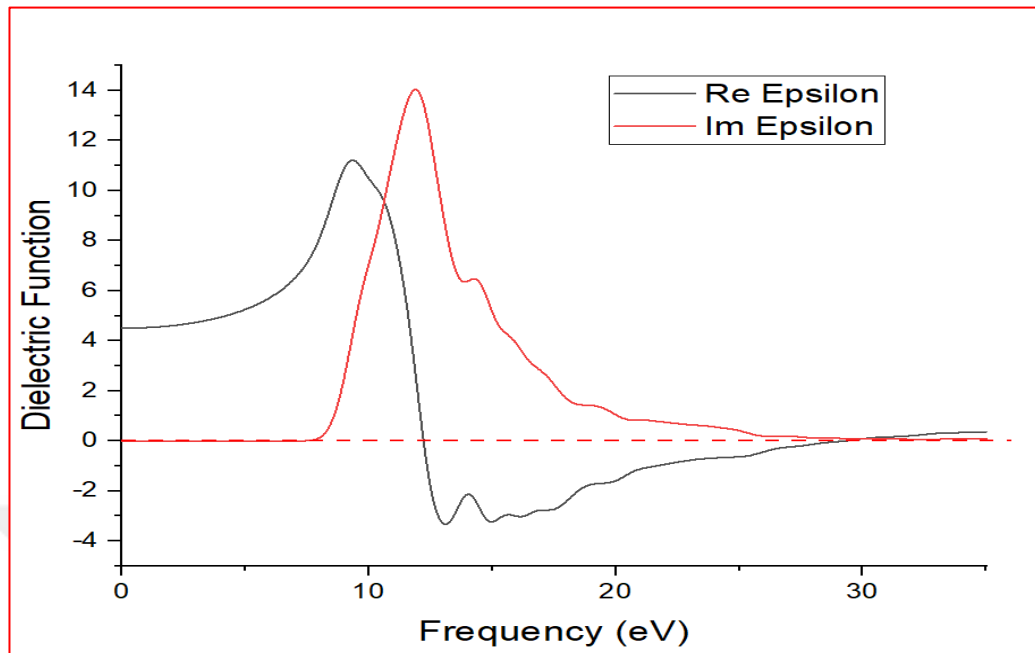


Figure 6. 12 Calculation of dielectric function of c-BN, (real and imaginary components)

6.11.6 Phonon of (c-BN)

The phonon of (c-BN) result is shown in Figures 6.13 and 6.14.

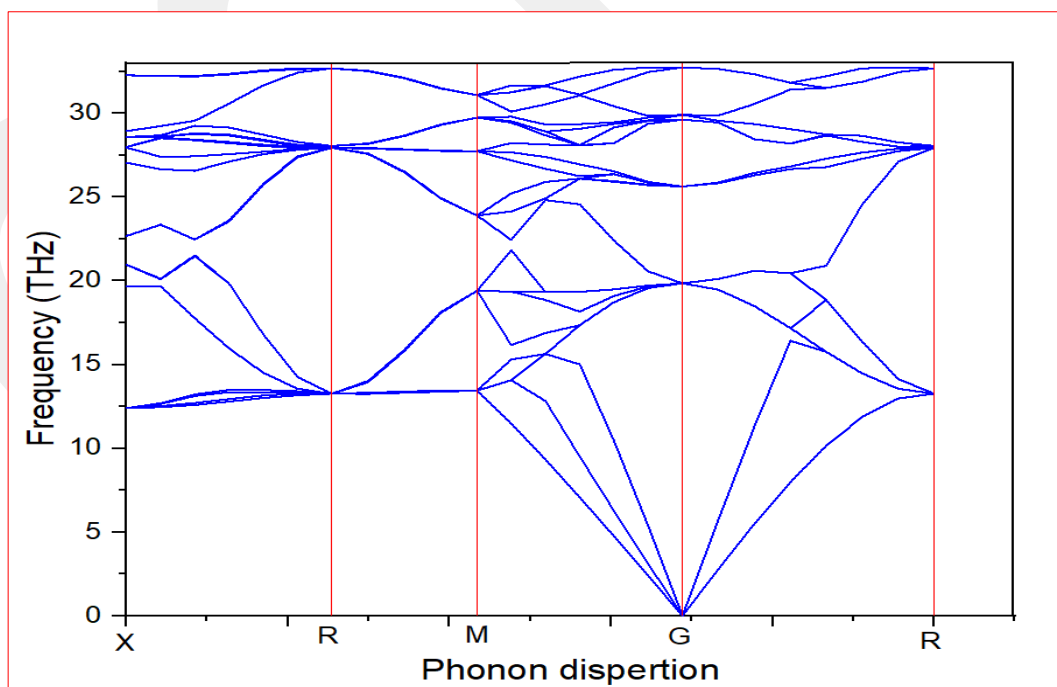


Figure 6.13 Phonon of the c-BN

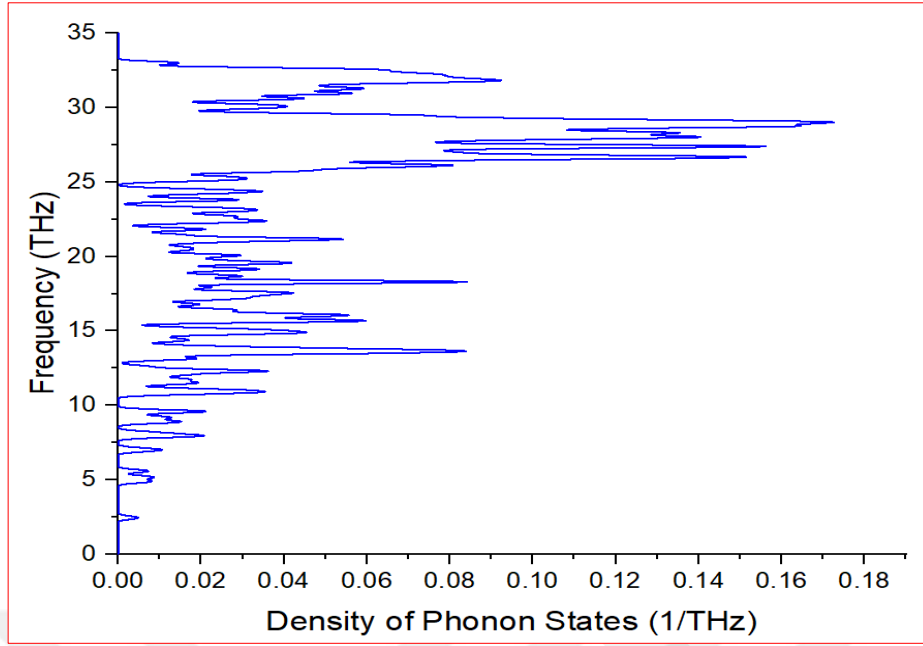


Figure 6.14 Density of Phonon State of c-BN

6.12 Thermodynamic properties of h-BN and c-BN Determined Using The Quasi Harmonic Debye Model

Two of a solid's most important thermodynamic characteristics are the equation of state (EOS) and chemical potential. A given crystalline phase's behaviour in response to changes in the macroscopic factors, primarily pressure (p) and temperature, is determined by the EOS of that phase (T). The thermodynamic properties of h-BN and c-BN are calculated using the quasi-harmonic Debye model (non-equilibrium Gibbs function) $G^*(V; P; T)$ as shown in Equation (6.28) :

$$G^*(V; P; T) = E(V) + PV + A_{vib}[\theta(V); T] \quad (6.28)$$

Where $E(V)$ is the total energy per unit cell, PV is the constant hydrostatic pressure condition, $A_{vib}[\theta(V); T]$ is vibrational Helmholtz free energy and $\theta(V)$ is the Debye temperature. The quasi-harmonic Debye model code Gibbs [151] has become a popular and inexpensive method for deriving thermal behaviour from energy versus volume. The data of energy versus volume was obtained from electronic structure crystal calculations. Energy calculation as a function of volume for both h-BN and c-BN phases is determined using the CASTEP software [152]. The intersection point

(V, E) between the h-BN and c-BN curves is when Volume (44.77669 A**3) and Energy (-174.47766 eV/atom) as shown in Figure 6.15.

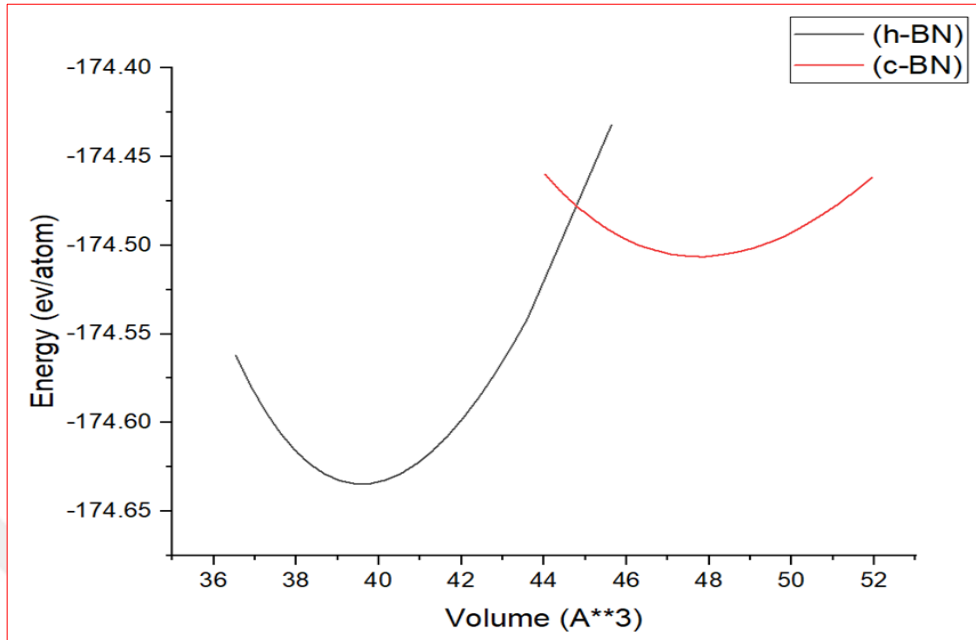


Figure 6.15 The energy versus volume for BN with two structures h-BN and c-BN

The quasi-harmonic Debye model is used to obtain the properties of h-BN and c-BN. The equilibrium configuration of the system will be the minimum of this Gibbs function, which depends, of course, on T and P. This scheme allows for quasiharmonic crystal equilibrium geometries and any other thermodynamic property of the crystal to be a function of the macroscopic parameters P and T. The difficulty of determining the Debye temperature is greatly simplified by the isotropic solid approximation, but it would be ideal to further minimize the number of parameters required to determine the Debye temperature of the system in any configuration.

There are two alternative strategies for this. First, imagine that the solid behaves like a fluid. The second possible method for the reduction of an elastic constant is based on the value of Poisson's ratio for the crystal. In a continuum, the Poisson ratio is defined as the ratio of transverse to longitudinal deformation when subjected to axial tension, and it can be demonstrated [153] that this ratio $\nu = -\epsilon_{\text{trans}} / \epsilon_{\text{longitudinal}}$ applies to an isotropic solid. Different curves are illustrated for h-BN and c-BN for example Bulk modulus and volume versus pressure in the temperature range of 0-2500 K, thermal

expansion (α), heat capacity and volume versus temperature in the pressure range of 0–7 GPa. The fitting routines work internally in atomic units (bohr³ and hartree). For the details of input and output for Gibbs code see (Appendix C).

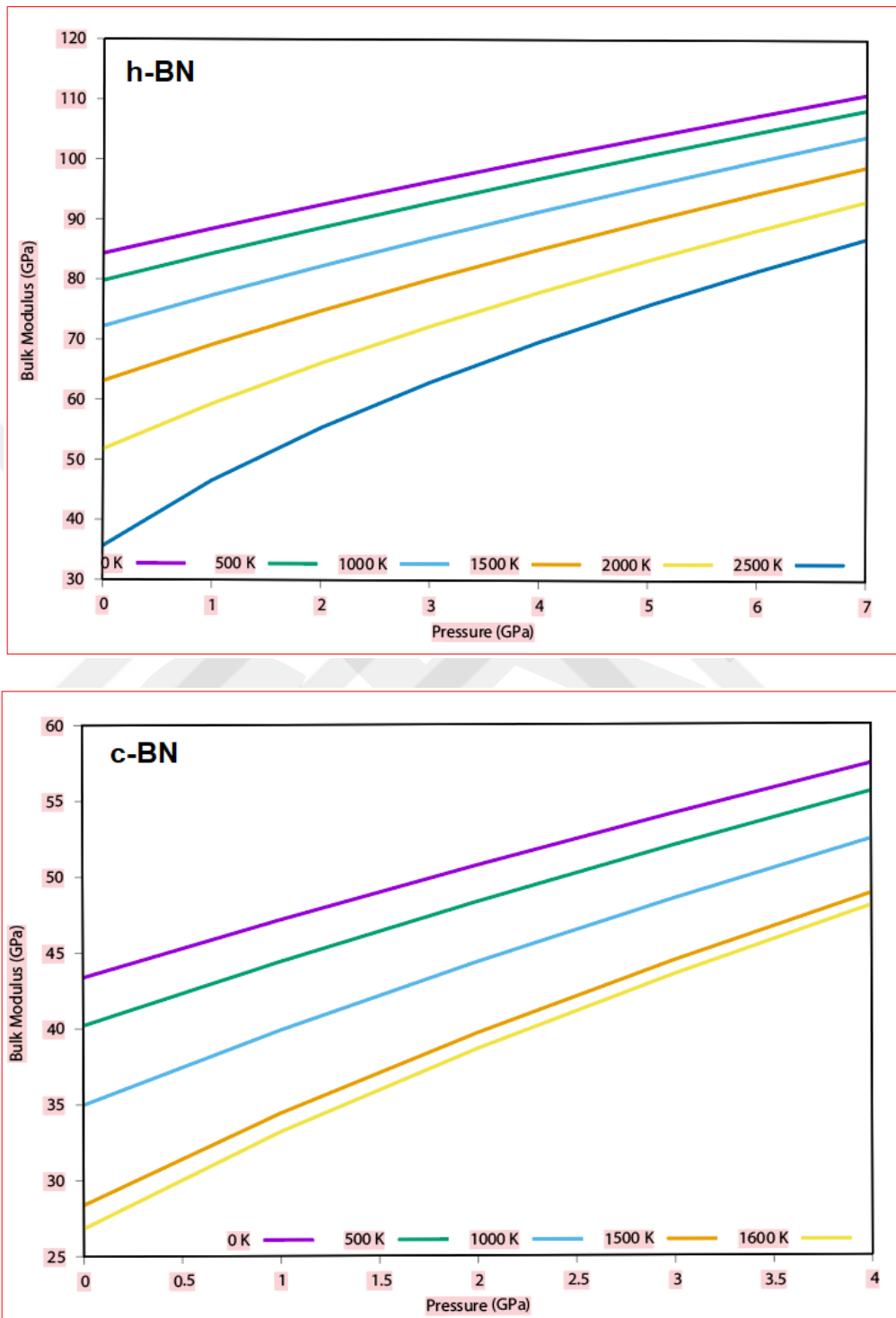


Figure 6.16 The bulk modulus versus pressure for h-BN and c-BN at different temperature

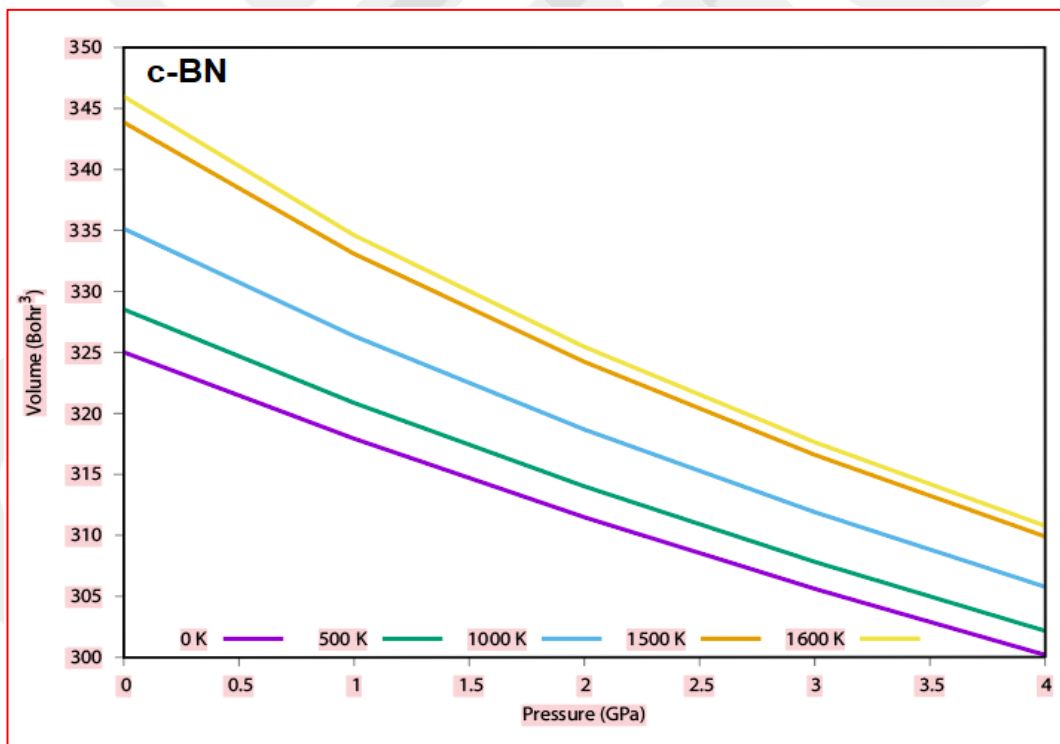
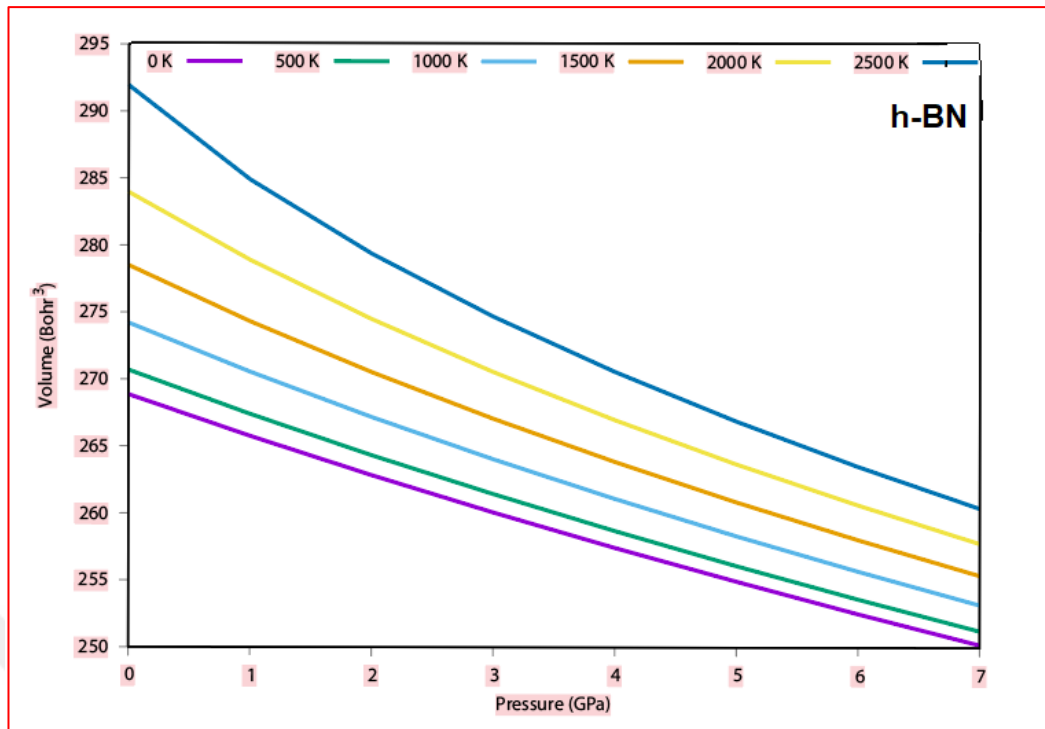


Figure 6.17 The volume versus pressure for h-BN and c-BN at different temperature

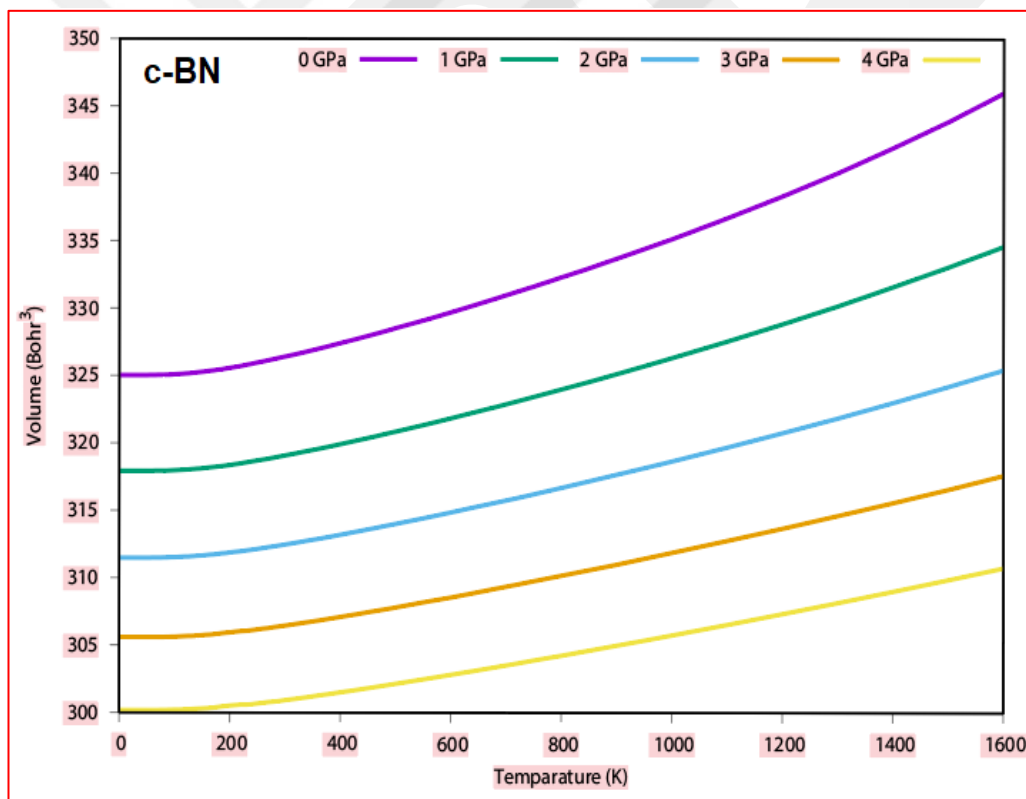
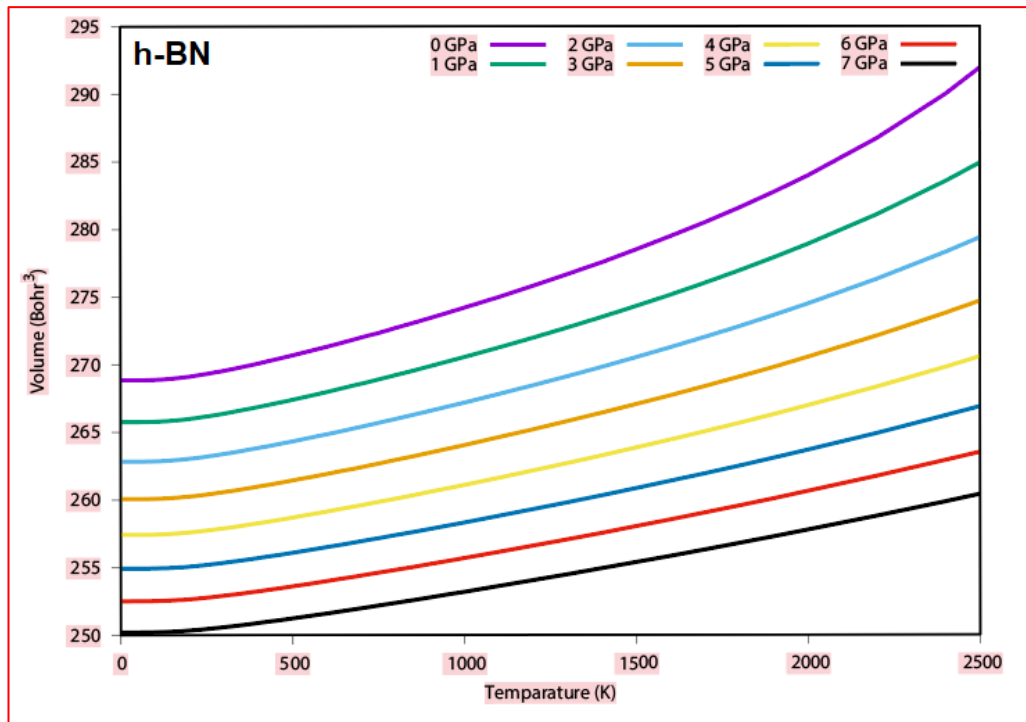


Figure 6.18 The volume versus temperature for h-BN and c-BN at different pressure

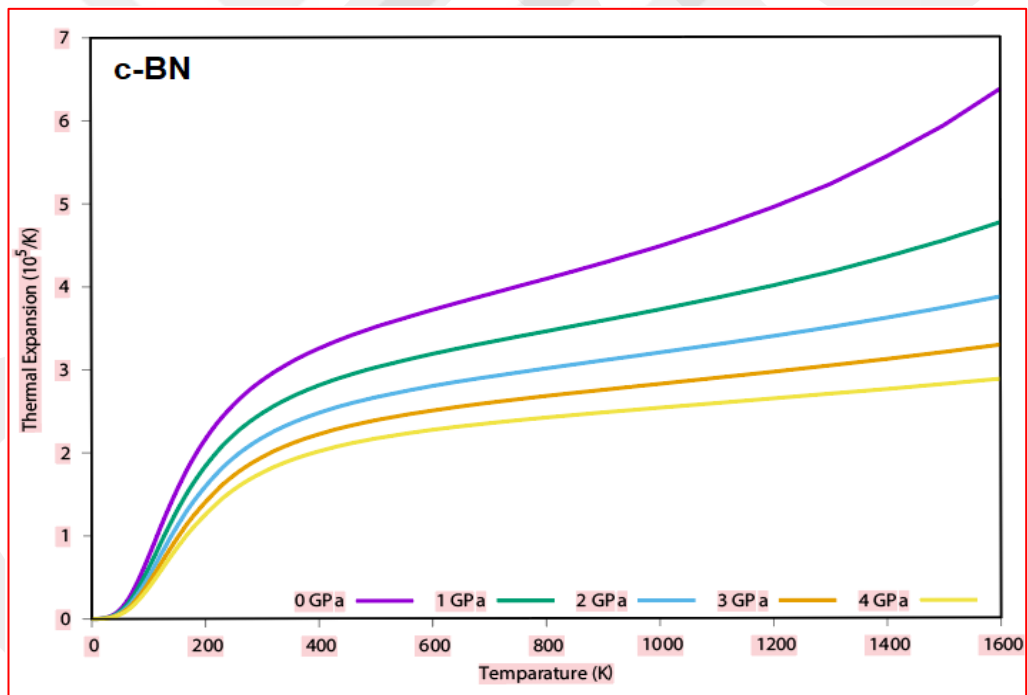
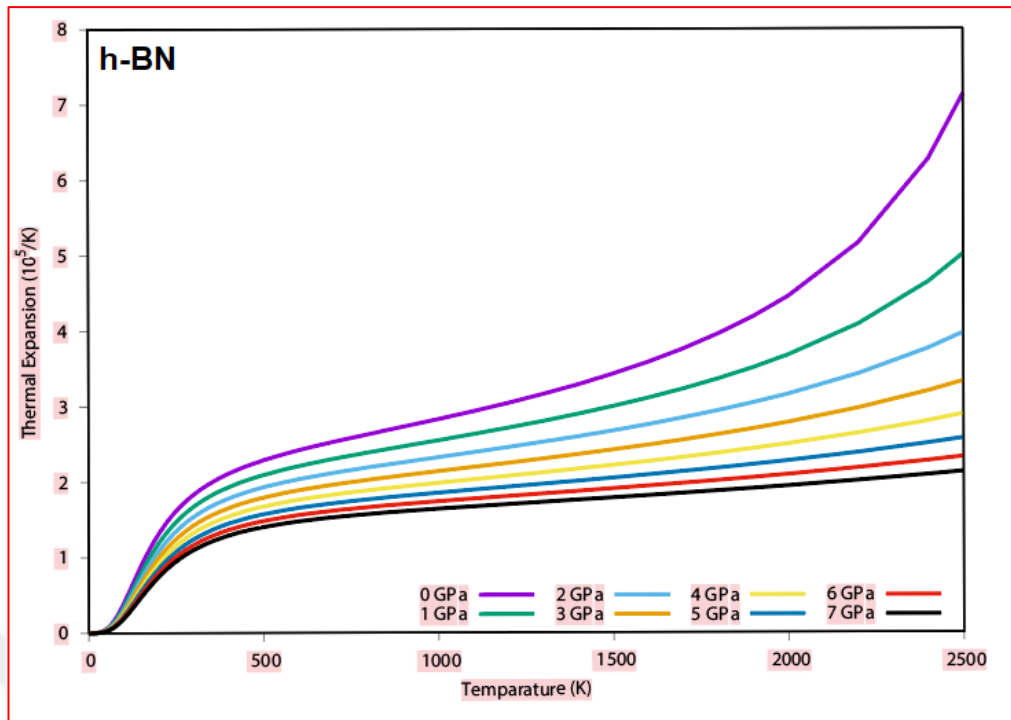


Figure 6.19 The thermal expansion versus temperature for h-BN and c-BN at different pressure

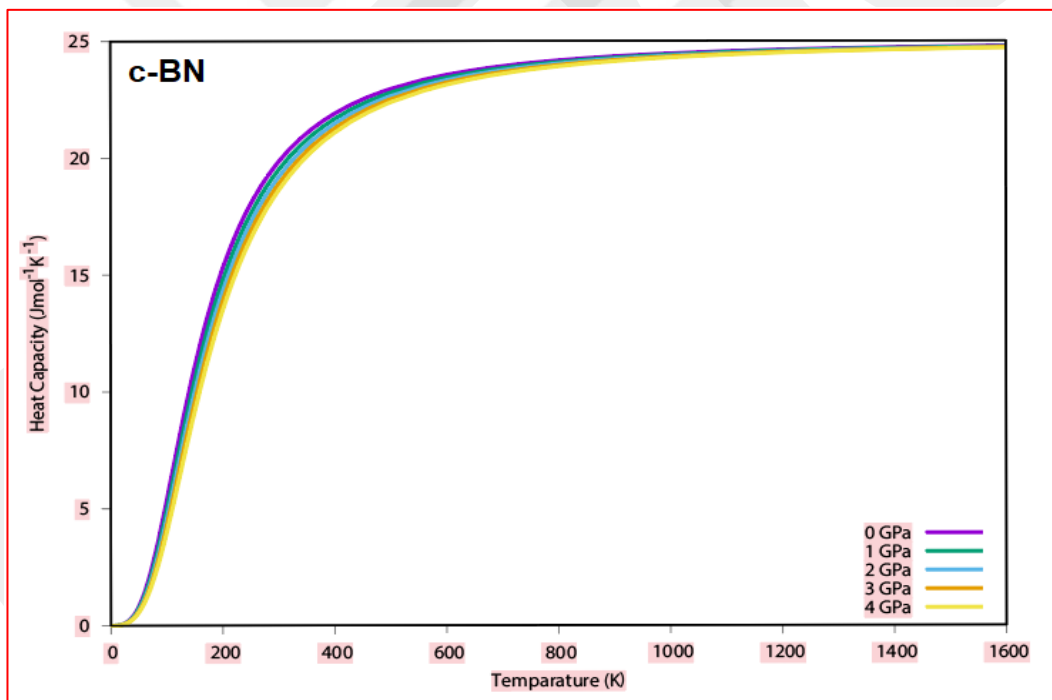
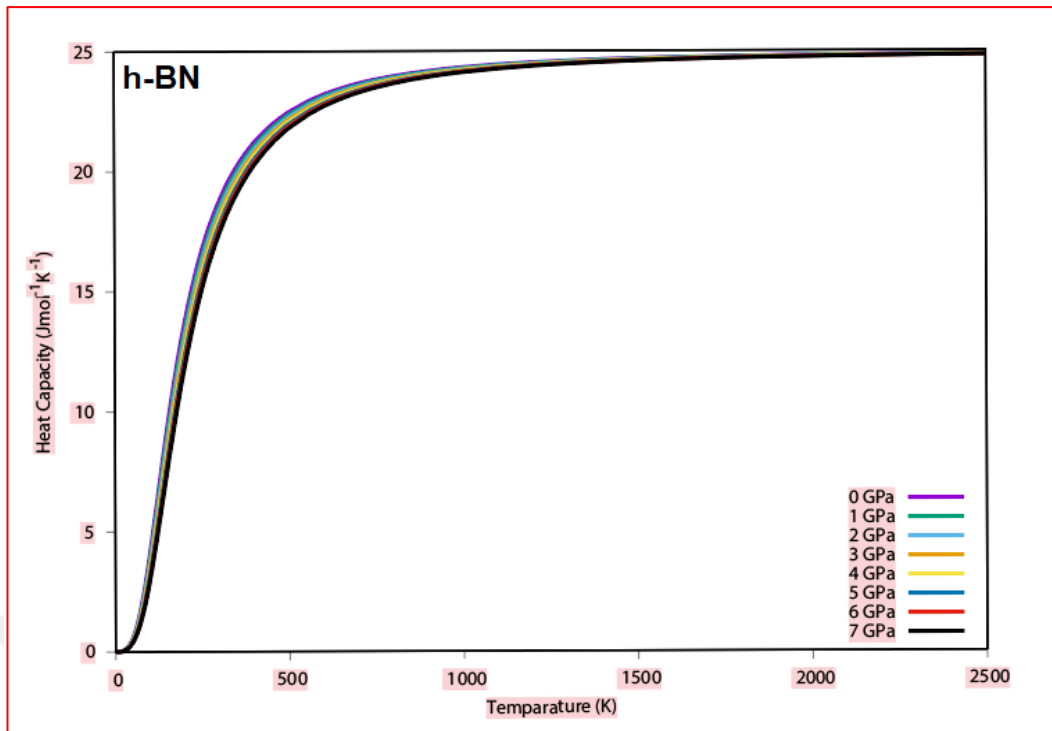


Figure 6.20 The heat capacity versus temperature for h-BN and c-BN at different pressure

CHAPTER 7

CONCLUSION AND SUGGESTIONS FOR FUTURE WORK

7.1 Conclusion

The Direct Simulation Monte Carlo (DSMC) Method is used to calculate probabilistic collisions between particles in the vacuum of a PVD system. The SamadiiTM/sciv program was utilized to model the BN coating in this investigation. Many models are built to study the effect of input parameters on the BN coating profile.

Three distinct bias voltages are used to generate three different BN coating models under the same conditions. The bias voltages are 0, 100 and 250 V.

The modelling of BN coatings at various substrate voltages reveals that the deposition rate decreases as the substrate voltage increases. The decrease in deposition rate caused a decrease in coating thickness.

The escaped rate of BN particles is highest than the deposition rate in substrate voltage (250V), therefore the deposition efficiency is low compared with two other types. With the progress of the BN coating model, the deposition efficiency increased. The highest deposition efficiency is when substrate voltage (0V) and the least when substrate voltage (250V).

The result of the models gives a good approximation with experiment results for both substrate voltage 0V and 100V with errors of 2.4% and 7% respectively. As well as the result of the Model when the substrate voltage is 250V, is very close to the experiment with an error of 0.7%.

Modelling the influence of the power supply on the deposition profile, the applied power is 900,1200, and 1500W with two substrate voltages 0 and 250V.

From the first group of three models (substrate voltage=0V), When the power supply increase from 900W to 1200W the thickness of the coating increases but when power is 1500W, the thickness becomes less than at power 1200W. That means we couldn't say the deposition rate is proportional to the power supply.

In the second group when substrate voltage is 250V, the thickness of the coating decrease when the power supply increases, and the effect of increasing of power supply on the deposition rate is limited.

Three models are built to study the effect of the volumetric gas flow rate change on the deposition profile. The volumetric flow rate for both gases Ar and N₂ will be changed. This change in flow rate will have the same Ar to N₂ ratio (5:1). The Ar: N₂ ratios are 80:16,40:8 and 10:2. From these three models, the highest deposition rate when Ar: N₂ is 80:16 . The deposition rate is 5.04 e18 (#/m². s) and the thickness is 2.2 μm.

When applied the 10:2 (Ar: N₂) the thickness of the coating decrease, mostly that's due to a decrease in Ar ionization Ar⁺ which is lead to a decrease in the number of sputtering particles BN. Despite that for the thin layer (nano-thickness) which is < 50 nm the 10:2 is efficient with a high deposition rate of 53%.

To study the effect of substrate position on the coating thickness (target to the substrate distance). Four substrates are defined with different TSD. The substrate position in the chamber plays a significant role in the coating profile.

The model shows that decreasing the T-S distance to 40 mm will increase thickness to 2149 nm compared with 882 nm when T-S is 80 mm.

To understand the effect of substrate material on the coating thickness, five substrates with the same geometry and same parameters are used. The type of materials is Al, D2, Ti, TiN, and glass. The thickness of coating from highest to lowest is TiN, D2, Ti, glass, and Al.

From the previous models, optimization thickness of the coating is possible by applying a power supply of 1200W, the substrate bias voltage is 0 V and optimizing the Ar: N₂ flow to 80:16 will lead to improving the coating thickness.

When comparing the Model-G1 (power supply=1100W, substrate bias voltage=0V and Ar/N₂=80/16), these input boundary conditions lead to an increase in the thickness of coating from 882 (model-A) to 1840 nm (model-G1).In the experiment, the thickness of the coating increased from 861 nm to 1940 nm (Run 203) with high homogeneity.

The same boundary conditions of Run 203 are applied to Run 209 but the TSD will be 50 mm. The thickness of coating when TSD is 100 mm and 50 mm for D2 substrate is 1900.7 nm and 3296.5 nm respectively. The thickness of the coating increases is 1395.8 nm. The hardness and adhesion are increased when TSD decreased to 50 nm. From the experiment Run 217, When substrate voltage increased to 180 V with power supply 1100, even with an increase in the gas volumetric flow rate of Ar: N₂ to 90: 18 sccm, the thickness of the coating is less than 50 nm. The good advantage of this experiment is the good hardness of the coating. The hardness is 11.2 GPa. FTIR result shows that the low-density BN crystal lattices (h-BN) transform into high-density polymorphs c-BN and w-BN. h-BN allotrope transforms into other phases like Turbostratic BN (t-BN), Explosive boron nitride (e-BN) and Amorphous BN (a-BN).

DSMC is used to find the properties in the vacuum such as temperature, pressure and gas fluxes. The result of the 2D field analysis for temperature and pressure of models is submitted. From this analysis, we try to predict the transformation of the BN allotrope. How the BN structure is changed.

To study the structure of BN coating and understand the correlation between BN phases, low-density phase (h-BN) and high-density phase (c-BN), CASTEP (Cambridge Serial Total Energy Package) software uses to understand the background of this correlation. CASTEP software uses to calculate the elastic such as the calculation of bulk modulus (B), shear modulus (G), Young's modulus (E), and Poisson's ratio.

The electronic and phonon properties of the h-BN and c-BN phases are calculated. The evaluated band gap is 4.461 eV and 6.546 eV for h-BN and c-BN respectively, indicating that the BN is a semiconductor material with a wide bandgap. In next step involves determining thermodynamic properties from energy against volume using the quasi-harmonic Debye model code approach. Different curves are illustrated for h-BN and c-BN for example Bulk modulus and volume versus pressure, thermal expansion (α), heat capacity and volume versus temperature. The results show that the bulk modulus increases as pressure increases and decreases as temperature decreases. The volume of the BN crystal is a function of pressures at different temperatures, the unit cell volume of the crystal increase as the pressure decreases. The volume increases with increasing temperature. The calculation of thermal expansion coefficient (α) and heat capacity (C), shows that the (α) increases as the pressure decreases. The (α) increases

with increasing temperature. When the temperature increases, the heat capacity goes up until arrives approximately at the linear situation at a higher temperature for both h-BN and c-BN. At low temperatures, the heat capacity changes tend to go to zero at absolute zero. The heat capacity decreases when the pressure increases. The temperature and pressure ranges in the thermal properties calculation are different for h-BN and c-BN due to structural stability differences. The maximum temperature and maximum pressure that can be applied to the h-BN structure without distortion are 2500 K and 7 GPa respectively. The maximum temperature and pressure applied on c-BN are 1600 K and 4 GPa respectively. Since the range of the parameters (temperature and pressure) are different, we couldn't find the correlation or the energy requirement to transform h-BN to c-BN in the PVD system (high temperature with vacuum pressure). We think the h-BN phase will not transform into the c-BN phase directly. This means there is an interphase between these two phases. The result shows that the h-BN phase is more stable than the c-BN under high pressure and temperature.

7.2 Suggestions for Future Work

Reactive magnetron sputtering is a well-known thin-film deposition method. This technique's fundamentals are conceptually simple and can be summarized in a few lines. However, the complex interplay of various physical and chemical sub-processes lies behind this simple thing.

The model begins with magnetic fields, progresses to electric fields, plasma, particle transport, solid particle interaction, chemical interactions between active gas and target plate particles, and concludes with thin-film growth. Since a sputtering system's Knudsen number ranges from 0.1 to 10, rarefied gas flow conditions must be considered. This study discovered a very good correlation between models and experiments. High-quality BN films were obtained at high deposition rates when low substrate voltage (0V), power supply (1100) W, and volumetric flow rate Ar, N₂ of 80 and 16 Scm, respectively are applied. As a result, Direct Simulation Monte Carlo (DMSC) appears to be the best approach for dealing with this issue. The first goal of this study (theoretical modelling of BN coating) is to optimize deposition rate, coating uniformity, and coating homogeneity. To reduce production times, process parameters must be optimized.

The second goal is to simulate the crystal structure of a thin film and determine the relationship between coating parameters and BN allotropes.

This study is not the end; it is only the beginning of more research. Our suggestions for future work are :

- The substrates in this study are simply modelled without rotation, so this model can be developed to study the effect of substrate rotation with direction on the coating.
- The MS model can be supplemented with induction coupled plasma (ICP). The experiment Run 209 parameters can be applied with inductively coupled plasma to increase the hardness of coating without losing the high deposition rate of BN particles.
- Study the effect of magnetic pole design on sputtering.
- This study can be expanded to model multiple targets made of various materials with different substrate materials and different types of power supply.
- The correlation between the h-BN and c-BN phase needs more studies.
- In this study, DFT is used to calculate the elastic properties such as the calculation of bulk modulus (B), shear modulus (G), Young's modulus (E), and Poisson's ratio. Then extended to calculate the electronic and phonon properties of the h-BN and c-BN. In the next step, the quasi-harmonic Debye model code method is used for deriving thermal behaviour from the energy versus volume of these two phases. This method can be used to study more BN phases such as (w-BN),(t-BN), (e-BN), (r-BN) and (a-BN).

REFERENCES

- [1] L. Ter Minassian-Sarag, B. Vincent, M. Adler, A. Barraud, N.V. Churaev, N. D.F. Eaton & J.N. Zemel, "Thin films including layers: Terminology in relation to their preparation and characterization". *Pure and applied chemistry journal*, volume 66.8, pp. 1667-1738, 2009.
- [2] K. Chopra, *Thin Film Device Applications*. New York, NY: Springer US, 1983.
- [3] I. Chambouleyron & J.M. Martínez, "Optical properties of dielectric and semiconductor thin films". *Journal of Applied Physics*, Volume 92.6, pp. 593-622, 2002.
- [4] P.S. Peercy, "The drive to miniaturization". *Nature journal*, volume 406(6799), pp. 1023-1026, 2000.
- [5] J.V. Barth, G. Costantini & K. Kern, "Engineering atomic and molecular nanostructures at surfaces". *Nanoscience and technology: a collection of reviews from Nature journals*, vol. 47, pp. 67-75. 2010.
- [6] H. Frey & H.R. Khan, *Handbook of thin-film technology*. Berlin, Springer, 2015, pp. 24-41.
- [7] R.J. Narayan, "Recent Developments in Functional Thin Films". *JOM*, volume 65(4), pp. 517, 2013.
- [8] M. Ohring, *Materials Science of Thin Films*. 2nd ed., San Diego, CA: Academic Press, 2002.
- [9] P.M. Martin, *Handbook of deposition technologies for films and coatings*. USA, William Andrew, science applications and technology, 2009.
- [10] C.V. Thompson, "Structure evolution during processing of polycrystalline films". *Annual review of materials science*, volume 30(1), pp.159-190, 2000
- [11] K.L. Choy, "Chemical vapour deposition of coatings". *Progress in materials science*, volume 48(2), pp. 57-170, 2003.

- [12] J. Hopwood, "Ionized physical vapor deposition of integrated circuit interconnects". *Physics of Plasmas*, volume 5(5), pp. 1624-1631, 1998.
- [13] G. Fox-Rabinovich, J.M. Paiva, I. Gershman, M. Aramesh, D. Cavelli, K. Yamamoto, ... & S. Veldhuis, "Control of self-organized criticality through the adaptive behaviour of nanostructured thin film coatings". *Entropy*, volume 18(8), pp.290, 2016.
- [14] H. Korhonen, A. Syväluoto, J.T. Leskinen & R. Lappalainen, "Optically transparent and durable Al₂O₃ coatings for harsh environments by ultrashort pulsed laser deposition". *Optics & Laser Technology*, volume 98, pp. 373-384, 2018.
- [15] A. Inspektor & P.A. Salvador, "Architecture of PVD coatings for metal cutting applications: A review". *Surface and Coatings Technology*, vol. 257, pp. 138-153, 2014.
- [16] G. Pinto, F.J.G. Silva, J. Porteiro, J.L. Míguez, A. Baptista & L. Fernandes, "A critical review on the numerical simulation related to physical vapor deposition". *Procedia Manufacturing*, vol. 17, pp. 860-869, 2018.
- [17] S. Maity, "Optimization of processing parameters of in-situ polymerization of pyrrole on woollen textile to improve its thermal conductivity". *Progress in Organic Coatings*, vol. 107, pp. 48-53, 2017.
- [18] F. Silva, R. Martinho, M. Andrade, A. Baptista & R. Alexandre, "Improving the wear resistance of moulds for the injection of glass fibre-reinforced plastics using PVD coatings: A comparative study". *Coatings*, vol. 7(2), pp. 28, 2017.
- [19] G. Skordaris, K.D. Bouzakis, T. Kotsanis, P. Charalampous, E. Bouzakis, O. Lemmer & S. Bolz, "Film thickness effect on mechanical properties and milling performance of nano-structured multilayer PVD coated tools". *Surface and Coatings Technology*, vol. 307, pp. 452-460, 2016.
- [20] M.Z.B. Abdullah, M.A. Ahmad, A.N. Abdullah, M.H. Othman, P. Hussain, & A. Zainuddin, "Metal release of multilayer coatings by physical vapour deposition (PVD)". *Procedia Eng*, vol. 148, pp. 254-260, 2016.
- [21] V. Imbeni, C. Martini, E. Lanzoni, G. Poli & I.M. Hutchings, "Tribological behaviour of multi-layered PVD nitride coatings". *Wear*, vol. 251(1-12), pp. 997-1002., 2001.

- [22] O. Auciello, A. Gras-Martí, J.A. Valles-Abarca & D.L. Flamm, *Plasma-surface interactions and processing of materials*. Spain, Springer Science & Business Media, Vol. 176, 2012.
- [23] P. Sigmund, “Theory of sputtering. The sputtering yield of amorphous and polycrystalline targets”. *Physical Review*, vol. 184(2), pp. 383, 1969.
- [24] M.W. Thompson, “Atomic collision cascades in solids”. *Vacuum*, vol. 66, pp.99-114,2002.
- [25] P. Ghekiere, “Structure evolution of biaxially aligned thin films deposited by sputtering”. Doctoral dissertation, Ghent University, Belgium, 2007.
- [26] S.M. Rossnagel & H.R. Kaufman, “Langmuir probe characterization of magnetron operation”. *Journal of Vacuum Science & Technology A: Vacuum, Surfaces, and Films*, vol. 4(3), pp. 1822-1825. 1986.
- [27] D.J. Field, S.K. Dew, & R. E. Burrell, “Spatial survey of a magnetron plasma sputtering system using a Langmuir probe”. *Journal of Vacuum Science & Technology A: Vacuum, Surfaces, and Films*, vol. 20(6), pp. 2032-2041, 2002.
- [28] M. A. Lieberman and A. J. Lichtenberg, *Principles of Plasma Discharges and Materials*. 1st edition, New York, NY: Wiley-Interscience, 1994.
- [29] D.M. Mattox, *Handbook of physical vapor deposition (PVD) processing*, 2nd ed., William Andrew, Oxford, UK, 2010.
- [30] R.A. Powell, S.M. Rossnagel, and PVD for Microelectronics: *Sputter Deposition applied to Semiconductor Manufacturing*. 26th ed., Academic Press, San Diego, 1999.
- [31] W. Westwood, *Sputter deposition*, 1st ed., AVS Education Committee, New York, 2003.
- [32] K. Strijckmans, R. Schelfhout & D. Depla, “Tutorial: Hysteresis during the reactive magnetron sputtering process”. *Journal of Applied Physics*, vol. 124(24),pp. 241-101, 2018.
- [33] S. Berg, H. O. Blom, T. Larsson, C. Nender, “Modeling of reactive sputtering of compound Materials”, *J. Vac. Sci. Technol.*, vol. A 5 (2), pp. 202–207, 1986.

- [34] D. Depla, R. De Gryse, “Target poisoning during reactive magnetron sputtering: Part i: the influence of ion implantation”. *Surf. Coat. Technol.* Vol. 183 (2-3), pp. 184–189, 2004.
- [35] S. Berg, T. Nyberg, “Fundamental understanding and modeling of reactive sputtering processes”. *Thin Solid Films*, Vol. 476 (2), pp. 215–230, 2005.
- [36] M.I. Petrescu and Mădălina-Gabriela Balint. “Structure and properties modifications in boron nitride. Part I: Direct polymorphic transformations mechanisms”. *UPB Sci. Bull., Series B 69*, vol. 1, pp. 35-42, 2007.
- [37] J.J. Pouch & S.A. Alterovitz, *Synthesis and properties of boron nitride. In Materials science forum*, Trans Tech Publications, vol. 54-55, Des.1990.
- [38] G. Will & P.G. Perkins, “Is there a new form of boron nitride with extreme hardness, *Diamond and related materials*, vol. 10(11), pp. 2010-2017, 2001.
- [39] M. Audronis, A.V. Valiulis & P. Silickas, “Recent developments in the deposition of c-BN coatings”. *Materials Science*, vol. 10(2), pp. 152-156, 2004.
- [40] K.S. Neo, M. Rahman, X.P. Li, H.H. Khoo, M. Sawa & Y. Maeda, “Performance evaluation of pure CBN tools for machining of steel”. *Journal of Materials Processing Technology*, vol. 140(1-3), pp. 326-331. 2003.
- [41] B. Cetin, H. Kaplan & G. Durkaya, “A new generation, promising engineering material: Cubic boron nitride (c-BN)”. *Hittite Journal of Science and Engineering*, vol. 2(1), pp. 85-90., 2015.
- [42] T. Özel, T. Thepsonthi, D. Ulutan & B. Kaftanoğlu, “Experiments and finite element simulations on micro-milling of Ti–6Al–4V alloy with uncoated and cBN coated micro-tools”. *CIRP Annals*, vol. 60(1), pp. 85-88., 2011.
- [43] W.H. Balmain, “Bemerkungen über die Bildung von Verbindungen des Bors und Siliciums mit Stickstoff und gewissen Metallen. *Journal für Praktische Chemie*, vol. 27(1), pp. 422-430, 1842.
- [44] L. Chkhartishvili, G.T.D. Nackebia, T. Bzhalava & I. Kalandadze, “hexagonal boron nitride as a solid lubricant additive” (an overview), *nano study*, vol. 14, pp. 91-98, 2016.

- [45] Wang, Jingang, Fengcai Ma, and Mengtao Sun. "Graphene, hexagonal boron nitride, and their heterostructures: properties and applications". *RSC advances* 7, vol. 27, pp. 16801-16822, 2017.
- [46] Z. Liu, Y. Gong, W. Zhou, L. Ma, J. Yu, J.C. Idrobo & P.M. Ajayan, "Ultrathin high-temperature oxidation-resistant coatings of hexagonal boron nitride". *Nature communications*, vol. 4(1), pp. 1-8. 2013.
- [47] J. Narayan & A. Bhaumik, "Research Update: Direct conversion of h-BN into pure c-BN at ambient temperatures and pressures in air". *APL Materials*, vol. 4(2), pp. 20-701, 2016.
- [48] C. Chen, D. Yin, T. Kato, T. Taniguchi, K. Watanabe, X. Ma & Y. Ikuhara, "Stabilizing the metastable superhard material wurtzite boron nitride by three-dimensional networks of planar defects". *Proceedings of the National Academy of Sciences*, vol. 116(23), pp. 11181-11186, 2019.
- [49] S.N. Grinyaev & V.V. Lopatin, "Chemical bond and electronic structure anisotropies in the graphitic and rhombohedral modifications of boron nitride". *Journal of structural chemistry*, vol. 38(1), pp. 25-33.1997.
- [50] S.S. Batsanov, "Features of phase transformations in boron nitride". *Diamond and related materials journal*, vol. 20(5-6), pp. 660-664, 2011.
- [51] J.R. Thomas, N.E. Weston & T.E. O'Connor, "Turbostratic boron nitride, thermal transformation to ordered-layer-lattice boron nitride". *Journal of the American Chemical Society*, vol. 84(24), pp. 4619-4622. 1962.
- [52] S. Alkoy, C. Toy, T. Gönül & A. Tekin, "Crystallization behavior and characterization of turbostratic boron nitride". *Journal of the European Ceramic Society*, vol. 17(12), pp. 1415-1422, 1997.
- [53] A. Sokotowska & A. Olszyna, "Electron assisted chemical synthesis of E-BN". *Journal of crystal growth*, vol. 116(3-4), pp. 507-510, 1992.
- [54] J. Bischoe & B.E. Warren, "An X-ray study of carbon black". *Journal of Applied Physics*, vol. 13(6), pp. 364-371, 1942.
- [55] B.E. Warren, "X-ray diffraction in random layer lattices". *Physical Review*, vol. 59(9), pp. 693, 1941.

[56] A.P. Hagen, "Inorganic reactions and methods". (Vol. 15, No. 1). *J. J. Zuckerman* (Ed.). New York etc.: VCH., 1986.

[57] J.Y. Huang, H. Yasuda & H. Mori, "HRTEM and EELS studies on the amorphization of hexagonal boron nitride induced by ball milling". *Journal of the American Ceramic Society*, vol. 83(2), pp. 403-409., 2000.

[58] E.J. Hamilton, S. E. Dolan, C.M. Mann, H.O. Colijn, C.A. McDonald & S.G. Shore, "Preparation of amorphous boron nitride and its conversion to a turbostratic, tubular form". *Science*, vol. 260(5108), pp. 659-661, 1993.

[59] S.I. Hirano, T. Yogo, S. Asada & S. Naka, "Synthesis of amorphous boron nitride by pressure pyrolysis of borazine". *Journal of the American Ceramic Society*, vol. 72(1), pp. 66-70., 1989.

[60] D.R. Ketchum, A.L. DeGraffenreid, P.M. Niedenzu & S.G. Shore, "Synthesis of amorphous boron nitride from the molecular precursor ammonia-mono-chloroborane". *Journal of materials research*, vol. 14(5), pp. 1934-1938.1999.

[61] A. Baptista, F. Silva, J. Porteiro, J. Míguez & G. Pinto, "Sputtering physical vapour deposition (PVD) coatings: A critical review on process improvement and market trend demand". *Coatings*, vol. 8(11), pp. 402, 2018.

[62] W. D. Sproul, D. J. Christie, D. C. Carter, "Control of reactive sputtering process". *Thin Solid Films*, vol. 491 (1), pp. (1-17), 2005.

[63] A.S. Kamenetskikh, N.V. Gavrilov, O.V. Koryakova & S.O. Cholakh, "BN coatings deposition by magnetron sputtering of B and BN targets in electron beam generated plasma". In *Journal of Physics: Conference Series* Vol. 857, No. 1, pp. (12-17). IOP Publishing, May 2017.

[64] B. Kaftanoğlu & N. Dökmetaş, "Boron nitride coating of tools and dies to improve performance in manufacturing applications". *International Journal of Mechatronics and Manufacturing Systems* 7, vol. 7(4-6), pp. 311-335, 2014.

[65] B. Kaftanoğlu & N. Dökmetaş, "Performance of boron nitride coated tools and dies". *Advances in Production Engineering & Management*, vol. 8(3), 2013.

[66] M.P. Allen, D.J. Tildesley, *Computer simulation of liquids*. Oxford, Oxford university press, 2017.

[67] M.C. Payne, M.P. Teter, D.C. Allan, T.A. Arias, a.J.D. Joannopoulos, “Reviews of Modern Physics” *.physics*, vol. 64, pp.1045–1097, 1992.

[68] G. Kresse, J. Furthmüller, *Vienna ab-initio simulation package (VASP)*, V. 5.4, Vienna, Austria, Vienna University, 2001.

[69] K. Binder, D.M. Ceperley, J.-P. Hansen, M.H. Kalos, D.P. Landau, D. Levesque, H. MuellerKrumbhaar, D. Stauffer, J.-J. Weis, *Monte Carlo methods in statistical physics*. Springer Science & Business Media, vol.6 2012.

[70] M. Ranjan, A. Sharma, A. Vaid, T. Bhatt, V. Nandalan, M.G. James, & S. Mukherjee, “BN/BNSiO₂ sputtering yield shape profiles under stationary plasma thruster operating conditions”. *AIP Advances*, vol. 6(9), pp. (95-224), 2016.

[71] J.M. Kapopara, A.R. Mengar, K.V. Chauhan & S.K. Rawal, “CFD analysis of sputtered TiN coating”. *Materials Today: Proceedings*, vol. 4(9), pp. 9390-9393., 2017.

[72] K. Bobzin, R.P. Brinkmann, T. Mussenbrock, N. Bagecivan, R.H. Brugnara, M. Schäfer & J. Trieschmann, “Continuum and kinetic simulations of the neutral gas flow in an industrial physical vapor deposition reactor”. *Surface and Coatings Technology*, vol. 237, pp. 176-181, 2013.

[73] A.F. Kanta, G. Montavon, M.P. Planche & C. Coddet, and C. “Artificial neural networks implementation in plasma spray process: Prediction of power parameters and in-flight particle characteristics vs. desired coating structural attributes”. *Surface and Coatings Technology*, vol. 203(22), pp. 3361-3369, 2009.

[74] D. Depla, “Dedicated Research on Advanced Films and Targets”, Internet: www.ugent.be/we/solidstatesciences/draft, Sep. 9, 2003 [Oct. 10, 2006]

[75] D. Depla, “RSD2013”, Internet: www.ugent.be/we/solidstatesciences/draft.webhosting.be/index.php?p=137, 1st Jan.2014 [1st Des. 2014]

[76] M. R. Samadii, “Samadii™/sciv v3.7.x-Static contact in vacuum user’s guide”, Internet: <https://sourceforge.net/software/product/Samadii/>, Oct.10th,2010 [10th May 2011]

[77] G.A. Bird, *Molecular Gas Dynamics and the Direct Simulation of Gas Flows*, Oxford, Oxford University Press, 1994, pp. 126-140.

- [78] C. White, M.K. Borg, T.J. Scanlon T. J., J.M. Reese, "A DSMC Investigation of Gas Flows in Microchannels with Bends". *Journal of Computers & Fluids*, vol. 21(2), pp. 1-12, 2012.
- [79] H. Tsien, "Superaerodynamics, the Mechanics of Rarefied Gas". *Journal of the Aeronautical Sciences*, vol. 13, pp. 653–664, 1946.
- [80] Ching Shen, *Rarefied gas flows Fundamental Simulation and Microflows*. Springer Publications, 2005.
- [81] J. Narayan & A. Bhaumik, "Research Update: Direct conversion of h-BN into pure c-BN at ambient temperatures and pressures in air". *APL Materials*, vol. 4(2), pp. 020-701., 2016.
- [82] S. Hogmark, S. Jacobson, M. Larsson, "Design and evaluation of tribological coatings. *Wear journal*, vol. 246, pp. 20–33, 2000.
- [83] Barshilia, C. Harish, A. Ananth, Jakeer Khan, and G. Srinivas. "Ar+ H2 plasma etching for improved adhesion of PVD coatings on steel substrates." *Vacuum 86*, vol. 8, pp. 1165-1173, 2012.
- [84] Thornton, A. John and L. lamb James, "Substrate heating rates for planar and cylindrical-post magnetron sputtering sources". *Thin Solid Films*, vol. 119, pp. 87-95, 1984.
- [85] J.A. Thornton. SAE Report #730544, New York, SAE, 1973.
- [86] W. D. Gill and Eric Kay. "Efficient low pressure sputtering in a large inverted magnetron suitable for film synthesis". *Review of Scientific Instruments*, vol. 36 (3), pp. 277-282, 1965.
- [87] De Gryse, Roger, Johan Haemers, W. P. Leroy, and Diederik Depla. "Thirty years of rotatable magnetrons". *Thin Solid Films*, vol. 520(18), pp. 5833-5845, 2012.
- [88] Chapin, S. John, "The planar magnetron". *Research Development*, vol. 25(1), pp. 37-40, 1974.

- [89] Greene, E. Joseph, "Tracing the recorded history of thin-film sputter deposition: From the 1800s to 2017". *Journal of Vacuum Science & Technology A: Vacuum, Surfaces and Films*, vol. 35, Issue 5, 2017.
- [90] Kelly, J. Peter and R. Derek Arnell. "Magnetron sputtering: a review of recent developments and applications". *Vacuum*, vol. 77, pp. 159-172, 2000.
- [91] E.Tool Box (2010), "Relative Permittivity - the Dielectric Constant". *Engineering ToolBox*, [online], Available at: https://www.engineeringtoolbox.com/relative-permittivity-d_1660.html, [2022]
- [92] S. McFadyen, "material-properties", <https://myelectrical.com/notes/entryid/177/material-properties> (May 10th, 2012)
- [93] S.S. Elovikov, E.Y. Zykova, A.A. Promokhov & V.E. Yurasova, "Experimental study and computer simulation of AlN and BN sputtering. In International Workshop on Nondestructive Testing and Computer Simulations in Science and Engineering", *International Society for Optics and Photonics*, Vol. 3687, pp. 268-273, 1999.
- [94] T. Hacaloğlu "Development of Boron Nitride coatings for single and multi-layer films for mechanical and biomedical applications", doctor of philosophy thesis, ATILIM University, Turkey, 2021.
- [95] B.Xu, YH. Lu, Y.P. Feng, & J.Y.Lin, "Density functional theory study of BN-doped graphene superlattice: role of geometrical shape and size". *Journal of Applied Physics*, vol. 108(7), pp. 073-711, 2010.
- [96] E.Kim & C. Chen, "First-principles study of phase stability of BN under pressure". *Physics Letters A*, vol. 319(3-4), pp. 384-389, 2003.
- [97] M Grimsditch, ES Zouboulis & A. Polian, "Elastic constants of boron nitride". *Journal of applied physics*, vol. 76(2), pp. 832-834, 1994
- [98] L. CAI, B. Xu, M. Lv, X. Fan, "The Analysis of the Transformation Mechanism of cBN Crystals with the First-Principle Calculation". *Journal of Chemistry*, vol. 2020, 2020.
- [99] M. Mirzaei, E. Karimi & M. Yousefi, "BN nanoflake for hazardous SO₂ gas capturing: DFT study". *Biointerface Research in Applied Chemistry*, vol. 12, pp. 359-365, 2022.
- [100] B. Xu, Y. Shi, M. Lv, Q. Guo, Q & G. Wang, G, "A DFT study on the transition mechanism of cBN single crystal". *Integrated Ferroelectrics*, vol. 182(1), pp. 161-169, 2017.

- [101] H. KÖKTEN & Ş. ERKOÇ, "A study on Si and P doped h-BN sheets: DFT calculations". *Turkish Journal of Physics*, vol. 38(3), pp. 369-374, 2014.
- [102] L. Stagi, J. Ren & P. Innocenzi, "From 2-D to 0-D boron nitride materials, the next challenge". *Materials*, vol. 12(23), pp. 3905, 2019.
- [103] D.Kim, H.S. Kim, M.W. Song, S.Lee & S.Y. Lee, "Geometric and electronic structures of monolayer hexagonal boron nitride with multi-vacancy". *Nano convergence*, vol. 4(1), pp. 1-8, 2017.
- [104] M. Bernardi, M. Palummo & J.C. Grossman, "Optoelectronic properties in monolayers of hybridized graphene and hexagonal boron nitride". *Physical review letters*, vol. 108(22), pp. 226-805, 2012.
- [105] C. He, L. Sun, C. Zhang, X. Peng, K. Zhang & J. Zhong, J, "Z-BN: a novel superhard boron nitride phase". *Physical Chemistry Chemical Physics*, vol. 14(31), pp. 10967-10971, 2012.
- [106] J. He, G. Liu, X. Li & G. Zhang, G, "Electronic structure and optical properties of B-, N-, and BN-doped black phosphorene using the First-Principles", *molecular modelling journal*, Vol.1(6), PP.1-21, 2022.
- [107] M.I. Khan, A. Majid, N. Ashraf & I. Ullah, "A DFT study on a borophene/boron nitride interface for its application as an electrode". *Physical Chemistry Chemical Physics*, vol. 22(6), pp. 3304-3313, 2020.
- [108] A.R. Soltani & M.T. Baei, "A DFT study on the structure and electronic properties of BN nanostructures adsorbed with dopamine", *Computation*, vol. 7(4), pp.6, 2019.
- [109] A. Haque & J. Narayan, "Conversion of h-BN into c-BN for tuning optoelectronic properties". *Materials Advances*, vol. 1(4), pp. 830-836, 2020.
- [110] A. Soltani, A. Sousaraei, M.B. Javan, M., and M. Eskandari & H. Balakheyli, "Electronic and optical properties of 5-AVA-functionalized BN nanoclusters: a DFT study". *New Journal of Chemistry*, vol. 40(8), pp. 7018-7026, 2016.
- [111] J. Beheshtian, A.A. Peyghan, M.B. Tabar & Z. Bagheri, "DFT study on the functionalization of a BN nanotube with sulfamide". *Applied surface science*, vol. 266, pp. 182-187. 2013.
- [112] Y.A. Korkmaz, C. Bulutay & C. Sevik, "Defect states in monolayer hexagonal BN: A comparative DFT and DFT-1/2 study". *Physica B: Condensed Matter*, vol. 584, pp. 411-959. 2020.
- [113] V. Thakur, N. Kumar, M.L. Verma, A.K. Choubey, S. Verma, B. Chettri, & B.K. Rao, "Density functional study on hybrid h-BN/graphene atomic chains". *Physica E: Low-dimensional Systems and Nanostructures*, vol. 124, pp. 114-316, 2020.

- [114] H. Kökten & Ş. Erkoç, “Oxygen-doped c-BN (110) surface: DFT calculations”. In IOP Conference Series: *Materials Science and Engineering*, Vol. 15(1), pp. 012-075, November 2010.
- [115] M. Topsakal, E. Aktürk & S.J.P.R.B. Ciraci, “First-principles study of two-and one-dimensional honeycomb structures of boron nitride”. *Physical Review B*, vol. 79(11), pp. 115-442, 2009.
- [116] R. Ahmed, S.J. Hashemifar & H. Akbarzadeh, “First principles study of structural and electronic properties of different phases of boron nitride”. *Physica B: Condensed Matter*, vol. 400(1-2), pp. 297-306., 2007.
- [117] Y.N. Xu & W.Y Ching, “Calculation of ground-state and optical properties of boron nitrides in the hexagonal, cubic, and wurtzite structures”. *Physical Review B*, vol. 44(15), pp. 77-87. 1991.
- [118] E.G. Lewars, “Computational chemistry: introduction to the theory and applications of molecular and quantum mechanics”, *Angewandte Chemie Journal*, vol. 116, pp. 5087-5089, 2004.
- [119] P. Hohenberg and W. Kohn, “Inhomogeneous electron gas”, *Phys. Rev.* 136, B864, 1964.
- [120] V. Kaliginedi, P. Moreno-García, H. Valkenier, W. Hong, V.M. García-Suárez, P. Buitter, J.L.M. Otten, J.C. Hummelen, C.J. Lambert, T. Wandlowski, “Correlations between molecular structure and single-junction conductance: a case study with oligo (phenylene-ethynylene)-type wires”. *J. Am. Chem. Society*, vol. 134(11), pp. 5262–5275, 2012.
- [121] C. Wang, A.S. Batsanov, M.R. Bryce, S. Martín, R.J. Nichols, S.J. Higgins, V.M. García-Suárez, C.J. Lambert, “Oligoene Single Molecule Wires”. *J. Am. Chem. Society*, vol. 131(43), pp. 15647–15654, 2009.
- [122] W. Kohn and L.J. Sham, “Self-consistent equations including exchange and correlation effects”. *Physical Review*, vol. 140(4A), pp. A1133–A1138, 1965.
- [123] E.H. Lieb, “Thomas-Fermi and related theories of atoms and molecules”. *Reviews of Modern Physics*, vol. 53(4), pp. 603–641, 1981.
- [124] D.R. Hartree, “The wave mechanics of an atom with a non-Coulomb central field”. Part I. *Theory and methods*, In *Mathematical Proceedings of the Cambridge Philosophical Society*, Vol. 24, No. 1, pp. 89-110, 1928.
- [125] R. M. Martin, “Electronic structure: basic theory and practical methods”. Master thesis, Cambridge University Press, UK. Jan. 2004.
- [126] J. P. Perdew and Y. Wang, “Accurate and simple analytic representation of the

electron-gas correlation energy,” *Phys. Rev. B*, vol. 45(23), pp. 13244–13249, Jun. 1992.

[127] J. P. Perdew, K. Burke, and M. Ernzerhof, “Generalized Gradient Approximation Made Simple,” *Phys. Rev. Lett.*, vol. 77(18), pp. 3865–3868, Oct. 1996.

[128] A. D. Becke, “Density-functional thermochemistry. III. The role of exact exchange,” *J. Chem. Phys.*, vol. 98(7), pp. 5648–5652, Apr. 1993.

[129] D. R. Hamann, M. Schlüter, and C. Chiang, “Norm-Conserving Pseudopotentials,” *Phys. Rev. Lett.*, vol. 43(20), pp. 1494–1497, Nov. 1979.

[130] D. Vanderbilt, “Soft self-consistent pseudopotentials in a generalized eigenvalue formalism,” *Phys. Rev. B*, vol. 41(11), pp. 7892–7895, Apr. 1990.

[131] P. E. Blöchl, “Projector augmented-wave method,” *Phys. Rev. B*, vol. 50, no. 24, pp. 17953–17979, Dec. 1994.

[132] “Bilbao Crystallographic Server.” [Online]. Available: <http://www.cryst.ehu.es/>. [Accessed: 04-Mar-2019].

[133] A. Jain et al., *The Materials Project: Accelerating Materials Design Through Theory-Driven Data and Tools in Handbook of Materials Modeling*. Cham: Springer International Publishing, 2018, pp. 1–34.

[134] M. A. Caro, S. Schulz, and E. P. O’Reilly, “Comparison of stress and total energy methods for calculation of elastic properties of semiconductors,” *J. Phys. Condens. Matter*, vol. 25(2), pp. 025-803, Jan. 2013.

[135] Y. Le Page and P. Saxe, “Symmetry-general least-squares extraction of elastic coefficients from ab initio total-energy calculations,” *Phys. Rev. B*, vol. 63, no. 17, pp. 174-103, Mar. 2001.

[136] F. Mouhat and F.-X. Coudert, “Necessary and sufficient elastic stability conditions in various crystal systems,” *Phys. Rev. B*, vol. 90, no. 22, pp. 22-4104, Dec. 2014.

[137] M. Born, “On the stability of crystal lattices. I,” *Math. Proc. Cambridge Philos. Soc.*, vol. 36, no. 02, pp. 160, Apr. 1940.

[138] Z. Wu, E. Zhao, H. Xiang, X. Hao, X. Liu, and J. Meng, “Crystal structures and elastic properties of superhard IrN₂ and IrN₃ from first principles,” *Phys. Rev. B*, vol. 76, no. 5, pp. 054-115, Aug. 2007.

[139] M.B. Baysal, G. Surucu, E. Deligoz E and H. Ozısık,” The effect of hydrogen on the electronic, mechanical and phonon properties of LaMgNi₄ and its hydrides for hydrogen storage applications Int”. *J. Hydrogen Energy*, Vol. 432, pp. 3397408, 2018.

[140] X.Q. Chen, h. Niu, D. Li & y. Li, “Modeling hardness of polycrystalline materials and bulk metallic glasses”. *Intermetallics*, vol. 19(9), pp. 1275-1281, 2011.

[141] U.K. Chowdhury, M.A. Rahman, M.T.H. Bhuiyan & M. L. Ali, “ Ab initio study on structural, elastic, electronic and optical properties of cuprate based superconductor”. *Cogent Physics*, vol. 3(1), pp. 1231-1361, 2016.

[142] S.F. Pugh, XCII. “Relations between the elastic moduli and the plastic properties of polycrystalline pure metals”. *The London, Edinburgh, and Dublin Philosophical Magazine and Journal of Science*, vol. 45(367), pp. 823-843, 1954.

[143] N. Frantsevich, F.F. Voronov, and S.A. Bokuta, *Elastic Constants and Elastic Moduli of Metals and Insulators*. Handbook (Kyiv: Naukova Dumka), 1983, pp. 60-180.

[144] E. Schreiber, O.L. Orson, L. Anderson and N. Soga, *Elastic Constants and Their Measurement* . New York, McGraw-Hill book, 1975, PP.1-196.

[145] G. Kern, G. Kresse & J. J. P. R. B. Hafner, “Ab initio calculation of the lattice dynamics and phase diagram of boron nitride”. *Physical Review B*, vol. 59(13), pp. 8551, 1999.

[146] A. Shuaibu, O.J. Adeyemi, U.R. Ushiekpan, O.G. Olowomofe, B.J. Akinade & O.A. Kafayat, “First principle study of structural, elastic and electronic properties of hexagonal boron nitride (hex-BN) single layer”. *American Journal of Condensed Matter Physics*, vol. 9(1), pp. 1-5, 2019.

[147] O.L. Anderson, “A simplified method for calculating the Debye temperature from elastic constants”. *J. Phys. Chem. Solids*, vol. 24, pp. 90-917, 1963.

[148] M.E. Levinshtein, S.L. Rumyantsev & M.S. Shur, *Properties of Advanced Semiconductor Materials: GaN, AlN, InN, BN, SiC, SiGe*. New York, John Wiley & Sons. 2001, pp. 49-66.

[149] M. Isik, G. Surucu, A. Gencer, N.M. Gasanly, “First-principles study of Bi₁₂GeO₂₀: Electronic, optical and thermodynamic characterizations”. *Materials Today Communications*, vol. 27, pp. 102-299, 2021.

[150] Y. Li, P. Wang, F. Hua, S. Zhan, X. Wang, J. Luo, & H. Yang, “First-principle approach-based bandgap engineering for cubic boron nitride doped with group IIA elements”. *AIP Advances*, vol. 8(3), pp. 035-106, 2018.

[151] M.A. Blanco, E. Francisco, and V. Luana. “Gibbs: isothermal-isobaric thermodynamics of solids from energy curves using a quasi-harmonic Debye model”. *Computer Physics Communications*, vol. 158(1), pp. 57 – 72, 2004.

[152] S.J. Clark, M.D. Segall, C.J. Pickard, P.J. Hasnip, M.I.J. Probert, K. Refson, M. C. Payne, "First-principles methods using CASTEP". *Zeitschrift Fur Krist.* Vol. 220 pp. 567–570, 2005.

[153] J. P. Poirier, *Introduction to the physics of the Earth's interior.* the UK. Cambridge University Press, Cambridge, 1991.

XCRI
GCRI

APPENDIX A

THE HISTORY FILE OF MODELLING OF BN COATING (MOEL-A1)

Metariver Technology
http://www.metariver.kr
samadii-sciv UI version: 3.7.5.g1
samadii-sciv solver version : v3.7.5.a3-x64
Sun Oct 17 22:19:15 2021
product key: S23I-H57S-MTV6-TH47
*module check
solver (GPU) : 1
collision kernel: 1
unstructured grid kernel: 1
electric/magnetic field import kernel: 1
particle in cell kernel: 1
chemical reaction kernel: 1
sputtering target: 1
working path: C:\Model-BN\Model-A1
volume mesh import [Node 19263/ element 93294]
creat particle number: 16 [#]
creat step : 1 [step]
particle number [in body] : 0
Search elements in cell
element number; 27490
cell number info
Field cell: 93294
CLL cell: 125000
Element in the cell:1192767
volume mesh in the cell:2623142
motion setup : 0 [1]
motion type : 0
motion body number : 0

motion number: 1
 GPU info
 driver ver. : 462.35
 #0 GeForce RTX 3070 Laptop GPU (0000:01:00.0)

* material info *

01 : mass[kg]
 02: viscosity coefficient[Ns/m²]
 03: viscosity index
 04 : Reference diameter[m]
 05: Wall Adsorption coefficients
 06: symmetry factor
 07 : density[kg/m³]
 08: degree of freedom: total
 09: degree of freedom: rotation
 10: collision number: rotation
 11 : collision number : vibration(C1)
 12 : collision number : vibration(C2)
 13 : characteristic temperature[K] : rotation
 14 : characteristic temperature[K] : vibration
 15 : characteristic temperature[K] : dissociation
 16 : characteristic temperature[K] : ionization
 17 : characteristic temperature[K] : reference
 18: variable wall adsorption coefficient
 19: wall adsorption temperature-1 (WAC=0.0)
 20: reference temperature (Tref)
 21: wall adsorption coefficient at Tref
 22: wall adsorption temperature-2 (WAC=1.0)

	Ar/	N2/	BN/	2N/
01 :	6.63e-26	4.65e-26	4.65e-26	4.65e-26
02 :	2.12e-05	1.66e-05	3.50e-05	1.66e-05
03 :	8.10e-01	7.40e-01	7.60e-01	7.40e-01
04 :	4.17e-10	4.17e-10	6.50e-10	4.17e-10
05 :	1.00e+00	1.00e+00	8.00e-01	1.00e+00
06 :	1.00e+00	1.00e+00	2.00e+00	1.00e+00

07 :	1.66e+00	1.25e+00	2.30e+03	1.25e+00
08 :	0.00e+00	0.00e+00	0.00e+00	0.00e+00
09 :	0.00e+00	0.00e+00	0.00e+00	0.00e+00
10 :	0.00e+00	0.00e+00	0.00e+00	0.00e+00
11 :	0.00e+00	0.00e+00	0.00e+00	0.00e+00
12 :	0.00e+00	0.00e+00	0.00e+00	0.00e+00
13 :	0.00e+00	2.88e+00	0.00e+00	2.88e+00
14 :	0.00e+00	3.37e+03	0.00e+00	3.37e+03
15 :	0.00e+00	1.14e+05	0.00e+00	1.14e+05
16 :	0.00e+00	1.81e+05	0.00e+00	1.81e+05
17 :	2.73e+02	2.73e+02	2.73e+02	2.73e+02
18 :	0	0	0	0
19 :	0	0	0	0

* body info *

inlet-Ar.elm

N: 6257 / E: 12510

[particle-inlet]

material: Ar

flowrate : 4.000000e+01 [sccm]

inlet velocity : 2.050000e-02

cosine distribution

A: 1.0000

N: 0.0000

B: 0.0000

M: 0.0000

temperature [K] : 5.760000e+02

diffusion rate [0-1.0] : 1.000000

wall adsorption coefficient [0-1.0] : 0.200000

inlet-N2.elm

N: 6257 / E: 12510

[particle-inlet]

material: N2

flowrate : 8.000000e+00 [sccm]

inlet velocity : 4.100000e-03

cosine distribution

A: 1.0000

N: 0.0000

B: 0.0000

M: 0.0000

temperature [K] : 5.760000e+02

diffusion rate [0-1.0] : 1.000000

wall adsorption coefficient [0-1.0] : 0.200000

target. elm

N: 572 / E: 988

cosine distribution

A: 1.0000

N: 0.0000

B: 0.0000

M: 0.0000

temperature [K] : 3.000000e+02

diffusion rate [0-1.0] : 0.000000

wall adsorption coefficient [0-1.0] : 0.000000

substrate-00.elm

N: 96 / E: 150

[deposition]

cosine distribution

A: 1.0000

N: 0.0000

B: 0.0000

M: 0.0000

temperature [K] : 5.760000e+02

diffusion rate [0-1.0] : 0.800000

wall adsorption coefficient [0-1.0] : 0.800000

substrate-01.elm

N: 96 / E: 150

[deposition]

cosine distribution

A: 1.0000

N: 0.0000
B: 0.0000
M: 0.0000
temperature [K] : 5.730000e+02
diffusion rate [0-1.0] : 0.800000
wall adsorption coefficient [0-1.0] : 0.800000
substrate-02.elm

N: 32 / E: 30

[deposition]

cosine distribution

A: 1.0000

N: 0.0000

B: 0.0000

M: 0.0000

temperature [K] : 5.760000e+02

diffusion rate [0-1.0] : 0.800000

wall adsorption coefficient [0-1.0] : 0.800000

substrate-03.elm

N: 32 / E: 30

[deposition]

cosine distribution

A: 1.0000

N: 0.0000

B: 0.0000

M: 0.0000

temperature [K] : 5.760000e+02

diffusion rate [0-1.0] : 0.800000

wall adsorption coefficient [0-1.0] : 0.800000

substrate-04.elm

N: 12 / E: 10

[deposition]

cosine distribution

A: 1.0000

N: 0.0000

B: 0.0000
M: 0.0000
temperature [K] : 5.760000e+02
diffusion rate [0-1.0] : 0.800000
wall adsorption coefficient [0-1.0] : 0.800000
substrate-05.elm
N: 12 / E: 10
[deposition]
cosine distribution
A: 1.0000
N: 0.0000
B: 0.0000
M: 0.0000
temperature [K] : 5.760000e+02
diffusion rate [0-1.0] : 0.800000
wall adsorption coefficient [0-1.0] : 0.800000
pole. elm
N: 629 / E: 1102
[rigid-constrained]
cosine distribution
A: 1.0000
N: 0.0000
B: 0.0000
M: 0.0000
temperature [K] : 3.000000e+02
diffusion rate [0-1.0] : 0.100000
wall adsorption coefficient [0-1.0] : 0.100000
* cell info *
cell number: 125000 [50/ 50/ 50]
cell size : 9.93e-03/ 8.60e-03/ 8.70e-03
min : -3.98e-02/ -2.95e-01/ -2.00e-01
max : 4.57e-01/ 1.35e-01/ 2.35e-01
* simulation condition *
base pressure : 1.333220e-08 [Pa]

base temperature : 3.000000e+02 [K]
 collision: VHS model
 output file create
 HCA file interval: 1000
 out file interval: 1000
 sorting number: 4
 sorting interval: 250
 * chemical reaction info *
 N : 4 | A,n,Ea
 exchange(forward) : BN + N2 -> BN + 2N
 1.300000e+16 0.000000e+00 1.000000e-25
 exchange(forward) : N2 + BN -> 2N + BN
 1.300000e+16 0.000000e+00 1.000000e-25
 exchange(reverse) : BN + 2N -> BN + N2
 1.000000e+20 1.000000e+00 0.000000e+00
 exchange(reverse) : 2N + BN -> N2 + BN
 1.000000e+20 1.000000e+00 0.000000e+00
 * volume mesh info *
 volume mesh node number: 19263
 volume mesh element number: 93294
 * electric field import *
 electric field number: 1
 [0] C:\Model-Agasratio\Model-A40/efield-0.efin
 frequency: 13.650 MHz
 phase difference : 0.000000e+00 [degree]
 * magnetic field import *
 magnetic field number: 1
 [0] C:\Model-Agasratio\Model-A40/mfield-0.mfin
 frequency: 13.650 MHz
 phase difference : 0.000000e+00 [degree]
 * motion #0 / 1
 Initial ITERATION : 0
 Start Time : +0.000000e+00 [s]
 End Time : +1.200000e-04 [s]

APPENDIX B

THE RESULTS OF THE EXPERIMENTS

B.1 Thickness Measurement Results

The thickness of BN coatings is measured with F20 Filmmetrics. 10 measurement is taken for each BN-coated substrate and their averages are calculated as shown in Table B.1.

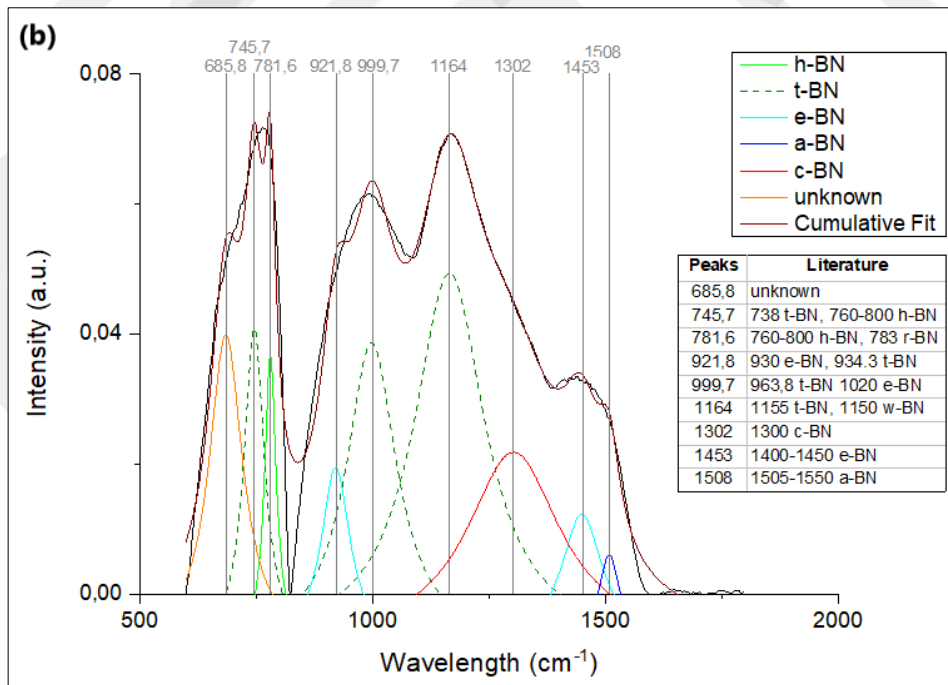
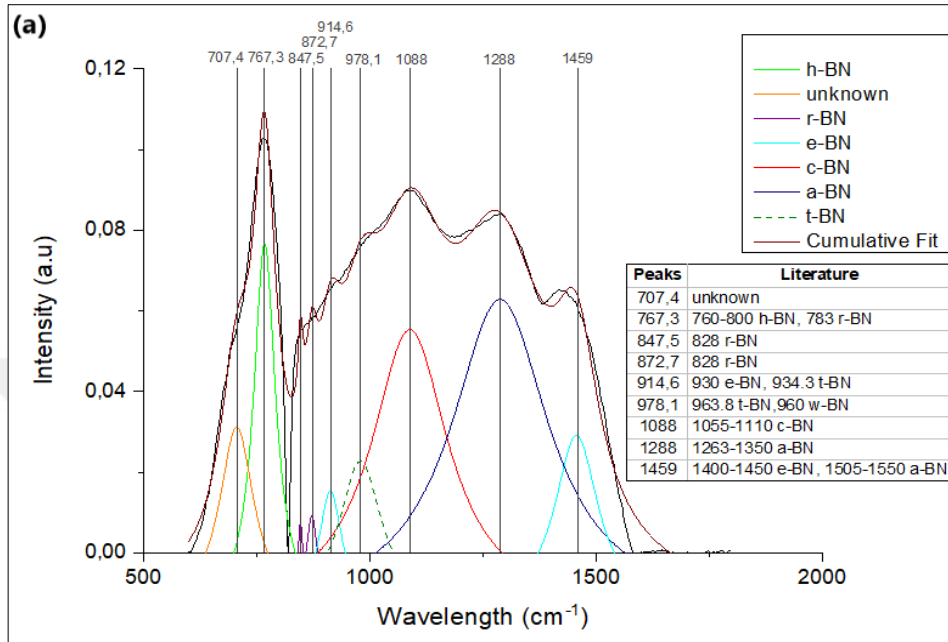
Table B.1 Result of thickness measurement in the experiments

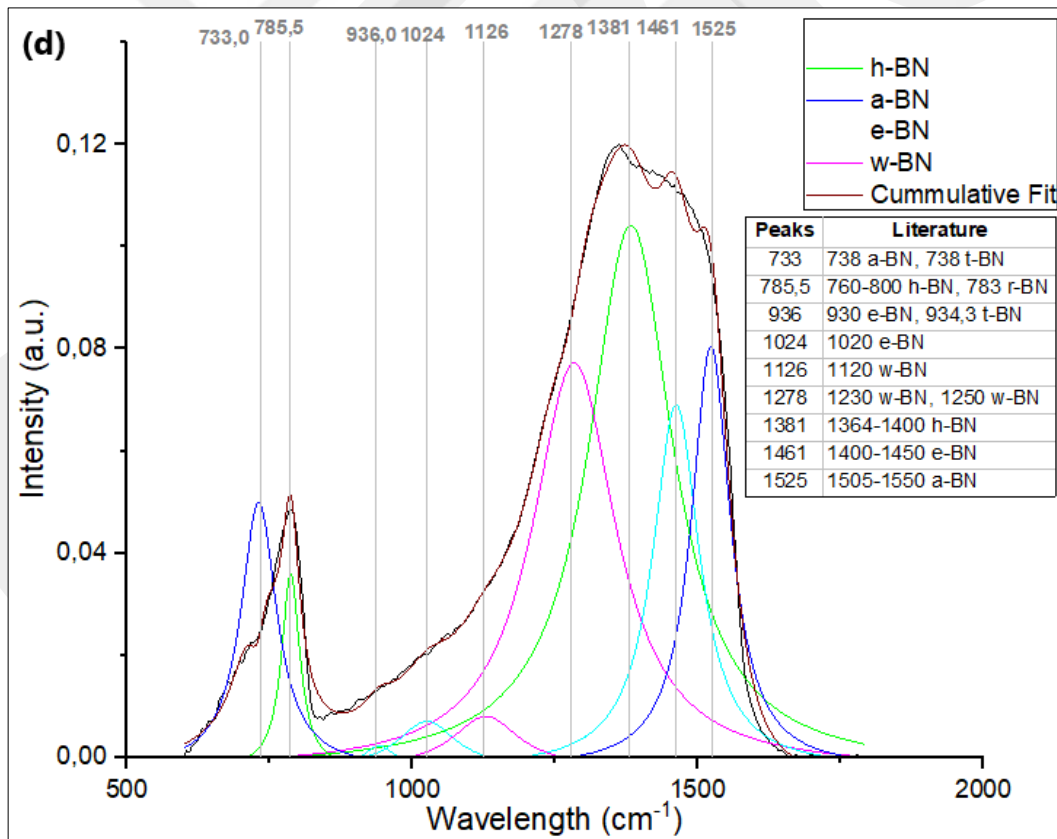
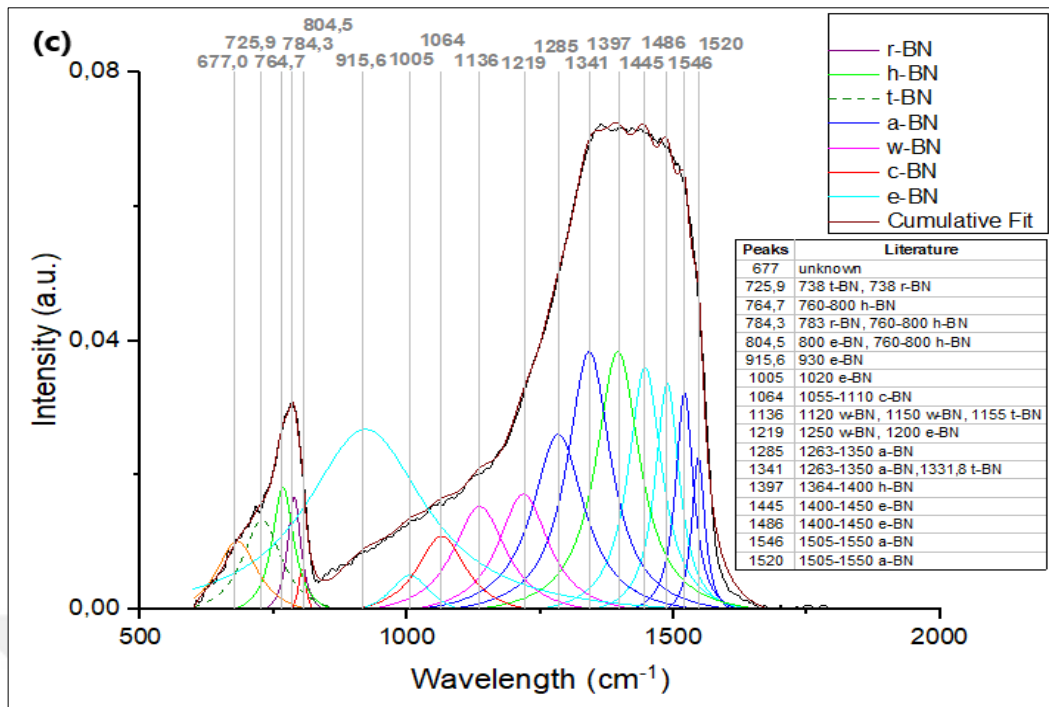
No.	Result of measurements (nm)										Average
RUN 152-D2	63.82	34.77	26.25	245.1	304.6	235.7	154.8	61.61	66.73	150.1	149.4073
RUN 153-D2	930.5	871.6	859.3	886.3	783	811.2	885.3				861.0286
RUN 154-D2	681.5	886.4	670	710.7	677.9	681.1	683.4	670.6	666.6	671.1	699.93
RUN 203-D2-1	1890	1816	1833	1891	1929	1972	1911	1902	1955	1908	1900.7
RUN 203-D2-2	351.5	334.7	325.0	359.2	378.9	399.9	359.2	360.2	352.9	342.9	356.44
RUN 203-D2-3	360.0	360.0	360.0	360.0	357.1	360.0	360.0	360.0	360.0	360.0	359.71
RUN 203-D2-4	206.7	201.8	199.6	195.3	196.7	198.3	208.5	201.1	199.8	196.3	200.41
RUN 209-D2-1	3219	3397	3111	3255	3364	3277	3264	3234	3322	3522	3296.5
RUN 209-D2-2	3450	3575	3500	3741	3971	3500	3440	3634	3116	3258	3518.5
RUN 209-D2-3	188.4	190.7	196	183.5	184.1	181	184	190.8	190.5	195.5	188.45
RUN 217-D2-1	The thickness is less than 50 nm, therefore we could not measure it.										
RUN 217-D2-3											

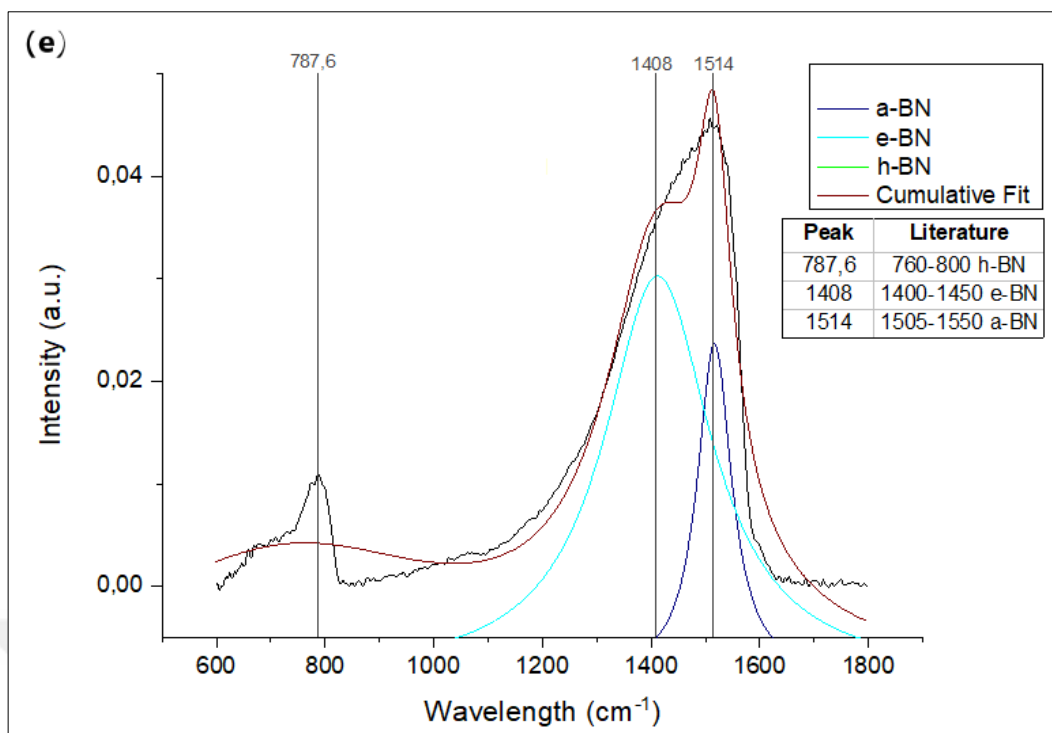
B.2 BN Phases Result (FTIR Analysis)

The Alpha FTIR device is used to examine the phases of the formed BN coatings.

FTIR Analysis as a function of TSD, (a) 50 mm, (b) 100 mm, (c) 200 mm, (d) 230 mm and (e) 290 mm







APPENDIX C

THE QUASI-HARMONIC DEBYE MODEL CODE FOR THE h-BN Structure

C.1 Input File (Sample. Inp)

```
BN
h-BN.out1
24.82
-6.41786245
0
0 0.20819
8 0.0 1.0 2.0 3.0 4.0 5.0 6.0 7.0 8.0 9.0 10.0 11.0 12.0 13.0 14.0 15.0 16.0 17.0 18.0 19.0
20.0 21.0 22.0 23.0 24.0 25.0 26.0 27.0 28.0 29.0 30.0
124 0.0 1.0 2.0 3.0 4.0 5.0 6.0 7.0 8.0 9.0 10.0 11.0 12.0 13.0 14.0 15.0 16.0 17.0 18.0
19.0 20.0 21.0 22.0 23.0 24.0 25.0 26.0 27.0 28.0 29.0 30.0 31.0 32.0 33.0 34.0 35.0
36.0 37.0 38.0 39.0 40.0 41.0 42.0 43.0 44.0 45.0 46.0 47.0 48.0 49.0 50.0 55.0 60.0
65.0 70.0 75.0 80.0 85.0 90.0 95.0 100.0 105.0 110.0 115.0 120.0 125.0 130.0 135.0
140.0 145.0 150.0 155.0 160.0 165.0 170.0 175.0 180.0 185.0 190.0 195.0 200.0 210.0
220.0 230.0 240.0 250.0 260.0 270.0 280.0 290.0 300.0 320.0 340.0 360.0 380.0 400.0
430.0 460.0 490.0 500.0 560.0 600.0 640.0 680.0 720.0 750.0 800.0 850.0 900.0 950.0
1000.0 1100.0 1200.0 1300.0 1400.0 1500.0 1600.0 1700.0 1800.0 1900.0 2000.0
2200.0 2400.0 2500.0 2800.0 3000.0 3300.0 3500.0
21
307.9391004 -6.410423106
294.279664 -6.414431455
291.6372321 -6.415023134
289.0095116 -6.415564833
286.3963674 -6.416052876
283.797867 -6.416488367
281.2139429 -6.416866159
278.6445952 -6.417187724
276.0896888 -6.417448283
273.5492912 -6.417652247
271.0232676 -6.417788591
268.5117528 -6.417859151
266.0145444 -6.417862459
263.5316423 -6.417797043
261.0630467 -6.417659597
258.6087575 -6.417446813
256.1686397 -6.417159426
253.7426933 -6.416793394
251.3309859 -6.416345776
248.9333149 -6.415814367
246.5497478 -6.41519733
```

C.2 Output File (Sample. Out)

Gibbs - (P, T) thermodynamics of crystals from (E, V) data
(c) M.A.Blanco, E.Francisco, and V.Luana, Universidad de Oviedo Questions, bugs, updates:
miguel@carbono.quimica.uniovi.es

BN

Number of data points: 21

Static EOS calculation - Numerical results $V_{\min}(\text{static}; P=0) = 267.12 \text{ bohr}^3$

$G_{\min}(\text{static}; P=0) = -0.02 \text{ kJ/mol}$

NUMERICAL EQUILIBRIUM PROPERTIES

=====

P(GPa)	G(kJ/mol)	V(bohr ³)	V/V0	B(GPa)	rel.err.
0.00	-0.02	267.12	1.00000	86.87	0.115550
1.00	23.68	264.13	0.98881	90.89	0.017648
2.00	47.13	261.30	0.97822	94.78	0.004732
3.00	70.32	258.61	0.96815	98.57	0.001852
4.00	93.29	256.05	0.95855	102.25	0.001209
5.00	116.03	253.60	0.94939	105.84	0.000928
6.00	138.55	251.26	0.94060	109.34	0.000801
7.00	160.87	249.00	0.93217	112.76	0.000925

NUMERICAL EOS PRESSURE DERIVATIVES

=====

P(GPa)	V(bohr ³)	V/V0	Pfit(GPa)	B(GPa)	B'	B''(GPa ⁻¹)
0.00	267.12	1.00000	0.00	86.87	4.0905	-0.142165
1.00	264.13	0.98881	1.00	90.89	3.9566	-0.126141
2.00	261.30	0.97822	2.00	94.78	3.8373	-0.112942
3.00	258.61	0.96815	3.00	98.57	3.7300	-0.101914
4.00	256.05	0.95855	4.00	102.25	3.6329	-0.092586
5.00	253.60	0.94939	5.00	105.84	3.5445	-0.084612
6.00	251.26	0.94060	6.00	109.34	3.4634	-0.077731
7.00	249.00	0.93217	7.00	112.76	3.3888	-0.071743

INPUT AND FITTED VALUES OF THE LATTICE ENERGY

=====

V(bohr ³)	E_inp(hartree)	E_fit(hartree)
246.549748	0.002665120	0.002659956
248.933315	0.002048083	0.002045894
251.330986	0.001516674	0.001516538
253.742693	0.001069056	0.001069749

